NASA TECHNICAL MEMORANDUM

NASA TM X-53647

October 15, 1967

NASA TM X-53647

AERO-ASTRODYNAMICS RESEARCH REVIEW NO. 6

AERO-ASTRODYNAMICS LABORATORY
RESEARCH AND DEVELOPMENT OPERATIONS
GEORGE C. MARSHALL SPACE FLIGHT CENTER
HUNTSVILLE, ALABAMA

NASA - GEORGE C. MARSHALL SPACE FLIGHT CENTER

TECHNICAL MEMORANDUM X-53647

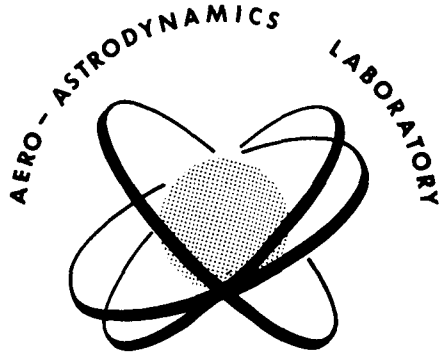

RESEARCH REVIEW NUMBER SIX

William D. Murphree - Editor

RESEARCH AND DEVELOPMENT OPERATIONS
AERO-ASTRODYNAMICS LABORATORY

October 15, 1967

PREFACE

The topics discussed in this sixth Aero-Astrodynamics Research Review cover a variety of subjects. Included are Flight Mechanics, Fluid Dynamics, Planetary Environments, Rarefied Gas Dynamics, Solar Physics, Selenography, and Thermodynamics. Also included, under the heading "Publications and Presentations," are the titles and abstracts of the reports and papers which have been prepared during the past year. First, NASA reports are listed, followed by those papers which have been presented at symposia and those which were printed in the open literature. It should be noted that no single review treats all subject areas being investigated by the Laboratory. Further, these reviews are not progress reports; rather it is attempted here to publish works of a research nature which have reached a milestone worthy of note. Other subjects will be discussed in forthcoming reviews.

It is hoped that these reviews will be interesting and helpful to other organizations engaged in space flight research and related efforts. Criticisms of this review and discussions concerning individual papers with respective authors are invited.

E. D. Geissler
Director, Aero-Astrodynamics Laboratory

CONTENTS. . .

VII. THERMODYNAMICS

VIII. PUBLICATIONS AND PRESENTATIONS

I. FLIGHT MECHANICS

THE IMPACT OF PROPELLANT VENTING ON ORBITAL TRAJECTORY RECONSTRUCTION

By

M. A. Horst and C. L. Varnado

SUMMARY

The results of a study of the impact which propellant venting in earth orbit has on post-flight orbit determination techniques and accuracy are presented. A precise post-flight determination of initial orbital conditions and resulting orbital ephemeris is required to evaluate the onboard guidance system, the orbital control system, and the analytical propellant vent model. The necessity of accounting for the effects of venting is emphasized by examining the orbital ephemeris of the SA-203* trajectory. For example, in one earth revolution, apogee increased 14 km, and by the end of revolution four, apogee had increased by 30 km. This increase was the direct result of propellant venting.

Several methods are available to model venting effects mathematically. One of these is to allow the aerodynamic drag coefficient to vary and use this parameter to account for the effects of venting. This is adequate for a nearly real time determination of initial orbital conditions, but the resulting ephemeris will not suffice for detailed post-flight analysis. Two other methods, which can be used for preliminary trajectory reconstruction, depend on an analysis of propellant behavior and heat transfer theory. These are, basically, a prediction model and an actual model based on telemetered tank pressures, mass loss and other information. The adequacy of these models is limited by present knowledge of the behavior of cryogenics in a low-g environment.

Finally, the most accurate method available to model the effects of venting on the orbital ephemeris is the utilization of the velocity data output from the inertial guidance system. These data reflect the effects of all forces acting on the vehicle and depict the most complete history of resulting vehicle motion. Use of these data not only provides the most accurate orbital ephemeris but also makes possible an accurate post-flight determination of guidance accelerometer bias errors.

I. INTRODUCTION

Over the past several years an Orbit Correction Program (OCP) has been developed for use in reconstructing the orbital flight profile of the Saturn family of vehicles from measured data. The OCP uses an iterative maximum likelihood least squares procedure to determine from tracking observations a "best estimate" set of parameters describing the orbital path of the vehicle. An initial estimate of these parameters is used to generate an orbit ephemeris, using the Cowell Equations of Motion, from which estimated station observations are calculated. These estimates are then compared with the actual tracking observations, and the residuals are used to correct the initial parameters such that the orbit ephemeris closely fits the actual tracking observations. In the past, various auxiliary parameters, such as atmospheric drag, gravitational harmonics, station location, data time bias, etc., were used to facilitate tracking observation fits. For the Saturn I and uprated Saturn I vehicles, these capabilities were adequate for a sufficiently accurate determination of the initial orbital conditions and resulting ephemeris. With the advent of the Saturn V space vehicles, however, the requirement for an additional capability to account for a small, continuous, perturbing force applied to the orbiting body becomes evident.

Saturn V orbiting vehicles have restart capability, which requires maintaining considerable quantities of cryogenic fuel and oxidizers on board during the parking orbit. Because these propellants have very low boiling points, some method must be provided to relieve the pressure buildup resulting from boiloff. Another requirement for restart is that the fuel and oxidizer be settled in the bottom of their respective tanks. Both these requirements are satisfied through the use of a propulsive venting system which allows the gases to be expelled either as they accumulate to a specified pressure level, on command, or continuously for propellant settling. Present planning calls

* Note: An objective of the SA-203 flight was to simulate a Saturn V orbital trajectory and orbital operations preparatory to S-IVB second ignition.

for continuous liquid hydrogen (LH_2) tank venting with ullage venting from the liquid oxygen (LOX) tank as required. The LH_2 venting results in a small, varying, but continuous, acceleration being applied to the orbiting vehicle. This acceleration, since it is applied over long periods of time (on the order of one hour or more), imparts a definite perturbation to the orbital ephemeris. The acceleration must be considered in any attempt to use radar tracking data to define the initial ephemeris conditions. This consideration is necessary, not only to provide an accurate orbital ephemeris, but also to provide a basis for improving the analytical models used to predict vent profiles.

The experimental basis for the information presented herein is the Saturn vehicle SA-203 flight. The specific objective of this flight was to examine the behavior of large amounts of cryogenic fuel and oxidizer in an orbital environment. The discussion following and the conclusions reached reflect the analysis of the data compiled on this flight.

II. METHODOLOGY

The analysis of the effect of disturbing forces on an orbiting body leads, broadly, to two questions. The first question is how to determine the magnitude and direction of the disturbing forces (force profile), and the second is how to incorporate these forces into the equations of motion which are the basis for orbit determination programs.

Three methods for determining the venting acceleration profile are available for Saturn V vehicles. The first is to develop a predicted vent profile based on an analytical analysis using heat transfer theory. Figure 1 shows the SA-203 unadjusted predicted pressure and guidance vent accelerations and velocitites for comparison. Present knowledge of the behavior of cryogenics in a low-g environment is not sufficient to satisfy post-flight evaluation accuracy requirements and targeting requirements for lunar injection; however, these data may be used to form a predicted mathematical model which will suffice for a nearly real-time, or "quick-look" evaluation. Since the complete analytical model cannot be implemented because of computer time and storage limitations, many simplifying assumptions must be made. This is accomplished by trying to predict the total venting acceleration expected based on tank heating cycles, vent orifice size and related information. This total acceleration is then divided into segments that are nearly linear over the time span covered to reduce the quantity of data processed. A simple linear interpolation scheme is used to calculate the total acceleration for the interval between the segment begin and end times. The direction numbers of the total velocity vector are used to break the total acceleration into components. This assumption drastically reduces the quantity of data processed and eliminates the requirement for a continuous time history of vehicle attitude during orbit. The acceleration components are then added to the equations of m .

The accuracy of this method of mathematically representing the venting effect may be somewhat impaired by several assumptions which may or may not be valid. One is the assumption that the acceleration will actually be linear for the chosen segments. Another is that the venting acceleration components will have the same ratio to each other as the vehicle inertial velocity components. Even if these assumptions are erroneous, the resultant initial conditions may still be valid so long as a compensating parameter (such as aerodynamic drag) is allowed to vary. This was done on the SA-203 flight; and, while the initial conditions obtained looked reasonable, the drag coefficient did not. This was remedied by increasing the magnitude of the accelerations (by 15 percent) until a nominal drag coefficient of 1.0 was obtained. Thus, the initial conditions of all parameters fell within the desired accuracy. This does not, however, present an accurate picture of the vent model or an accurate ephemeris, since drag is an effect averaged over the entire orbit and the venting profile is oscillatory rather than continuous.

The second method available to determine the venting acceleration profile is the on-board measurement of pressure in the respective tanks (Fig. 1). These measurements are correlated with mass loss rates, vent orifice size, orifice centerline orientation with respect to the vehicle body axes, and vehicle mass, to calculate the accelerations produced by the venting. The problems inherent in using this method to determine the venting profile are as follows:

1. Orientation of vehicle body axes must be known.
2. Continuous orbital telemetry coverage is not always available.
3. Vent orifice size and alignment are uncertain.
4. Pressure measuring system (located inside tanks) contains inaccuracies.

5. The pressure differential between inside of tank and vent orifice is uncertain.

6. Aerodynamic drag and atmospheric model are uncertain.

7. Short duration, high impulse-producing vents cannot be modeled accurately.

8. There is a large quantity of data to be considered.

Once the acceleration profile has been determined, the same procedures are used to incorporate these data in the equations of motion as was described in the preceding discussion of the predicted vent model. Because of the uncertainties listed above, no great emphasis should be placed on the adequacy or accuracy of the derived venting accelerations. The pressure data are usually the first post-flight data received which allows construction of a mathematical venting model from actual, rather than predicted, values. Once again, as in using the predicted model, the aerodynamic drag coefficient resulting from using this vent model on SA-203 was unrealistic. The pressure derived accelerations were decreased (by 25 percent) in order to obtain a drag coefficient of 1.0 and acceptable values for other parameters. All of the above uncertainties are lumped into pressure vent adjustments since the separate error sources cannot be identified.

The third method available to determine the venting profile is to use the output of the ST-124 inertial guidance system. This system has its origin at the ST-124 stable platform, and its axes are defined as follows:

X is parallel to a normal through the reference ellipsoid at the launch site.

Y completes a right-handed system.

Z is along the firing azimuth.

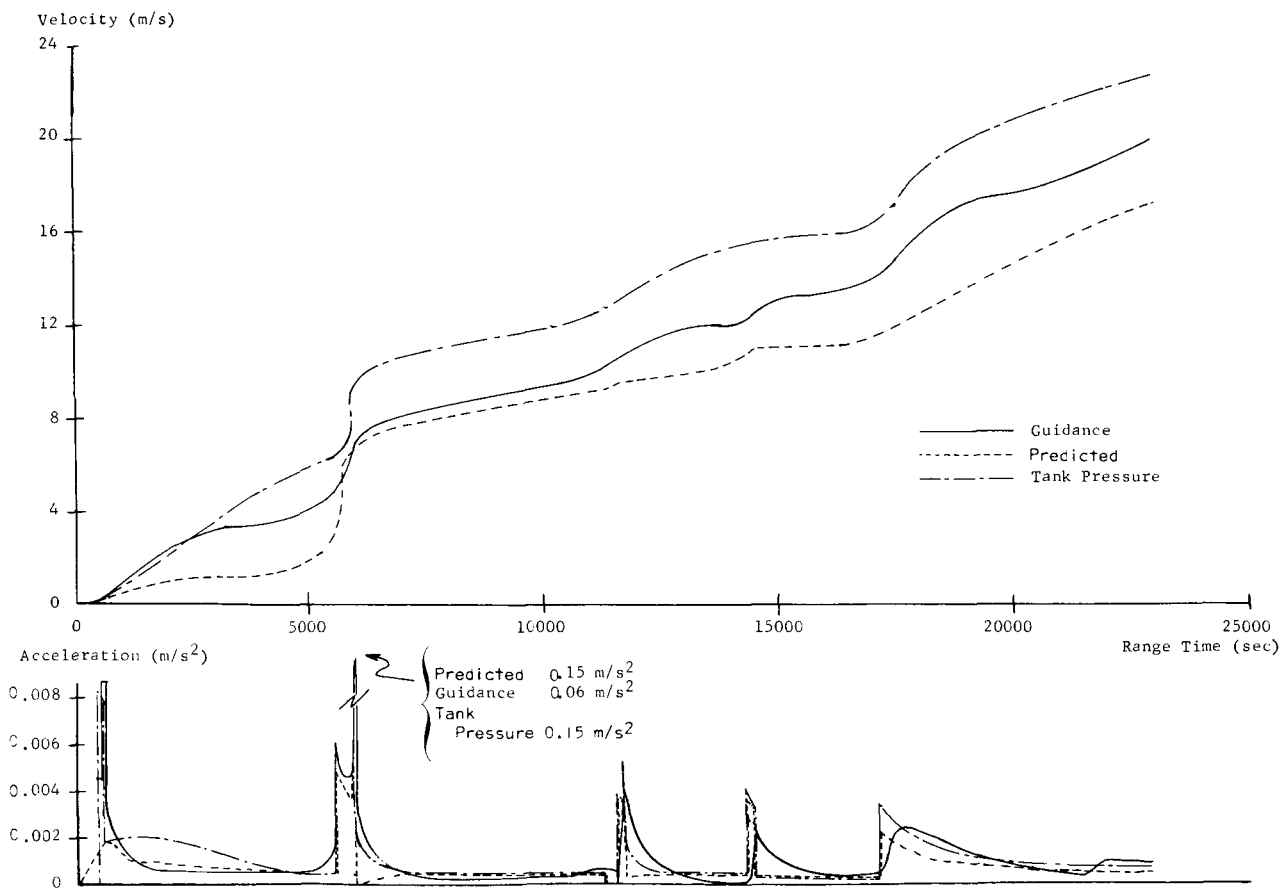

FIGURE 1. SA-203 VENT MODELS

The system becomes inertial at guidance reference release. The output data are the accumulated velocity counts in each of the three axes of the inertial system, as sensed by the guidance accelerometers. Figure 2 shows the guidance outputs obtained during the SA-203 orbital lifetime.

The problems inherent in using this method to determine vent accelerations are (1) uncertainty in accelerometer outputs and (2) a large quantity of data to be considered.

The uncertainties in the accelerometer outputs measuring in a low-g environment are due to three error sources: angular misalignment, accelerometer bias, and sensitivity threshold. Analysis of available data indicates that the accelerometer bias errors constitute the only significant error source. Three-sigma accelerometer misalignments plus three-sigma constant drift errors contribute less than 0.05 m/s velocity error in 22,000 seconds of orbital flight under SA-203 conditions. Since the least significant bit of the telemetered guidance velocity words are 0.05 m/s, error contributions due to angular misalignments are considered insignificant. The sensitivity threshold, i.e., the smallest value of acceleration which the accelerometer can sense, is somewhat harder to define and evaluate. The ST-124 guidance accelerometers were designed to accurately sense accelerations in the 1 g to 5 g range. Their performance in a 10^{-6} g to 10^{-4} g acceleration range was virtually unknown. Again, SA-203 orbital data were used to answer the sensitivity question. Several OCP solutions were made using telemetered guidance velocities and actual tracking data and assuming that acceleration biases were the only error source. Bias error magnitudes were determined from powered flight guidance analysis, each individual revolution, various revolution combinations, and various tracking data combinations. These bias magnitudes all agree very well with the laboratory measurements of bias errors obtained before flight on SA-203. The

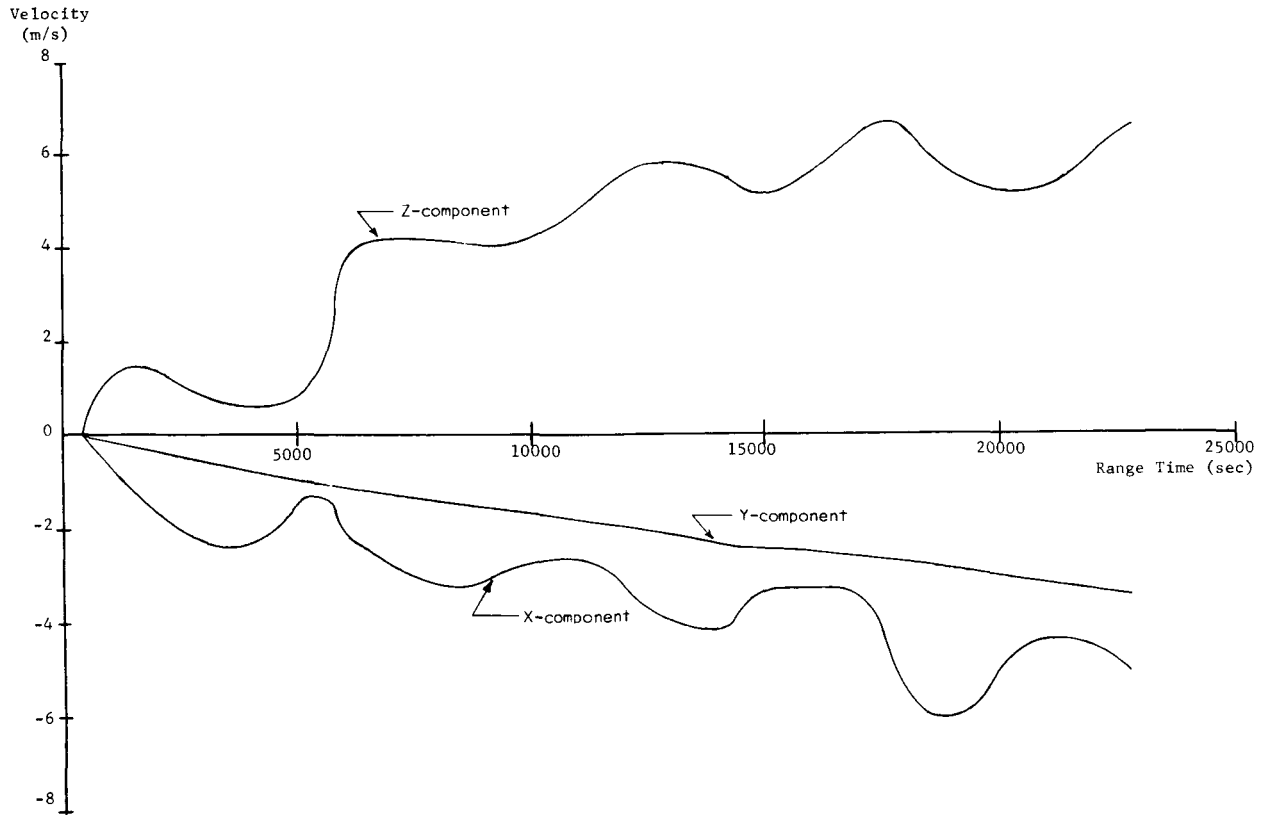

FIGURE 2. SA-203 GUIDANCE COMPONENT VELOCITY PROFILE

discrepancies are less than the laboratory measurement tolerances. The various OCP solutions also yielded initial orbital conditions and tracking residuals which were consistent and very reasonable. The above studies indicate that the problem of uncertainty in accelerometer output can be eliminated by including three additional variables, in the orbital state vector of the OCP, which represent a bias error in each acceleration component.

The disadvantage of large quantities of data is overcome by applying a polynomial curve fit to the component velocity data. This polynomial is then differentiated, and the resulting (acceleration) polynomial is input to the OCP and evaluated at each integration step. The curve-fit routine used is designed to insure that the "break-points" of the various segments meet and continue the same trend. An additional constraint placed on the curve fit is that the integral of the polynomial be equal to the integral of the raw data. In other words, any errors induced by the curve fit process should cancel out. Several tests were made on SA-203 data to assure that polynomials actually did represent accurately the velocity data. In one of these tests, the actual data and the value calculated from fourth degree polynomials were compared. The maximum deviation was 0.7 percent, but the vast majority of the data differed by 0.1 percent or less. In another test, the position error was determined. This was done by calculating the integral of the actual velocity data and the integral of the velocity polynomial at corresponding times. The maximum error in this test was 60 meters, which occurred approximately midway in a 14,000 second span. The position at the end points of various segments represented by the polynomials agreed almost exactly (less than 1 meter difference) with the actual data. If more accuracy is desired, shorter data arcs can be fitted or higher degree polynomials can be used.

Using the inertial guidance velocity data to model the venting acceleration offers the following advantages:

1. Comparative ease in obtaining complete orbital coverage.

2. Ease in "edit" and removal of erroneous data.

3. Data reflection of the effect of all forces acting on the vehicle.

4. Accurate determination of guidance accelerometer bias.

5. Independent check of analytical vent model.

The guidance system uses an on-board data compression and storage system to record the velocity data. This information is read out over ground stations on command. Experience shows that it is possible to retrieve a complete time history of the data if as few as two stations can interrogate the vehicle per revolution. Since the data obtained have a low random noise content, a variate difference program may be effectively employed to quickly eliminate any spurious data. The large number of data points combined with polynomial fitting allows questionable data to be eliminated without replacement. Since the accelerometers sense all forces acting on the vehicle, the aerodynamic drag factor and any unknown torques are no longer a problem. The SA-203 studies indicate that the intercorrelation between the three bias errors and the correlation between the bias errors and the initial condition errors are less than 0.7. The error contributed to the bias estimates due to using acceleration polynomials are negligible. The SA-203 accelerometer bias error estimates obtained from the orbital analysis agreed very well with preflight laboratory measurements. An accurate orbital ephemeris generated from data which are not propulsion or propellant related makes a firm base for trajectory simulations aimed at verifying the analytical vent model. If pressure data are used in orbit determination, all errors are accounted for by shifting the level of the pressure vents. Trajectory simulation will then only recover the shifts that were incorporated and may thus lead to false conclusions.

Table I presents a comparison of SA-203 initial orbital conditions, in Apollo Standard Coordinate Systems 1 and 10, obtained from the various vent models discussed in this section. Also included in the comparison are two cases which did not consider a venting profile. All cases used observations from five C-Band radar sites distributed over 5600 seconds of flight. The results shown for each case are taken from the fifth least squares iteration of the OCP.

III. CONCLUSIONS

Several conclusions may be drawn from the SA-203 analysis. The primary conclusion is that the venting accelerations must be accounted for in the orbit determination scheme in some manner. The importance of doing so is emphasized by examining the changes that venting caused in the SA-203 orbital conditions. For example, apogee increased by 14 km after one revolution and by 30 km after four revolutions as a result of venting. The various initial conditions shown in Table I further emphasize the necessity of accounting for venting in some manner.

TABLE I. SA-203 INITIAL ORBITAL CONDITIONS

PARAMETER			POLYNOMIAL VENT MODEL	DIFFERENCE FROM POLYNOMIAL VENTS			
				ADJUSTED PRESSURE VENT MODEL	ADJUSTED PREDICTED VENT MODEL	NO VENTS NO DRAG VARIATION	NO VENTS DRAG VARIES*
EARTH FIXED VELOCITY		(m/s)	7387.9	0.2	- 0.4	5.1	- 0.6
AZIMUTH		(deg)	81.989	- 0.002	- 0.003	0.005	- 0.030
ELEVATION		(deg)	0.002	0.004	0.010	0.045	0.013
RADIUS		(m)	6563370.7	- 97.7	110.3	-6677.8	- 130.7
LATITUDE		(deg)	31.1615	- 0.0002	0.0005	- 0.0064	- 0.0038
LONGITUDE		(deg)	293.6786	0.0003	0.0009	0.0075	0.0015
EARTH FIXED	X_e	(m)	31479.9	-110.3	-126.5	-6632.8	- 145.2
POSITION	Y_e	(m)	45154.2	34.3	- 35.7	760.4	463.3
COMPONENTS (PACSS 10)	Z_e	(m)	1438312.5	- 0.3	71.8	- 883.1	30.6
EARTH FIXED	$\dot{X}_e$	(m/s)	-1614.0	0.5	0.1	3.9	1.6
VELOCITY	$\dot{Y}_e$	(m/s)	362.2	- 0.1	- 0.5	0.4	- 4.1
COMPONENTS	$\dot{Z}_e$	(m/s)	7200.3	0.3	- 0.2	6.0	- 0.1

*FINAL COEFFICIENT OF DRAG -21.6

The fourth column of Table I presents a case which has no venting information considered and no variable aerodynamic drag coefficient. The resulting initial orbital conditions are in very poor agreement with the other cases. The last column of this table illustrates that the initial conditions are substantially improved if the vent model is represented by a variable drag coefficient. This simple model yields sufficiently accurate initial conditions to satisfy most nearly real-time and quick-look requirements. In fact, the SA-203 study indicates that this simple model yields better results than the unadjusted predicted or pressure vent models unless the drag coefficient is allowed to vary. The variable drag coefficient concept is not sufficient for detailed postflight evaluation since a variation in drag coefficient is essentially a constant shift in acceleration for nearly circular orbits. Thus, in the case of the simple model discussed above, a constant acceleration would replace the acceleration profile shown in Figure 1. Although the initial conditions are fairly good, the resulting orbital ephemeris leaves something to be desired. The second and third columns of Table I compare the initial conditions from the pressure and predicted vent model cases with those from the case using the polynomial vent model. Agreement is fairly good, but it must be pointed out that the accelerations produced by these models have been decreased 25 percent and increased 15 percent, respectively. Even though the initial conditions are in good agreement, the ephemeris resulting from using these cases may not be as accurate as desired since any error in the predicted drag coefficient is reflected as a vent acceleration adjustment. Also the vent adjustments are applied uniformly to the acceleration history since no mechanism is available to determine the proper adjustment distribution between LH_2 continuous vents, LOX ullage vents, and fuel lead vents.

The vent model using the polynomials derived from guidance data yields the most accurate orbital ephemeris and initial conditions. This is true for several reasons. The guidance data reflect the effects of all the forces acting on the vehicle. Therefore, errors in drag or unknown torques do not affect the orbit determination scheme. Also, the changes due to short duration vents will appear when they actually occur and will not be averaged over long time periods. Analysis reveals that the accelerometer bias errors are by far the major source of error in the guidance

data. These bias errors must be considered as additional variables in the OCP or the data corrected for known bias errors before use in the OCP. An important by-product of the polynomial vent model method is the accurate determination of guidance accelerometer bias errors. This will aid the post-flight guidance error analysis because bias errors are highly correlated with several other guidance errors during powered flight. The precision orbital ephemeris obtained from this method will make possible the improvement and verification of the analytical vent model through flight simulation techniques.

EARTH ORBITAL LIFETIME AND SATELLITE DECAY

By

Robert H. Benson, Edwin F. Fleischman, and Robert J. Hill

ABSTRACT

The prediction of the orbital characteristics of satellites confronts engineers and scientists with several challenging problems concerning the structure of an upper atmosphere as well as low density aerodynamics and the orbital mechanics of uncontrolled bodies. In particular, drastic changes in upper air density are caused by fluctuations of solar output. Although a pronounced periodicity has been observed in solar activity, no reliabile prediction is possible yet over extended periods of time.

I. INTRODUCTION

An increasingly important factor in mission analysis and mission planning is the prediction of satellite decay and orbital lifetime. It is well known that, in general, the greater the altitude the longer the orbital lifetime. However, since higher orbiting altitudes cost fuel and/or payload, it is often necessary to find the minimal orbital energy which will insure necessary stay time above a given altitude. Orbital decay prediction is especially critical in the case of rendezvous and multiple payload missions. When an actual mission is being monitored, a fast and accurate decay prediction is an extremely helpful, if not an essential, tool for mission verification and operational decision making.

Near the time of reentry of passive vehicles it is necessary that satellites be tracked as frequently as possible to perform a proper reentry analysis. Orbital lifetime predictions have proved to be a cost saving factor in alerting the world wide tracking network to the time when more intense surveillance becomes necessary.

The ability to accurately simulate orbital decay is not without engineering and scientific rewards. It will be pointed out in the course of this paper how the ability to accurately predict orbital lifetime depends on an understanding of the dynamics of the upper atmosphere and low density aerodynamics. Hence, the ability to accurately simulate the history of decayed satellites gives the scientist and engineer the ability to verify proposed hypotheses concerning these disciplines.

The article is divided into three main sections as follows: (1) a discussion of the lifetime prediction model; (2) past experience and results; and (3) soft spots or the areas which need increased research and effort.

II. THE LIFETIME MODEL

The general philosophy of any lifetime model must be to accurately compute orbital decay or the time history of energy loss over long periods of time. These periods of orbital lifetime may be as short as a few orbits or as long as six years. In order to compute energy loss over long periods, ordinary time step integration to obtain position and velocity cannot be utilized; instead, the simpler equations for the time rate of change of apogee and perigee are integrated. Integrating the "apogee dot" and "perigee dot" equations permits fast and accurate simulation of the energy loss of the vehicle.

As is stated in the Introduction, the primary cause of satellite decay in the less than 700 km altitude domain is aerodynamic resistance to the vehicle. These aerodynamic factors are influenced by the drag coefficient, the effective drag area, the density of the atmosphere, and the elements of the vehicle's orbit. Of course, the elements of the orbit are predominately affected by lunar and solar perturbations, the gravitational potential of an aspherical earth, and aerodynamic resistance.

The equations used to compute orbital decay are those of the rate of change of apogee and perigree denoted respectively by $\dot{A}$ and $\dot{P}$. The equations for $\dot{A}$ and $\dot{P}$ assume the general form:

$$\dot{A} = \frac{C}{2\pi M}\sqrt{\frac{a(1+e)}{(1-e)^3}}\int_0^{2\pi}\frac{D(\nu)(1+\cos\nu)\,d\nu}{K(\nu)} \text{ (km/day)} \quad (1)$$

$$\dot{P} = \frac{C}{2\pi M}\sqrt{\frac{a(1-e)}{(1+e)^3}}\int_0^{2\pi}\frac{D(\nu)(1-\cos\nu)\,d\nu}{K(\nu)} \text{ (km/day)} \quad (2)$$

where

C = -86.4×10^6, converting seconds meters to days kilometers
M is the mass of the orbiting configuration (kg)
a is the semimajor axis (km)
e is the orbital eccentricity
ν is the true anomaly (deg)
$K(\nu)$ is the gravitational function
$D(\nu)$ is the aerodynamic resistance function.

Equations 1 and 2 are derived starting with the solution of the two-body problem and adding perturbative terms of previously mentioned forces. For a detailed derivation of these equations, see [1] and [2].

Most of the above terms are self explanatory except $K(\nu)$ and $D(\nu)$. The symbol $K(\nu)$ represents the entire sum of gravitational accelerations including the earth's harmonics, the moon and the sun. Actually, the gravitational perturbations experienced by the vehicle are not directly a function of the true anomaly but are a function of position which in turn is computed from the orbital elements and the true anomaly. The function $D(\nu)$ describes generally the drag on the vehicle and can be factored as follows:

$$D(\nu) = (C_D)(A_{ref})(\rho)(1+2\ e\ \mathrm{Cos}\ \nu + e^2)^{1/2}. \quad (3)$$

In the two-body problem, $V^2 = \mu/a\,(1+2\ e\ \mathrm{Cos}\ \nu + e^2)$, where μ is the gravitational constant and V^2 is the square of the satellite's velocity. It would seem at first glance that since $D(\nu)$ is factorable, as in equation (3), the factors C_D, A_{ref}, and ρ could be brought outside the integrals of equations (1) and (2); this is, however, not always the case, since for computational purposes, they are partially or totally considered as functions of ν. For example, if a vehicle is tumbling in the flight plane at the rate of one-half orbital period and the orbit is eccentric, the C_D, A_{ref}, and ρ could all be, and actually are, computed indirectly as functions of the true anomaly. Admittedly, the above example is an over simplification but various aspects of C_D and A_{ref} will be dealt with later in more detail.

In the above simplified example, it was stated that ρ could be a function of true anomaly. In actuality, ρ is computed in the lifetime model as a function of time and altitude. It has been found from satellite decay that the density of the rarefied upper atmosphere varies directly with the eleven-year solar cycle. Hence, in predicting orbital lifetime, it is important to predict the level of solar activity. There are several accepted measures of solar activity, two of which are the most convenient to work with for the purposes of predicting lifetime. These two measures are the solar decimeter radiation or the 10.7 cm solar flux (10^{-22} watts/m^2/cps) denoted by $F_{10.7}$ and the smoothed sunspot number denoted by R_Z. It would be highly desirable to determine the effects of solar activity on the atmosphere by using $F_{10.7}$ since it can be more precisely measured. However, because of the limited amount of solar flux data available (recorded since 1947), it is preferable to use sunspot data in the statistical prediction of solar activity. These sunspot data have been recorded since 1749; however, the accuracies of the sunspot count are subject to human error.

The quantities, $F_{10.7}$ and the monthly average $\bar{F}_{10.7}$, are used in the equations to compute the atmospheric density. Unfortunately, solar flux data, as stated above, are available only for the last one and three-fourths cycles while sunspot data are available over 19 cycles. This problem is circumvented by the excellent correlation between $\bar{F}_{10.7}$ and smoothed sunspot numbers.

Figure 1 shows the high correlation between these variables. The three equations on Figure 1 give the piecewise linear regression functions that are used to map sunspot numbers onto $\bar{F}_{10.7}$.

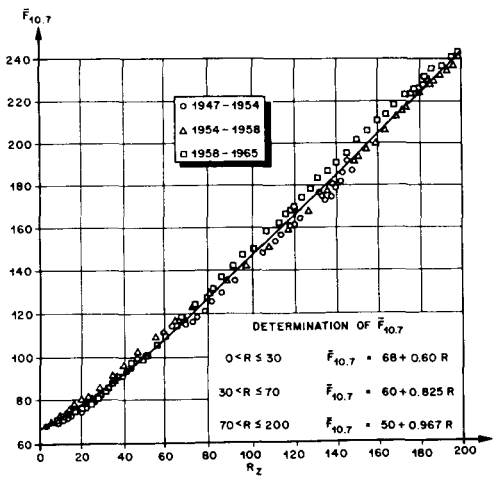

FIGURE 1. CORRELATION OF $\bar{F}_{10.7}$ WITH SMOOTHED SUNSPOT NUMBER

Before going into the prediction of solar activity, a discussion of the equations for computing density as a function of time and altitude will be covered. The actual equation used in the calculation of density is:

$$\rho = \rho_o(h)\ (S/S_o)^K\ D(\psi) \qquad (kg/m^3) \qquad (4)$$

where

- $\rho_o(h)$ is an altitude dependent atmosphere such as the 1962 U. S. Standard
- S/S_o is a heating parameter
- K is a function of altitude
- $D(\psi)$ represents the diurnal bulge effects (see equation 8).

The quantity (S/S_o) which is denoted as a heating parameter is a function of $F_{10.7}$, $\bar{F}_{10.7}$, the geomagnetic index, K_p, and time. The actual equation for S is:

$$S = \left[25 + .8\,\bar{F}_{10.7} + .4(F_{10.7} - \bar{F}_{10.7}) + 10\,K_p\right]\ e^{g(t)} \qquad (5)$$

where

$$g(t) = .025 \cos\left[2\pi\left(\frac{t - 38047}{365.25}\right)\right] + .06 \cos\left[4\pi\left(\frac{t - 38047}{365.25}\right)\right] \qquad (6)$$

and g(t) represents the seasonal effects on the density of the atmosphere. Since equation (6) represents seasonal effects, it must be referenced to some ephemerial quantity. The epoch chosen for this equation is the Modified Julian Day 38047 and t is the modified Julian Day of the epoch of the satellite orbital elements under consideration. The quantity S_o is a constant which is unique to the base atmosphere ρ_o (h). For the 1962 U. S. Standard atmosphere, S_o is 200. The quantity K which is a function of altitude is:

$$K = .81\left[3 + 2.5\left(\frac{h - 360}{240}\right) - .5\left(\frac{h - 360}{240}\right)^2\right] \qquad (7)$$

where h is the altitude of the satellite in kilometers. It can be shown that K is monotonically increasing with altitude in the region of interest (120-700 km); and, since K is an exponent, it is deduced that the higher the altitude, the greater is the effect of solar activity. The diurnal effect is given by the equation:

$$D(\psi) = \frac{1 + .19\,(e^{.0055\,h} - 1.9)\left(\frac{1 + \cos\psi}{2}\right)^3}{1 + .19\,(e^{.0055\,h} - 1.9)\left(\frac{1 + \cos 75^o}{2}\right)^3} \qquad (8)$$

The angle ψ in equation (8) is the angle between the geocentric vectors to the vehicle and through the center of the diurnal bulge. The position of the diurnal bulge is computed in the lifetime model from the sun's ephemeris.

The prediction of solar activity which is presently considered to be a statistical problem is accomplished by a modification of the Lincoln-McNish method. Briefly, the method measures, in the least square sense, the departure of the cycle being predicted from the mean of all the previous cycles. Figure 2 is a graph showing a superposed plot of all of the recorded sunspot numbers. It is noticed that at the beginning and end of the cycles, the variance bands

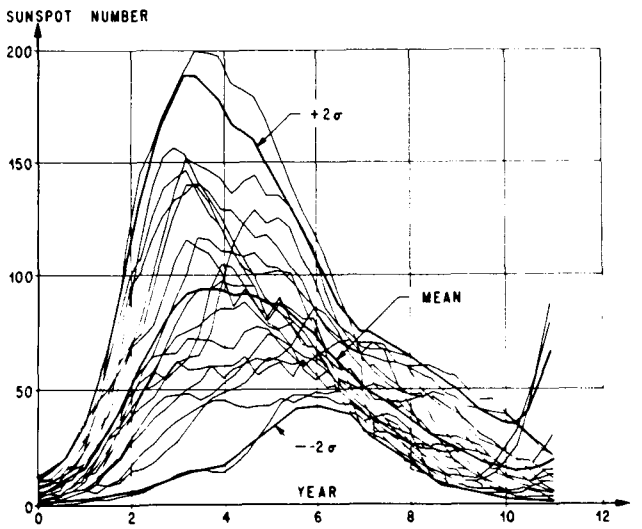

FIGURE 2. SUPERPOSED SOLAR CYCLES (NUMBERS 1-19)

are rather tight while at the time the peak should occur, the variability is quite large. Figure 3 presents a prediction of the present solar cycle by the above method. As more information is gained about

the present cycle, the prediction is, as a matter of routine, updated.

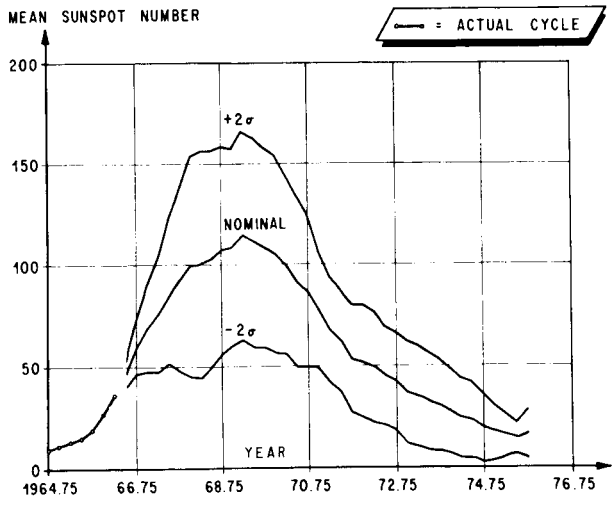

FIGURE 3. PREDICTION OF SOLAR ACTIVITY

The empirical relationship between solar activity and atmospheric density was given earlier. Figure 4 presents the predicted atmospheric density at four discrete altitudes; it is pointed out that the change in the density is greater at the higher altitudes. The effects of the statistical bounds of sunspot prediction on the atmospheric density are plotted in Figure 5. Also shown in this figure are the time invariant 1959 ARDC and the 1962 U. S. Standard atmospheres. Reference to equations (1) and (2) vividly illustrates the amount of error that would be made by using such time invariant atmospheres for lifetime computations.

The function $D(\nu)$, equation (3), which is a factor of equations (1) and (2), the basic lifetime equations, contains the factor C_D which is the aerodynamic drag coefficient. In the altitude domain of interest for orbital lifetime (above 120 km), the continuum aerodynamics used for the denser atmosphere are no longer valid and must be replaced by calculations based on free molecular flow theory. Recently, a great deal of research and engineering effort has been expended in defining the critical parameters in free molecular flow aerodynamic theory. Schamberg's analysis of these flow regimes permits a general form for the drag coefficient, C_D, to be expressed as

$$C_D = 2\left[1 + \phi\left(1 - \alpha\left(1 - \frac{T_w}{T_i}\right)\right)\right] f(\gamma) \qquad (9)$$

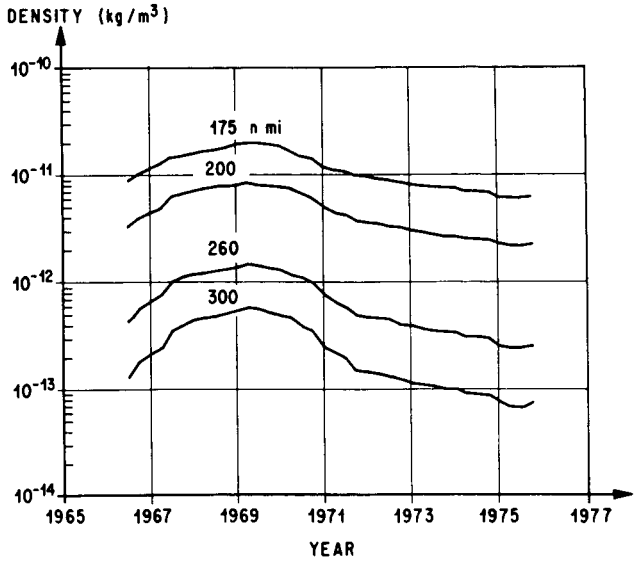

FIGURE 4. UPPER ATMOSPHERIC DENSITY OVER THE 11-YEAR SOLAR CYCLE FOR DISCRETE ALTITUDES

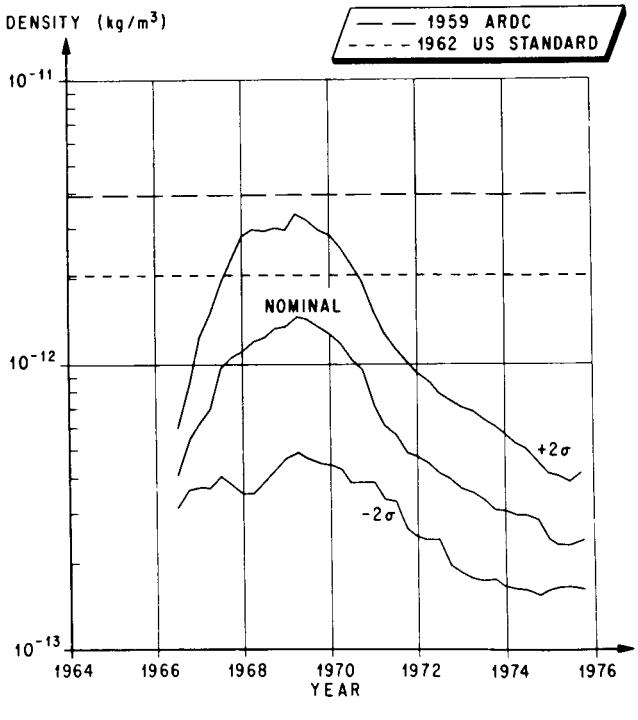

FIGURE 5. DENSITY AT 260 NAUTICAL MILES

where

ϕ is a function dependent on the type of reflection of incoming molecules

α is the energy accommodation coefficient

T_w is the surface temperature of the body (deg K)

T_i is the kinetic temperature of the incoming molecules (deg K)

$f(\gamma)$ is a function of the geometry and attitude of the orbiting body.

There are assumptions concerning the parameters in equation (9) which should be mentioned:

(1) ϕ varies from 1 to 2/3 depending on specular or diffuse reflection, respectively. In the computation of lifetime, diffuse reflection is assumed.

(2) T_w can be assumed to be a constant $300^{o}K$ over all altitudes, since the ratio T_w/T_i varies from 0.01 to 0.004, thus rendering the small temperature influence insignificant.

(3) $\alpha = 1$; it is actually a function of the weight ratio of incoming molecules and surface atoms. Also, speed ratio and physical surface properties may be of influence. It is, therefore, somewhat dependent on surface material plus composition of the atmosphere. However, a value close to one seems to be fairly representative for satellites. Final knowledge of accurate values for α will have to come from laboratory test work and ultimately from the analysis of actual satellite decay in orbit.

(4) $f(\gamma)$ is a deterministic function which assumes the satellite to be tumbling about a transverse axis which is perpendicular to both the flight direction and the axis of symmetry of the body. The method just described is called the preferred tumbling method and replaces the older equivalent sphere method which assumed that one-fourth the total surface of the vehicle was presented to the direction of motion when the vehicle was in a random tumble.

The references concerning hyperthermal free molecular flow aerodynamics are numbers 3 through 16.

III. PAST EXPERIENCE AND RESULTS

Extensive studies have been performed to verify the validity of the orbital lifetime model. Perhaps the only true test of such a model is to compare the computed decay of satellites to the observed decay. This test has been performed for a sample of 39 satellites which have lifetimes ranging from 3 to 525 days. These satellites were in orbit during periods ranging from maximum to minimum solar activity. A comparison is facilitated by examining the ratio of actual lifetime to computed lifetime. Figure 6 presents a scatter diagram of this variable. Let it be emphasized that Figure 6 is not a graph of prediction but rather a graph demonstrating the validity of the model when the unknowns are reduced to a minimum. For example, the solar cycle for these cases was known since the computations were made post decay. The mean of these ratios is one. The standard deviation of the ratio is 0.082 which is probably caused by the uncertainty of the C_D. If the same set of

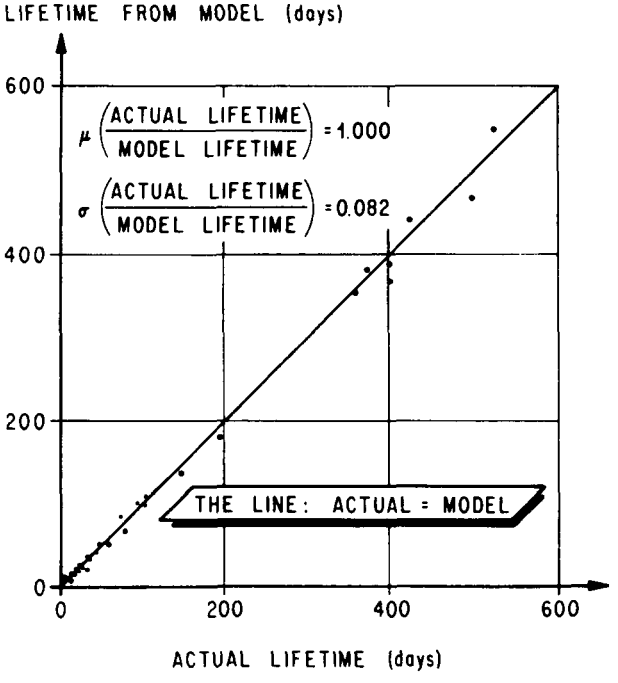

FIGURE 6. LIFETIME FROM MODEL VERSUS ACTUAL LIFETIME (USING 39 VEHICLES)

satellites is studied by making use of a solar activity prediction that would have been made prior to launch, then it is seen in Figure 7 that the mean becomes 0.978 with a standard deviation of 0.117. This illustrates the importance of the uncertainties in density prediction.

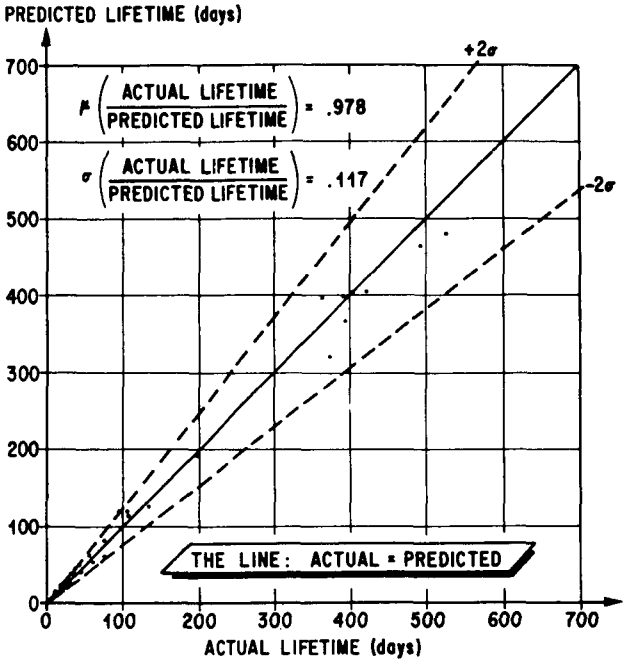

FIGURE 7. PREDICTED LIFETIME VERSUS ACTUAL LIFETIME (USING 39 VEHICLES)

The Saturn vehicle, SA-5, which had an orbital lifetime of over 800 days and decayed on April 30, 1966, was intensively studied to verify the density models and the aerodynamic characteristics. The C_D was computed in two ways, one using preferred tumbling geometry and the other using equivalent sphere geometry. Figure 8 presents five computed decay curves for SA-5; the one plotted as a dashed curve represents a C_D computation incorporating the equivalent sphere techniques, while the solid lines incorporate preferred tumbling techniques. The two decay curves at the left, terminating between 200 and 300 days are results of applying the solar activity invariant 1959 ARDC and 1962 U.S. Standard atmospheres. When these base atmospheres are shifted according to solar activity as in equations (4) through (8), the results more nearly compare with the actual decay. In fact, using the preferred tumbling technique

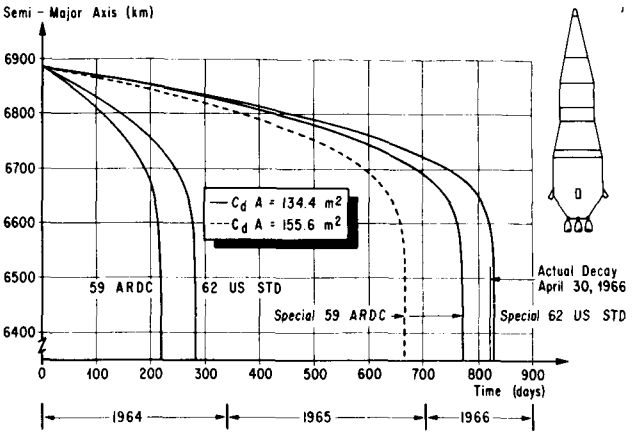

FIGURE 8. SA-5 DECAY

of C_D computation and the shifted or special 1962 density, the results obtained are within two days of the actual decay of this satellite.

As can be seen from the above comparisons of actual and computed lifetime, the art of lifetime predictions has achieved a creditable level of sophistication and reliability. However, it is realized that this piece of coal, though far from the metabolic state, is not as yet a diamond.

IV. SOFT SPOTS

The term "soft spots" is used to imply that there are areas in the aforementioned techniques which need more developmental effort. For the sake of clarity, the soft spots are divided into three major categories. These categories are:

1. Solar Activity Prediction
2. C_D Computation
3. Long Term Attitude Prediction.

The prediction of solar activity or what is equivalent to the determination of atmospheric density is a critical element in lifetime prediction. It is realized that the method used for density prediction and consequently lifetime analysis leaves room for improvement. There are certain weaknesses, the most glaring of which is the present inability to predict more realistically into the next solar cycle. It is hoped that improvements in the prediction of the next cycle might be obtained by

tying it more closely to previous cycles rather than just averaging on all previous cycles. Also, it is hoped that the dependence of solar activity on other observable physical phenomena may be established. (See reference 17).

The second soft spot, C_D computation, is still very much in the theoretical stages of development. In fact, at the present time, all of the experimental data have been obtained from satellite decay, and the lack of knowledge of the orbiting attitude of these bodies makes it impossible to separate the terms such as accommodation coefficient, molecular reflection, etc. At the present time, there is a very minimal amount of controlled laboratory data which are badly needed to substantiate the various theoretical findings.

In the future, it may be possible to develop rigidly controlled satellite programs which would eliminate the unknown factors related to hyperthermal free molecular flow areodynamics that exist in the present orbiting configurations.

However, the qualitative influence of the uncertainty in the knowledge of C_D, for a given geometrical configuration, is sometimes much less significant than the long term attitude prediction. In the past, the weight and volume of satellites limited irregularities in the geometric shapes; thus, most of the early satellites were constructed as spheres, cylinders, cones, etc. With the advent of larger launch vehicles and more complex orbital missions, a growing complexity in satellite shapes must be considered. As an example, Pegasus C/SA-10 is a relatively unusual configuration as can be seen in Figure 9. Pegasus C has dramatically illustrated the importance of knowing the orbiting attitude of the vehicle. Figure 10 is presented in evidence of this fact. The dotted lines show the predicted decay making the assumption that the vehicle is in a random tumble while the solid lines show the predicted decay using the attitude observed by active attitude sensors on the vehicle. Pegasus C is presently orbiting with the body spinning in the orbital plane such that the large meteoroid panels are tending to present a minimum drag area. The vehicle is also precessing about the maximum moment of inertia with a cone angle of about 30°. Referring to Figure 10, the difference in the two lifetime predictions is 1100 days, assuming the vehicle was in a random tumble.

Even though Pegasus C is an unusual configuration, the application of space science in earth orbit

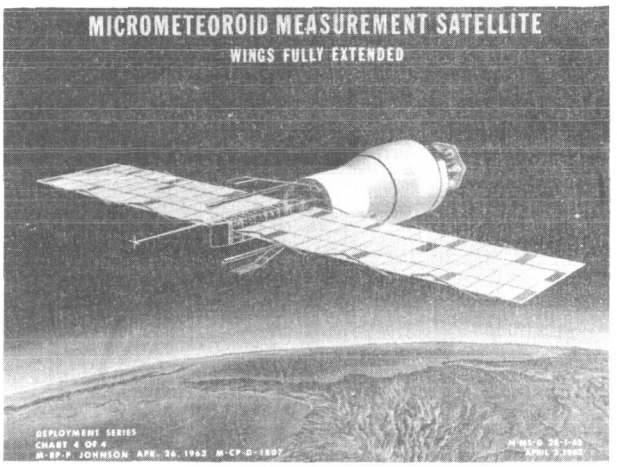

FIGURE 9. PEGASUS C/SA - 10

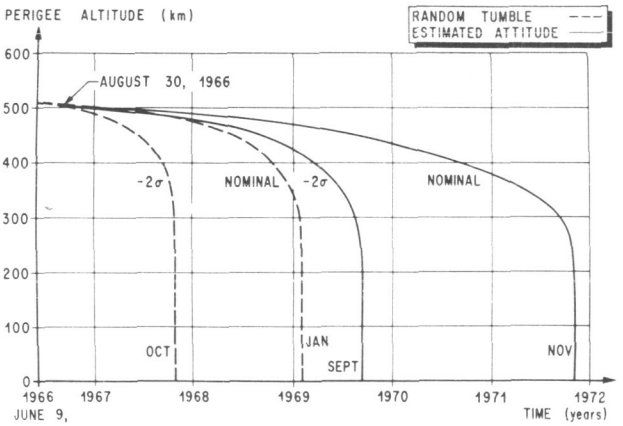

FIGURE 10. SA-10 NOMINAL DECAY OF PERIGEE

will demand the use of complex shapes with very pronounced deviations from symmetry. Hence, the need for continued research efforts in the long term prediction of asymptotic attitudes is apparent. In any investigation or analysis of long term attitude prediction, the effects of aerodynamic torques, gravity gradient torques, geomagnetic torques, solar radiation pressure torques, etc., must be taken into account and their description on at least a statistical basis is a prerequisite for attitude prediction. The remaining task is then the establishment of efficient mathematical procedures to define the effective attitude over considerable time spaces short of step-by-step numerical integration.

V. CONCLUSIONS

The ability to predict long time characteristics of orbiting satellites has recently been much improved. In general, the main factor of uncertainty is caused by lack of understanding of the upper atmosphere. Further efforts towards development of better predictions of solar output fluctuations, possibly based on identification of other observable causes for such fluctuations, appear to be warranted.

Better definition of gas-surface interactions will hopefully be obtained by laboratory experiments and probably even more promising by well planned orbital experiments.

Long term attitude prediction needs improvements particularly for some of the highly asymmetrical uncontrolled satellite configurations.

REFERENCES

1. McNair, Ann R.; and Boykin, E. P.: Earth Orbital Lifetime Prediction Model and Program. NASA TM X-53385, February 1, 1966.

2. Kilgo, H. F.: MSFC/LMSC Satellite Orbit Decay and Orbital Lifetime Program. LMSC/HREC A710725, Technical Report HREC/0082-I, Lockheed Missiles & Space Company, Huntsville, Alabama, June 18, 1965.

3. Sentman, Lee H.: Free Molecule Flow Theory and Its Application to the Determination of Aerodynamic Forces. Lockheed Missiles & Space Company, LMSC 448541, October, 1961.

4. Sentman, Lee H.: Effect of Degree of Thermal Accommodation of Free Molecule Aerodynamic Coefficients. Lockheed Missiles & Space Company, Sunnyvale, California, ARS Journal, September 1962.

5. Schamberg, R.: A New Analytic Representation of Surface Interaction for Hyperthermal Free Molecular Flow with Application to Neutral-Particle Drag Estimates of Satellites. ASTIA Document Number AD 215301, January 8, 1959.

6. Maslach, G. J., et al.: Recent Experimental and Theoretical Extensions of Nearly Free Molecular Flow. Report No AS-64-11, Institute of Engineering Research, University of California, Berkeley, California, June 22, 1964.

7. Hamel, Bernard B.: A Model for the Transition Regime in Hypersonic Rarefied Gas Dynamics. Space Sciences Laboratory, Missile and Space Division, General Electric Company, Preprint No. 63-438. Paper presented at AIAA Conference on Physics of Entry into Planetary Atmosphere, MIT, August 26-28, 1963.

8. Shen, S. F.: An Improved Method for the Transition Regime in Rarefied Gas Flows and its Application to the Linearized Plane Couette Flow. NOLTR 61-68, U.S. Naval Ordnance Laboratory, White Oak, Maryland, December 13, 1961.

9. Sherman, F. S.: Transition Flow. TR HE-150-201, Institute of Engineering Research, University of California, Berkeley, California, August 15, 1962.

10. Kane, E. D.: Drag Forces on Spheres in Low Density Supersonic Gas Flow. TR HE-150-65, Department of Engineering, University of California, Berkeley, California, February 15, 1950.

11. Sreekanth, A. K.: Drag Measurements on Circular Cylinders and Spheres in the Transition Regime at a Mach Number of 2. UTIA Report No. 74, Institute of Aerophysics, University of Toronto, April 1961.

12. Wegener, Peter P.; and Ashkenas, Harry: Wind Tunnel Measurements of Sphere Drag at Supersonic Speeds and Low Reynolds Numbers. TR No. 34-160, Jet Propulsion Laboratory, CIT, Pasadena, California, June 1961.

13. Masson D. J., et al.: Measurements of Sphere Drag from Hypersonic Continuum to Free Molecule Flow. AD 252 909, The Rand Corporation, Santa Monica, California, RM-2678, November 3, 1960.

14. Maslach, G. J.; and Schaaf, S. A.: Cylinder Drag in the Transition from Continuum to Free Molecule Flow. HE-150-194, Institute of Engineering Research, University of California, Berkeley, California, March 20, 1962.

15. Maslach, G. J.: Supplementary Cylinder Drag Data for Transition Flow Conditions. Institute of Engineering Research, University of California, Berkeley, California, Report No. AS-63-3, July 1, 1963.

16. Peters, B. J.: Results of a Wind Tunnel Test of the Agena B Booster Vehicle After Payload

REFERENCES (Concluded)

Separation in the Chance Vought Hypervelocity Wind Tunnel. (LMSC Test S-14), LMSD Report 800804, June 27, 1961.

17. Jose, Paul D.: Sun's Motion and Sunspots. Astrophysical Journal, vol. 70, no. 3, pp. 193-200, April 1965.

BIBLIOGRAPHY

Arriaga, Nilo: Relations Between Solar Activity and the Center of Gravity of the Planetary System. J. Geophys. Res., vol. 60, 1955.

Baker, R. M. L., Jr.; and Makemson, Maud W.: An Introduction to Astrodynamics. Academic Press, New York, 1960.

Bracewell, R. N.: The Sunspot Number Series. Nature, no. 4354, vol. 171, p. 649.

Compilation of Solar-Geophysical Data. Abstracted from CRPL-F Part B, U. S. Department of Commerce, Environmental Science Service Administration (Formerly Central Radio Propagation Laboratory), Boulder, Colorado.

Goldberg, Leo; Deutsch, A. J.; and Layzer, D., editors: Annual Review of Astronomy and Astrophysics, vols. I and II.

Granger, C. W. J.: A Statistical Model for Sunspot Activity. Astrophys. J. vol. 126, pp. 152-158

King-Hele, D. G.; and Rees, Janice M.: The Decrease in Upper-Atmosphere Density Between 1957 and 1963, as Revealed by Satellite Orbits. Royal Aircraft Establishment, Technical Note Space 32, May 1963.

Jacchia, L.: Journal of Geophysical Research. Vol. 65, no. 9, p. 2775.

Kozai, Yoshihide: The Motion of a Close Earth Satellite. The Astron. J. vol 64, no. 1274, November 1959.

Kurtz, F.; and McNair, A.: Satellite Lifetime. ABMA Report No. DA-TN-9-59, January 29, 1959.

Ladner, James E.; and Ragsdale, George C.: Earth Orbital Satellites Lifetime. George C. Marshall Space Flight Center MTP-AERO-62-77, October 24, 1962.

McNish, A. G.; and Lincoln, J. V.: Prediction of the Present Sunspot Cycles. Trans. Am. Geophys. Union, vol. 35, Oct. 1954, p. 709, no. 5.

McNish, A. G.; and Lincoln, J. V.: Prediction of Sunspot Numbers. Trans, Am. Geophys. Union, vol. 30, no. 5, Oct. 1949, p. 673.

Minzner, R. A.; Champion, K. S. W.; and Pond, H. L.: The ARDC Model Atmosphere. Air Force Survey in Geophysics no. 115, August 1959.

Nicolet, M.: Solar Radio Flux and Temperature of the Upper Atmosphere. Geophys. Res. vol. 68, no. 22, November 15, 1963.

Paetzhold, H. K.: Corpuscular Heating of the Upper Atmosphere. J. Geophys. Res., vol. 67, no. 7, July 1962, p. 2741.

Paetzhold, H. K.: Solar Activity Effects in the Upper Atmosphere Deduced from Satellite Observations. Space Research III, Proc. Third International Space Science Symposium, Cospar, 1962, p. 28.

Poe, R. F.: A Review of the Geophysical Model. Lockheed Missiles & Space Company, Tracking Note No. 2, September 25, 1961.

Research in Space Science. Smithsonian Institution Astrophysical Observatory, Cambridge, Massachusetts, Special Reports 103, 117, 120, 126, 142, and 159.

Small, H. W.: Atmospheric Density Between 70 and 200 Nautical Miles from Satellite Observations. Tracking Note No. 23 LMSC/A376332, Lockheed Missiles & Space Company, July 25, 1964.

Small, H. W.; and Johnston, R. C.: A High-Speed Computer Program for Predicting the Decay of Earth Satellites. Lockheed Missiles & Space Company TM 53-73-11, LMSC/A374573, May 13, 1963.

BIBLIOGRAPHY (Concluded)

Stewart, John Q.; and Panofsky, H. A. A.: The Mathematical Characteristics of Sunspot Variations. Astrophys. J., vol. 88, no. 4, Nov. 1938, p. 385.

U. S. Standard Atmosphere, 1962. COESA, Washington, D. C., December 1962.

Wasko, P. E.; and King, T. A.: Earth's Aerospace Properties from 100-100,000 Km Altitude. MTP-AERO-63-2, October 24, 1962.

POWERED FLIGHT TRAJECTORY DETERMINATION TECHNIQUES AS APPLIED TO SATURN V VEHICLES

By

J. B. Haussler

ABSTRACT

The onboard telemetered guidance data and the external tracking data when combined in a composite solution can produce a smooth, continuous trajectory of sufficient accuracy for use in a detailed post-flight evaluation. In solving for guidance and tracker error model coefficients, there are several assumptions and limitations imposed by the nature of the data available and the computer facility utilized. Justification is given for using truncated error models and for the assumption that guidance error model coefficients and tracker error model coefficients can be considered uncorrelated. By using the telemetered guidance as the generating parameter and estimating the error coefficients with the Kalman recursive method, a very efficient and versatile computer program resulted. Up to 18 guidance error coefficients and up to 10 tracker error coefficients from as many as 15 different trackers can be estimated in a single solution. Although the guidance and tracker coefficients do not represent a detailed evaluation of those systems, they do furnish information which can assist in the analysis of these systems. Results on actual data from recent Saturn vehicles verify the method as a practical tool for obtaining a post-flight trajectory.

I. INTRODUCTION

On the Saturn V vehicles, because of the extended length of the powered phase and the S-IVB restart, new techniques are necessary to obtain an acceptable powered flight trajectory. This post-flight trajectory is used in the evaluation of vehicle subsystems. A smooth, continuous, precision trajectory is required to evaluate the guidance and propulsion system.

Since there is no single tracking site which can track the entire powered flight, it is essential to make a composite fit of several stations. In previous methods, discontinuities often appeared in the resulting trajectory because there was no foolproof way to determine the weights to apply to the various tracking data, and the methods were quite sensitive to the weights. Also, the noise or random error in the tracking data was present in the output trajectory. On Saturn V vehicles there will be fewer tracking systems to cover a longer powered phase and this necessitates extracting the maximum amount of information from all the data available to establish a post-flight trajectory.

The telemetered guidance velocity data has become the most accurate single trajectory data source although the guidance hardware errors must be accurately considered. These velocity data include all of the nongravity forces felt by the vehicle and if the guidance errors were known, an extremely accurate trajectory could be obtained with relative ease. The guidance data are available for the entire powered phase of flight. The tracking data (C-band radar, Unified S-band radar and GLOTRAC) contain tracker hardware errors and random error. It logically follows that if a combined solution can be obtained by solving for the guidance error coefficients, the tracker error coefficients and the errors in the initial position and velocity components, then by applying the guidance errors back to the telemetered guidance data a smooth continuous best estimate trajectory will result.

II. FEASIBILITY STUDY

Before this method was implemented there were several things that had to be determined:

(1) Are the guidance error model coefficients and the tracker error model coefficients highly correlated?

(2) How far can the tracker error model be truncated and still represent the systematic errors in the data?

(3) Does the truncated tracker error model that represents the systematic error in the data vary depending on the geometrical relationship between the tracker location and the vehicle flight path?

A study was initiated in which a C-band radar error model and a guidance error model were implemented in a single solution. The C-band radar error model [1] consists of 25 terms. For this study the refraction correction error terms were not included but, in addition, three survey components (East, North and Vertical) were considered. The guidance error model [2] was composed of three accelerometer biases, two accelerometer scale factors, one nonorthogonality, three platform misalignments, three constant drifts and six g-dependent drifts for a total of eighteen terms. The guidance error model, which was derived using small angle approximations, in matrix form is

$$\begin{bmatrix} A_{XT} \\ A_{YT} \\ A_{ZT} \end{bmatrix} = \begin{bmatrix} 1.+\mathrm{SFX} & 0 & 0 \\ 0 & 1.+\mathrm{SFY} & 0 \\ 0 & 0 & 1. \end{bmatrix} \begin{bmatrix} A_{XM} \\ A_{YM} \\ A_{ZM} \end{bmatrix} + \begin{bmatrix} B_X \\ B_Y \\ B_Z \end{bmatrix}$$

$$+ \begin{bmatrix} 0 & \Theta_Z & -\Theta_Y \\ -\Theta_Z & 0 & \Theta_X \\ \Theta_Y & -\Theta_X & 0 \end{bmatrix} \begin{bmatrix} A_{XM} \\ A_{YM} \\ A_{ZM} \end{bmatrix} + \begin{bmatrix} 0 & 0 & 0 \\ -\delta & 0 & 0 \\ 0 & 0 & 0 \end{bmatrix} \begin{bmatrix} A_{XM} \\ A_{YM} \\ A_{ZM} \end{bmatrix}$$

where:

$$\Theta_X = \delta_X + \dot{\delta}_X T + g(X)V_X + g(Y)V_X$$

$$\Theta_Y = \delta_Y + \dot{\delta}_Y T + g(X)V_Y + g(Y)V_Y$$

$$\Theta_Z = \delta_Z + \dot{\delta}_Z T + g(X)V_Z + g(Y)V_Z$$

A_{XT}, A_{YT}, A_{ZT} - true acceleration

A_{XM}, A_{YM}, A_{ZM} - measured acceleration

SFX, SFY - accelerometer scale factors

B_X, B_Y, B_Z - acceleration biases

δ - nonorthogonality

δ_X, δ_Y, δ_Z - orthogonal misalignment

$\dot{\delta}_X$, $\dot{\delta}_Y$, $\dot{\delta}_Z$ - constant drift rates

$g(X)V_X$, $g(X)V_Y$, $g(X)V_Z$ - g-dependent drifts

$g(Y)V_X$, $g(Y)V_Y$, $g(Y)V_Z$ -

A trajectory of a typical Uprated Saturn I vehicle was used to represent the flight path. By varying the location of a single C-band radar and making several solutions with simulated data, the effect of geometry on error significance and correlation could be determined. It was assumed that there was one tracker in the launch area (T1), one near the end of the powered phase (T2), and one off to the side of the flight path (T3). This represents the extremes in geometry and all other locations can be considered as combinations of these three cases.

Terms were eliminated from the radar error models according to two criteria. The first criterion was that terms which could not be determined with sufficient accuracy to be of significance should be eliminated. The Kalman procedure implemented here assigned values to these terms, but the confidence in the assigned values was the same as the confidence in the original estimate. To assist in determining the significance of the value assigned to an error term, a figure of merit was defined.

$$\text{Figure of merit} = \frac{\sigma_0 - \sigma_F}{\sigma_0} \cdot 100$$

where:

σ_0 = standard deviation of initial error coefficient estimate

σ_F = standard deviation of the final output error coefficient estimate

The figure of merit is the percentage improvement of confidence over the initial estimate. If the error coefficient is ideally determined, the figure of merit is 100 and if there is no improvement in the initial estimate of the error coefficient, the figure of merit is zero. The figures of merit for the three geometrically different tracker locations are shown in Table I. In each of the three cases shown there are 10 error model coefficients with zero or near zero figures of merit. This means that these terms can be eliminated without degrading the solution, since very little confidence can be placed on the numbers assigned to these error coefficients.

TABLE I. FIGURES OF MERIT

C-BAND RADAR ERROR	TRACKER LOCATION		
	T1	T2	T3
RANGE MEASUREMENT			
Bias	98	89	92
Dynamic error ($\dot{R}$)	98	99	94
Dynamic error ($\ddot{R}$)	0	0	0
Dynamic error ($\dddot{R}$)	0	0	0
Time dilation	82	81	17
Frequency error	97	97	96
AZIMUTH MEASUREMENT			
Bias	33	33	34
Dynamic error ($\dot{A}$)	0	0	0
Dynamic error ($\ddot{A}$)	0	0	0
Dynamic error ($\dddot{A}$)	0	0	0
Tracker mislevel (SinA)	47	61	45
Tracker mislevel (CosA)	44	50	60
Misalignment	30	31	31
Nonorthogonality	29	52	63
Time dilation	0	1	0
ELEVATION MEASUREMENT			
Bias	21	30	31
Dynamic error ($\dot{E}$)	0	0	0
Dynamic error ($\ddot{E}$)	0	0	0
Dynamic error ($\dddot{E}$)	0	0	0
Tracker mislevel (CosA)	56	45	42
Tracker mislevel (SinA)	62	72	88
Time dilation	0	4	0
Antenna droop	51	32	35

The second criterion for eliminating terms was correlation. If two terms were highly correlated (correlation coefficient greater than 0.70), one could be eliminated and the total error of both terms would then be thrown into the remaining term. This study confirmed what one would expect; namely, that the correlation varied considerably depending on the geometrical relation between the tracker location and the vehicle flight path. Because of the high geometry dependence, there were no error model terms which could be eliminated in all of the three cases studied.

In this study the correlation between the tracker error model coefficients and the guidance error model coefficients was quite small with a maximum correlation coefficient of 0.20. More than 95 percent of the correlation coefficients were less than 0.10.

The survey error terms had a rather high figure of merit and also exhibited high correlation with other tracker errors. However, for powered trajectory construction the majority of the tracking data will be from the Cape area or from the Eastern Test Range stations which have been surveyed quite accurately. On Saturn V vehicles there will be C-band radar tracking data available from an insertion ship which will be stationed somewhere beyond Bermuda. This data will have to have special attention since location errors will probably be the most significant systematic error.

III. TRACKER ERROR MODEL JUSTIFICATION

To verify that a truncated error model could represent the systematic errors in radar tracking data a detailed analysis was performed on 15 sets of C-band radar data from three Uprated Saturn I vehicles [3]. The post-flight trajectory was considered accurate and was transformed to the radar measured parameters and differenced with the actual data. Using these differences many solutions for the estimates of the error coefficients were made. The main emphasis here was to obtain the best fit possible with an error model truncated as far as possible. In implementing this procedure, several constraints were applied, such as: certain timing errors occur in all three parameters, the same survey error must be present in all three parameters, etc. These constraints had the effect of eliminating some terms from the error model. In this analysis, highly correlated terms were eliminated if they were of little significance. The significance was determined by plotting the contribution that the individual terms made to the total error. If correlated errors were both significant, then a study was made of the unit variance of the solution. If the removal of one of the correlated coefficients did not cause an appreciable increase in the unit variance, then that error term was truncated from the error model.

The frequency of occurrence of the error model coefficients for the 15 actual sets of data are shown in Table II. It is interesting to note that even though 11 coefficients appear in these 15 cases, only one set of data (Merritt Island on AS-202) requires as many as 9 error model terms to model the systematic error. Another interesting fact is, that of the 11 error model coefficients only the elevation bias (C_0) appears in all of the 15 truncated error models. The tracker mislevel term (b_4) which appeared in only 2 of the 15 cases was also eliminated. This leaves a truncated C-band radar error model of 10 terms.

TABLE II. FREQUENCY OF OCCURRENCE

RADAR	UPRATED SATURN I VEHICLE	C-BAND RADAR ERROR MODEL COEFFICIENTS											NO. OF TERMS FOR EACH DATA SET
		A_0	A_1	A_5	A_6	b_0	b_2	b_4	b_5	b_7	c_0	c_2	
PATRICK (0.18)	AS-201		X		X	X				X	X		5
	AS-202	X	X		X	X	X		X		X	X	8
	SA-203	X		X	X	X	X				X	X	7
MERRITT ISLAND (19.18)	AS-201		X	X		X					X	X	5
	AS-202	X		X	X	X	X	X		X	X	X	9
	SA-203	X		X	X	X	X				X	X	7
GRAND BAHAMA (3.18)	AS-201	X	X	X		X	X	X			X		7
	AS-202	X	X		X	X	X		X		X	X	8
	SA-203	X	X	X			X		X	X	X	X	8
GRAND TURK (7.18)	AS-201		X	X		X	X		X		X	X	7
	AS-202	X	X		X	X	X		X		X	X	8
	SA-203	X	X		X	X					X		5
ANTIGUA (91.18)	AS-201	X	X	X		X	X		X		X	X	8
	AS-202		X		X	X				X	X		5
BERMUDA (BDA)	SA-203	X		X		X	X				X	X	6
TOTAL NUMBER OF OCCURRENCES		11	11	9	9	14	11	2	6	4	15	11	

The truncated error model which is considered sufficient to model the systematic error is:

$$R = A_0 + A_1\dot{R} + A_5R + A_6\ (-0.022\ \text{cosec}E)$$

$$A = b_0 + A_1\dot{A} + b_2\ddot{A} + b_5\ \text{Tan}E\ \text{cos}A + b_7\ \text{Tan}E$$

$$E = c_0 + A_1\dot{E} + c_2\ddot{E} + b_5\ (-\text{sin}A)$$

$$+ A_6 \left[\left(\frac{0.022}{R\text{sin}E} - 10^6 \right) \text{cotan}E \right]$$

where:

A_0 - Range bias
A_1 - Timing error
A_5 - Frequency error
A_6 - Refraction error
b_0 - Azimuth bias
b_2 - Dynamic lag in azimuth
b_5 - Tracker mislevel
b_7 - Nonorthogonality
c_0 - Elevation bias
c_2 - Dynamic lag in elevation

IV. COMPUTER IMPLEMENTATION

I will now briefly summarize the important items that influenced the manner in which the tracker error model was implemented in the large post-flight trajectory program:

(1) The guidance error model coefficient and the tracker error model coefficients are virtually uncorrelated.

(2) The systematic errors in the C-band radar data can be modeled with a truncated error model.

(3) The geometrical relationship between the tracker site and the vehicle's flight path primarily affects the correlation between error terms and not the number of terms required in the truncated model.

A computer program has been developed which uses the telemetered guidance data as the generating

parameter and solves for the guidance error model coefficients, the C-band radar error model coefficients and the initial position and velocity component errors. The guidance error model consists of 18 terms and is very adequate for the ST-124 guidance system on the Saturn vehicles. The guidance error model implemented is the same as used in the feasibility study. The truncated 10 term C-band radar error model has been implemented. The program can estimate these error coefficients from a virtually unlimited number of different radar sites. With the present instrumentation available, one can expect less than 10 radars to track during the powered portion of a Saturn trajectory. If all 10 terms are estimated for each radar this will be only 100 tracker error terms which can readily be handled by the program. The initial position and velocity component errors will only be estimated for the S-IVB second burn or when the trajectory is initialized at some point other than the launch site.

The Kalman recursive method, which gives a point by point updating is utilized. The simplified version of the Kalman recursive equations implemented are:

$$X_i = X_{i-1} + C_i (Y_i - H_i X_{i-1})$$

$$K_i = (1 - C_i H_i) K_{i-1}$$

$$C_i = K_{i-1} H_i^T (H_i K_{i-1} H_i^T + Q_i)^{-1}$$

where:

X_i - State vector at time i

Y_i - Observation vector at time i

K_i - Covariance matrix of the error in the state vector at time i

C_i - Kalman recursive correction matrix at time i

H_i - Matrix of partial derivatives relating the state to the observations at time i

I - Identity matrix

Q_i - Covariance matrix of the measurement noise at time i

i-1 - Refers to the previous time point.

The computer (an IBM 7094) places limitations on the program and influences greatly the manner in which theory is implemented. By considering the fact that there is very little correlation between the guidance error coefficients and the tracker error coefficients, it is possible to estimate them separately. In other words, at each time point an estimate is made of the guidance error coefficients; then using these updated guidance coefficients an estimate of the tracker error coefficients is made. This requires much smaller matrices and therefore, much less computer core storage. The assumption is also made that the tracker errors from the different radar sites are completely uncorrelated. This assumption is not completely valid and probably induces some error in the estimate of the tracker coefficients. This does not cause any problem since the tracker error coefficients are not intended to be an accurate analysis of the tracking systems, but are merely used as a tool to obtain a better trajectory.

The tracking data used as observations in this program consist mainly of C-band radar measured parameters, Unified S-band measured parameters and GLOTRAC measured parameters. Considerable preprocessing is required before these data are used. The data are corrected for refraction and known systematic errors. Before the data are used as observations in the composite solution rather extensive editing and filtering are applied. Filtering is done so that the solution is not biased or otherwise adversely affected by selecting one sample per second and not the 10 or 20 samples per second that are measured. This saves considerable computer time and gives excellent results.

Although GLOTRAC measured parameters can be used as observations, the GLOTRAC error model coefficients will not be estimated by the program. The GLOTRAC system will support only the first few Saturn V vehicles. The Unified S-band error model coefficients will be included when a truncated model that sufficiently represents the systematic error in the system can be established. To date there has been almost no Unified S-band tracking data to analyze to determine a truncated error model.

Estimates of the guidance errors and tracker errors are obtained, but these are used as tools to obtain a trajectory and do not represent a detailed guidance and tracker analysis. There are several features which are unique to this method:

(1) The output trajectory retains the smoothness of the guidance data and is not affected by the random errors in the tracking data.

(2) A trajectory can be computed over intervals where no tracking data are available.

(3) The trajectory can be constrained to exactly fit endpoints.

(4) A virtually unlimited number of tracking sites can be used as observations simultaneously.

(5) Any combination of guidance and tracker errors may be solved for in a single run.

(6) Because the recursive method is used, the buildup versus time of the state vector parameters can be determined. This helps isolate inconsistent data.

(7) A very versatile output can, on option, present various residual plots, the covariance matrix at each time point, various residual statistics, etc.

V. RESULTS

The method has been proven to be a valuable tool in post-flight trajectory construction on Uprated Saturn I vehicles and should be even more valuable on Saturn V vehicles. Four cases using SA-203 data were run and are presented here. In Case 1, all 18 guidance error model coefficients are estimated and no tracker errors are considered. In Case 2, the g-dependent drift terms and the accelerometer bias errors are truncated from the guidance model and again no tracker errors are considered. Case 3 considers the full guidance error model and the 10 term tracker error model for each of the 4 radars used as observations. Case 4 considers the truncated guidance error model used in Case 2 and the full set of tracker errors.

Table III presents the differences in an earth-fixed launch pad centered coordinate system between the position and velocity components of the insertion point obtained from these four cases and the insertion point obtained from the orbit determination program. Insertion time is an arbitrarily chosen time after the completion of thrust decay. It should be noted that the insertion point obtained from the orbit determination program may not be as accurate as normal because SA-203 carried the LH_2 experiment which resulted in considerable venting. This venting changed the magnitude of the vehicle's total velocity by approximately 20 m/s in four revolutions. For post-flight evaluation purposes, we claim the position and velocity components to be accurate within ± 500 m and ± 2 m/s, respectively, at insertion from the powered flight solution if C-band radar is the only tracking data available beyond the very early portion of flight. The total position vector and velocity vector can be determined to within ± 250 m and ± 1 m/s, respectively. Table III vividly illustrates that varied although reasonable results can be obtained by changing the parameters estimated in the state vector. In other

TABLE III. INSERTION POINTS DIFFERENCED WITH ORBITAL SOLUTION

	Case 1	Case 2	Case 3	Case 4
No. of Guidance Errors	18	9	18	9
No. of Tracker Errors	0	0	10	10
ΔX (meters)	-107	-89	- 21	- 36
ΔY (meters)	- 11	-66	-204	-144
ΔZ (meters)	- 8	-16	- 30	- 39
$\Delta \dot{X}$ (meters/sec)	- 1.3	- 0.5	- 0.8	- 0.8
$\Delta \dot{Y}$ (meters/sec)	0.8	- 0.1	0.5	- 1.1
$\Delta \dot{Z}$ (meters/sec)	2.0	1.7	1.4	1.3

words, the endpoint obtained is not very sensitive to the combination of errors estimated.

Table IV presents the average residuals for the radar measured parameters from each of the cases previously mentioned. Cases 3 and 4 which estimate tracker error model coefficients have residuals which are approximately an order of magnitude smaller than the cases which estimated only the guidance error coefficients. This shows that the guidance error model cannot represent the tracker errors, and therefore, verifies that the guidance errors and tracker errors are not highly correlated. Figure 1 presents a typical slant range observation residual curve for cases considering tracker errors and not considering tracker errors. This shows that the tracker error model adequately represents the systematic error in the observations.

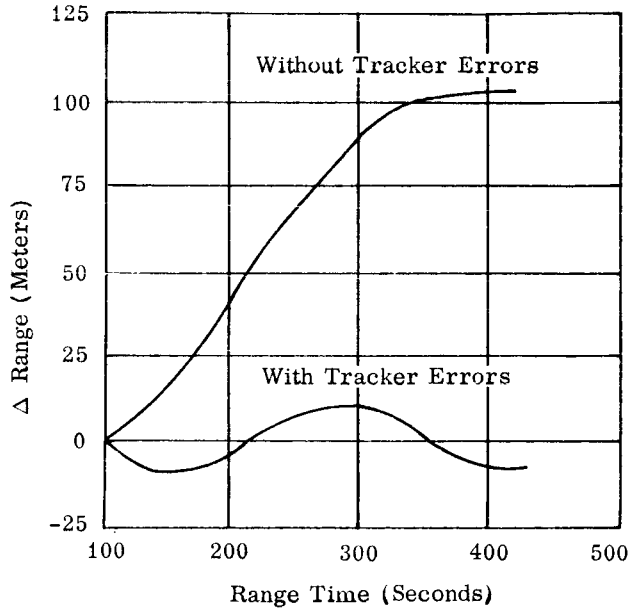

FIGURE 1. TYPICAL SLANT RANGE RESIDUAL

It should be emphasized that the primary concern is to generate a trajectory, and it does not matter if the magnitude or combination of the error coefficients are unrealistic. However, if there are large compensating guidance errors estimated, the shape of the trajectory may be warped. It may be necessary to eliminate some guidance errors from the state vector or reduce the input variances on some errors in order to produce guidance difference curves which are realistic. The guidance difference curves are obtained by differencing the telemetered guidance velocity components and the guidance velocity components which result from the trajectory obtained by this method.

To obtain the best possible trajectory from this method, a proper balance must be achieved among a good endpoint, small tracker residuals and a realistic

TABLE IV. AVERAGE TRACKER RESIDUALS FROM VARIOUS CASES

		Case 1	Case 2	Case 3	Case 4
No. of Guidance Errors		18	9	18	9
No. of Tracker Errors		0	0	10	10
Radar 0.18	Azimuth (deg)	3.72×10^{-3}	3.79×10^{-3}	1.93×10^{-4}	7.79×10^{-5}
	Elevation (deg)	2.23×10^{-3}	1.18×10^{-3}	6.46×10^{-4}	-2.30×10^{-3}
	Range (meters)	24.7	23.3	-4.7	-9.1
Radar 3.18	Azimuth (deg)	-2.97×10^{-3}	-2.91×10^{-3}	-1.77×10^{-4}	-2.64×10^{-4}
	Elevation (deg)	-2.86×10^{-2}	-3.01×10^{-2}	-6.38×10^{-3}	-9.22×10^{-3}
	Range (meters)	61.7	60.3	3.1	-1.9
Radar 7.18	Azimuth (deg)	-1.13×10^{-3}	-1.02×10^{-3}	9.40×10^{-5}	5.98×10^{-4}
	Elevation (deg)	-1.56×10^{-2}	-1.55×10^{-2}	-3.11×10^{-3}	4.59×10^{-3}
	Range (meters)	13.3	8.5	4.0	1.7
Radar 19.18	Azimuth (deg)	-1.50×10^{-3}	-1.51×10^{-3}	-1.46×10^{-4}	-1.23×10^{-4}
	Elevation (deg)	-2.31×10^{-2}	-2.45×10^{-2}	-2.45×10^{-3}	4.70×10^{-3}
	Range (meters)	35.5	34.2	-2.7	6.7

shape in the guidance difference curves. The confidence placed on the trajectory will depend on how well this proper balance is achieved. This method is fairly sensitive to the combination of data used, the weights applied to the observations and the variances assigned to the parameters to be estimated. For a normal vehicle, it would be necessary to run between 10 and 20 cases before an acceptable trajectory could be obtained.

VI. CONCLUSIONS

This method is a powerful tool for establishing a smooth continuous powered flight trajectory. Perhaps SA-203 was not a fair test for the method since there was an abundance of data (although not as consistent as desired) and the burn time was considerably shorter than will be experienced on Saturn V vehicles. It is felt that the full capability of the method will be utilized on Saturn V vehicles where the first powered phase approaches 700 seconds. Near the end of this phase of flight, a single ship based C-band radar may provide the only tracking data. The capability to either solve for or constrain to endpoints will be very important for the S-IVB second burn phase.

REFERENCES

1. Cummings, C. S.; Ackerson, R. H.; Baron, A.S.; et al.:RCA MTP: The Accuracy of ETR Instrumentation. ETR-TR-65-7, May 1965.

2. Chapman, R. A.: A Method of Determining the Source of Errors in Guidance Measurements and the Resultant Errors in Earth-Fixed Components. MTP-AERO-62-76, October 22, 1962.

3. Junkin, B. G.: A Tracking System Error Model Regression Analysis for Systematic Error Evaluation of Apollo-Saturn Radar Flight Test Data. NASA TMX-53487, July 5, 1966.

TRAJECTORY APPLICATION METHOD (TAM)

By

John P. Sheats

ABSTRACT

A simulation technique (TAM) for the post-flight evaluation of the propulsion system performance has been developed which incorporates the time history trajectory parameters from the post-flight observed trajectory as input. This technique represents a significant reduction in time required to perform stage propulsion system evaluations. The development and some advantages and disadvantages of this technique are given. The propulsion system evaluation was performed on the S-IB stage of AS-201, AS-203, and AS-202 utilizing both the proposed technique and a conventional simulation technique; the results and comparison of both methods are presented.

DEFINITION OF SYMBOLS

Symbol	Definition
* AA	Average * A_m between two time intervals printed out at the latter time point.
A_E	Nozzle exit area (Engines 1 through n).
ALISPO	Average instantaneous sea level specific impulse.
A_m	Total calculated platform (inertial) acceleration.
* A_m	Total platform (inertial) acceleration from Observed Mass Point Trajectory (OMPT).
* AMACH	Average Mach number between t and t_{-1} as observed.
AREA	Cross sectional area of vehicle.
A_T	Throat area (Engines 1 through n).
AVDFLOX	Average propellant mass loss rate.
AVDMM	Average total weight loss rate of the vehicle.
AVFJIO	Average total sea level longitudinal thrust.
BDRAG	Base drag (input as table or equation).
CD	Drag coefficient (table look-up vs. Mach).
CCDD	Average CD between two time points.
CF	Sea level thrust coefficient.
CFV	Vacuum thrust coefficient (pulled from data tape).
CXCA	Required CD as based on acceleration difference (DA).
CXCVE	Required CD as based on earth-fixed velocity difference (DDVE).
CXCVI	Required CD as based on integrated acceleration differences (DDIAT).
DA	Difference in total acceleration (calculated minus measured).
DCXA	Required drag coefficient change at any time as based on acceleration difference (DA).

Symbol	Definition
DCXVE	Required CD change based on DDVE.
DCXVI	Required CD change based on DDIAT.
DD	Average vehicle aerodynamic longitudinal drag between t and t_{-1}.
DDVE	Difference of DVE between two time points.
DDIAT	Difference between DIAT from one time point to another divided by time difference.
DFA	Required instantaneous thrust change as based on acceleration difference (DA).
DFLOX	Propellant mass loss rate (from data tape).
DFVE	Required instantaneous thrust change based on DDVE.
DFVI	Required instantaneous thrust change based on DDIAT.
DIAT	Integrated difference between A_m and $*A_m$.
DMA	Required mass change at any time as based on acceleration difference (DA).
DMASS ($\dot{w}$)	Total vehicle mass loss rate (from data tape).
DMVE	Required mass change based on DDVE.
DMVI	Required mass change based on DDIAT.
DRAG	Total vehicle aerodynamic longitudinal drag.
DVE	Difference between calculated and measured earth-fixed velocity.
DWA	Required instantaneous flow rate change based on DA.
DWVE	Required instantaneous flow rate change based on DDVE.
DWVI	Required instantaneous flow rate change based on DDIAT.
FAI	Total longitudinal drag force.
FB	Vertical buoyancy force.
$FE_{(1-n)}$	Local individual engine turbine exhaust thrust (from data tape).
$FEI_{(1-n)}$	Sea level turbine exhaust for engines (1-n).
$F\text{-}ENG_{(1-n)}$	Local engine thrust (1-n)
FF	Average local thrust (FJI) between t and t_{-1}.
FJI	Total local longitudinal thrust.
FJIO	Total sea level longitudinal thrust.
FLTTT (FT)	Flight time as measured from first motion.
FMI(F)	Total local longitudinal effective force.
$FO_{(1-n)}$	Individual engine sea level thrust.
GCTTT (T)	Time from guidance reference release.
IAT	Integral of A_m.
* IAT	Integral of $*A_m$.
K	Vehicle firing direction East of North.
KVAL	Thrust multiplier (local thrust correction constant).

Symbol	Definition
LISPO	Instantaneous sea level specific impulse.
* MACH	Mach number as pulled from OMPT.
MASS (M)	Instantaneous mass.
M_i	Initial vehicle mass.
MM	Average mass between t and t_{-1}.
OMPT	Observed Mass Point Trajectory or Measured Trajectory.
PACX	Partial derivative of acceleration difference with respect to drag coefficient.
PAF	Partial derivative of acceleration difference with respect to thrust.
PAM	Partial derivative of acceleration difference with respect to mass.
PAW	Partial derivative of acceleration difference with respect to flow rate.
$P_{C_{(1-n)}}$	Individual engine chamber pressure (from data tape).
PO (P_0)	Sea level pressure.
PO-* P	Local pressure difference.
* PRESS (* P)	Ambient pressure from OMPT.
PVCX	Partial derivative of velocity difference with respect to drag coefficient.
PVF	Partial derivative of velocity difference with respect to thrust.
PVM	Partial derivative of velocity difference with respect to mass.
PVW	Partial derivative of velocity difference with respect to flow rate.
* Q	Dynamic pressure from OMPT.
* QQ	Average dynamic pressure between time points.
* RHO	Local atmospheric density from OMPT.
R_0	Radial distance from geocentric center of the earth to launch pad.
$\vec{r_0}$	Initial components of the vehicle position vector referenced to the geocentric center of the earth.
RTIME (t)	Range time.
TT	Midpoint time between two data points.
VE (V_e)	Calculated earth-fixed velocity.
* VE (* V_e)	Measured earth-fixed velocity
VOLUME	Total vehicle volume.
ϕ_0	Geodetic latitude of the launch site.
ψ_0	Geocentric latitude of launch site.
ω	Angular rotational velocity of earth.
$\ddot{X}_m$, $\ddot{Y}_m$, $\ddot{Z}_m$	Calculated platform (inertial) acceleration components.
* $\ddot{X}_m$, * $\ddot{Y}_m$, * $\ddot{Z}_m$	Measured platform (inertial) acceleration components.

Matrix Identification

$$[K] = \begin{vmatrix} \sin K & 0 & \cos K \\ 0 & 1 & 0 \\ -\cos K & 0 & \sin K \end{vmatrix}$$

$$[\phi_0] = \begin{vmatrix} 1 & 0 & 0 \\ 0 & -\cos\phi_0 & -\sin\phi_0 \\ 0 & \sin\phi_0 & -\cos\phi_0 \end{vmatrix}$$

$$[\omega] = \begin{vmatrix} \cos\omega T & -\sin\omega T & 0 \\ \sin\omega T & \cos\omega T & 0 \\ 0 & 0 & 1 \end{vmatrix}$$

$$[\dot{\omega}] = \begin{vmatrix} -\omega\sin\omega T & -\omega\cos\omega T & 0 \\ \omega\cos\omega T & -\omega\sin\omega T & 0 \\ 0 & 0 & 0 \end{vmatrix}$$

$$[\dot{\omega}_0] = \begin{vmatrix} 0 & -\omega & 0 \\ \omega & 0 & 0 \\ 0 & 0 & 0 \end{vmatrix}$$

$$\vec{r}_0 = \begin{vmatrix} -R_0 \cos K \sin B_0 \\ R_0 \cos B_0 \\ R_0 \sin K \sin B_0 \end{vmatrix}$$

$$= \begin{vmatrix} X_0 \\ Y_0 \\ Z_0 \end{vmatrix} \quad \text{where:} \quad B_0 = (\phi_0 - \psi_0)$$

I. INTRODUCTION

The post-flight propulsion system analysis on each Saturn stage is usually performed by two methods. The first method of determining the stage propulsion system flight performance is a reconstruction of the telemetered flight data including calculated propellant residuals. This flight reconstruction method is a mathematical model of the stage propulsion system utilizing a table of influence coefficients to determine engine performance. The second method utilizes a trajectory simulation to generate adjustments that are enforced on the results from the flight reconstruction method so that the resulting calculated trajectory will match the observed trajectory. This second method, trajectory simulation, will be discussed.

The post-flight propulsion system performance simulation on each Saturn stage has been accomplished using either three-degree-of-freedom or six-degree-of-freedom trajectory computer programs. These, combined with a weighted least squares program, provide the linear adjustment of the post-flight propulsion system parameters (thrust, mass low rate and/or initial mass) and the predicted aerodynamic drag coefficient required for the trajectory parameters of the computed trajectory to match those derived from the tracking data observed during flight [1].

All of the tracking data observed during flight are converted from the various tracker measurements with the origin at the tracking site to the trajectory parameters in a coordinate system with the origin at the launch site. All of these tracking data are used in conjunction with the guidance system outputs to obtain a best estimate of the trajectory. The meteorological data observed at the launch time are combined with the best estimate of trajectory to yield what is called the Observed Mass Point Trajectory (OMPT) or measured trajectory. In all the propulsion system simulations performed on Saturn stages flown, an attempt has been made to compute a trajectory which matches the measured trajectory. There are several difficult problems (which will be discussed later) associated with this procedure; however, these problems could possibly be circumvented to a large degree if some of the trajectory parameters representing the altitude-time history of the measured trajectory are used as input to the simulation program.

A simulation program called the Trajectory Application Method (TAM) was developed to investigate the advantages and disadvantages of this approach.

II. SIMULATION PROBLEMS

Two basic problems are associated with the usual simulation programs that do not use the observed trajectory parameters representing altitude-time history from the measured trajectory or OMPT.

A. ALTITUDE EFFECTS

The meteorological data (atmospheric density, pressure, temperature, and wind data) are independently observed functions of altitude. These data are combined with trajectory parameters from the best estimate of trajectory to compute several altitude-dependent parameters, such as dynamic pressure, Mach number, and the thrust gain from increased altitude. The relationship between altitude and the meteorological data is observed independently and is assumed correct. However, the altitude from conventional simulation programs will initially be incorrect since the initial values of the propulsion system parameters have not been adjusted. Thus, meteorological data, which are referenced to the correct altitude, are introduced into the trajectory computation at either an earlier or later time (depending on the propulsion parameter adjustments required) than needed to satisfy the measured trajectory parameters. This scheme will eventually converge to the correct relationship as the adjustments to the propulsion system parameters and the aerodynamic drag coefficient converge to the appropriate solution.

B. ATTITUDE EFFECTS

The simulation programs often compute the attitude of the vehicle in the same fashion used in the precalculated or operational trajectory programs, except that the flight sequence and attitude program are considered fixed. The vehicle attitude as computed in this way is a function of the propulsion and trajectory parameters. Thus, if the propulsion parameters are incorrect, the resultant altitude-time history and attitudes will be incorrect. These, too, will eventually converge to the correct relationships as the propulsion parameters and aerodynamic drag coefficient adjustments converge to the appropriate solution. Also, the telemetered attitudes are sometimes used as inputs to the simulation programs. The problems associated with this approach are the time and bias shifts which may be inherent in telemetered data.

The effect of these two problems cannot be separated. After several iterations these problems can be resolved, but a large number of both man-hours and computer hours are required. Since this type of simulation requires a substantial amount of computer time for a single run, the turn-around time on the computer is longer than would be necessary with a more simplified simulation.

III. TAM DEVELOPMENT

The Trajectory Application Method was developed to circumvent some of the problems associated with the usual propulsion system simulations. In addition, a capability to estimate the instantaneous adjustments required was built into the program. The advantages and disadvantages of the TAM approach and some flight results are presented in subsequent paragraphs.

A. ALTITUDE AND ATTITUDE EFFECTS

1. Altitude Effects. The following parameters, representing the altitude-time history, are input directly as a function of time: ambient pressure, density, Mach number, dynamic pressure and altitude. These parameters are used wherever they are required in the various computations insuring an altitude-time history compatible with the measured trajectory. Observed ambient temperature and wind effects are included in the calculation of dynamic pressure and Mach number. This eliminates the convergence problems associated with an incorrect altitude-time history, thereby placing the vehicle in its proper environment for drag considerations although adjustments to propulsion parameters may yet be required.

2. Attitude Effects. The measured platform (inertial) acceleration components from the OMPT or measured trajectory are input as a function of time. The unit vector of the acceleration is established.

$$*A_m = \left(*\ddot{X}_m{}^2 + *\ddot{Y}_m{}^2 + *\ddot{Z}_m{}^2 \right)^{1/2}$$

$$*\overrightarrow{A_m}' = \frac{*\ddot{X}_m}{*A_m} i + \frac{*\ddot{Y}_m}{*A_m} j + \frac{*\ddot{Z}_m}{*A_m} k.$$

The calculated platform acceleration components using the components of $*\overrightarrow{A_m}'$ are computed from the total acceleration $\left(\frac{FMI}{MASS}\right)$ proportional to those observed in the measured trajectory. This method replaces the transformation from the body-fixed to platform coordinate system.

$$\ddot{X}_m = \left(\frac{*\ddot{X}_m}{*A_m}\right)\left(\frac{FMI}{MASS}\right)$$

$$\ddot{Y}_m = \left(\frac{*\ddot{Y}_m}{*A_m}\right)\left(\frac{FMI}{MASS}\right)$$

$$\bar{Z}_m = \left(\frac{*\ddot{Z}_m}{*A_m}\right)\left(\frac{FMI}{MASS}\right) \quad .$$

This scheme eliminates the necessity for either computing the attitude or directly inputting the telemetered attitude information and also insures compatibility with the measured trajectory parameter components.

B. GRAVITY CONSIDERATIONS

The trajectory parameters, after a correct solution for propulsion system parameters and aerodynamic drag coefficient adjustments have been obtained, should be identical to those in the measured trajectory or OMPT. Therefore, the gravity contributions to the trajectory parameters needed to convert from inertial space-fixed coordinates are identical. The components of acceleration, velocity, and position due to gravity are input directly from the measured trajectory as a function of time, thus forcing the gravity contributions to the trajectory parameters in TAM to be equivalent to those in the measured trajectory. This approach reduces the system of second order differential equations to be solved in the usual types of simulations to simple linear equations.

C. ESTIMATED INSTANTANEOUS ADJUSTMENTS

Redundant instantaneous adjustments to the propulsion system parameters and aerodynamic coefficients are made by comparing the (1) inertial acceleration, (2) inertial velocity, and (3) earth-fixed velocity computed in TAM with those input from the measured trajectory at each time point. There is a requirement for partial derivatives of the trajectory parameters with respect to the parameters for which required adjustments are sought. These partial derivatives can be obtained by conventional perturbation methods. However, a highly simplified approach to determining these partial derivatives can be developed, when the appropriate simplifying assumption is made. The assumption to be made is that the derivations produced in inertial and earth-fixed acceleration resulting from a deviation in either the propulsion parameters or aerodynamic drag coefficient are approximately equivalent. The partial derivatives shown below can be used for both inertial and earth-fixed accelerations.

$$\left(\frac{\partial A_m}{\partial F}\right)_t = -\left(\frac{1}{MASS}\right)_t = PAF$$

$$\left(\frac{\partial A_m}{\partial M_i}\right)_t = \left(\frac{A_m}{MASS}\right)_t = PAM$$

$$\left(\frac{\partial A_m}{\partial \dot{w}}\right)_t = \left(\frac{A_m \cdot FT}{MASS}\right)_t = PAW$$

$$\left(\frac{\partial A_m}{\partial C_x}\right)_t = \left(\frac{*Q \cdot AREA}{MASS}\right)_t = PACX$$

These partial derivatives which are used for both inertial and earth-fixed accelerations have proven quite adequate in several test cases. Also, these partial derivatives may be integrated with respect to time to yield partial derivatives that may be used with velocity and position differences. Since position and velocity data are generally quite smooth, it may be desirable to use these in lieu of (or in addition to) acceleration data.

The instantaneous adjustments to the propulsion system parameters and the aerodynamic drag coefficient are determined by dividing the difference between the trajectory parameters computed in TAM and input from the measured trajectory or OMPT by these partial derivatives at each time point. It must be assumed that the entire difference in the trajectory parameters is a result of any one of the adjustments.

Engineering judgment combined with a priori knowledge of the accuracy of the parameters being adjusted can be used to give an estimate of how much each of the parameters to be adjusted contributes to the difference between the computed and measured trajectory parameters. The estimated instantaneous adjustments can be used to determine if any significant trends or discontinuities could exist in the parameters to be adjusted. (If any discontinuities exist in the trajectory parameter input from OMPT, these would also be reflected in the estimated instantaneous adjustments.)

Usually initial corrections are applied to the propulsion parameters before any attempt is made to establish the adjustment to the aerodynamic drag coefficient. Normally, only a constant shift to the propulsion parameters is considered even though estimated instantaneous adjustments are available. The instantaneous adjustments for the aerodynamic drag coefficient are considered applicable.

D. OVERALL ADJUSTMENTS

The difference between the trajectory parameters computed in TAM and input from OMPT can also be used with a conventional weighted least squares program to solve for an overall constant shift or bias in the propulsion system parameters. The partial derivatives required can either be those established using perturbation techniques or those partial derivatives determined in the simplified approach. Usually, the a priori knowledge of the accuracy of the parameters to be adjusted is included in the least squares solution. Any conventional least squares computer program can be used with TAM to obtain propulsion adjustments such as the one shown below.

$$P = \left[W_0^{-1} + \sum \left(C^T W_{IP}^{-1} C\right)\right]^{-1} \left[\sum \left(C^T W_{IP}^{-1} R\right)\right]$$

where:

P = (nx1) matrix of the propulsion adjustments.

W_0 = (nxn) diagonal matrix consisting of the squares of the accuracies associated with measured propulsion parameters.

C = (mxn) matrix of partial derivatives of the trajectory data with respect to the parameters P.

W_{IP} = (mxm) diagonal matrix consisting of the squares of the accuracies associated with trajectory data.

R = (mx1) matrix of the difference between the calculated and observed trajectory usually referred to as the residual matrix.

The diagonal elements of the covariance matrix $\left[W_0^{-1} + \sum \left(C^T W_{IP}^{-1} C\right)\right]^{-1}$ are the statistical variances of the parameter adjustments, and the off-diagonal elements are the covariances of the parameter adjustments. The square roots of the diagonal elements are the standard deviations of the adjustments and the off-diagonal elements are an indication of the correlation between the adjustments.

The matrix $\left[\sum (C^T W_{IP}^{-1} R)\right]$ represents the sum of the weighted squares of the residuals that are to be minimized subject to the constraints imposed by W_0.

E. ADVANTAGES AND DISADVANTAGES

There are several advantages and at least one disadvantage of the TAM approach over conventional simulation techniques.

1. Advantages. The advantages, other than those for which the scheme was originally devised, are discussed as follows:

Altitude effects

a. The altitude-dependent functions are given versus time thereby eliminating tape interpolation.

b. Fewer equations are required, thus eliminating unnecessary computations.

Attitude effects

a. Control equations are eliminated.

b. Moment and angular motion equations are eliminated.

c. Computation or input of attitude angles is eliminated.

Gravity considerations

a. The system of second order differential equations, usually required in most simulations, is reduced to simple linear equations.

b. Complex integration schemes are not required.

Partial derivatives

The simplified approach for computing the partial derivatives eliminates the necessity of consecutive computer runs usually required for the conventional perturbation schemes.

All of these effects aid in separating the propulsion parameter and aerodynamic drag coefficient adjustments and also reduce the number of iterations required to obtain a valid solution. The TAM simulation technique is far less complex and more economical with respect to machine time than either the six-degree-of-freedom or three-degree-of-freedom simulation programs. Both the man-hours and machine-hours required for an evaluation are significantly reduced through the use of this program.

2. Disadvantages. The TAM program was devised for use in post-flight evaluation of propulsion system performance with a high degree of dependence on input data obtained from the measured trajectory. This is the principal limitation and disadvantage of this approach. Since the altitude-time history and vehicle attitudes are used as inputs, TAM cannot be used to show the effects of propulsion parameter and aerodynamic drag perturbations on trajectory parameters.

F. FLIGHT RESULTS

The flight results using this simplified technique are compared with the flight results using a conventional three-degree-of-freedom (3D) simulation program for three S-IB stage Saturn IB flights in the table below. This table shows the excellent result obtainable with the TAM simulation technique. This approach is as efficient and reliable for use with the latter or upper stages as with those stages for which drag effects are of more concern. The set of equations used in the TAM simulation is given in the Equation Listing. The required integrations can be accurately accomplished with either the Trapezoidal or Simpsons Rule since only integration of linear equations is necessary.

		AVERAGE SEA LEVEL LONG. THRUST (LB)	AVERAGE TOTAL PROPELLANT FLOW-RATE (LB/SEC)	AVERAGE SEA LEVEL LONG. ISP (SEC)
AS-201	3D	1,613,560	6153.98	262.20
	TAM	1,612,754	6151.89	262.16
	% DEV.	-0.05%	-0.034%	-0.015%
AS-203	3D	1,660,471	6285.18	264.19
	TAM	1,659,928	6283.40	264.18
	% DEV.	-0.03%	-0.03%	-0.005%
AS-202	3D	1,631,558	6234.70	261.69
	TAM	1,631,374	6234.86	261.65
	% DEV.	-0.01%	0.003%	-0.001%

$$\% \text{ DEV.} = \frac{\text{TAM-3D}}{\text{3D}} \times 100$$

IV. CONCLUSIONS

The TAM simulation technique, described under Section III, yields results which are well within the accuracy tolerances of the more conventional simulation schemes. The use of this program for the trajectory simulation represents a significant reduction in both man-hours and machine-hours required for an evaluation of the propulsion system performance. The TAM simulation technique is not a tool for studying the effects of propulsion system parameters and aerodynamic drag coefficient perturbations upon the trajectory parameters representing the altitude-time history or vehicle-attitude, but represents a most efficient means of obtaining the post-flight evaluation of the propulsion system performance.

REFERENCES

1. Jackson, J. W.: Propulsion System Evaluation through Flight Simulation. MTP-AERO-62-69, August 31, 1962, MSFC.

2. Office of Manned Spaceflight: Project Apollo Coordinate System Standards, SE-008-001-1, June 1965.

LIST OF EQUATIONS

$$CF_{(1-n)} = CFV_{(1-n)} - \left(\frac{A_{E_{1-n}} P_0}{A_{T_{1-n}} P_{C_{1-n}}} \right) \quad (1)$$

$$FO_{1-n} = (CF)_{1-n} (A_T)_{1-n} (P_C)_{1-n} \quad (2)$$

$$F\text{-}ENG_{1-n} = FO_{1-n} + A_{E_{1-n}} (P_0 - * PRESS) \quad (3)$$

$$** FJI = [\cos 6^\circ \Sigma (F\text{-}ENG_{1-4} + FE_{1-4}) + \cos 3^\circ \Sigma (F\text{-}ENG_{5-8}) + \Sigma FE_{5-8}] KVAL \quad (4)$$

$$FMI = FJI + FAI + FB \quad (5)$$

$$FB = (* RHO)(VOLUME) \quad (6)$$

$$FAI = -(BDRAG) - (DRAG) \quad (7)$$

$$DRAG = (CD)(* Q)(AREA) \quad (8)$$

$$** FJIO = \cos 6^\circ \Sigma [FO_{1-4} + FEI_{1-4}] + \cos 3^\circ \Sigma [FO_{5-8}] + \Sigma FEI_{5-8} \quad (9)$$

$$LISPO = \left(\frac{FJIO}{DFLOX} \right) \quad (10)$$

$$ALISPO = \left(\frac{AVFJIO}{AVDFLOX} \right) \quad (11)$$

$$AVFJIO = \left(\frac{1}{FLTTT} \right) \int_{t_i}^{t_n} (FJIO)\, dt \quad (12)$$

$$AVDFLOX = \left(\frac{1}{FLTTT} \right) \int_{t_i}^{t_n} (DFLOX)\, dt \quad (13)$$

$$MASS = M_i + \int_{t_i}^{t_n} (DMASS)\, dt \quad (14)$$

* Input data from tape

** The equations illustrate the S-IB stage, Saturn IB, where the 4 inboard engines are canted 3° and the 4 outboard engines are canted 6°. However, on stages where engines are not canted these considerations can be dropped.

$$A_m = \left(\frac{FMI}{MASS}\right) \tag{15}$$

$$\ddot{X}_m = \left(\frac{*\ddot{X}_m}{*A_m}\right) A_m, \qquad \ddot{Y}_m = \left(\frac{*\ddot{Y}_m}{*A_m}\right) A_m, \qquad \ddot{Z}_m = \left(\frac{*\ddot{Z}_m}{*A_m}\right) A_m \tag{16}$$

$$\dot{\vec{X}}_m = \int_{t_i}^{t_n} (\ddot{\vec{X}}_m)\, dt, \qquad \vec{X}_m = \int\int_{t_i}^{t_n} (\ddot{\vec{X}}_m)\, dt^2 \tag{17}$$

$$IAT = \int_{t_i}^{t_n} (A_m)\, dt \qquad *IAT = \int_{t_i}^{t_n} (*A_m)\, dt \tag{18}$$

$$DIAT = (IAT - *IAT) \tag{19}$$

$$\ddot{\vec{X}}_s = \ddot{\vec{X}}_m + *\ddot{\vec{X}}_G$$

$$\dot{\vec{X}}_s = \dot{\vec{X}}_{so} + \dot{\vec{X}}_m + *\dot{\vec{X}}_G$$

$$\vec{X}_{sc} = \vec{r}_o + \dot{\vec{X}}_{so}\, T + \vec{X}_m + *\vec{X}_G \tag{20}$$

$$\vec{X}_s = \vec{X}_{sc} - \vec{r}_o$$

$$\dot{\vec{X}}_e = \{[K]^T[\phi_o]^T[\omega]^T[\phi_o][K]\,\dot{\vec{X}}_s\} + \{[K]^T[\phi_o]^T[\dot{\omega}]^T[\phi_o][K]\,\vec{X}_{sc}\}$$

$$\vec{X}_e = \{[K]^T[\phi_o]^T[\omega]^T[\phi_o][K]\,\vec{X}_{sc}\} - \vec{r}_o \tag{21}$$

$$DA = \left(A_m - *A_m\right) \tag{22}$$

$$V_e = \left(\dot{X}_e^2 + \dot{Y}_e^2 + \dot{Z}_e^2\right)^{1/2} \tag{23}$$

$$DVE = \left(V_e - *V_e\right) \tag{24}$$

$$*A_m = \left(*\ddot{X}_m^2 + *\ddot{Y}_m^2 + *\ddot{Z}_m^2\right)^{1/2} \tag{25}$$

$$DDVE = \left[\frac{(DVE_t - DVE_{t-1})}{(t - t_{-1})} \right] \tag{26}$$

$$DDIAT = \left[\frac{(DIAT_t - DIAT_{t-1})}{(t - t_{-1})} \right] \tag{27}$$

$$TT = \frac{1}{2} (t + t_{-1}) \tag{28}$$

$$FF = \frac{1}{2} (FJI_t + FJI_{t-1}) \tag{29}$$

$$DD = \frac{1}{2} (DRAG_t + DRAG_{t-1}) \tag{30}$$

$$*AA = \frac{1}{2} (*A_{m_t} + *A_{m_{t-1}}) \tag{31}$$

$$*QQ = \frac{1}{2} (*Q_t + *Q_{t-1}) \tag{32}$$

$$MM = \frac{1}{2} (MASS_t + MASS_{t-1}) \tag{33}$$

$$CCDD = \frac{1}{2} (CD_t + CD_{t-1}) \tag{34}$$

$$DFA = -(DA)\ (MASS) = \frac{DA}{PAF} \tag{35}$$

$$DFVE = -(DDVE)\ (MM) = \frac{DDVE}{PVF} \tag{36}$$

$$DFVI = -(DDIAT)\ (MM) = \frac{DDIAT}{PVF} \tag{37}$$

$$DMA = \left(\frac{FMI}{*A_m} \right) - MASS = \frac{DA}{PAM} \tag{38}$$

$$DMVE = \left(\frac{FF - DD}{*AA - DDVE} \right) - MM = \frac{DDVE}{PVM} \tag{39}$$

$$DMVI = \left(\frac{FF - DD}{*AA - DDIAT} \right) - MM = \frac{DDIAT}{PVM} \tag{40}$$

$$DWA = \frac{DA}{PAW} \tag{41}$$

$$DWVE = \frac{DDVE}{PVW} \tag{42}$$

$$DWVI = \frac{DDIAT}{PVW} \tag{43}$$

$$*AMACH = \frac{1}{2}\,(*MACH_t + *MACH_{t-1}) \tag{44}$$

$$DCXA = \left[\frac{(DA)\ (MASS)}{*Q\ (AREA)}\right] = \frac{DA}{PACX} \tag{45}$$

$$DCXVE = \left[\frac{(DDVE)\ (MM)}{*QQ\ (AREA)}\right] = \frac{DDVE}{PVCX} \tag{46}$$

$$DCXVI = \left[\frac{(DDIAT)\ (MM)}{*QQ\ (AREA)}\right] = \frac{DDIAT}{PVCX} \tag{47}$$

$$CXCA = CD + DCXA \tag{48}$$

$$CXCVE = CCDD + DCXVE \tag{49}$$

$$CXCVI = CCDD + DCXVI \tag{50}$$

$$PACX = \left(\frac{*Q \cdot AREA}{MASS}\right) \tag{51}$$

$$PVCX = \left(\frac{*QQ \cdot AREA}{MM}\right) \tag{52}$$

$$PVM = \left(\frac{\partial DDVE}{\partial MASS}\right)_t = \left(\frac{*AA}{MM}\right)_t \tag{53}$$

$$PAM = \left(\frac{\partial A_m}{\partial M_i}\right)_t = \left(\frac{*A_m}{MASS}\right)_t \tag{54}$$

$$PVF = \left(\frac{\partial DDVE}{\partial F}\right)_t = \left(\frac{-1}{MM}\right)_t \tag{55}$$

$$PAF = \left(\frac{\partial A_m}{\partial F}\right)_t = \frac{-1}{MASS} \tag{56}$$

$$PVW = \left(\frac{\partial DDVE}{\partial \dot{w}} \right)_t = \left(\frac{*AA \cdot FLTTT}{MM} \right)_t \tag{57}$$

$$PAW = \left(\frac{\partial A_m}{\partial \dot{w}} \right)_t = \left(\frac{*A_m \cdot FLTTT}{MASS} \right)_t \tag{58}$$

$$RADD = \left(X_e^2 + Y_e^2 + Z_e^2 \right)^{1/2} \tag{59}$$

$$\dot{\vec{X}}_{so} = [K]^T [\phi_o]^T [\dot{\omega}_o] [\phi_o] [K] \vec{r}_o \tag{60}$$

A COMPUTER SIMULATION OF THE ORBITAL LAUNCH WINDOW PROBLEM

Archie C. Young* and Pat R. Odom**

ABSTRACT

Studies of manned interplanetary missions and systems involving orbital assembly concepts must carefully consider orbital launch window characteristics. In the general case, many variables are involved and parametric analyses must be performed to define the tradeoffs in orbital launch window design for a specified mission. This paper presents a digital computer simulation designed to provide a rapid means for accurate parametric analysis of the general orbital launch window problem. Numerical results are presented for three selected missions: A 1975 Venus flyby, a 1975 Mars low energy flyby, and a 1982 Mars stopover mission. These data illustrate the effect of mission parameters on orbital launch window characteristics. The data for the Mars flyby mission are compared to results obtained in a detailed calculus of variations analysis.

NOMENCLATURE

$\hat{A}_0$	unit vector toward ascending node of parking orbit on coplanar departure date
$\hat{A}_h$	unit vector toward ascending node of escape hyperbola
Δa	angle between outgoing asymptote and parking orbit plane
C_3	twice the total hyperbolic escape energy per unit mass
C_{3_0}	twice the total hyperbolic escape energy per unit mass on coplanar departure date
e_h	eccentricity of escape hyperbola
f_s	injection stage structural weight per unit weight of propellant
g_o	acceleration of gravity at earth's surface
i	inclination of parking orbit
I_{sp}	vacuum specific impulse of orbital launch system
JD	Julian departure date
JD_0	Julian date for coplanar departure
k	number of $\Delta\rho$ steps in computer determination of optimum ρ
m_h	angular momentum of escape hyperbola
n	apsidal ratio of parking orbit (r_a/r_p)
$\hat{P}_h$	unit vector in direction of escape hyperbola periapsis
$\bar{R}$	injection position vector
$\hat{R}$	injection unit position vector
R	radius of injection
r_a	apoapsis radius of parking orbit
r_p	periapsis radius of parking orbit
$\hat{S}$	unit vector in direction of outgoing asymptote of escape hyperbola (aim vector)
$\hat{S}_0$	unit vector in direction of outgoing asymptote of escape hyperbola on coplanar departure date (aim vector)
T	total vacuum thrust of orbital launch system

* Aerospace Engineer, Advanced Studies Office, Aero-Astrodynamics Laboratory, Marshall Space Flight Center, Huntsville, Alabama.

** Chief, Mission Analysis Branch, Systems Section, Northrop Space Laboratories, Huntsville, Alabama.

$\bar{V}$	velocity vector in parking orbit at point of injection maneuver
V	magnitude of velocity in parking orbit at point of injection maneuver
$\bar{V}_h$	velocity vector in escape hyperbola at point of injection maneuver
V_h	magnitude of velocity in escape hyperbola at point of injection manuever
$\overline{\Delta V}$	velocity increment vector for injection maneuver
ΔV	magnitude of injection velocity increment
ΔV_g	gravity loss velocity during injection maneuver
ΔV_m	minimum daily injection velocity increment assuming coplanar departure
ΔV_t	total characteristic injection velocity increment
W_f^*	fixed cutoff weight of orbital launch system after injection
$\hat{W}_h$	unit vector in direction of angular momentum vector of escape hyperbola
W_0	total weight of orbital launch system at ignition for injection maneuver
W_p	total usable propellant required for injection maneuver
$W_{p_{max}}$	maximum usable propellant weight for specified cutoff weight W_f^* of orbital launch system
α	right ascension of outgoing asymptote of escape hyperbola
α_0	right ascension of outgoing asymptote of escape hyperbola on coplanar departure date
β	angle between injection position vector $\bar{R}$ and outgoing asymptote $\hat{S}$
γ	flight path angle in parking orbit at point of hyperbolic escape injection (measured with respect to local vertical)
γ_h	flight path angle in hyperbola at point of injection maneuver (measured with respect to local vertical)
δ	declination of outgoing asymptote of escape hyperbola
δ_0	declination of outgoing asymptote of escape hyperbola on coplanar departure date
θ	true anomaly in parking orbit at point of hyperbolic injection
μ	gravitational constant for central body
ρ	angle between ascending node and injection position in parking orbit
ρ_a	angle between parking orbit ascending node and projection of outgoing asymptote onto parking orbit plane
ρ_{0pt}	injection position for minimum injection maneuver velocity increment
$\Delta\rho$	step size on injection position for computer determination of optimum ρ
σ	nondimensional ratio, $C_3R/2\mu$
ϕ	true anomaly in escape hyperbola at point of injection maneuver
ϕ_a	true anomaly of outgoing asymptote in hyperbola
ω	argument of periapsis of parking orbit
ω_h	argument of periapsis of escape hyperbola
ω_0	argument of periapsis of parking orbit on coplanar departure date
$\dot{\omega}$	time rate of change of parking orbit argument of periapsis
Ω	right ascension of ascending node of parking orbit
Ω_h	right ascension of ascending node of escape hyperbola
Ω_0	right ascension of ascending node of parking orbit on coplanar departure date
$\dot{\Omega}$	time rate of change of right ascension of parking orbit ascending node

$[\,]_j$ rotation matrix about a coordinate axis j

I. INTRODUCTION

The determination of orbital launch window characteristics is of major importance in the analysis of manned interplanetary missions and systems. The orbital launch window problem is directly involved in the selection of mission trajectories, the development of orbit operational concepts, and the design of orbital launch systems.

Early feasibility studies of interplanetary missions generally consider the earth departure window only in terms of energy requirements for coplanar injection maneuvers. More comprehensive preliminary design analyses of mission and systems (particularly involving orbital assembly and checkout concepts) must consider departure operations as influenced by the orbital launch window created by non-coplanar injection requirements. Usually, the actual departure injection window is much smaller in duration than that determined by energy requirements alone because of orbital launch window characteristics over the departure period.

The orbital launch window problem arises because of the dynamic nature of the relative geometry between the outgoing asymptote of the escape trajectory and the earth parking orbit. The orientation of the escape hyperbola asymptote relative to the earth is a function of time. The required energy level of the hyperbola also varies with time. In addition, the inertial orientation of the parking orbit is a function of time because of perturbations caused by the earth's oblateness. Thus, a coplanar injection onto the escape trajectory can be made only at a point in time when the outgoing asymptote is contained by the plane of parking orbit. In this case, the optimum position in parking orbit for the injection maneuver is at the periapsis of the escape hyperbola. If the parking orbit is elliptical, then its periapsis should be located at this position for an optimum single-impulse injection (minimum velocity increment, ΔV). Even though this condition may be planned as the nominal situation, it will not generally represent the more probable injection geometry. The general case of an injection maneuver performed at a time other than the coplanar time will involve both a path angle and a plane change and, therefore, a ΔV penalty. This would occur, for example, in the event of a time delay in this injection. In this case, the optimum position in the parking orbit for execution of the maneuver will not, in general, be at the periapsis of the escape hyperbola.

This paper describes an analytical digital computer simulation of the earth orbital launch window problem associated with interplanetary missions, and demonstrates its application to parametric mission studies. The simulation was developed to provide a means for rapid definition of orbital launch window characteristics for given missions based on a realistic analytical model. Although other modes are possible, only the single impulse departure mode is treated in this analysis. For example, a two-impulse transfer can be performed. The first impulse injects the vehicle onto a hyperbola coplanar with the parking orbit. The second impulse is executed out on the asymptote to maneuver the vehicle into the final hyperbolic plane required by the escape trajectory. This mode has been analyzed for departure from circular parking orbits by Deerwester et al. [1]. The two-impulse mode is a possible means of lengthening the orbital launch window; however, its advantage is not usually significant [1].

II. ANALYTICAL MODEL

The analytical procedure has been developed for determining the minimum impulsive velocity increment required for injection from a given circular or elliptical parking orbit onto a non-coplanar escape hyperbola specified by an energy level and outgoing asymptote direction. An initial parking orbit orientation is calculated for coplanar launch on a specified date with associated hyperbolic escape conditions. For any other date before or after the coplanar date, the minimum velocity increment for injection into specified hyperbolic conditions is determined. The optimum position in parking orbit for the maneuver is determined along with a complete set of auxiliary parameters for each launch date. These parameters completely define the injection conditions (velocity and position vectors), characteristics of the escape hyperbola, and all associated vector data. The angles defining the orientation of the impulsive thrust direction are computed relative to the parking orbit.

The analytical model is based on the following assumptions:

(1) The orbital launch vehicle is treated as a point mass in a general elliptical parking orbit. Both the parking orbit and escape hyperbola are based on restricted two-body mechanics.

(2) On the coplanar date, the parking orbit is established such that its periapsis coincides with the periapsis of the optimum coplanar escape hyperbola.

(3) The motion of the parking orbit is approximated by accounting for the nodal regression and the advance of periapsis based on equations for these perturbations from Krause [2].

(4) The hyperbolic escape injection maneuver is executed with a single impulsive velocity change.

(5) Gravity losses for vehicle performance calculation are determined from a table look-up procedure based on parametric integrated trajectory data.

Figure 1 shows the basic geometry of the analytical model. The fundamental coordinate frame established for the analysis is an equatorial system with the x-axis in the equatorial plane pointing to the vernal equinox, the z-axis normal to the equatorial plane pointing north, and the y-axis completing a right-handed triad. An auxiliary orbital coordinate system is shown with the ξ-axis in the parking orbit plane pointing in the direction of the orbit ascending node, the ζ-axis pointing in the direction of the parking orbit angular momentum vector, and an η-axis completing the right-handed triad.

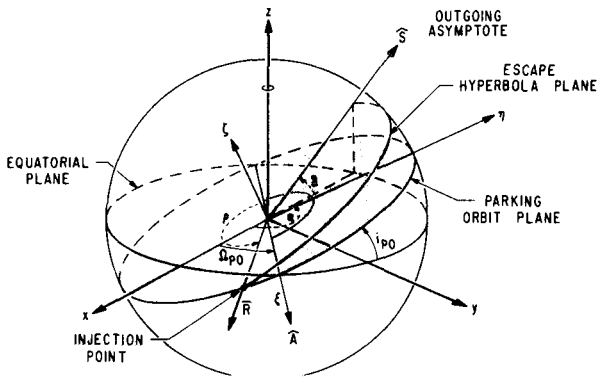

FIGURE 1. NON-COPLANAR ORBITAL LAUNCH GEOMETRY

Figure 2 gives the in-plane geometry of the escape hyperbola.

The analytical procedure consists of four steps as as follows:

(1) Initial Parking Orbit Orientation

(2) Parking Orbit Motion

(3) Determination of Velocity Vectors

(4) Injection Maneuver Computations

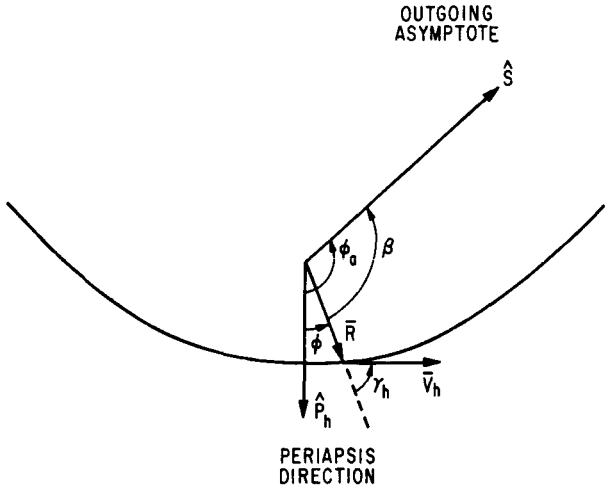

FIGURE 2. IN-PLANE GEOMETRY OF ESCAPE HYPERBOLA

A. INITIAL PARKING ORBIT ORIENTATION

For a given coplanar departure date JD_0 with associated hyperbolic escape conditions (α_0, δ_0, C_{3_0}), and a parking orbit defined by r_p, n, and i, the orientation of the parking orbit is established for optimum coplanar injection. This requires the determination of the right ascension of the ascending node Ω_0 and the argument of periapsis ω_0 of the parking orbit. The outgoing asymptote unit vector $\hat{S}_0$ is defined by

$$\hat{S} = \begin{bmatrix} S_{0x} \\ S_{0y} \\ S_{0z} \end{bmatrix} = \begin{bmatrix} \cos\alpha_0 \cos\delta_0 \\ \sin\alpha_0 \cos\delta_0 \\ \sin\delta_0 \end{bmatrix} \quad (1)$$

The right ascension of the ascending node of the parking orbit is given by

$$\sin\Omega_0 = \frac{-S_{0x}S_{0z} \pm S_{0y}\left[(S_{0x}^2 + S_{0y}^2)\tan^2 i - S_{0z}^2\right]^{1/2}}{(S_{0x}^2 + S_{0y}^2)\tan i} \quad (2)$$

$$\cos\Omega_0 = \frac{S_{0x}}{S_{0y}}\sin\Omega_0 + \frac{S_{0z}}{S_{0y}\tan i} \quad (3)$$

The plus and minus sign in the expression for $\sin\Omega_0$ shows that for a given parking orbit inclination there exist two possible parking orbit planes that contain the outgoing asymptote on the coplanar date. Therefore,

two solutions can be carried through the analysis. The equations are identical for both solutions; but the initial parking orbit orientation causes differences in numerical results between the two solutions for given missions. The choice of initial parking orbit orientation will be discussed in the presentation of parametric data for example missions.

The argument of periapsis of the parking orbit on the coplanar date is determined by the equation

$$\omega_0 = 2\pi - \cos^{-1}\left(1 + \frac{r_p C_{3_0}}{\mu}\right) + \cos^{-1}(\hat{A}_0 \cdot \hat{S}_0), \quad (4)$$

where $\hat{A}_0$ is a unit vector in the direction of the ascending node of the parking orbit given by

$$\hat{A}_0 = (\cos \Omega_0, \sin \Omega_0, 0) \quad (5)$$

The angle determined by $\hat{A}_0 \cdot \hat{S}_0$ is considered between 0 and 2π .

B. PARKING ORBIT MOTION

The second step of the analysis is to determine the inertial orientation of the parking orbit on any specified date JD before or after the coplanar date. The right ascension of the ascending node and argument of periapsis are determined by the equations,

$$\Omega = \Omega_0 + \dot{\Omega}(JD - JD_0) \quad (6)$$

and

$$\omega = \omega_0 + \dot{\omega}(JD - JD_0) \quad (7)$$

where the nodal regression rate $\dot{\Omega}$ and rate of advance of periapsis $\dot{\omega}$ are based on expressions derived in Krause [2].

C. DETERMINATION OF VELOCITY VECTORS

The third step of the procedure is to define the velocity vectors in the parking orbit and escape hyperbola as a function of position in parking orbit and hyperbolic conditions ($\hat{S}$, C_3) on the specified non-coplanar date. This is conveniently done by defining the orbital coordinate system ξ, ζ , η, illustrated in Figure 1. The angle ρ in the ξ-η plane defines position in the parking orbit as measured from the line of nodes.

The parking orbit position $\bar{R}$ and velocity $\bar{V}$ vectors in the equatorial reference frame (x, y, z system) are determined as a function of ρ as follows:

$$\bar{R} = R\hat{R}, \quad (8)$$

where

$$R = \frac{2n\, r_p}{(n+1)\left[1 + \left(\frac{n-1}{n+1}\right)\cos(\rho - \omega)\right]} \quad (9)$$

and

$$\hat{R} = [-\Omega]_3[-i]_1 \begin{bmatrix} \cos\rho \\ \sin\rho \\ 0 \end{bmatrix} . \quad (10)$$

The velocity is given by

$$\bar{V} = V\hat{V}, \quad (11)$$

where

$$V = \left\{2\mu\left[\frac{1}{R} - \frac{1}{r_p(n+1)}\right]\right\}^{1/2} \quad (12)$$

and

$$\hat{V} = [-\Omega]_3[-i]_1[-\rho]_3 \begin{bmatrix} \cos\gamma \\ \sin\gamma \\ 0 \end{bmatrix} . \quad (13)$$

The local flight path angle γ is determined by the expression

$$\gamma = \sin^{-1}\left[\frac{1}{r_p RV}\left(\frac{2n\mu}{n+1}\right)^{1/2}\right] , \quad (14)$$

where

$$0 \leqq \gamma \leqq \frac{\pi}{2} \quad \text{for} \quad 0 \leqq (\rho - \omega) \leqq \pi$$

and

$$\frac{\pi}{2} < \gamma < \pi \quad \text{for} \quad \pi < (\rho - \omega) < 2\pi .$$

The angle $(\rho - \omega)$ is the true anomaly θ of the position $\bar{R}$ in the parking orbit.

The velocity vector $\bar{V}_h$ (x, y, z reference frame) in the escape hyperbola at a position $\bar{R}$ may be expressed in the form

$$\bar{V}_h = V_h \left[\hat{R} \cos \gamma_h + (\hat{W}_h \times \hat{R}) \sin \gamma_h\right] , \quad (15)$$

where

$$V_h = \left(C_3 + \frac{2\mu}{R}\right)^{1/2} \quad (16)$$

$$\hat{W}_h = \frac{\hat{R} \times \hat{S}}{\sin\beta} \quad (17)$$

$$\beta = \cos^{-1} (\hat{R} \cdot \hat{S}) \quad (0 \leqq \beta < 2\pi) \quad (18)$$

$$\gamma_h = \sin^{-1} (m_h / RV_h) , \quad (19)$$

where m_h is the angular momentum of the escape hyperbola given by

$$m_h = \mu \left(\frac{e_h^2 - 1}{C_3}\right)^{1/2} \quad (20)$$

The eccentricity e_h of the hyperbola may be written as a function of the true anomaly ϕ_a of the outgoing asymptote in the hyperbolic plane (Fig. 2). This expression is

$$e_h = (\tan^2 \phi_a + 1)^{1/2} \quad (21)$$

It can be shown (see appendix) that

$$\tan \phi_a = -\sigma \sin \beta - [(1+\sigma)^2 - (1+\sigma \cos \beta)^2]^{1/2} \quad (22)$$

where

$$\sigma = \frac{C_3 R}{2\mu} . \quad (23)$$

The quadrant of the path angle γ_h is determined by the true anomaly ϕ in the hyperbola given by

$$\phi = \phi_a - \beta . \quad (24)$$

If $0 \leqq \phi \leqq \pi$, then $0 \leqq \gamma_h \leqq \pi/2$. If $\pi < \phi < 2\pi$, then $\pi/2 < \gamma_h < \pi$.

D. INJECTION MANEUVER COMPUTATIONS

Now the velocity increment vector for injection from the parking orbit onto the escape hyperbola at any position ρ can be determined by the vector difference

$$\overline{\Delta V} = \bar{V}_h - \bar{V} . \quad (25)$$

The optimum injection position, ρ_{0pt}, can be determined by varying ρ over a selected range of values until a minimum $|\overline{\Delta V}|$ is found. At this point all associated vector data and parameters can be calculated, such as, plane change angle, path angle change, in-plane and out-of-plane angles defining $\overline{\Delta V}$ relative to the parking orbit, geocentric injection latitude, etc.

For reference, the minimum velocity increment ΔV_m for injection on each date during a departure period based on a daily coplanar launch is given by

$$\Delta V_m = \left(C_3 + \frac{2\mu}{r_p}\right)^{1/2} - \left[\frac{2n\mu}{r_p (n+1)}\right]^{1/2} . \quad (26)$$

III. ORIENTATION OF ESCAPE HYPERBOLA

The in-plane size and shape of the escape hyperbola are defined by the semi-major axis $a_h = \mu/C_3$ and eccentricity e_h. The orientation of the hyperbola is defined by the following equations for the inclination i_h, right ascension of the ascending node Ω_h, and the argument of periapsis ω_h:

$$i_h = \cos^{-1} \left(\hat{W}_{h_z}\right) \quad (27)$$

where $\hat{W}_{h_z}$ is the z-component of the unit normal to the hyperbolic plane in the direction of angular momentum.

$$\Omega_h = \tan^{-1} \left(\frac{\sin \Omega_h}{\cos \Omega_h}\right) \quad (28)$$

where

$$\sin \Omega_h = \frac{\hat{W}_{h_x}}{\sin i_h}$$

$$\cos \Omega_h = \frac{-\hat{W}_{h_y}}{\sin i_h} \quad .$$

Finally,

$$\omega_h = \tan^{-1}\left(\frac{\sin \omega_h}{\cos \omega_h}\right), \tag{29}$$

where

$$\sin \omega_h = \hat{P}_h \cdot (\hat{W}_h \times \hat{A}_h)$$

$$\cos \omega_h = \hat{P}_h \cdot \hat{A}_h \quad .$$

The unit vector toward periapsis, $\hat{P}_h$, and unit vector $\hat{A}_h$ toward the ascending node are given by

$$\hat{P}_h = \left\{-\hat{R} - \frac{1}{\mu}\left[(\bar{R} \times \bar{V}_h) \times \bar{V}_h\right]\right\} / e_h \tag{30}$$

and

$$\hat{A}_h = \frac{\hat{k} \times \hat{W}_h}{\sin i_h}, \tag{31}$$

where $\hat{k}$ is the unit vector normal to the equatorial plane.

IV. COMPUTER SIMULATION

The analytical model described above has been programmed for the IBM 7094 digital computer. This program provides a rapid means for complete parametric investigations of orbital launch window characteristics for interplanetary mission and systems studies.

The program performs an automatic search on the injection position ρ in the parking orbit to determine the optimum position (within a one-degree tolerance) for minimum ΔV injection for each day over the departure period. Either direct or retrograde motion escape trajectories can be considered. For incoming injection (true anomaly ϕ of injection point in hyperbola between π and 2π), only solutions with periapsis radii of the escape hyperbola greater than 6470 km are considered admissible. This constraint is imposed to insure that the vehicle does not pass through the atmosphere following the injection maneuver.

An option is included in the program to permit consideration of either or both parking orbit solutions for given cases based on the choice of initial orbit orientation (Ω_0).

The push-button window characteristics can be analyzed with the program by consideration of injection maneuver requirements on each side of the optimum injection position, ρ_{0pt}, determined for each day over the departure period.

The computer simulation includes a routine for computation of orbital launch system performance. A vehicle system is specified by the fixed injection cutoff weight (W_f^*), maximum propellant load $W_{p_{max}}$ corresponding to the structural weight (f_s) per weight in excess of $W_{p_{max}}$, the total vehicle vacuum thrust (T), and the vacuum specific impulse (I_{sp}). The computer routine determines the initial weight of the vehicle required in parking orbit across the departure period. Estimates of gravity losses are included in the calculations by interpolation in a table of losses built into the program based on parametric integrated trajectory data.

The initial weight required in parking orbit is determined by the equation

$$W_0 = \frac{\left(W_f^* - \tau f_s W_{p_{max}}\right) e^{\Delta V_t / g_0 I_{sp}}}{1 - \tau f_s \left(e^{\Delta V_t / g_0 I_{sp}} - 1\right)}; \tag{32}$$

where ΔV_t is the characteristic injection velocity increment determined by the sum of the impulsive increment ΔV and the gravity loss ΔV_g. If the required usable propellant exceeds $W_{p_{max}}$, then $\tau = 1$; if the required propellant is less or equal to $W_{p_{max}}$ then $\tau = 0$. The performance calculation is an iterative process since ΔV_g is a function of the initial thrust-to-weight ratio, T/W_0. The required propellant for injection is

$$W_p = W_0 \left(1 - e^{-\Delta V_t / g_0 I_{sp}} \right) . \qquad (33)$$

The final cutoff weight is given by

$$W_f = W_f^* + \tau f_s \left(W_p - W_{p_{max}} \right) \qquad (34)$$

where $\tau = 0$ for $W_p \leqq W_{p_{max}}$ or $\tau = 1$ for $W_p > W_{p_{max}}$.

Input to the program consists of the following data:

Parking orbit parameters: r_p, n, i

Hyperbolic injection conditions on coplanar date: JD_0, α_0, δ_0, C_{3_0}

Hyperbolic injection conditions on each noncoplanar date considered: JD, α, δ, C_3

Injection position range: $\Delta\rho$, k

Vehicle data: W_f^*, $W_{p_{max}}$, T, I_{sp}, f_s.

The program has the capability for generating approximately 100 cases per minute where each case is the determination of optimum injection data for a specified departure date and mission.

V. NUMERICAL RESULTS FOR EXAMPLE MISSIONS

Interplanetary mission profile design uses the energy requirement to perform the mission as one of the principle criteria for profile selection. If a selected mission vehicle has to be assembled in orbit or otherwise spend a period of time in orbit, then an investigation of the orbital launch window sensitivity and duration is essential in order to evaluate the overall performance requirements and implication on systems design. The resultant evaluation will have an impact on orbit selection and even the design of the orbital launch vehicle such that the planned mission will have the highest possible probability for success. The orbital launch window analysis can be done efficiently and rapidly by utilizing the computer model presented in this paper.

The parameters that affect the orbital launch window include the parking orbit inclination, altitude, and eccentricity, and the declination and right ascension of the outgoing asymptote or aim vector $\hat{S}$. Generally the parking orbit altitude would be limited to a lower value which would be chosen. For a selected mission, the declination and right ascension of the aim vector are specified across some mission window; therefore, they are preselected values. The problem associated with the orbital launch window is the selection of the most efficient parking orbit inclination and orientation corresponding to the selected set of aim vectors across the mission window. A circular parking orbit is the most sensitive and adversely affected by the perturbation caused by earth's oblateness. Thus, if the declination and right ascension of the aim vectors do not differ significantly throughout the mission window, it may be advantageous to select an elliptical parking orbit since the perturbation effects are less than on a circular orbit. A 485-km circular parking orbit with a 30-degree inclination has a nodal regression rate of 6.69 degrees per day. An elliptical parking orbit with $r_p = 485$ km, $r_a/r_p = 7$, and an inclination of 30 degrees has a nodal regression rate of only 0.27 degrees per day and an advancement of the apsidal axis of 0.46 degrees per day. The orbital launch window for the elliptical parking orbit is generally one fairly wide window, whereas for a circular orbit that has an inclination greater than the declination of the aim vector generally there are two short injection windows. The parametric mission data to follow will illustrate this point.

For a given parking orbit inclination, there are two possible orientations of the orbit plane that will contain the aim vector as was shown by equation (2). The plus sign should be chosen for the radical in the equation if the aim vector has a positive declination. This selection of orientation will result in the orbit plane rotating such that after the nominal coplanar date the plane will have a smaller angular distance between the other set of aim vectors. For aim vectors with a negative declination the negative sign on the radical should be selected.

Three interplanetary missions were selected to obtain parametric data for the earth orbital launch window: a 1975 Venus flyby mission, a 1975 Mars low energy flyby mission, and a 1982 Mars stopover mission using a Venus swingby on the earth-return leg.

VI. 1975 VENUS FLYBY MISSION

Table I gives the earth departure dates and the orientation of the aim vector and energy levels for the example 1975 Venus flyby mission. The energy (C_3) requirement for the 30-day mission window is a smooth flat curve, and the right ascension of the aim vector is varying slowly. The declination of the aim vector is changing relatively rapidly, beginning at the opening of the mission window with a declination of -27.54 degrees. At the end of the window the declination has moved to -6.91 degrees. This trend on the declination will require a longer period of time for the parking orbit to rotate around to where the orbit will contain the aim vector for another coplanar injection. A parking orbit with a low inclination is desirable for this mission. Figure 3 gives the resultant orbital launch window characteristics for a 485-km altitude circular orbit with a 28.9-degree inclination. Plotted in the figure is the curve for coplanar injection throughout the mission window. A dashed line at 100 m/sec above the maximum ΔV requirement is drawn in. Two different nominal coplanar injection dates are given for orientation of the parking orbit: Julian 244-2559 and 244-2563. In order to stay under the superimposed dashed line for 100 m/sec above mission window ΔV requirement for orbital launch window, there exists a 3-day injection window around the first nominal coplanar date selected. The injection window opens up again about 10 days later and has a duration of 5 days. The second selected nominal coplanar launch date results in a 3-day injection window around the coplanar date.

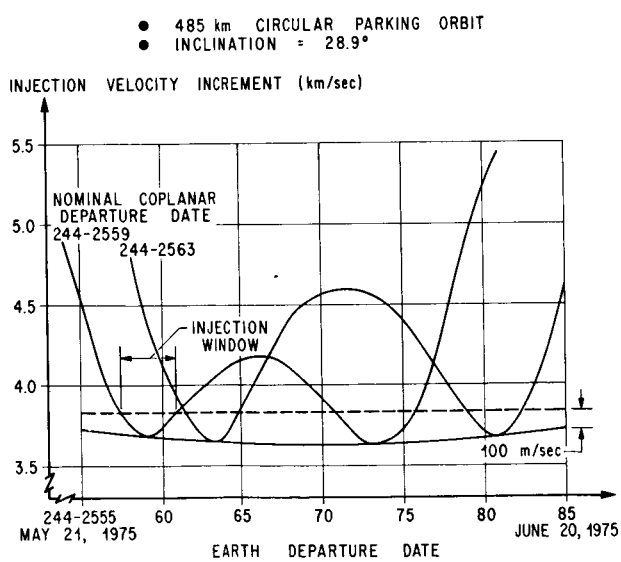

FIGURE 3. ORBITAL LAUNCH WINDOW CHARACTERISTICS FOR 1975 VENUS FLYBY MISSION

TABLE I. EARTH DEPARTURE DATA FOR 1975 VENUS FLYBY MISSION

Earth Departure Date JD	δ (deg)	α (deg)	C_3 (km^2/sec^2)
244- 2555	-27.54	148.24	12.7535
2557	-26.24	148.21	12.1857
2559	-24.95	148.03	11.7121
2561	-23.66	147.77	11.3279
2563	-22.65	146.75	10.9501
2565	-21.26	146.25	10.7151
2567	-19.85	145.67	10.5593
2569	-18.45	145.04	10.4821
2571	-17.02	144.32	10.4821
2573	-15.58	143.56	10.5593
2575	-14.09	142.23	10.5593
2577	-12.60	141.43	10.7932
2579	-11.15	140.67	11.1082
2581	- 9.70	139.88	11.5090
2583	- 8.29	139.12	12.0201
2585	- 6.91	138.39	12.6259

The injection window for this case opens again 14 days later and continues for 3 days. The ΔV peak between the two injection windows is greater on the second selected nominal launch date (244-2563) because the parking orbit gets a greater angular distance from the aim vector. If a shorter time span between the two injection windows is desired, then a selected nominal coplanar launch date at the opening of the mission window should be chosen. Given in Figure 4 is the orbital launch window from an elliptic parking orbit with r_p = 6863 km (485 km altitude) and $r_a/r_p = 7$. One injection window of 8 days occurs around each of the selected nominal coplanar injection dates.

VII. 1975 MARS FLYBY MISSION

Table II shows the aim vector condition throughout the 30-day mission window. The orbital window results are shown in Figure 5. With 100 m/sec allocated for orbital launch window above the maximum

mission window requirement, a 485-km, 35-degree inclination circular parking orbit results in a 17-day injection window, a 37-degree inclination gives a 19-day injection window, and a 39-degree inclination gives a 21-day injection window.

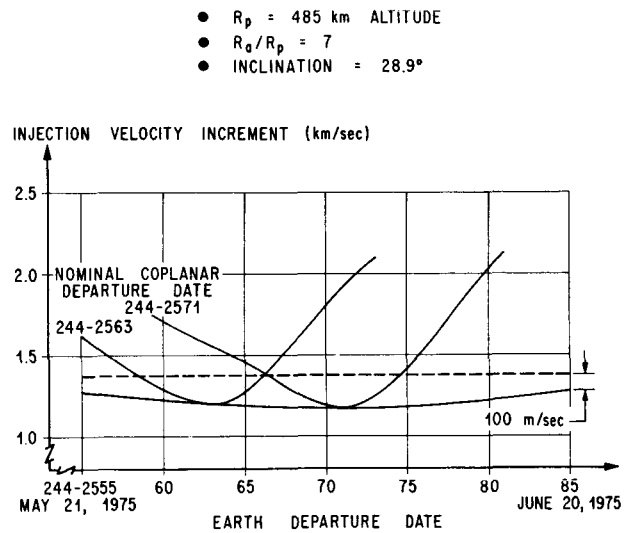

FIGURE 4. ORBITAL LAUNCH WINDOW CHARACTERISTICS FOR 1975 VENUS FLYBY MISSION

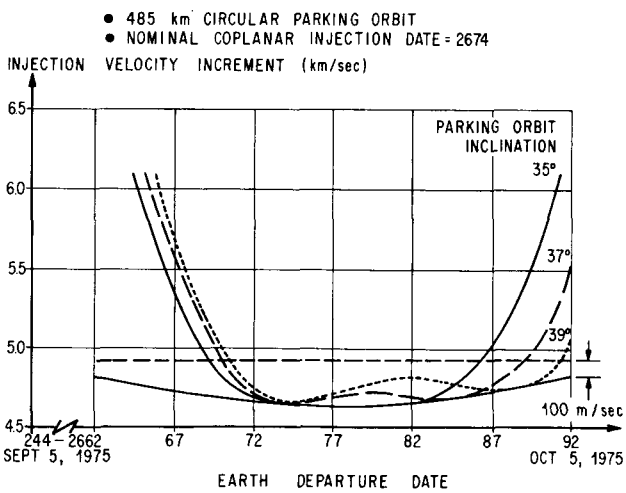

FIGURE 5. ORBITAL LAUNCH WINDOW CHARACTERISTICS FOR 1975 MARS FLYBY MISSION

TABLE II. EARTH DEPARTURE DATA FOR 1975 MARS FLYBY MISSION

Earth Departure Date JD	δ (deg)	α (deg)	C_3 (km^2/sec^2)
244- 2662	33.11	95.23	38.53
2664	33.19	94.51	37.54
2666	33.27	93.66	36.59
2668	33.34	92.67	35.52
2670	33.40	91.55	35.06
2672	33.45	90.29	34.46
2674	33.47	88.91	33.98
2676	33.46	87.40	33.66
2678	33.42	85.79	33.46
2680	33.22	84.54	34.011
2682	33.11	82.77	34.15
2684	32.96	80.95	34.43
2686	32.67	79.58	35.49
2688	32.45	77.71	36.16
2690	32.18	75.85	37.10
2692	31.82	74.51	38.79

VIII. 1982 MARS STOPOVER MISSION

Parametric orbital launch window data were obtained for a 1982 Mars stopover mission which uses a Venus swingby on the inbound leg. Table III presents the aim vector throughout the 30-day mission window. Circular and elliptical parking orbits with inclinations of 30 and 34 degrees, and two selected nominal coplanar injection dates were considered. Figures 6 and and 7 show the results for the circular parking orbit. Figures 8 and 9 give the injection window data for the elliptical parking orbit.

TABLE III. EARTH DEPARTURE DATA FOR 1982 MARS STOPOVER MISSION VIA VENUS INBOUND SWINGBY

Earth Departure Date JD	δ (deg)	α (deg)	C_3 (km^2/sec^2)
244- 4920	16.20	187.00	11.7327
4922	17.50	187.50	11.3279
4924	19.00	187.90	10.9303
4926	20.50	188.30	10.5404
4928	22.20	188.60	10.1570
4930	23.90	188.90	9.9679
4932	25.80	189.20	9.7806
4934	27.70	189.40	9.7806
4936	29.70	189.60	9.5951
4938	31.80	189.70	9.5951
4940	33.90	189.80	9.7806
4942	36.00	190.00	9.9679
4944	38.10	190.10	10.1570
4946	40.20	190.20	10.5404
4948	42.20	190.30	10.9303
4950	44.20	190.50	11.5294

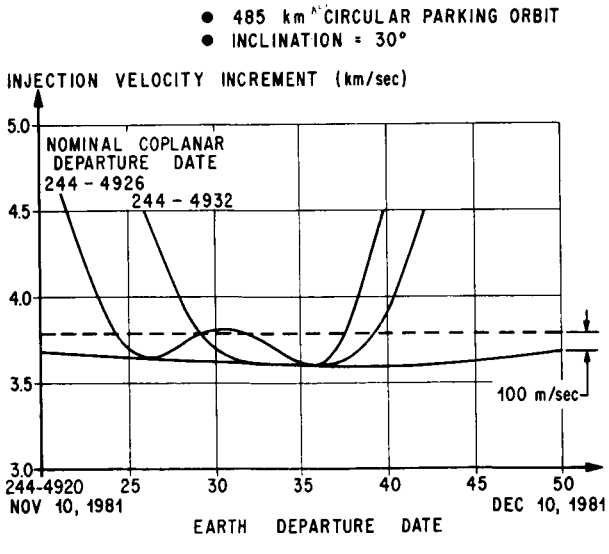

FIGURE 6. ORBITAL LAUNCH WINDOW CHARACTERISTICS FOR 1982 MARS STOPOVER MISSION UTILIZING VENUS SWINGBY MODE ON INBOUND LEG

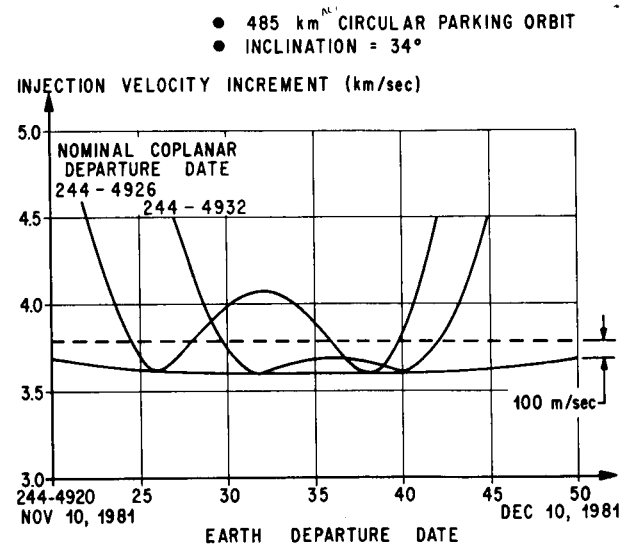

FIGURE 7. ORBITAL LAUNCH WINDOW CHARACTERISTICS FOR 1982 MARS STOPOVER MISSION UTILIZING VENUS SWINGBY MODE ON INBOUND LEG

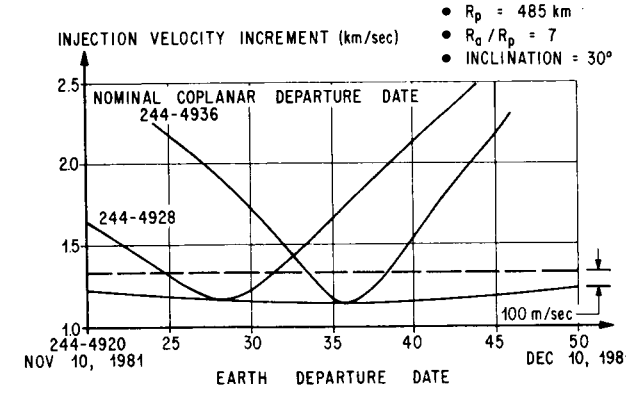

FIGURE 8. ORBITAL LAUNCH WINDOW CHARACTERISTICS FOR 1982 MARS STOPOVER MISSION UTILIZING VENUS SWINGBY MODE ON INBOUND LEG

IX. ORBITAL PUSH-BUTTON WINDOW: 1982 MARS STOPOVER MISSION

The incremental velocity requirements given in Figures 6 through 9 are obtained by injection at the

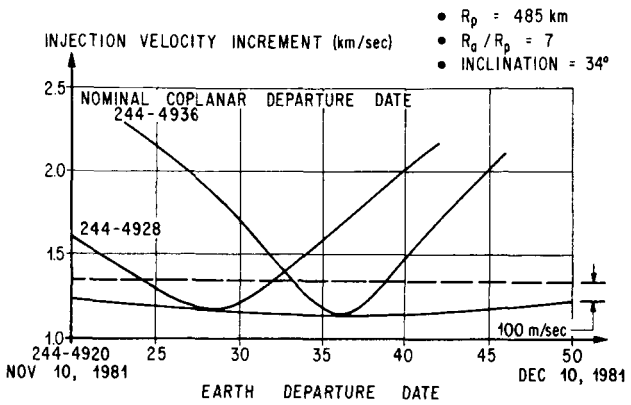

FIGURE 9. ORBITAL LAUNCH WINDOW CHARACTERISTICS FOR 1982 MARS STOPOVER MISSION UTILIZING VENUS SWINGBY MODE ON INBOUND LEG

optimum point in the parking orbit. However, if the actual injection occurs somewhere on either side of these optimum injection points, then a push-button window must be superimposed on the orbital injection window. A reasonable time span for a push-button window is on the order of ± 2 minutes from the optimum injection point. This amounts to ± 8 degrees in a 485-km circular orbit and ± 10.6 degrees in an elliptic parking orbit with $r_a/r_p = 7$. Figure 10 shows the push-button window requirement associated with the optimum injection point on the nominal coplanar departure date of 244-5526 shown in Figure 6 (circular parking orbit). A push-button window ΔV allocation of 40 m/sec will permit injection ± 1.5 minutes from the optimum injection point. The elliptical parking orbit push-button window is illustrated in Figure 11. The slope of this curve is not as steep as that shown for the circular parking orbit case. This can be explained by the fact that the relative difference of the path flight angle between the hyperbola and ellipse does not build up as fast as the relative difference between the hyperbola and the circular parking orbit. An allocation of 40 m/sec for the push-button window will permit injection ± 2.25 minutes from the optimum injection location in the elliptical orbit.

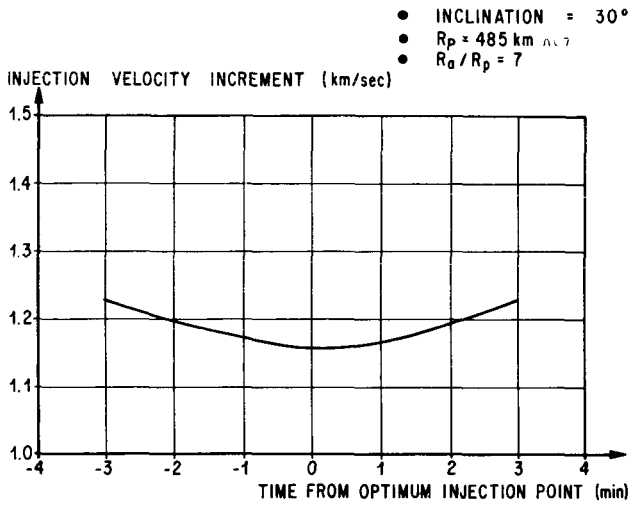

FIGURE 10. PUSH-BUTTON WINDOW CHARACTERISTICS FOR 1982 MARS STOPOVER MISSION

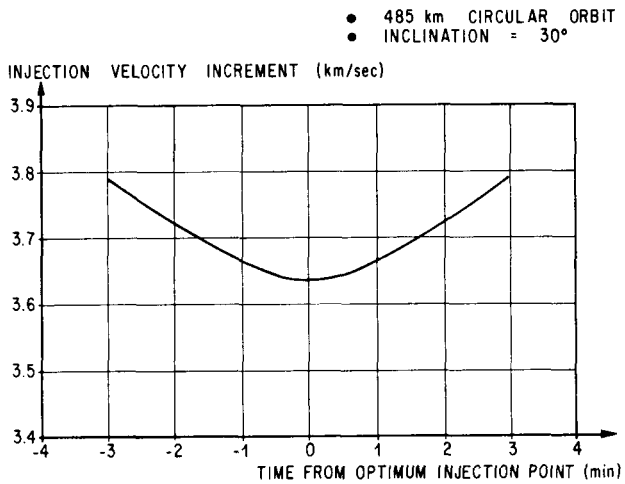

FIGURE 11. PUSH-BUTTON WINDOW CHARACTERISTICS FOR 1982 MARS STOPOVER MISSION

X. COMPARISON OF COMPUTER MODEL RESULTS WITH INTEGRATED PROGRAM RESULTS

The final geometry of the desired injection maneuver cutoff surface containing the outgoing asymptote of aim vector $\hat{S}$ as determined by the computer

model compares very closely with an actual integrated trajectory based on calculus of variations techniques. To demonstrate a comparison of results, a geocentric cutoff surface required for a 1975 Mars flyby mission was simulated with a calculus of variations trajectory program and with the analytical computer model. An orbital launch vehicle was placed into a 485-km, 35-degree inclination circular parking orbit with a planned departure date of 244-2674 (September 17, 1975). However, it was assumed that the vehicle did not get a "go ahead" on the planned departure date, thus requiring a launch out of orbit on an off-nominal date. The implication and performance sensitivity of departing on a later date are given in Table IV, which compares the results from an integrated calculus of variations trajectory program and the analytical computer model. The results are seen to be in excellent agreement.

TABLE IV. COMPARISON OF INTEGRATED AND COMPUTER MODEL RESULTS FOR 1975 MARS FLYBY MISSION

Earth Departure Date		W_f(lbs)	W_0(lbs)	ω_h	Ω_h	i_h	e_h
244-2674	Integrated Results	260 962	800 000	304.56	18.81	35.11	1.59
	Computer Model Results	260 962	800 205	304.93	18.14	35.00	1.59
244-2676	Integrated Results	261 533	800 000	311.94	8.18	33.93	1.58
	Computer Model Results	261 533	801 000	312.22	7.60	33.88	1.58
244-2678	Integrated Results	261 605	800 000	320.96	355.62	33.42	1.58
	Computer Model Results	261 605	800 300	321.27	355.02	33.42	1.58
244-2680	Integrated Results	260 684	800 000	331.68	341.84	33.87	1.59
	Computer Model Results	260 684	800 445	332.08	341.14	33.95	1.59
244-2686	Integrated Results	245 485	800 000	358.87	303.83	42.59	1.62
	Computer Model Results	245 485	802 003	359.59	302.63	43.21	1.61

244-2674 selected as the nominal coplanar injection date.

VEHICLE PARAMETERS: Thrust 410 000 lbs

Initial Weight 800 000 lbs (for the integrated cases)

Specific Impulse 426 sec

XI. CONCLUSIONS

The following conclusions are drawn on the basis of the work summarized by this paper:

(1) The analytical method presented in this paper for simulation of the orbital launch window provides a rapid means of generating realistic parametric data for mission studies.

(2) The simulation provides a vector and geometrical data sufficient for use as good starting points in detailed departure trajectory analyses based on calculus of variations of steepest descent techniques.

(3) Parking orbit inclination, initial orientation, and r_a/r_p ratio are the key parameters in selection of the optimum orbital launch window within mission constraints. The program can also be utilized in the analysis of arrival and escape phases for planetary capture or stopover missions. (Orbital launch window problems for any of the planets or moons can be analyzed with the computer model presented in this paper.)

APPENDIX

DERIVATION OF EQUATION FOR TRUE ANOMALY OF OUTGOING ASYMPTOTE

For a given injection position vector $\bar{R}$, outgoing asymptote vector $\hat{S}$ and energy level C_3, it is required that the eccentricity e_h of the escape hyperbola containing these vectors be determined. The eccentricity is a function of the hyperbolic true anomaly ϕ_a of the outgoing asymptote vector $\hat{S}$; i.e.,

$$e_h = -\frac{1}{\cos \phi_a} = (\tan^2 \phi_a + 1)^{1/2} . \qquad (A\text{-}1)$$

Therefore, the problem becomes one of determining an expression of ϕ_a.

Define a nondimensional parameter σ as follows:

$$\sigma = \frac{C_3 R}{2\mu} . \qquad (A\text{-}2)$$

The conic equation for the escape hyperbola may then be written in the form

$$2\sigma = \frac{e_h^2 - 1}{1 + e_h \cos \phi} , \qquad (A\text{-}3)$$

where ϕ is the true anomaly of the position $\bar{R}$. Consider the geometry of $\hat{S}$ relative to the parking orbit plane (ξ, ζ, η reference frame) shown in Figure A1. The unit position vector $\hat{R}$ in the ξ, ζ, η system is given by

$$\hat{R} = (\cos \rho, \sin \rho, 0) .$$

The asymptote vector $\hat{S}$ in the ξ, ζ, η system becomes

$$\hat{S} = (\cos \rho_a \cos \Delta a, \sin \rho_a \cos \Delta a, \sin \Delta a) .$$

The angle β between the $\hat{R}$ and $\hat{S}$ vectors is introduced by forming the dot product

$$\cos \beta = \hat{R} \cdot \hat{S} \quad (0 \leqq \beta \leqq 2\pi) \qquad (A\text{-}4)$$

$$\cos \beta = \cos \rho \cos \rho_a \cos \Delta a + \sin \rho \sin \rho_a \cos \Delta a$$

or

$$\cos \beta = \cos (\rho - \rho_a) \cos \Delta a .$$

From the definitions of ϕ, ϕ_a, and β we have the relation

$$\phi = \phi_a - \beta \quad (0 \leqq \phi < 2\pi) . \qquad (A\text{-}5)$$

Or we may write

$$\cos \phi = \cos (\phi_a - \beta) = \cos \phi_a \cos \beta + \sin \phi_a \sin \beta . \qquad (A\text{-}6)$$

Now combining equations (A-1), (A-3), and (A-6) we obtain a quadratic equation in $\tan \phi_a$:

$$\tan^2 \phi_a + 2\sigma \sin \beta \tan \phi_a - 2\sigma(1 - \cos \beta) = 0. \qquad (A\text{-}7)$$

The two solutions are

$$\tan \phi_a = -\sigma \sin \beta \pm [\sigma^2 \sin^2 \beta + 2\sigma (1 - \cos \beta)]^{1/2} \qquad (A\text{-}8)$$

which have the more convenient form

$$\tan \phi_a = -\sigma \sin \beta \pm [(1 + \sigma)^2 - (1 + \sigma \cos \beta)^2]^{1/2} . \qquad (A\text{-}9)$$

In the general case, ϕ_a will be a second quadrant angle; therefore, $\tan \phi_a < 0$. This implies in equation

(A-8) that the absolute value of the second term on the right side cannot exceed $\sigma \sin \beta$ if the plus sign on the second term is used. Since $2\sigma(1 - \cos \beta) > 0$ in the second term, it is observed that

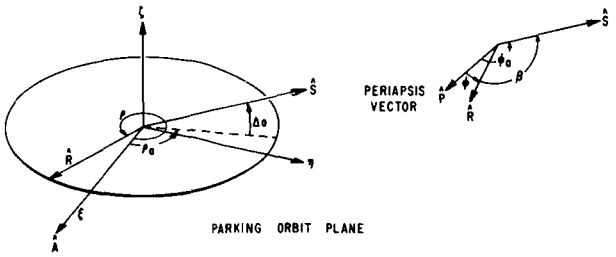

FIGURE A1. GEOMETRY OF OUTGOING ASYMPTOTE RELATIVE TO PARKING ORBIT PLANE

$$[\sigma^2 \sin^2 \beta + 2\sigma(1-\cos \beta)\ ]^{1/2} > \sigma \sin \beta\ .$$

Thus, only the minus sign root is permissible.

REFERENCES

1. Deerwester, J. M.; McLaughlin, J. R.; and Wolfe, J. F.: Earth-Departure Plane Change and Launch Window Considerations for Interplanetary Missions. J. Spacecraft Rockets, vol. 2, pp 169-174, 1966.

2. Krause, H. G. L.: The Secular and Periodic Perturbations of the Orbit of an Artificial Earth Satellite. Presented at the Seventh International Astronautic Congress, Rome, Italy, 1956.

II. FLUID DYNAMICS

STUDIES OF FUEL SLOSHING UNDER SIMULATED LOW GRAVITY CONDITIONS

by

F. T. Dodge* and L. R. Garza*
F. M. Bugg** and H. J. Buchanan**

SUMMARY

Experimental measurements are given for the slosh force and resonant frequency in laterally vibrated, cylindrical tanks under conditions of moderately small Bond numbers ($10 < Bo < 100$). Four different diameter tanks and three liquids are tested. All of the liquids have zero degree contact angles on the tank walls. The sloshing exhibits the resonant force peak and swirling motion familiar from high-gravity sloshing.

A theoretical analysis also is set forth, and, according to it, the sloshing mass in an equivalent mechanical model is always smaller for low gravity sloshing than for high gravity sloshing. In the Bond number regime used in the tests, the theory predicts only a small change in the resonant frequency as compared to the high-g case. Comparisons of the predictions of the equivalent mechanical model and the experimental data show that the model adequately predicts the slosh force and resonant frequency.

LIST OF SYMBOLS

Bo - Bond Number, $\rho g R_o^2/T$

F(R) - nondimensional meniscus height

g - acceleration due to gravity

h - height of bottom of meniscus above bottom of tank

h_o - height of fixed mass above tank bottom

h_w - meniscus height at tank wall

$h_{c.m.}$ - height of center-of-mass above tank bottom

h_1 - height of fundamental slosh mass above tank bottom

k_1 - spring constant for fundamental slosh mode

m_o - rigidly attached mass in mechanical model

m_T - total liquid mass

m_1 - vibrating mass of fundamental slosh mode

R_o - radius of tank

R, θ, Z - nondimensional cylindrical coordinate system

T - surface tension

$x_o(X_o)$ - dimensional (nondimensional) excitation amplitude

ϵ - nondimensional wave height

ν - kinematic viscosity

ρ - density of liquid

τ - nondimensional time

Φ - nondimensional velocity potential

$\omega(\Omega)$ - dimensional (nondimensional) excitation frequency

ω_n - resonant frequency of fundamental slosh mode

I. INTRODUCTION

The free surface wave motion, or sloshing, of liquid in large propellant tanks has long been

*Southwest Research Institute, Department of Mechanical Sciences, San Antonio, Texas.
**Aero-Astrodynamics Laboratory, George C. Marshall Space Flight Center/NASA.
This research was supported by Contract NAS8-20290.

recognized as an important part of stability and control analyses. However, nearly all the previous experimental and theoretical work has been limited to situations in which the steady axial acceleration of the tank (gravity or thrust or both) is large; see, for example, the review given in Ref. 1. But with the advent of space vehicles designed to restart after an extended period of near weightlessness, interest in problems of "low gravity" propellant oscillations has increased. In this nearly weightless state, many normally small forces must be accounted for in determining the liquid's behavior; the most important is usually the interfacial tension between the liquid and the ullage gas.

The dimensionless parameter indicating when interfacial tension is important is the Bond number, $Bo = \rho g R_o^2/T$. Very low gravity fluid mechanics are characterized by $Bo < 1$, while high-g problems occur for $Bo > 100$. But the intermediate range, $1 < Bo < 100$, is important in rocket technology, since this is the usual range of Bo for large boosters in waiting orbits [2, 3], and for this reason it is the moderately low gravity range of sloshing that is the subject of the studies reported here.

Although Satterlee and Reynolds [4] previously have published data for resonant frequencies, the data presented in this report are the first, as far as is known to the authors, which give both slosh forces and resonant frequencies as a function of Bo.

II. EXPERIMENTAL PROCEDURE

Experimental data for even moderately low gravity sloshing are not obtained easily. Laboratory facilities that can duplicate an actual small axial acceleration, such as drop towers, are usually not able to provide low gravity for a sufficiently long time to get consistent and reliable data for the slosh force and resonant frequency. An alternative method, and the one used here, is to simulate low gravity by using small diameter tanks; in this way, the interfacial or capillary forces can be made comparable to the gravity forces so that this is a suitable low gravity test for our purposes.

Figure 1 is a view of the experimental setup, and a closeup of the model tanks and support system is shown in Figure 2. The bar in the lower right-hand corner of Figure 2 holds an electromagnetic probe used to measure the displacement of the support relative to a fixed coordinate

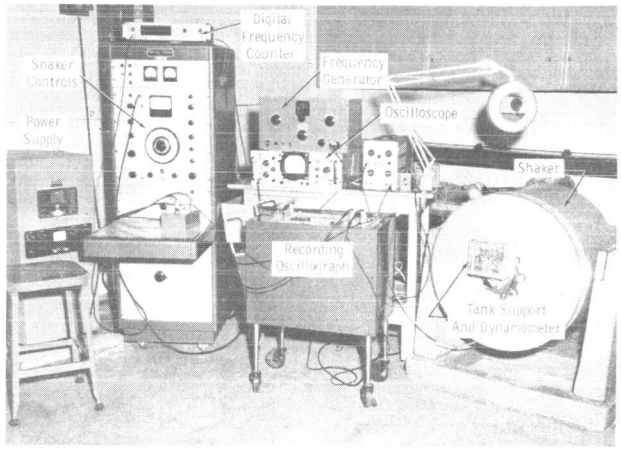

FIGURE 1. VIEW OF EXPERIMENTAL APPARATUS

system. The tanks, which in this case are about 1 in. in diameter, are attached directly to the flexure arms of the force measuring apparatus (the "dynamometer"). Semiconductor strain gages having a gage factor of 118 are mounted on the flexure arms, which are aluminum strips 0.0055 in. thick, 0.312 in. wide, and about 7/16 in. long. The dynamometer is bolted to the base, which is then mounted on the armature of an electrodynamic shaker; this arrangement allows the tanks to be excited in pure translation.

Four different glass tanks, having diameters ranging from 1.36 in. to 0.384 in., are used with three different liquids: distilled water, methanol, and carbon tetrachloride (CCl_4). All of the liquids are reagent grade and all have static contact angles at the liquid-tank-air contact line of zero degrees, measured in the liquid.

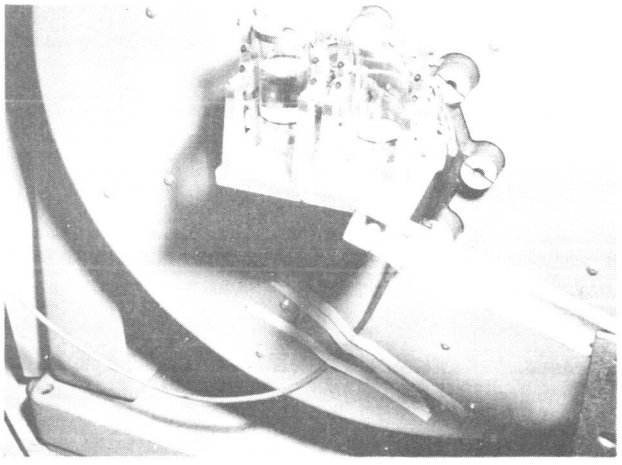

FIGURE 2. VIEW OF GLASS TANKS AND DYNAMOMETER

Before each series of tests, the tanks are cleaned in a detergent-and-water solution and rinsed with ethanol and distilled water. (In some of the tests using distilled water, the tanks are also cleaned in a NaOH solution and a hot chromic acid solution.) Then, the tops of the tanks are covered with a clean, flexible plastic wrapper; this is removed only briefly when the test liquid is put in. All of the hardware coming into contact with the test liquid is cleaned in the same manner, which allows the liquid free surface to be kept reasonably free of contamination during the actual testing.

Two tanks are used during the experiments. One, called the active tank, contains the test liquid, and the other, the balance tank, is used to cancel the output force signal of the empty active tank. In other words, the output signal of each of the strain gage arrays are combined in a bridge such that they exactly cancel when both tanks are empty and the apparatus is vibrated. Consequently, after liquid is put in the active tank, the signal reaching the recording oscillograph is due only to the force exerted on the active tank by the sloshing liquid.

After cancelling the force signal of the empty tanks as nearly as is practical, the displacement probe is calibrated by setting known static displacements of the shaker's armature with a dial indicator and recording the probe signal on the oscillograph. After this calibration, the residual force signal of the empty tanks is recorded for various excitation frequencies and amplitudes; the displacement signal is also recorded for reference.

Then, liquid is put in the active tank. The first liquid in each series of tests is always distilled water because it is the most easily contaminated. The other test liquids, methanol and CCl_4, are both good cleaners and not very susceptible to contamination, but, even so, the active tank is always rinsed with distilled water before each change in liquids.

Next, the sloshing forces are recorded for various excitation amplitudes and frequencies in a frequency band centered on the experimentally determined resonant frequency for the fundamental slosh mode; again, the displacement signal is recorded simultaneously. Because the slosh forces are very small, even as small as 0.0001 pound, they are easily masked by external noise. To prevent this, the force signal is passed through an electronic filter having a bandpass of 2 to 30 cps. Also, a rigid plastic dust cover, which can be seen in Figure 1, is put over the apparatus to keep stray air currents from exciting the tanks and thus giving spurious responses in the bandpass range of the filter. A clean sinusoidal force signal is usually obtained by these methods.

After the sloshing tests, the liquid is removed and known weights, usually rolled up strips of brass shim stock, are put in the active tank. The force output of the weights, for various excitations, then is recorded. Because the amplitude of the force exerted on the tanks by the weights can be computed exactly ($=\omega^2 x_o$ times the mass of the weights), the force signal is calibrated by plotting the amplitude of this signal (after subtracting whatever residual signal was noted previously, with due regard to the phase angles of the two signals with respect to the displacement) against the calculated force. Finally, the sloshing force is obtained by subtracting the residual signal from the slosh force signal and comparing the result with the force calibration curve.

The accuracy of the various measurements is as follows. The excitation frequency can be determined and held constant to within about 3 parts in a thousand. The excitation amplitude can be determined and held constant to within an absolute precision of about ± 0.0005 inch. Amplitudes of the force signals can be read to about 1 part in 100, with the exception that for extremely small signals the accuracy is about 1 part in 10. Phase angles between excitation amplitude and force output traces can be determined from the oscillograph records to within $\pm 20°$; these angles are used only in subtracting the small residual signals of the empty tanks from the much larger dynamic force signals. The height of the liquid in the tank can be measured to within ± 0.010 in., and the meniscus height to about ± 0.015 inch. The overall accuracy of the slosh force data, after being reduced, thus is estimated to be within $\pm 5\%$ of their true values.

III. EXPERIMENTAL RESULTS

As was implied by the preceding discussion, the objective of the experimental program was to determine the slosh forces and resonant frequencies as a function of Bo for liquids whose contact angle on the tank walls is zero degrees. No attempt was made to measure the sloshing moment on the tank as this would have complicated the instrumentation problem considerably.

During the sloshing, the contact angles of methanol and CCl_4 always remained equal to their

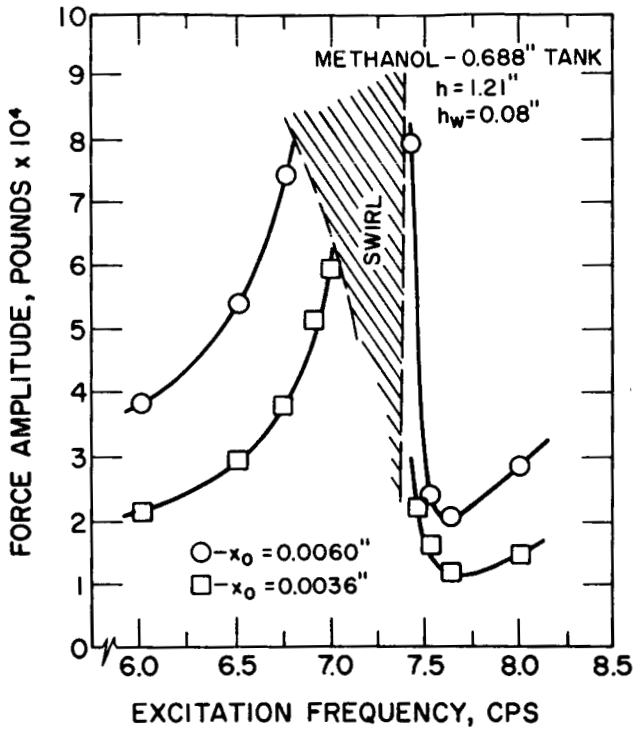

FIGURE 3. RESPONSE CURVE FOR METHANOL, BOND NUMBER = 26

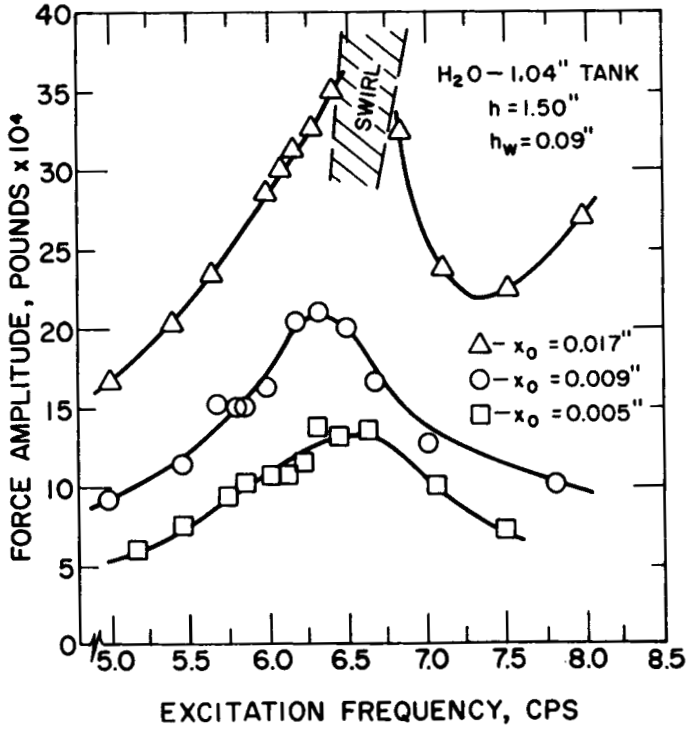

FIGURE 4. RESPONSE CURVE FOR WATER, BOND NUMBER = 23

static values (zero degrees), at least as nearly as could be determined from visual observations. The distilled water, however, appeared to "stick" to the walls, causing large departures of its contact angle from the static value. As will be seen, this hysteresis of the contact angle causes considerable discrepancies between the slosh force data for water and those for methanol and CCl_4.

Figures 3 and 4 show typical response curves for methanol and distilled water, the Bond number in both cases being about 25; because of differences in ρ/T for the two liquids, Bo equality requires tanks of different diameters. In contrast, Figure 5 shows the force response for methanol in a tank of the same diameter as that for the water in Figure 4. (The solid lines in these figures are faired curves through the experimental data.) There is a pronounced resonance for methanol, as can be seen from Figures 3 and 5. The curves, in fact, are qualitatively similar to resonance curves for ordinary high-g sloshing. Near the resonance, the sloshing is of the rotary or "swirling" type encountered in high-g sloshing [5, 6] in which the surface wave rotates around the tank. The shaded areas shown in the figures indicate in a crude way the boundaries of the swirling zone. Once swirling occurs, the slosh force also rotates around the tank, and, thus, the forces in this zone cannot be determined nor the exact resonant frequency found.

The response curves for water, Figure 4, are not similar to those for methanol, either for Bo equality, Figure 3, or for tank diameter equality, Figure 5. Comparing Figures 4 and 5, the resonance peak for water is near 6.5 cps instead of the 5.9 cps found for methanol. Yet the theoretical

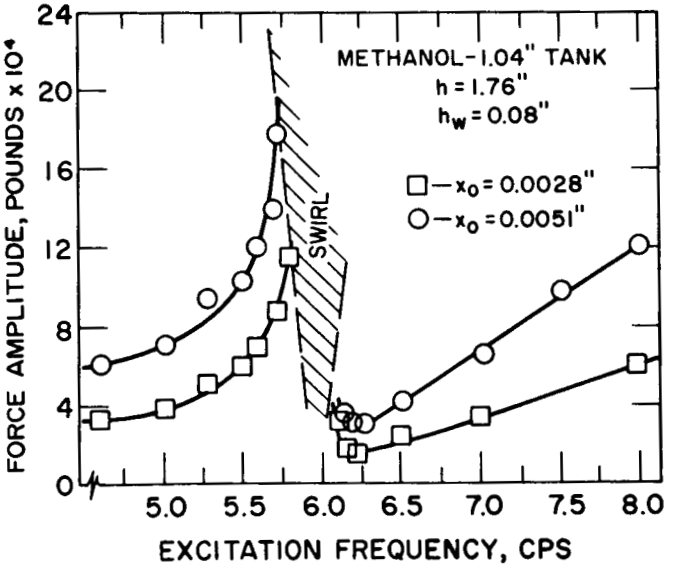

FIGURE 5. RESPONSE CURVE FOR METHANOL, BOND NUMBER = 55

shift in resonant frequency because of the difference in Bo is not nearly of this magnitude, as will be seen in the next section. Comparing Figure 4 to either Figure 3 or 5, the curves for water appear to be heavily damped. Furthermore, the boundaries of the swirling motion, which depend greatly on the amount of damping present, are not crossed except for large values of the excitation amplitude. Yet the viscosity of all the liquids is approximately the same (ν_{H_2O} = 0.0101 cm/sec, ν_{CCl_4} = 0.0097 cm/sec, $\nu_{methanol}$ = 0.0059 cm/sec); certainly, the differences in the viscous damping are not sufficient to explain the differences between the responses. The differences, then, must be caused by the water's sticking to the tank walls. In fact, it is known that contact angle hysteresis does cause energy dissipation similar to viscous damping [7], but not much more than this is known about it.

The water behaved in the same anomalous manner in the other tanks, and, since the interest here is in liquids that do not stick to the walls, these being the most important kinds in missile applications, the response curves for water in the other tanks are not shown.

Typical response curves for CCl_4 are shown in Figures 6 and 7 for Bo's of 45 and 14. They are similar to the curves for methanol, except

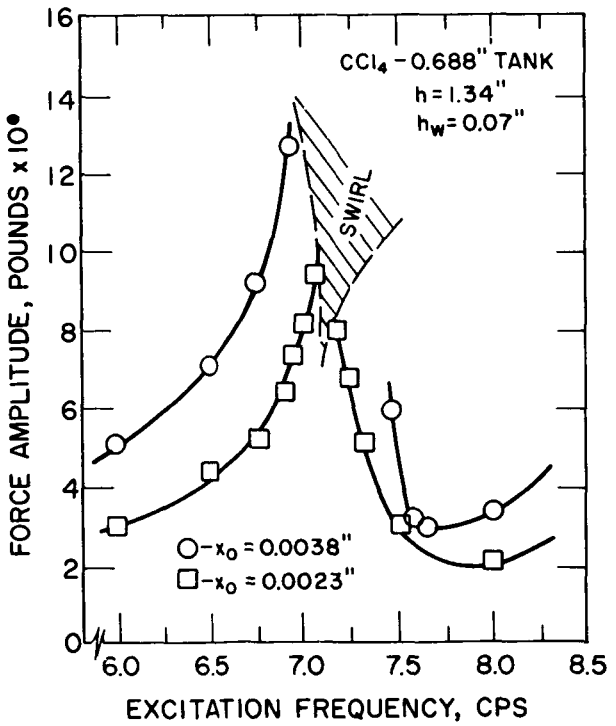

FIGURE 6. RESPONSE CURVE FOR CARBON TETRACHLORIDE, BOND NUMBER = 45

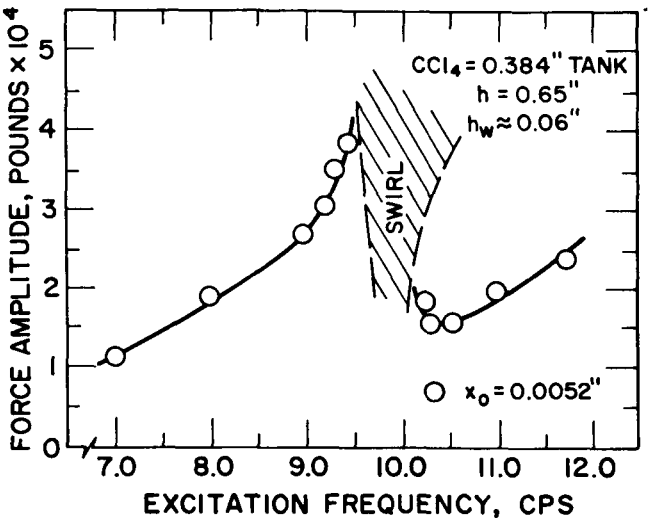

FIGURE 7. RESPONSE CURVE FOR CARBON TETRACHLORIDE, BOND NUMBER = 14

that the forces for CCl_4 are generally larger because of its higher density.

IV. EQUIVALENT MECHANICAL MODEL

The resonant frequencies and slosh forces and moments are displayed in a form convenient for stability and control analyses by an equivalent mechanical model such as the one shown in Figure 8. One spring-mass oscillator is included for each slosh mode. In applications, however,

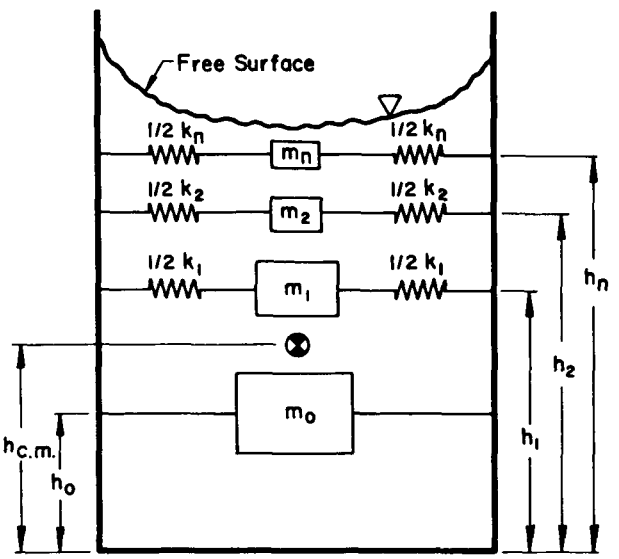

FIGURE 8. SCHEMATIC OF EQUIVALENT MECHANICAL MODEL

the oscillator for the fundamental mode is the only one usually required.

The parameters of the mechanical model are determined by comparing the force and moment predictions of the model to those derived from a potential flow analysis of the sloshing. Such analyses are ordinarily based on a flat free surface, but in low gravity environments even the equilibrium free surface is highly curved; this is illustrated in Figure 9. Accordingly, the usual theory cannot be used here. Instead, it must be modified to include the changes brought about by a curved free surface. In particular, the dynamic and kinematic free surface conditions become

$$\frac{\partial \Phi}{\partial \tau} + \epsilon - \frac{1}{Bo}\left[\frac{1}{R}\frac{\partial}{\partial R}\left(R\,\frac{\partial \epsilon}{\partial R}\Big/\sqrt[3]{1+(dF/dR)^2}\right) + \frac{1}{R^2}\frac{\partial}{\partial \theta}\left(\frac{\partial \epsilon}{\partial \theta}\Big/\sqrt{1+(dF/dR)^2}\right)\right] - X_o \Omega^2 R\cos\theta \sin\Omega\tau = 0 \qquad (1)$$

and

$$\frac{\partial \epsilon}{\partial \tau} - \frac{\partial \Phi}{\partial Z} + \left[\frac{dF}{dR}\left(\frac{\partial \Phi}{\partial R}\right)\right] = 0 \qquad (2)$$

where Φ and ϵ are the nondimensional velocity potential and wave height, respectively; R, θ, Z are the nondimensional cylindrical coordinates; and F(R) is the nondimensional height of the equilibrium free surface, measured above its low point on the tank axis. Quantities in Eqs. (1) and (2) having the dimensions of length have been nondimensionalized by dividing them by R_o, and those having the dimensions of time by dividing them by $(R_o/g)^{1/2}$. The bracketed terms in Eqs. (1) and (2) are absent in high-g analyses. One other necessary change is related to the contact angle hysteresis. The "unstuck" or zero hysteresis case is the one of interest here; this is written mathematically as

$$\frac{dF}{dR} = \infty \quad \text{for } Z = 1 \qquad (3)$$

$$\frac{\partial \epsilon}{\partial R} = 0 \quad \text{for } Z = 1 \qquad (4)$$

Equation (3) states that the equilibrium contact angle is zero degrees, while Eq. (4) implies that the dynamic contact angle always equals the equilibrium angle.

Equations (1) through (4) and the rest of the usual potential flow equations can be solved as shown in Ref. 8. With these results, the parameters of the mechanical model shown in Figures 10 and 11 are obtained.

Figure 10 gives the magnitude of the slosh mass and spring constant for the fundamental mode. As can be seen, the slosh mass for Bo < 100 is always less than for the high-g case; as an example, for Bo = 10 the mass is about 10% smaller than that predicted by a high-g theory.

Assuming that the masses of the higher modes are negligibly small, the magnitude of the rigidly attached mass, m_o, can be computed as

$$m_o = m_T - m_1 = \pi\rho R_o^2(h + 0.264\,h_w) - m_1 \qquad (5)$$

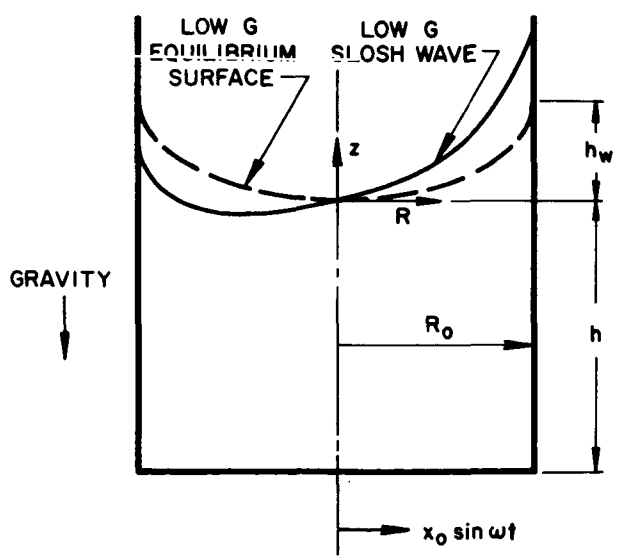

FIGURE 9. CYLINDRICAL TANK AND COORDINATE SYSTEM

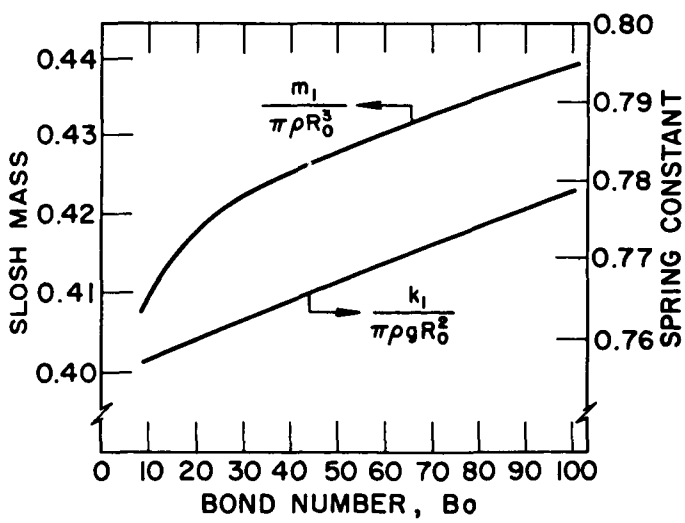

FIGURE 10. FUNDAMENTAL SLOSH MASS AND SPRING CONSTANT

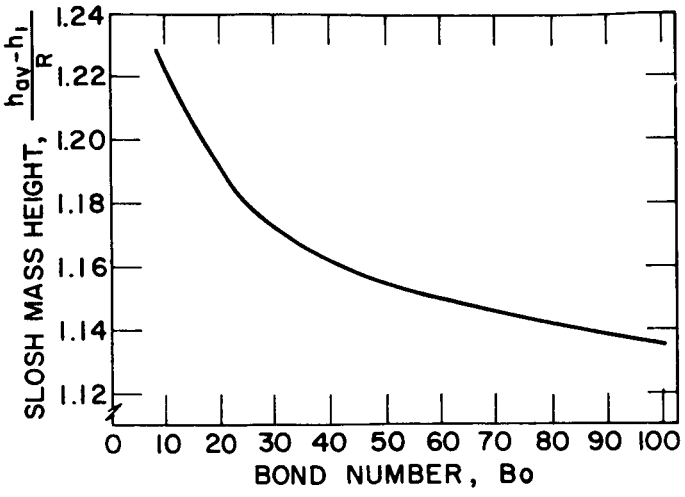

FIGURE 11. HEIGHT OF FUNDAMENTAL SLOSH MASS ABOVE BOTTOM OF TANK

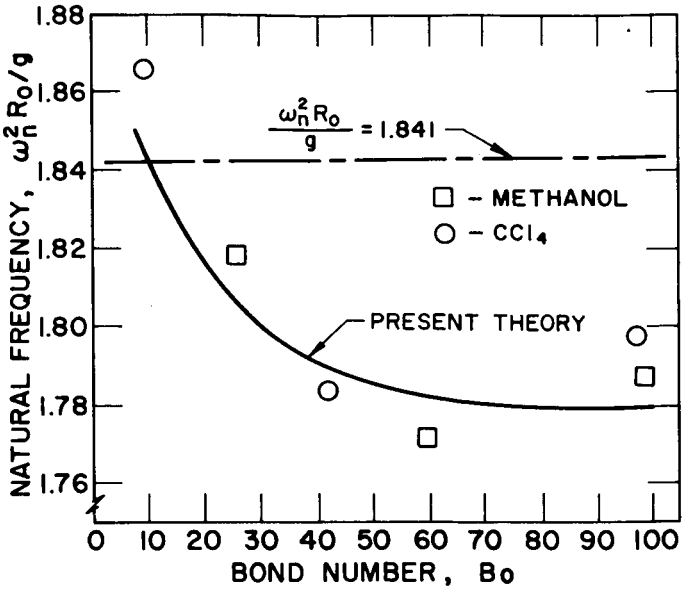

FIGURE 12. COMPARISON OF EXPERIMENTAL AND THEORETICAL RESONANT FREQUENCY

where h is the height of the bottom of the meniscus above the bottom of the tank, h_w is the meniscus height, and m_T is the total mass of liquid. The meniscus height, h_w, is a function of Bo and is calculated from

$$\left(\frac{h_w}{R_o}\right)^3 Bo - \left(\frac{h_w}{R_o}\right)^2 - \frac{2}{3} = 0, \quad Bo \gtrsim 10 \qquad (6)$$

The height, h_l, of the fundamental slosh mass above the tank bottom is shown in Figure 11 in terms of Bo and the average liquid depth, $h_{av} = h + 0.264\, h_w = m_T/\pi\rho R_o^2$. The center-of-mass height, $h_{c.m.}$, is

$$h_{c.m.} = \frac{h + 0.528\, h_w + 0.128\, \frac{h_w^2}{h}}{2\left(1 + 0.264\, \frac{h_w}{h}\right)} \qquad (7)$$

so that, using this formula, the height above the tank bottom to the rigidly attached mass is

$$h_o = \frac{m_T h_{c.m.}}{m_o} - \frac{m_l h_l}{m_o}$$

Now, using the information contained in Figures 10 and 11 and the above formulas, the equivalent mechanical model for any Bo and liquid mass can be obtained. However, the graphs and equations are valid only for $h/R_o > 2$ and $10 < Bo$.

V. COMPARISON WITH EXPERIMENTS

Figure 12 shows a comparison between the experimental values of the resonant frequency and the resonant frequency predicted by the mechanical model ($\omega_n = \sqrt{k_1/m_1}$). The experimental values (the small symbols) were determined from the response curves by assuming the resonant frequency lies halfway between the swirl boundaries for the smallest excitation amplitude; this is not an exact procedure, but the approximation improves as the width of the swirl region decreases. While there is considerable scatter of the data about the theoretical curve, the general trend of the data and the theory is in agreement.

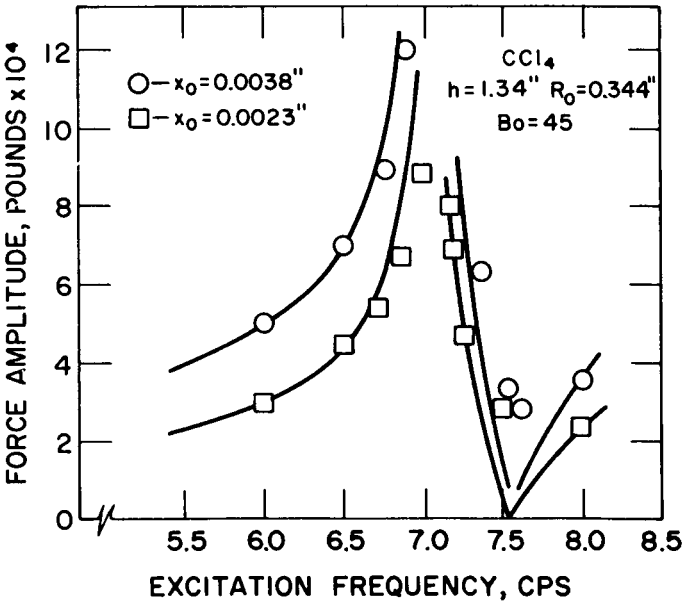

FIGURE 13. COMPARISON OF EXPERIMENTAL AND THEORETICAL FORCE RESPONSE, Bo = 45

Figures 13 and 14 compare the predictions of the equivalent mechanical model for slosh force with the previously given test results for methanol, Bo = 26, and CCl_4, Bo = 45. The small squares and circles are the experimental data, the solid lines the theory. The model compares very well with the tests, as can be seen; the data for other tanks and Bo's compare equally well.

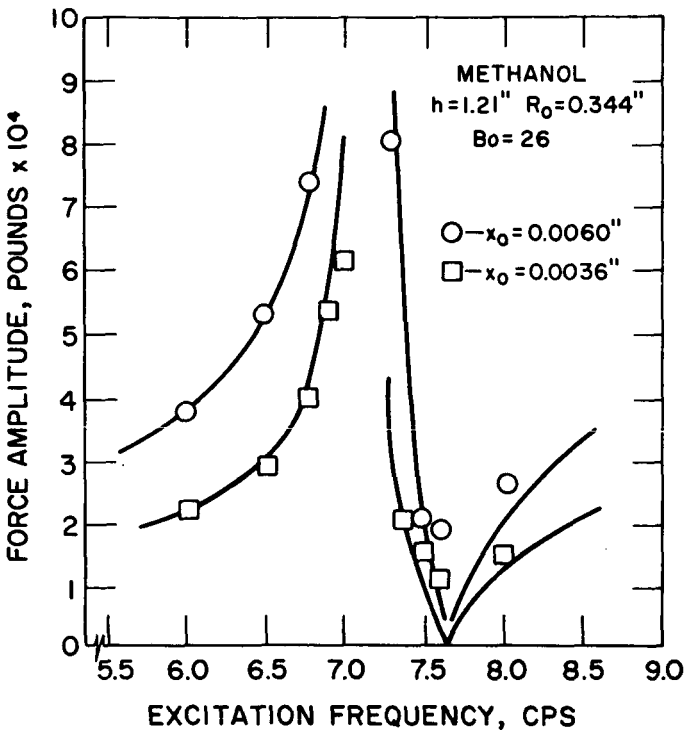

FIGURE 14. COMPARISON OF EXPERIMENTAL AND THEORETICAL FORCE RESPONSE, Bo = 26

The slosh damping was not determined during the experiments nor used in the theory, but visual observations of the number of cycles required for the sloshing to decay indicated that the damping was not large, except for the water. This is verified by the good comparison between the idealized theory and the results of the tests.

VI. CONCLUSIONS

Taken together, the experiments and the theory show that the amount of liquid taking part in low gravity sloshing ($10 < Bo < 100$) is less than in high-g sloshing, at least for the conditions used here: zero degree contact angle and no contact angle hysteresis. For Bo = 10, the decrease in the size of the slosh mass, as an example, is about 10%. This is a reasonable result because, for a tank of the same size containing the same amount of liquid, more of the liquid is in contact with the walls for small Bo than for large (because of the curved interface); thus, more of the liquid must follow the motion of the tank; that is, more of the liquid's mass must be assigned to m_o and less to m_1 in the mechanical model.

The difference in the resonant frequency for $10 < Bo < 100$ and for the high-g case is not large, never being more than about 5%. However, for $Bo < 10$ the trend of the data and the theory indicates that the dimensionless resonant frequency, $\omega_n^2 R_o/g$, rapidly becomes much larger than the high-g limit; this also agrees with Satterlee and Reynold's data [4], although their results indicate that the resonant frequency for any $Bo < 100$ should always be greater than the high-g frequency.

The experimental program demonstrated the feasibility of simulating low-gravity sloshing. The amount of damping present for nonsticking liquids was not large, nor does it appear that it will be for other such tests, as long as $Bo > 5$. However, care must be used to insure that the tanks are clean and the liquids pure. Also, tank materials and liquids must be chosen which will duplicate the desired value of the static contact angle and the conditions of stuck or unstuck contact lines.

REFERENCES

1. The Dynamic Behavior of Liquids in Moving Containers, ed. by H. N. Abramson. NASA Special Publication SP-106, February 1967.

2. Ryan, R. S., and Buchanan, H.: An Evaluation of the Low G Propellant Behavior of a Space Vehicle During Waiting Orbit. NASA TM X-53476, June 1966.

3. Swalley, F. E., Platt, G. K., and Hastings, L. J.: Saturn V Low Gravity Fluid Mechanics Problems and Their Investigation by Full-Scale Orbital Experiment. Fluid Mechanics and Heat Transfer Under Low Gravity, Proceedings of the 1965 Symposium sponsored by USAFOSR and Lockheed Missiles and Space Co., ed. H. Cohen and M. Rogers. No publisher given, pp. 1-1 to 1-24.

4. Satterlee, H. M., and Reynolds, W. C.: The Dynamics of the Free Liquid Surface in Cylindrical Containers Under Strong Capillary and Weak Gravity Conditions. TR No. LG-2, Department of Mechanical Engineering, Stanford University, Palo Alto, California, May 1964.

5. Hutton, R. E., : An Investigation of Resonant, Nonlinear, Nonplanar Free Surface Oscillations in a Liquid. NASA TN D-1870, May 1963.

6. Abramson, H. N., Chu, W.-H., and Kana, D. D.: Some Studies of Nonlinear Lateral Sloshing in Rigid Containers. J. Applied Mechanics, Trans. ASME, Series E, vol. 33, pp. 777-784, December 1966.

7. Miles, J. W.: Damping of Gravity Waves by Surface Films. Paper 23, 6th Symposium on Naval Hydrodynamics, Vol. II, Washington, D.C., September 1966.

8. Dodge, F. T., and Garza, L. R.: Experimental and Theoretical Studies of Liquid Sloshing at Simulated Low Gravities. TR No. 2, Contract NAS8-20290, Southwest Research Institute, San Antonio, Texas, October 1966.

III. PLANETARY ENVIRONMENTS

THE ENVIRONMENT OF MERCURY

By

Otha H. Vaughan, Jr.*

SUMMARY

Presented are the results of an extensive literature survey to establish engineering environmental criteria for the planet Mercury. The three model atmospheres developed during the course of the survey are based on the studies of Rasool, Gross, and McGovern who used a surface temperature of 520°K and a surface pressure of the following ranges:

	Pressure	Mean Molecular Weight
Minimum Density Model	1000 dyn/cm^2	44
Mean Density Model	5000 dyn/cm^2	42
Maximum Density Model	5000 dyn/cm^2	35.6

The atmospheric constituents assumed for our models were CO_2, N_e, A, and N_2.

The surface conditions expected on Mercury are based primarily on radar data. Since Mercury exhibits a radar reflectivity (0.060) similar to that of the moon, the surface roughness based on a scale of radar wavelengths appears to be comparable with the surface roughness of the moon as deduced by radar studies. Additional information on the magnetic field, rotation rate, albedo, temperature, and other environmental design criteria is included.

I. INTRODUCTION

Although the planet Mercury has not yet been seriously considered in the United States space exploration program, in view of the information obtained from the Ranger, Orbiter, Surveyor, and the Mariner programs, Mercury will probably become an object of interest as more progress is made. Any effort at the present time to design a suitable spacecraft either for flyby missions or for landing on Mercury is restricted to a set of environmental criteria which have been obtained only from earth-based measurements and observations. This paper presents the results of an in-house effort to develop Mercury environmental design criteria guidelines using data obtained from an extensive survey of papers, articles, and reports, many of which vary widely in their findings and interpretation of data.

II. BACKGROUND

Mercury, the smallest of the major planets, has a diameter of only 4844 km ± 15 km, according to deVaucouleurs [1], and is the innermost planet of the solar system. According to Ray [2], its mean distance from the sun is 0.3871 A.U. (about 57,900,000 km). Mercury's orbit around the sun has a perihelion of 45,980,000 km and an alphelion of 69,780,000 km, its orbital eccentricity (0.2056) being greater than any other planet in the solar system excluding that of Pluto. Mercury's orbital path and location with respect to the sun make this planet very difficult to observe since at its most favorable elongation it recedes only 28° from the sun [3] in the plane of the ecliptic. However, Mercury has been observed by astronomers for two thousand years, dating back to at least 265 B.C. Several volumes [4, 5, 6] have been written about the techniques of observing and obtaining environmental data for the planets of our solar system. References 4, 5, and 6 provide probably the most comprehensive source of this type of data. Geophysical and astronomical data for Mercury are summarized in Table I.

* Scientific Assistant Aerospace Environment Division, Aero-Astrodynamics Laboratory.

TABLE I. PLANETARY GEOPHYSICAL AND ASTRONOMICAL DATA FOR MERCURY
(References 2, 9, 10, 24 and 25)

Mean Distance (Earth = 1 A.U.)	0.387099 A.U.
Orbital Velocity	47.87 km/sec
Sidereal period	87.969 days
Inclination to ecliptic	7.00399°
Eccentricity	0.205627
Equatorial radius	2422 km
Flattening	-
Mass of planet to mass of earth	0.056
Mean density	5.13 gm/cm^3
Velocity of escape	4.2 km/sec
Rotation period	58.4 ± 0.4 days
Inclination of equator to orbit	0°
Gravitational parameter	21,685.53 km^3/sec^2
Visual albedo	0.056
Mass of Sun to mass of planet	6,120,000
Theoretical temperature	
(Spherical black body)	441°K
(Hemispherical black body)	525°K
(Sub-solar black body)	624°K

III. ATMOSPHERE

For many years it was generally conceded that Mercury had no atmosphere because of the low escape velocity and because it was believed to be in captured rotation which would cause large temperature extremes on the sunlit and dark sides of the planet. This hypothesis was further supported by the apparent absence of any significant diffusion or reflection of light. The sharply defined appearance of Mercury as it crossed the face of the sun also seemed to suggest that there was no atmosphere. In recent years (1965), it has been discovered that Mercury is not in captured rotation but is in direct rotation with a sidereal period of 59 ± 5 days. This somewhat alleviates the extreme temperatures that would be experienced if it were in captured rotation, and, according to Kozyrev [7, 8] allows the planet to recapture hydrogen from the sun. In addition to these new discoveries, some recent studies have tended to support the idea that Mercury has at least a tenuous atmosphere. This is based mainly on polarization studies [9, 10, 11], thermal brightness studies [12-19], and spectrographic data [5, 7, 19, 20, 21, 22]. Kozyrev [7, 8] went so far as to conclude that the amount of hydrogen on Mercury indicates a genuine atmosphere rather than an ionospheric condition. Rasool, Gross, and McGovern [23] have interpreted polarization and spectroscopic data as showing the presence of an atmosphere with a probable pressure of 0±0.01 to 10.0 mb. Based on data from Rasool, Gross, and McGovern [23], we have constructed the following models by using a modified computer program of Kern and Schilling [24]. It is assumed for purposes of these models that the atmosphere is not in circulation and that the atmosphere is stable against gravitational escape and the solar wind effects.

1. Minimum Density Model. This model assumes that Mercury's atmosphere is 100 percent CO_2. The surface pressure was assumed to be 1000 dyn/cm^2 (1mb) and the surface temperature was assumed to be 520°K with a lapse rate of 4.32°K/km.

2. Mean Density Model. This model assumed that Mercury's atmosphere was composed of 50 percent argon and 50 percent CO_2. The surface pressure was assumed to be 5000 dyn/cm^2 (5 mb) and the surface temperature was assumed to be 520°K with a lapse rate of 5.30°K/km.

3. Maximum Density Model. This model assumes that the Mercury atmosphere is composed of 60 percent CO_2, 25 percent N_e, and 15 percent N_2. The surface pressure was assumed to be 5000 dyn/cm^2 (5mb) and the surface temperature was assumed to be 520°K with a lapse rate of 3.86°K/km.

Atmospheric pressure and density curves are presented in Figures 1 and 2, and other engineering parameters are presented in Tables II through VIII. Since these models are only as good as the input information, they must be considered as very rough approximations. However, we believe that this information is accurate enough for use as design criteria guidelines, at least for the present time. As new data become available, more realistic atmospheric models can be constructed.

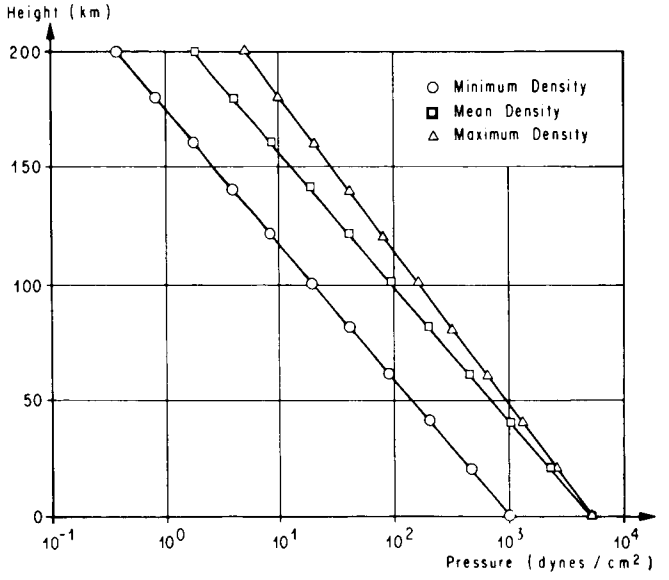

FIGURE 1. ATMOSPHERIC PRESSURE VERSUS HEIGHT

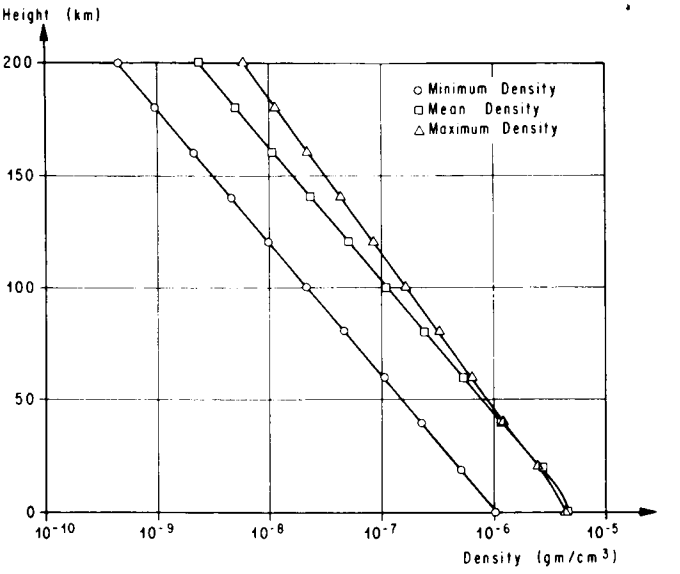

FIGURE 2. ATMOSPHERIC DENSITY VERSUS HEIGHT

TABLE II. ATMOSPHERIC PRESSURE

Z(km)	Minimum Density Model (dyn/cm^2)	Mean Density Model (dyn/cm^2)	Maximum Density Model (dyn/cm^2)
0	1.00000000×10^{3}	5.00000000×10^{3}	5.00000000×10^{3}
10	6.89355854×10^{2}	3.49268627×10^{2}	3.70559695×10^{3}
20	4.58554727×10^{2}	2.33550190×10^{3}	2.67742709×10^{3}
30	3.01474878×10^{2}	1.53534140×10^{3}	1.87717236×10^{3}
40	1.98861598×10^{2}	1.01267437×10^{3}	1.30730120×10^{3}
50	1.31605353×10^{2}	6.70128034×10^{2}	9.13028646×10^{2}
60	8.73780373×10^{1}	4.44889467×10^{2}	6.39463592×10^{2}
70	5.81996849×10^{1}	2.96303205×10^{2}	4.49112962×10^{2}
80	3.88877110×10^{1}	1.97967655×10^{2}	3.16293014×10^{2}
90	2.60652296×10^{1}	1.32681330×10^{2}	2.23359263×10^{2}
100	1.75247744×10^{1}	8.92005150×10^{1}	1.58155762×10^{2}
110	1.18186954×10^{1}	6.01521821×10^{1}	1.12284366×10^{2}
120	7.99461627×10^{0}	4.06861546×10^{1}	7.99270040×10^{1}
130	5.42402492×10^{0}	2.76018456×10^{1}	5.70419928×10^{1}
140	3.69085441×10^{0}	1.87806679×10^{1}	4.08140700×10^{1}
150	2.51882956×10^{0}	1.28159504×10^{1}	2.92969964×10^{1}
160	1.72394313×10^{0}	8.77087922×10^{0}	2.10538762×10^{1}
170	1.18327381×10^{0}	6.01968613×10^{0}	1.51779900×10^{1}
180	$8.14463867 \times 10^{-1}$	4.14313470×10^{0}	1.09688478×10^{1}
190	$5.62171650 \times 10^{-1}$	2.85953253×10^{0}	7.94621656×10^{0}
200	$3.89101680 \times 10^{-1}$	1.97905702×10^{0}	5.77033037×10^{0}

TABLE III. ATMOSPHERIC TEMPERATURE

Z(km)	Minimum Density Model (°K)	Mean Density Model (° K)	Maximum Density Model (° K)
0	5.20000000×10^{2}	5.20000000×10^{2}	5.20000000×10^{2}
10	4.76453012×10^{2}	4.66574297×10^{2}	4.80934940×10^{2}
20	4.32906024×10^{2}	4.13148594×10^{2}	4.41869880×10^{2}
30	4.32906024×10^{2}	4.13148594×10^{2}	4.02804819×10^{2}
40	4.32906024×10^{2}	4.13148594×10^{2}	4.02804819×10^{2}
50	4.32906024×10^{2}	4.13148594×10^{2}	4.02804819×10^{2}
60	4.32906024×10^{2}	4.13148594×10^{2}	4.02804819×10^{2}
70	4.32906024×10^{2}	4.13148594×10^{2}	4.02804819×10^{2}
80	4.32906024×10^{2}	4.13148594×10^{2}	4.02804819×10^{2}
90	4.32906024×10^{2}	4.13148594×10^{2}	4.02804819×10^{2}
100	4.32906024×10^{2}	4.13148594×10^{2}	4.02804819×10^{2}
110	4.32906024×10^{2}	4.13148594×10^{2}	4.02804819×10^{2}
120	4.32906024×10^{2}	4.13148594×10^{2}	4.02804819×10^{2}
130	4.32906024×10^{2}	4.13148594×10^{2}	4.02804819×10^{2}
140	4.32906024×10^{2}	4.13148594×10^{2}	4.02804819×10^{2}
150	4.32906024×10^{2}	4.13148594×10^{2}	4.02804819×10^{2}
160	4.32906024×10^{2}	4.13148594×10^{2}	4.02804819×10^{2}
170	4.32906024×10^{2}	4.13148594×10^{2}	4.02804819×10^{2}
180	4.32906024×10^{2}	4.13148594×10^{2}	4.02804819×10^{2}
190	4.32906024×10^{2}	4.13148594×10^{2}	4.02804819×10^{2}
200	4.32906024×10^{2}	4.13148594×10^{2}	4.02804819×10^{2}

TABLE IV. ATMOSPHERIC DENSITY

Z(km)	Minimum Density Model (gm/cm^3)	Mean Density Model (gm/cm^3)	Maximum Density Model (gm/cm^3)
0	$1.01769805 \times 10^{-6}$	$4.85719522 \times 10^{-6}$	$4.11705119 \times 10^{-6}$
10	$7.65677131 \times 10^{-7}$	$3.78144393 \times 10^{-6}$	$3.29906944 \times 10^{-6}$
20	$5.60557064 \times 10^{-7}$	$2.85557021 \times 10^{-6}$	$2.59443540 \times 10^{-6}$
30	$3.68535886 \times 10^{-7}$	$1.87723040 \times 10^{-6}$	$1.99539601 \times 10^{-6}$
40	$2.43096989 \times 10^{-7}$	$1.23817616 \times 10^{-6}$	$1.38963457 \times 10^{-6}$
50	$1.60880057 \times 10^{-7}$	$8.19351787 \times 10^{-7}$	$9.70530865 \times 10^{-7}$
60	$1.06814679 \times 10^{-7}$	$5.43957216 \times 10^{-7}$	$6.79736781 \times 10^{-7}$
70	$7.11458036 \times 10^{-8}$	$3.62283845 \times 10^{-7}$	$4.77397937 \times 10^{-7}$
80	$4.75380141 \times 10^{-8}$	$2.42050986 \times 10^{-7}$	$3.36213036 \times 10^{-7}$
90	$3.18632602 \times 10^{-8}$	$1.62226738 \times 10^{-7}$	$2.37426350 \times 10^{-7}$
100	$2.14230396 \times 10^{-8}$	$1.09063638 \times 10^{-7}$	$1.68116356 \times 10^{-7}$
110	$1.44476827 \times 10^{-8}$	$7.35468380 \times 10^{-8}$	$1.19355996 \times 10^{-7}$
120	$9.77296354 \times 10^{-9}$	$4.97461258 \times 10^{-8}$	$8.49607783 \times 10^{-8}$
130	$6.63056186 \times 10^{-9}$	$3.37482099 \times 10^{-8}$	$6.06344772 \times 10^{-8}$
140	$4.51185953 \times 10^{-9}$	$2.29627371 \times 10^{-8}$	$4.33845256 \times 10^{-8}$
150	$3.07912582 \times 10^{-9}$	$1.56697994 \times 10^{-8}$	$3.11208512 \times 10^{-8}$
160	$2.10742239 \times 10^{-9}$	$1.07239739 \times 10^{-8}$	$2.23798419 \times 10^{-8}$
170	$1.44648491 \times 10^{-9}$	$7.36014663 \times 10^{-9}$	$1.61338944 \times 10^{-8}$
180	$9.95635739 \times 10^{-10}$	$5.06572573 \times 10^{-9}$	$1.16596620 \times 10^{-8}$
190	$6.87222857 \times 10^{-10}$	$3.49629171 \times 10^{-9}$	$8.44666645 \times 10^{-9}$
200	$4.75654666 \times 10^{-10}$	$2.41975239 \times 10^{-9}$	$6.13374373 \times 10^{-9}$

TABLE V. GEOMETRIC PRESSURE SCALE HEIGHT

Z(km)	Minimum Density Model (km)	Mean Density Model (km)	Maximum Density Model (km)
0	2.80745636×10^{6}	2.94114476×10^{6}	3.46988989×10^{6}
10	2.59305107×10^{6}	2.66020552×10^{6}	3.23504259×10^{6}
20	2.37493679×10^{6}	2.37447765×10^{6}	2.99609443×10^{6}
30	2.39389825×10^{6}	2.39343548×10^{6}	2.75302018×10^{6}
40	2.41293514×10^{6}	2.41246869×10^{6}	2.77491290×10^{6}
50	2.43204742×10^{6}	2.43157727×10^{6}	2.79689232×10^{6}
60	2.45123510×10^{6}	2.45076124×10^{6}	2.81895845×10^{6}
70	2.47049817×10^{6}	2.47002059×10^{6}	2.84111128×10^{6}
80	2.48983664×10^{6}	2.48935531×10^{6}	2.86335081×10^{6}
90	2.50925049×10^{6}	2.50876542×10^{6}	2.88567705×10^{6}
100	2.52873974×10^{6}	2.52825090×10^{6}	2.90808999×10^{6}
110	2.54830439×10^{6}	2.54781176×10^{6}	2.93058964×10^{6}
120	2.56794443×10^{6}	2.56744801×10^{6}	2.95317598×10^{6}
130	2.58765986×10^{6}	2.58715963×10^{6}	2.97584904×10^{6}
140	2.60745068×10^{6}	2.60694663×10^{6}	2.99860879×10^{6}
150	2.62731690×10^{6}	2.62680900×10^{6}	3.02145525×10^{6}
160	2.64725852×10^{6}	2.64674676×10^{6}	3.04438842×10^{6}
170	2.66727552×10^{6}	2.66675990×10^{6}	3.06740829×10^{6}
180	2.68736792×10^{6}	2.68684841×10^{6}	3.09051486×10^{6}
190	2.70753572×10^{6}	2.70701231×10^{6}	3.11370814×10^{6}
200	2.72777890×10^{6}	2.72725158×10^{6}	3.13698812×10^{6}

TABLE VI. ATMOSPHERIC NUMBER DENSITY

Z(km)	Minimum Density Model (cm^{-3})	Mean Density Model (cm^{-3})	Maximum Density Model (cm^{-3})
0	$1.39353400 \times 10^{16}$	$6.96767001 \times 10^{16}$	$6.96767001 \times 10^{16}$
10	$1.04844175 \times 10^{16}$	$5.42449958 \times 10^{16}$	$5.58332315 \times 10^{16}$
20	$7.67570824 \times 10^{15}$	$4.09632927 \times 10^{16}$	$4.39080519 \times 10^{16}$
30	$5.04636213 \times 10^{15}$	$2.69289608 \times 10^{16}$	$3.37699491 \times 10^{16}$
40	$3.32872723 \times 10^{15}$	$1.77616968 \times 10^{16}$	$2.35180829 \times 10^{16}$
50	$2.20293073 \times 10^{15}$	$1.17536410 \times 10^{16}$	$1.64251997 \times 10^{16}$
60	$1\ 46261347 \times 10^{15}$	$7.80309254 \times 10^{15}$	$1.15038200 \times 10^{16}$
70	$9.74199535 \times 10^{14}$	$5.19697925 \times 10^{15}$	$8.07945089 \times 10^{15}$
80	$6.50938059 \times 10^{14}$	$3.47223309 \times 10^{15}$	$5.69004703 \times 10^{15}$
90	$4.36303643 \times 10^{14}$	$2.32715040 \times 10^{15}$	$4.01818773 \times 10^{15}$
100	$2.93345695 \times 10^{14}$	$1.56452316 \times 10^{15}$	$2.84519000 \times 10^{15}$
110	$1.97832128 \times 10^{14}$	$1.05503294 \times 10^{15}$	$2.01997292 \times 10^{15}$
120	$1.33821196 \times 10^{14}$	$7.13610578 \times 10^{14}$	$1.43787055 \times 10^{15}$
130	$9.07922879 \times 10^{13}$	$4.84119701 \times 10^{14}$	$1.02617385 \times 10^{15}$
140	$6.17808955 \times 10^{13}$	$3.29401573 \times 10^{14}$	$7.34236821 \times 10^{14}$
150	$4.21624719 \times 10^{13}$	$2.24784029 \times 10^{14}$	$5.26687214 \times 10^{14}$
160	$2.88569361 \times 10^{13}$	$1.53835924 \times 10^{14}$	$3.78754954 \times 10^{14}$
170	$1.98067188 \times 10^{13}$	$1.05581659 \times 10^{14}$	$2.73048954 \times 10^{14}$
180	$1.36332408 \times 10^{13}$	$7.26680803 \times 10^{13}$	$1.97327342 \times 10^{14}$
190	$9.41014303 \times 10^{12}$	$5.01544734 \times 10^{13}$	$1.42950820 \times 10^{14}$
200	$6.51313965 \times 10^{12}$	$3.47114649 \times 10^{13}$	$1.03807070 \times 10^{14}$

TABLE VII. POTENTIAL DENSITY SCALE HEIGHT

Z(km)	Minimum Density Model (km)	Mean Density Model (km)	Maximum Density Model (km)
0	3.67039677×10^6	4.21475119×10^6	4.69332704×10^6
10	3.36302230×10^6	3.78172034×10^6	4.34074031×10^6
20	3.05564783×10^6	3.34868948×10^6	3.98815357×10^6
30	2.33723995×10^6	2.33678812×10^6	3.63556683×10^6
40	2.33723995×10^6	2.33678812×10^6	2.68786225×10^6
50	2.33723995×10^6	2.33678812×10^6	2.68786225×10^6
60	2.33723995×10^6	2.33678812×10^6	2.68786225×10^6
70	2.33723995×10^6	2.33678812×10^6	2.68786225×10^6
80	2.33723995×10^6	2.33678812×10^6	2.68786225×10^6
90	2.33723995×10^6	2.33678812×10^6	2.68786225×10^6
100	2.33723995×10^6	2.33678812×10^6	2.68786225×10^6
110	2.33723995×10^6	2.33678812×10^6	2.68786225×10^6
120	2.33723995×10^6	2.33678812×10^6	2.68786225×10^6
130	2.33723995×10^6	2.33678812×10^6	2.68786225×10^6
140	2.33723995×10^6	2.33678812×10^6	2.68786225×10^6
150	2.33723995×10^6	2.33678812×10^6	2.68786225×10^6
160	2.33723995×10^6	2.33678812×10^6	2.68786225×10^6
170	2.33723995×10^6	2.33678812×10^6	2.68786225×10^6
180	2.33723995×10^6	2.33678812×10^6	2.68786225×10^6
190	2.33723995×10^6	2.33678812×10^6	2.68786225×10^6
200	2.33723995×10^6	2.33678812×10^6	2.68786225×10^6

TABLE VIII. ATMOSPHERIC COLUMNAR MASS ABOVE A GIVEN ALTITUDE

Z(km)	Minimum Density Model (gm/cm^2)	Mean Density Model (gm/cm^2)	Maximum Density Model (gm/cm^2)
0	2.85714286×10^0	1.42857143×10^1	1.42857143×10^1
10	1.98543991×10^0	1.00594180×10^1	1.06726301×10^1
20	1.33128758×10^0	6.78048764×10^0	7.77317344×10^0
30	$8.82237413 \times 10^{-1}$	4.49302985×10^0	5.49336547×10^0
40	$5.86577267 \times 10^{-1}$	2.98706121×10^0	3.85611489×10^0
50	$3.91267928 \times 10^{-1}$	1.99231718×10^0	2.71447032×10^0
60	$2.61827891 \times 10^{-1}$	1.33310926×10^0	1.91614974×10^0
70	$1.75765578 \times 10^{-1}$	$8.94848555 \times 10^{-1}$	1.35634066×10^0
80	$1.18361889 \times 10^{-1}$	$6.02550909 \times 10^{-1}$	$9.62695869 \times 10^{-1}$
90	$7.99529014 \times 10^{-2}$	$4.06988831 \times 10^{-1}$	$6.85135768 \times 10^{-1}$
100	$5.41732916 \times 10^{-2}$	$2.75740241 \times 10^{-1}$	$4.88897491 \times 10^{-1}$
110	$3.68170932 \times 10^{-2}$	$1.87383499 \times 10^{-1}$	$3.49783444 \times 10^{-1}$
120	$2.50964272 \times 10^{-2}$	$1.27720591 \times 10^{-1}$	$2.50904130 \times 10^{-1}$
130	$1.71576388 \times 10^{-2}$	$8.73120061 \times 10^{-2}$	$1.80439051 \times 10^{-1}$
140	$1.17644512 \times 10^{-2}$	$5.98626299 \times 10^{-2}$	$1.30093220 \times 10^{-1}$
150	$8.08983932 \times 10^{-3}$	$4.11615701 \times 10^{-2}$	$9.40302595 \times 10^{-2}$
160	$5.57889186 \times 10^{-3}$	$2.83836433 \times 10^{-2}$	$6.81329315 \times 10^{-2}$
170	$3.85817379 \times 10^{-3}$	$1.96277439 \times 10^{-2}$	$4.94892414 \times 10^{-2}$
180	$2.67563955 \times 10^{-3}$	$1.36108371 \times 10^{-2}$	$3.60343585 \times 10^{-2}$
190	$1.86068043 \times 10^{-3}$	$9.46450469 \times 10^{-3}$	$2.63004540 \times 10^{-2}$
200	$1.29748076 \times 10^{-3}$	$6.59927353 \times 10^{-3}$	$1.92414812 \times 10^{-2}$

IV. TEMPERATURE

Until it was discovered that Mercury rotates on its axis, it was believed that the planet experienced great temperature extremes, the daytime subsolar temperatures being estimated as great as 690°K and the dark side being estimated as low as about 5°K. In 1936, Petit and Nicholson [5, 10] made infrared radio emission measurements over a number of phase angles, obtaining a temperature at the subsolar point of 610°K. Walker, in 1960, calculated the mean subsolar temperature to be 621°K, by assuming that the planet did not rotate, that the interior was in thermal steady state, that the specific rate of radioactive heat production was equal to that of chondritic meteorites (1.33 cal deg^{-1} cm^{-1} m^{-1}), and that the planet was at a mean orbital distance. Because of the orbital eccentricities, these temperatures can have extremely large variations according to its distance from the sun. Howard and his associates [13] in 1961, using the 3.5 cm band, measured a brightness temperature of 1050 ± 350°K. These observations were not of sufficient precision to reveal a dependence of the mean brightness temperature with respect to phase; however, preliminary analysis did imply an average brightness temperature of 400 ± 80°K for phase angles of near 90°. Further analysis of the data by Barrett [26] postulated that the dark side temperatures were not as low as 28°K as predicted by Walker [27], but could be in the range of at least 270°K.

By means of microwave equipment (1.53 cm), Welch and Thornton in September 1964 [17] obtained brightness measurements of Jupiter, Saturn and Mercury while Mercury's average illumination was about 25 percent. When these data were analyzed, they obtained a mean disk temperature of 465° ± 115°K for Mercury. By assuming a subsolar temperature of 620°K and a pole darkening proportional to cos $1/2\ \theta$, Welch and Thornton postulated that the contribution of temperature from the illuminated part of the disk was about 100°K. Also, by assuming that the properties of the surface materials of Mercury are similar to the moon, as indicated by polarization studies, Welch and Thornton explained the large dark side contribution to the disk temperature as a result of internal radioactive heat sources. Field [19], however, after an interpretation of the data of Howard, Barrett and Haddock [13], believed that the higher-than-expected temperature of the dark side was the result of an atmosphere which would transport the heat to the dark side. In April 1965, Epstein [18] and his associates, in making brightness measurements in the 3.4 mm band, obtained a value of 220° ± 35°K for the dark side temperature. The most significant results were that there appeared to be no dependence of temperature on variation in phase. These data seemed to be in disagreement since other measurements at 8 mm indicated that a large variation with phase should occur at the smaller wavelength of 3 mm if the surface materials of Mercury were like that of the moon. Recent radio thermal measurements at 19 mm by Kaftan-Kassim and Kellermann [28] of NARO during February and March 1966 revealed that Mercury's day-to-night range in brightness temperature is about 75°K centered on a mean value of 288°K. Later, using his 3.4 mm data, Epstein reported that he also found these day-to-night variations.

At the present time, it is generally agreed that the unilluminated side of Mercury has a brightness temperature of at least 270°K. Since the planet is now considered to be in both direct and in nonsynchronous rotation with respect to its orbit, the temperature environment of the planet can now be established in more realistic terms. However, there are still many unanswered thermal environmental problems with respect to this planet.

V. ROTATION

Based on the large amount of observational data of Mercury by Schiaparelli, Baum, Lyot, Dollfus, and others, the rotational rate of Mercury was thought to be in "captured rotation" with a sidereal period of approximately 88 days. Recent radar measurements by Pettengill and his associates [29] at Arecibo, Puerto Rico, during the 1965 inferior conjunction of Mercury indicated that the rotational period was different from the orbital period. The rotation of the planet is now considered to be direct with a sidereal period of 59 ± 5 days. Although the direction of the pole is not well determined from these limited data, the authors agree that it is approximately normal to the planetary orbit. Analysis of these data by Peale and Gold [30] implies that the rotation rate is between 56.6 and 88 days, that Mercury has little permanent rigidity, and that the nonsynchronous rotation may be explained in terms of solar tidal effects. Analysis of the same data by Colombo and Shapiro [31, 32] suggests that the rotational period is 58.65 days (0.66 of the orbital period) and that the rigidity of the planet is higher than permitted by Peale and

Gold. McGovern, Rasool, and Gross [33] in their analysis of 50 drawings of Mercury produced from visual observations by Antoniadi, Lyot and Dollfus, and Baum concluded that in addition to the previously accepted 88 days, there exists, based on 6 pairs of these drawings, at least three possible values for the rotation rate: 50.1, 58.4, and 70.2 days. Recently, McGovern, Rasool, and Gross [23] have indicated that a period of rotation of 43.6 days could also be possible; however, the 58.4 ± 0.4 days represent the best value for the rotational rate, at the present time, since it is consistent with both the radar and observational data.

VI. MAGNETIC FIELD

Information on the magnetic field of Mercury is very meager. Because Mercury has a very slow rotational rate, a very low magnetic field intensity is expected. McGovern, Rasool, and Gross [23] estimate the magnetic field intensity of Mercury, based on extrapolation of Mariner II data, to be $\sim 300\gamma$ at one planetary radius, and the dipole field at the surface is estimated to be 0.024 gauss.

VII. ALBEDO, POLARIZATION, AND SURFACE CONDITIONS

The polarization of reflected light from Mercury is similar to the moon as noted by Dollfus [11], and the variation of brightness with phase is almost the same as the moon as noted by Kozyrev [7]. The visual or bond albedo for this planet is 0.056 [5]. Polarization and photometric data [5, 34] indicate the surface of Mercury is much like that of the moon (see Fig. 3). Then, by analogy, the surface of Mercury is covered by fine-grained materials, blocks, and craters of numerous sizes as seen by Orbiter, Surveyor, and Russian Luna spacecraft which recently have photographed and landed on the moon. Since Mercury is now believed to have somewhat of an atmosphere (at least from 1 to 5 mb), then the fine-grained materials produced from the impacts of large craters could be held in suspension in the atmosphere and transported by surface winds estimated to be 120 m/sec [24] if the atmospheric pressure is 5 mb and if it consists mainly of CO_2. Evidence for dust clouds was offered by Antoniadi [3] to explain some of the haze which appeared to have obscured surface features. This transportation of materials would tend to smooth the topography; however, if the soil has some adhesion, no large scale movement of materials should occur. Thus, a suitable surface model for design purposes at the present time would be a model developed from the lunar surface data with some modifications.

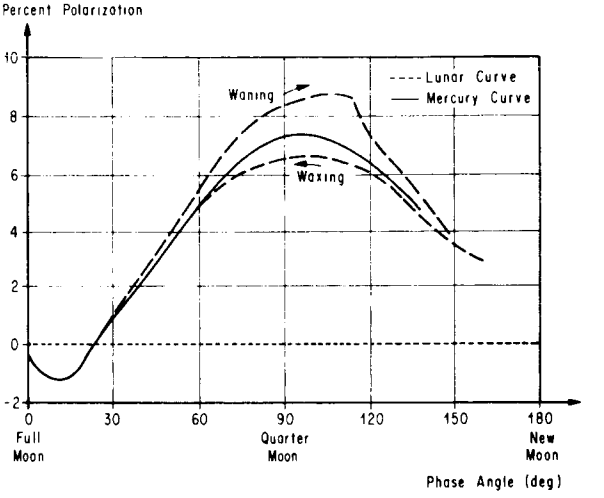

FIGURE 3. POLARIZATION CURVE FOR MERCURY AND MOON (AFTER B. LYOT)

VIII. CONCLUSIONS

Present theories regarding the environment of Mercury are based only on earth-based measurements and telescopic observations. In the coming years, with the data obtained by Orbiter and Surveyor and probes of Venus and Mars, we will be able to better define the environmental parameters required for a Mercury mission. It is recommended that at least one scientific probe be launched within the next five years to provide more information about Mercury.

REFERENCES

1. deVaucouleurs, G.: Geometric and Photometric Parameters of the Terrestrial Planets. Rand Corporation, Santa Monica, California, March 1964, N64-19984 NASA contract no. NASR-21 (04), unclassified.

2. Ray, Archie E.: Foundations of Astrodynamics. Macmillan Co., New York, New York .

3. Sandner, W.: The Planet Mercury. Faber and Faber, London, 1963.

4. Kuiper, G. P.: The Earth as a Planet. The University of Chicago Press, Chicago, Illinois, vol. 2, 1954.

5. Kuiper, G. P.; and Middlehurst, B. M. : Planets and Satellites. The University of Chicago Press, Chicago, Illinois, vol. 3, 1961.

6. Kuiper, G. P.; and Middlehurst, B.M.: The Moon, Meteorites, and Comets. The University of Chicago Press, Chicago, Illinois, vol. 4, 1963.

7. Kozyrev, N.A.: The Atmosphere of Mercury. Sky and Telescope, vol. 27, 1964, pp. 339-341.

8. Kozyrev, N.: The Atmosphere of Mercury. The Journal of the British Astronomical Association, vol. 73, 1963, pp. 345-346.

9. Heath, M.B.B.: The Brightness of Mercury at Its Greatest Elongations. Journal of the British Astronomical Association, vol. 68, 1958, pp. 30-32.

10. Kiess, C.C.; and Lassovsky, K.: The Known Physical Characteristics of the Moon and the Planets. Air Research and Development Command, Wright-Patterson Air Force Base, Ohio, July 1958, TR-11, AD115617, unclassified.

11. Dollfus, A.: Polarization Studies of Planets. Planets and Satellites. Chicago, Illinois, The University of Chicago Press, 1961.

12. Barrett, A. H.: Microwave Spectral Lines as Probes of Planetary Atmospheres. Mem. Soc. Roy. Sci. Liege 7, 1962, pp. 197-219.

13. Howard, W. E.; Barrett, A. H.; and Haddock, F. T. : Measurement of Microwave Radiation from the Planet Mercury. The Astrophysical Journal, vol. 136, 1962, pp. 995-1004.

14. Kotel'nikov, V.A., et al.: Radar Probes of the Planet Mercury. (Foreign title not available.) Translated into English from Russian by Joint Publications Research Service, Washington, D. C., JPRS-18211, OTS 63-21357, N64-10498, vol. 147, no. 6, December 21, 1962, pp. 1320-1323.

15. Barrett, A. H.: Passive Radio Observations of Venus, Saturn, Mercury, Mars, and Uranus, Session III. Mass. Inst. of Tech., Research Lab. of Electronics, Cambridge, 1966, NSG-419, contract no. DA-36-039-AMC-032000(E), published in Radio Science PI565-73, AD-633-794.

16. Field, G. B.: Atmosphere of Mercury. The Astronomical Journal, vol. 67, 1962, pp. 575-576.

17. Welch, W. J.; and Thornton, D. D.: Recent Planetary Observations at Wavelengths Near 1 CM. Astronomical Journal, vol. 70, no. 2, 1965, pp. 149-150.

18. Epstein, E. E.: Disk Temperatures of Mercury and Mars at 3.4 MM. Astrophysical Journal, vol. 143, February 1966, pp. 597-598, A66-22786, contract no. AF 04(695)-469.

19. Field, G.: The Atmosphere of Mercury. John Wiley and Sons, Inc., New York, New York, 1964, pp. 269-276, A65-33300. (The Origin and Evolution of Atmospheres and Oceans; Proceedings of a Conference, National Aeronautics and Space Administration, Goddard Space Flight Center, Goddard Institute for Space Studies, New York, New York, April 8-9, 1963; A65-33278 21-30.)

20. News About Mercury (Carbon Dioxide Has Been Revealed in This Planet's Atmosphere). Foreign Technology Division, Wright-Patterson Air Force Base, Ohio, October 1965, TT-65-64151, AD-622 361, FTD-TT-65-1240, unclassified.

21. Spinrad, H.; and Hodge, P.W.: An Explanation of Kozyrev's Hydrogen Emission Lines in the Spectrum of Mercury. Icarus, vol. 4, April 1965, pp. 105-108, A65-23491.

22. Spinrad, H.; Field, G.B.; and Hodge, P.W.: Spectroscopic Observations of Mercury. Astrophysical Journal, vol 141, April 1, 1965, pp. 1155-1160, A65-25226.

23. Rasool, S.I.; Gross, S. H.; and McGovern, W. E.: The Atmosphere of Mercury. NASA TM X-57322, Goddard Space Flight Center.

24. Kern, L.C.; and Schilling, G. F.: Modat: A Computer Program for the Construction of Model Atmospheres. Memo RM-4204-RP, The Rand Corp., July 1964.

REFERENCES (Concluded)

25. Krause, H. G.: Astronomical Constants of the Solar System. Unpublished Manuscript, Marshall Space Flight Center, Huntsville, Alabama, 1965

26. Barrett, A.H.: Passive Radio Observations of Mercury, Venus, Mars, Saturn, and Uranus. Symposium on Planetary Atmospheres and Surfaces, Dorado, Puerto Rico, May 24-27, 1965. Journal of Research, Section D - Radio Science, vol. 69D, December 1965.

27. Walker, J.C.C.: The Thermal Budget of the Planet Mercury. Astrophysical Journal, vol. 133, January 1961, pp. 274-280.

28. Kaftan-Kassim, M.A.; and Kellermann, K.I.: Temperature of Mercury. Sky and Telescope, April 1967.

29. Pettengill, G.H.; and Dyce, R. B.: A Radar Determination of the Rotation of the Planet Mercury. Arecibo Ionospheric Observatory, Puerto Rico, 1965, AD 629 334, contract no. AF 49(638)-1156, (published in Nature, vol. 206, no. 4990, June 19, 1965, p. 1240), unclassified.

30. Peale, S.J.; and Gold, T.: Rotation of the Planet Mercury. Nature, vol. 206, June 19, 1965, pp. 1240-1241, A65-27014.

31. Colombo, G.: Rotational Period of Mercury. Nature, November 6, 1965, p. 575.

32. Colombo, G.; and Shapiro, I.: The Rotation of the Planet Mercury. Astrophysical Journal, July 1966, vol. 145.

33. McGovern, W.E.; Gross, S.H.; and Rasool, S.I.: Rotation Period of the Planet Mercury. Nature, vol. 208, October 23, 1965, p. 375, A66-12891.

34. Moore, P.: Conditions on the Surface of Mercury. Journal of the British Interplanetary Society, vol. 13, 1964, pp. 318-324.

BIBLIOGRAPHY

1. Kuiper, G. P.: Mercury. Encyclopedia Britannica 1964, vol. 15, p. 271.

2. Radar Studies Planet Orbits. Marshall Star Space Information Digest, November 23, 1966.

3. Pettengill, G. H.: Recent Arecibo Observations of Mercury. Symposium on Planetary Atmospheres and Surfaces, Dorado, Puerto Rico, May 24-27, 1965, paper. Journal of Research, Section D - Radio Science, vol. 69D, December 1965, pp. 1627-1628, A66-20119.

4. Hodge, P.; Interactions of the Planet Mercury with Interplanetary Material. Proceedings of the Eleventh International Astrophysical Symposium, Liege, Belgium, July 9-12, 1962, A63-25349.

5. Evans. J.V.; Brockelman, R.A.; Henry, J.C.; Hyde, M.G.; and Kraft, L.G.: Radio Echo Observation of Venus and Mercury at 23 CM Wavelength. Mass. Inst. of Tech., Lincoln Lab., May 1965, JA-2573, AF 19(628)-5167, published in Astronomical Journal, vol. 70, no. 7, pp. 486-501, September 1965, AD-624-731, unclassified.

6. Epstein, E.E.; Oliver, J.P.; and Schorn, R.A.: Further Observations of Planets and Quasi-Stellar Radio Sources at 3 MM. Technical Report April 10, 1965 to April 29, 1966, Aerospace Corporation, Laboratory Operation, El Segundo, Calif., July 1966, Report no. TR-669 (9230-04)-1, SSD TR-66-122, unclassified, AD-487-702, contract no. AF 04(695)-669, NAS7-100.

7. Schilling, G.F.: Atmospheres of the Planets. Rand Corporation, Santa Monica, California, September 1964, report no. P-2964, AD-606 026, unclassified.

8. Van Tassel, R. A.; and Salisbury, J. W.: Planetary Environments. Air Force Cambridge Research Laboratories, 1965, N66-10998, Handbook of Geophysics and Space Environment, N66-10986-02-13.

9. Kellermann, K. I.: 11-CM Observations of the Temperature of Mercury. Nature, vol. 205, March 13, 1965, pp. 1091-1092, A65-22205.

10. Hoop, H. H.: Mercury Atmosphere and Surface. Report RSIC 633, January 1967.

IV. RAREFIED GAS DYNAMICS

ORBITAL DYNAMICS OF SPHERICAL SATELLITES (ODYSSEY I)

By

J. Ballance, R. Smith, A. Few and E. Sullivan

SUMMARY

Four different experiments designed to study the several phenomena that result in forces and moments acting on earth-orbiting spacecraft and satellites are discussed. The areas of information such as density, aerodynamic coefficients, momentum and energy accommodation coefficients, reflected particle distribution, and refined model atmospheres are considered and discussed as phenomena which are, in part, requirements for refining earth-orbiting spacecraft dynamics, lifetime, and attitude prediction techniques. A design and operation scheme for implementing the experiments aboard a Saturn launch vehicle is outlined.

I. INTRODUCTION

Active and passive stability and control characteristics, as well as lifetime prediction techniques, are fundamental problems facing the designer of earth-orbiting spacecraft and satellites. Mission requirements have become more and more complex requiring, in some instances, minimum lifetime specifications of several years' duration, in addition to detailed attitude histories during the lifetime of unique configurations such as those being considered for the AAP cluster mission. Needless to say, an accurate model atmosphere and aerodynamic characteristics are required if certain mission requirements are to be assured with any reliability. Present methods of determining the various low density aerodynamic characteristics and model atmospheric data required in the prediction of spacecraft lifetime and attitude histories are based on combinations of theoretical analysis and experimental data from satellites now in orbit, sounding rockets, and ground-based facilities.

Theoretical methods of calculating aerodynamic forces are usually applicable only for the free molecular flow regime, and confidence in those methods is limited by the lack of knowledge of the gas molecule-surface interaction characteristics. No adequate theoretical tools exist to handle the transitional flow regime. Because of these unknown factors, one can say that theory fails to provide the designer with adequate information in either the transitional or free molecular flow regimes. Sounding rockets have a potential for use in conducting upper atmospheric experiments; however, they require quite complex instrumentation because of the rocket's small payload capability and have a relatively short flight duration. Although ground facilities have been valuable tools in conducting some simulated flight conditions, for several reasons they do not allow satellite orbit environment to be simulated in detail. The basic disadvantage is that non-representative atmospheric gases are usually used.

The shortcomings of existing methods and techniques which confront the designer who must choose the proper model atmosphere and associated phenomena which result in the forces and moments acting on the earth orbiting spacecraft are clearly evident. Current models of the upper (>90 km) atmosphere of the earth are based on a wealth of density data above 200 km (computed from the analysis of the orbital decay of several satellites and a few measurements from instruments onboard Explorer 17) and a somewhat smaller data sample below 200 km (computed from the orbital decay analysis of some U. S. Air Force satellites combined with very few measurements from instruments on rocket launched probes). The parameters which make up the drag forces that affect an orbiting spacecraft are the ambient density, ρ ; the aerodynamic drag coefficient, C_D; and the area to mass ratio, A/m. Other sources which must also be considered include solar radiation pressure for those satellites with perigee altitudes above $\sim$400 km, and those forces arising from the nonsphericity of the earth.

Atmospheric densities computed from orbital decay analyses are usually based on an assumed value of 2.2 for C_D. Cook [1] recently concluded that the drag coefficient between 140 and 400 kilometers at times of low solar activity and between 140 and 600

kilometers at times of high solar activity is almost independent of height; however, it may be 10 percent too low. At heights above 400 and 600 kilometers, the drag coefficient increases with height to an asymptotic value between 2.6 and 2.7 which is nearly reached at 800 kilometers. The relative uncertainty in C_D should not increase with height; therefore, the likely error is estimated at 15 percent with a maximum possible error of about 30 percent. Since computed values of density are inversely proportional to C_D, we must count on similar uncertainties from this cause in the model densities below 600 kilometers at times of high solar activity and below 400 kilometers at times of low solar activity, provided we assume that we know exactly the A/m ratio, the solar radiation effects, and the effects of the earth's nonsphericity. We can eliminate two of these additional error sources, the effects of uncertainty in the A/m ratio and the solar radiation pressure effects, by choosing only spherical satellites of known constant mass having perigees below ~400 kilometers and still above the very ill-defined region where the satellite enters the transitional aerodynamic flow regime and theoretical models for computing drag coefficient breakdown. The magnitude of the error from the third source, the nonsphericity of the earth, is still problematical. Gabbard [2] in an analysis of five satellites presents evidence of a satellite resonance phenomenon with geopotential tesseral terms of order m = 16, 17, and 32 to corroborate the evidence of others with terms of order m = 13 and 14. He further states that an accurate determination of the descriptive parameters must, therefore, be the result of a joint geopotential-atmospheric experiment.

The accuracy of the number densities of N_2, O_2, and O can be roughly estimated from the disagreement of the different mass spectrometer results and also from the independent determinations based on the attenuation of solar extreme ultraviolet radiation in the lower thermosphere. A systematic uncertainty of a factor of two might still exist in some of the measured number densities.

Harris and Priester [3] summarized the estimated total ranges of uncertainty in the total density, temperature, and constituent number densities due to systematic errors for the long term variation of the main physical parameters in the following tables:

TABLE I. TOTAL DENSITY

(Long-term behavior for March or September-December averages (semi-annual effect) after short-term variations (27-day variation, geomagnetic effect) have been considered)

Altitude km	Error (Percent) High Solar Activity	Error (Percent) Low Solar Activity
120	± 50	± 50
200	+ 40, - 10	± 25
300	+ 40, - 10	± 25
400	± 25	± 25
600	± 25	± 25
800	unknown	± 25

TABLE II. TEMPERATURE

Altitude (km)	Error (Percent)
120	± 30
200	± 20
300	± 15
400	± 10
600	± 10
800	± 10

The range of uncertainty in the number densities at 120 kilometers is represented by two factors with which the numerical values in the CIRA 1965 model atmosphere ought to be multiplied. The estimated factors for N_2, O_2, O, He, and A are 0.5 and 1.5. It therefore becomes obvious that additional means must be sought to determine these phenomena more accurately. Consequently, four inflight experiments have been proposed to fly "piggy-back" on board a Saturn launch vehicle. The experimental results are expected to provide information in areas such as geodesy, aerodynamic coefficients, momentum and energy accommodation coefficients, reflected particle distributions and refinements to existing model atmospheres. The discussion which follows deals with a brief description of the proposed experiments: (1) multi-sphere ensemble, (2) paddlewheel satellite, (3) gas-surface interactions, (4) densitometer, including the scientific and engineering application

benefits. The carrier design and operational considerations for all four experiments are also discussed.

II. THE EXPERIMENTAL PROGRAM

A. MULTI-SPHERE SATELLITE EXPERIMENT

Within the possibilities of present technology, a reasonable experiment can be designed which yields a measurement of atmospheric density, experimental data on the drag coefficient of a sphere in near-free-molecule flow, and a detailed representation of the earth's gravitational potential below 200 km. This multiple objective is natural, or even inevitable, since satellite accelerations depend primarily upon the atmospheric density, the details of the interaction of the satellite with the atmosphere, and the gravitational forces. Such an experiment requires that an ensemble of spherical satellites be placed in essentially identical orbits. These bodies would be similar in most of their characteristics, but would differ in those which allow a separation and identification of the factors which enter into the aerodynamic drag and gravitational forces (see Fig. 1). In arriving at a practical experiment, the satellite tracking accuracy now attainable must be recognized. The accuracy obtained with the existing network of Baker-Nunn cameras has been assumed.

B. AERODYNAMIC DRAG REPRESENTATION

To design the experiment, a representation of the drag coefficient for near-free-molecule flow must be adopted. The choice is somewhat subjective, since a review of published literature reveals difficulty in obtaining agreement between theory and experiment. Data of the sort obtainable from a satellite experiment would be particularly valuable to compare with theory for parameter values difficult to obtain in the laboratory, such as large Knudsen number.

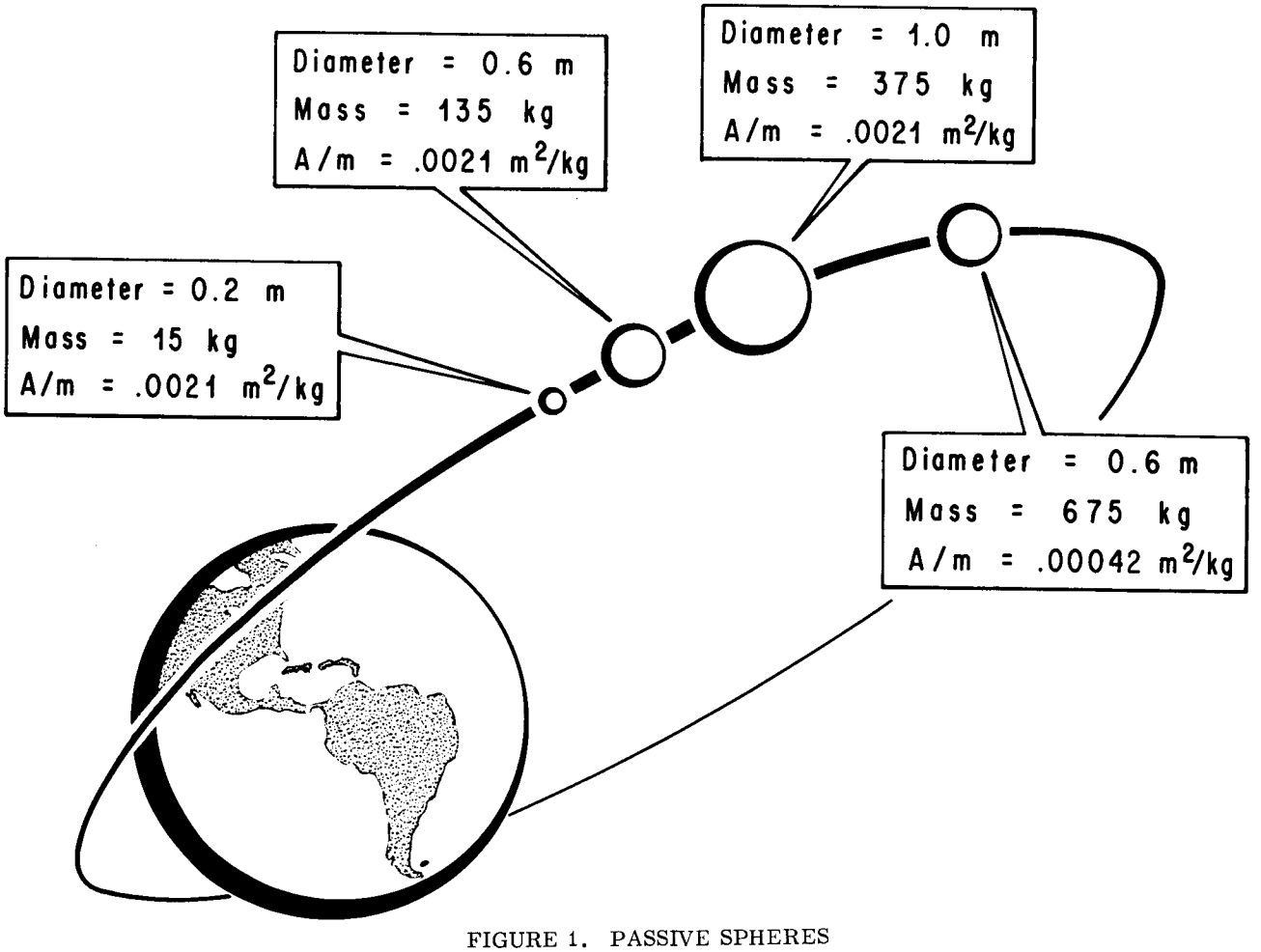

FIGURE 1. PASSIVE SPHERES

Most of the theoretical expressions for the near-free-molecule flow drag coefficient of a sphere have the form

$$C_D = C_{Dfm} - \frac{1}{K} F(S_b, S_\infty), \qquad (1)$$

where

C_{Dfm} is the value of the drag coefficient for free-molecule flow,

K is the free stream Knudsen number (free stream mean free path/sphere diameter)

$$K = \frac{w}{\sqrt{2}\, N_0\, \sigma^2\, \rho D}, \qquad (2)$$

$F(S_b, S_\infty)$ = function to represent the transition flow characteristic,

S_b is the molecular speed ratio of the gas diffusely emitted from the surface

$$S_b = U/\sqrt{2RT_b/w}, \qquad (3)$$

S_∞ is the molecular speed ratio for the free stream,

$$S_\infty = U/\sqrt{2RT_\infty/w}. \qquad (4)$$

T_b is the surface temperature of the orbiting body,

T_∞ is the temperature of the atmosphere,

U is the satellite velocity relative to the atmosphere,

w is the mean molecular weight of the air molecules

N_0 is Avagadro's Number, $N_0 = 6.02 \times 10^{23}$ atoms/gm mole

σ is effective collision diameter of air, $\sigma = 3.65 \times 10^{-10}$ meter

R is the universal gas constant, $R = 8.3170 \times 10^7$ erg/mole °K

In this same notation, for diffuse reflection [4],

$$C_{Dfm} = 2 + \frac{1.18}{S_b} \qquad (5)$$

Different forms of the function $F(S_b, S_\infty)$ have been derived by various authors using different procedures [5]:

(Baker and Charwat) $$F = 0.24\, S_b + 1.06, \qquad (6a)$$

(Willis) $$F = \frac{0.165\, S_b + 1.44 - 1.13/S_b}{S_\infty}, \qquad (6b)$$

(Rose) $$F = \frac{0.33\, S_b - 0.12}{S_\infty}. \qquad (6c)$$

In their review of this topic, Maslach et al. conclude that the last two expressions give the best agreement with laboratory data.

Using equation (2) to express 1/K in terms of ρ, w, and D, we get a representation of the aerodynamic drag per unit mass of the satellite:

$$\frac{\text{drag}}{\text{unit mass}} = \frac{1}{2} C_D \frac{A}{m} U^2 \rho = \frac{1}{2}\left[C_{Dfm} - BF(S_b, S_\infty) D\rho\right] \frac{A}{m} \rho U^2, \qquad (7)$$

where A is the cross-section area of the sphere, m is the mass of the sphere, and

$$B = \frac{\sqrt{2}\pi\, \sigma^2\, N_0}{w}. \qquad (7a)$$

For the purpose of the experiment under discussion, we can consider several of the quantities in this representation to be known. The velocity of the satellite can be found from the orbital elements obtained by tracking the satellite. The surface temperature of the sphere can be calculated using proved techniques [6]. The mean molecular weight and the effective collision diameter of the air molecules vary quite slowly with altitude in the interval of interest, and appropriate values from the literature can be used. The diameter and mass of the sphere are parameters to be adjusted in the design of the experiment, but will be known quantities for an actual body.

If equation (5) is accepted as correct, only the atmospheric density ρ and the values of $F(S_b, S_\infty)$ remain to be determined from appropriate analysis of tracking data. The value of ρ is of obvious geophysical interest. The experimental values of $F(S_b, S_\infty)$ are valuable for comparison with theoretical values derived by various procedures (equations (6)).

To estimate the magnitude of the second term of equation (7) relative to the first term, we can use the theoretical expressions for F with values of ρ from a standard atmosphere [7]. Values for equation (6b) are shown in Table III.

TABLE III. DRAG COEFFICIENT FOR 1-M-DIAMETER SPHERE*

Altitude (km)	K	$BF(S_b, S_\infty)D\rho$	C_{Dfm}	C_D
120	3.1	0.084	2.062	1.978
130	9.4	0.035	2.063	2.028
140	19.2	0.019	2.063	2.044
150	32.6	0.012	2.064	2.051
160	50.2	0.009	2.064	2.056
170	72.2	0.006	2.065	2.059

*The following values are used in the table:

atmospheric model from reference [7] with exosphere temperature = 1300° K,

F is given by equation (6b),

$T_b = 300°K$,

$U = 8.2$ km/sec.

The effect of atmospheric drag on the anomalistic period P of a satellite has been conveniently expressed by Sterne [8]. If the rotation of the atmosphere is neglected, the rate of change of the period is

$$\frac{\Delta P}{P} = \frac{dP}{dt} = -\frac{3}{2}\frac{A}{m}\rho_P a \int_0^{2\pi} C_D \frac{\rho}{\rho_P}\frac{(1 + e\cos E)^{3/2}}{(1 - e\cos E)^{1/2}}\,dE, \quad (8)$$

where ρ_P is the density at perigee, a the semimajor axis, e the eccentricity, and E the eccentric anomaly. As explained by Jacchia [9], this equation is the usual starting place for determinations of atmospheric density because the period and its changes are rather directly obtained from tracking data.

To simplify notation, it is convenient to define quantities f_1 and f_2 by

$$f_1 = \int_0^{\pi} \frac{\rho}{\rho_P}\frac{(1 + e\cos E)^{3/2}}{(1 - e\cos E)^{1/2}}\,dE, \quad (9)$$

and

$$f_2 = \int_0^{\pi} \left(\frac{\rho}{\rho_P}\right)^2 \frac{(1 + e\cos E)^{3/2}}{(1 - e\cos E)^{1/2}}\,dE. \quad (10)$$

Tables of f_1 are given by Jacchia and Slowey [10] and similar tables of f_2 are easily constructed. Using this notation and the adopted expression for C_D in equation (8) gives [11]

$$\frac{dP}{dt} = -3\,af_1\frac{A}{m}C_{Dfm}\,\rho_P + 3\,af_2\,B\frac{A}{m}\,D\,F\,\rho_P^2. \quad (11)$$

In this equation, B has been treated as a constant because it varies much more slowly with altitude than does ρ.

To investigate near-free-molecule-flow aerodynamics and atmospheric density at low altitudes, we suggest two spherical satellites having identical A/m and having surface preparations that ensure equal surface temperatures. These spheres should be launched by the same vehicle into initial orbits as nearly identical as practical. The diameter of one sphere, D(1), should be as small as possible and still allow reliable photographic tracking with the Baker-Nunn cameras. The diameter of the second, D(2), should be as large as can be contained within the available launch vehicle. Using simple procedures discussed below, values for the rate of change of the periods P(1) and P(2) can be obtained from tracking data. For two satellites under these conditions, equation (11) gives two linear simultaneous equations (12) and (13) for unknowns $C_{Dfm}\,\rho_P$ and $BF\rho_P^2$. The coefficients multiplying these unknowns involve only quantities known a priori or determined from tracking data. The quantities f_1 and f_2 are functions of the atmospheric scale height near perigee, as well as of

the orbital elements, but the value of the scale height can be estimated with sufficient accuracy for computing f_1 and f_2:

$$\left[-3\,af_1\frac{A}{m}\right]C_{Dfm}\rho_P + \left[3\,af_2\,D(1)\frac{A}{m}\right]BF\rho_P^2 = \frac{dP(1)}{dt} \qquad (12)$$

and

$$\left[-3\,af_1\frac{A}{m}\right]C_{Dfm}\rho_P + \left[3\,af_2\,D(2)\frac{A}{m}\right]BF\rho_P^2 = \frac{dP(2)}{dt} \quad . \qquad (13)$$

Under the assumption that the orbits are identical, these have the simple solutions

$$C_{Dfm}\rho_P = \frac{1}{\left(3\,af_1\frac{A}{m}\right)[D(2) - D(1)]}\left[D(1)\frac{dP(2)}{dt} - D(2)\frac{dP(1)}{dt}\right] \qquad (14)$$

and

$$BF\rho_P^2 = \frac{1}{\left(3\,af_2\frac{A}{m}\right)[D(2) - D(1)]}\left[\frac{dP(2)}{dt} - \frac{dP(1)}{dt}\right] \quad . \qquad (15)$$

If the perigee altitude were above the near-free-molecule-flow region for the adopted satellite diameters, the periods would have the same rate of change and equation (14) would reduce to the usual expression applied to determine $C_{Dfm}\rho_P$. Thus equation (14) is only the familiar expression with a simple correction for the case of near-free-molecule flow. If a value of C_{Dfm} is accepted from equation (5) or from some other source [12], equation (14) yields a value for ρ_P. Using this value for ρ_P with equation (15) gives a value for BF, which is a measure of the departure from free-molecule-flow aerodynamics. If B is considered known, a value of F follows immediately.

The accuracy with which F is obtained depends critically upon the selection of satellite and orbit parameters such that the rates of change of the periods differ significantly. Variation of ρ_P during the interval of observation can also limit the accuracy obtained.

Equations (14) and (15) are intended only to illustrate the principal features of the analysis. For example, as the satellites separate, the assumption of identical orbits begins to break down; however, first-order corrections for this can be introduced. The effects of an initial separation velocity between the spheres and the rotation of the atmosphere can likewise be incorporated.

Introducing into the experiment a third sphere, again with the same A/m but with a still different diameter, D(3), would provide a useful check on the results. A third equation of the form (12) is not independent, but it must be consistent with (12) and (13). A demonstration of the required consistency would lend substantial credence to the solution. This is particularly true because equations (12) and (13) will always have a solution, but this solution is by no means guaranteed to be meaningful, as it assumes equation (1) is correct. Given three or more equations of the form of (12) with reasonable consistency, a least-squares solution can be obtained replacing equations (14) and (15).

On the other hand, there is some reason to believe that a term proportional to $(D\rho_P)^2$ should be added to equation (1) [13]. If this should be necessary, equation (11) would have a corresponding additional term involving ρ_P^3, f_3, and a coefficient characterizing the importance of this added term. Data on three spheres of different size then would be required to investigate the departure from free-molecule-flow aerodynamics, but otherwise the same procedures could be followed.

The simple experiment sketched in the previous section can be extended to alleviate the weaknesses that result because the orbits become different as the spheres separate. This is accomplished by adjusting slightly the masses and hence the A/m ratios to just balance the expected drag differences caused initially by departure from free-molecule-flow aerodynamics. For the two-sphere case, this requires that (A/m) (1) and (A/m) (2) be chosen so that

$$\frac{dP(1)}{dt} = \frac{dP(2)}{dt} \quad . \qquad (16)$$

This implies that

$$\frac{\frac{A}{m}(1)}{\frac{A}{m}(2)} = \frac{f_1 C_{Dfm} - f_2 D(2)\, BF\rho_P}{f_1 C_{Dfm} - f_2 D(1)\, BF\rho_P} \quad . \tag{17}$$

Because BF and ρ_P are imperfectly known, equation (17) cannot be exactly satisfied; however, the best estimates of these can be used to achieve a first approximation. Also, as the eccentricities of the orbits decrease, the values of f_1 and f_2 change, which may generate a departure from equation (17).

Corresponding to equations (14) and (15) for this generalized case are the equations

$$C_{Dfm}\,\rho_P = \frac{1}{[3\, af_2 \frac{A}{m}(1)\, \frac{A}{m}(2)]\, [D(2) - D(1)]} \left[D(1) \frac{A}{m}(1)\, \frac{dP(2)}{dt} - D(2) \frac{A}{m}(2)\, \frac{dP(1)}{dt} \right] \tag{18}$$

and

$$BF\rho_P^2 = \frac{1}{[3\, af_2 \frac{A}{m}(1)\, \frac{A}{m}(2)]\, [D(2) - D(1)]} \left[\frac{A}{m}(1)\, \frac{dP(2)}{dt} - \frac{A}{m}(2)\, \frac{dP(1)}{dt} \right] \quad . \tag{19}$$

Perhaps it is worth noting that these equations are meaningful whether or not equation (17) is satisfied.

In the following discussions and examples, the point of view of the previous section will be retained because the spatial separation of the spheres is an easily pictured measure of the observability of the desired quantities. However, an actual execution of the experiment would probably employ the more general approach of this section.

Changes of atmospheric density as a function of time, are well known above 200 km, but less is known of their magnitude at lower altitudes [14]. Measurements of changes that may occur are as interesting as determinations of the density. An investigation of temporal phenomena would be facilitated by the inclusion of a very heavy sphere in the ensemble. This sphere could have the same size and surface preparation as one of the other spheres, but it should have as great a mass as practical.

The high-density body will remain in orbit longer than the lighter bodies in the aerodynamics experiment. The knowledge of the drag coefficient generated in the initial phases of the experiment is directly applicable to the later history of the heavy body. An analysis of the orbit of the long-lived satellite in the usual way is useful in the measurement of the variation of atmospheric density as a function of time and of solar and geophysical events.

The determination of accurate orbits for the satellites in the suggested experiment depends upon an adequate representation of the geopotential. Fortunately, the philosophy of the experiment minimizes the demands on the geopotential representation. Because the perigee of the suggested satellites will be quite low, and if the eccentricity is not too great, the effect of high-order harmonics in the gravitational field may be greater than that experienced by satellites in more distant orbits. Thus the adopted standard representation of the geopotential may not account for all detectable gravitational perturbations on an individual satellite. This may introduce an increased "noise level" in the orbit-determination process.

If this should become troublesome, the same dense sphere used for temporal atmospheric variation also may relieve this problem. If the additional sphere is denoted by 4, then from equation (8),

$$\frac{dP(4)}{dt} = \frac{m(1)}{m(4)} \frac{dP(1)}{dt} \quad . \tag{20}$$

If, further, m(4) is significantly larger than m(1), perhaps by a factor of 5 or 10, then equation (20) provides accurate values of dP(4)/dt from the larger more easily measured values of dP(1)/dt.

A similar situation prevails for the drag-included changes in the other orbital elements of sphere 4. These can be expressed with relatively greater accuracy from the drag measured by sphere 1. But the drag on sphere 4 is already relatively small because A/m is small. Hence, the uncertainty associated with drag on sphere 4 is something like m(1)/m(4) less than that on sphere 1.

Drag corrections derived from sphere 1 can be applied to the orbit of sphere 4, and this orbit examined for the adequacy of the adopted geopotential. If the residuals between observation and calculation approach the accuracy of the observations, then the adequacy of the geopotential is strongly verified. In this case, the analysis of atmospheric effects on the

• light satellites can proceed with assurance that the "noise" induced by uncertainty in the geopotential is small. Asking that the residuals approach the observational accuracy is probably too stringent. Presumably, the geopotential is sufficient if the residuals of the corrected orbit for sphere 4 are small compared to the uncertainty in the determination of the separations induced by differences in C_D for the high-drag spheres.

If the residuals for the corrected orbit of sphere 4 are greater than expected, the orbit can perhaps provide information for an improved determination of the geopotential. In an imprecise sense, the corrected orbit is a low-perigee, drag-free orbit.

The difference in the rate of change of the periods of the spheres is a measure of the detectability of the departure from free-molecule flow aerodynamics. A more easily interpreted measure is the separation of the satellites after some time interval. This can be estimated using the theoretical values of the required parameters. Assuming for this estimate that there is negligible initial separation velocity, the expected separation in mean anomaly is given by the equation

$$\Delta M = \frac{3\, BF(S_b, S_\infty)}{2\overline{P}^2} \frac{A}{m} \rho_p^2\, a\, f_2 [D(i) - D(j)]\, t^2 \qquad (21)$$

where ΔM is in revolution, $\overline{P}$ is the mean period of the two satellites for the interval, t, time since launch, D(i) and D(j) are diameters of two of the spheres, a is the semi-major axis, e is the eccentricity, E is the eccentric anomaly, B and f_2 are the same as equation (7a) and 10.

If the atmospheric density at a particular altitude is an objective of the experiment, this altitude determines the perigee radius.

By using the sphere parameters as shown in Figure 1, and considering a lifetime of 180 days, Figure 2 presents the apogee altitude requirements for various perigee attitudes for the smallest sphere assuming that it is always in free molecular flow. A theoretical value for the function $F(S_b, S_\infty)$ can then be chosen, and the expected separation of the smallest sphere from a larger sphere can be determined. The results for a sphere of 2 meters (10 times larger than the smallest sphere) are shown in Figure 3. It is seen that for a perigee of 160 km, the separation distance would be about 45 degrees in 90 days. With 160 km as the desired perigee altitude, 90 days the observed time, and less than 25 degrees separation for observation requirements, it is seen that the largest sphere must be less than 2 meters in diameter. A complete description of this experiment can be found in Reference 15.

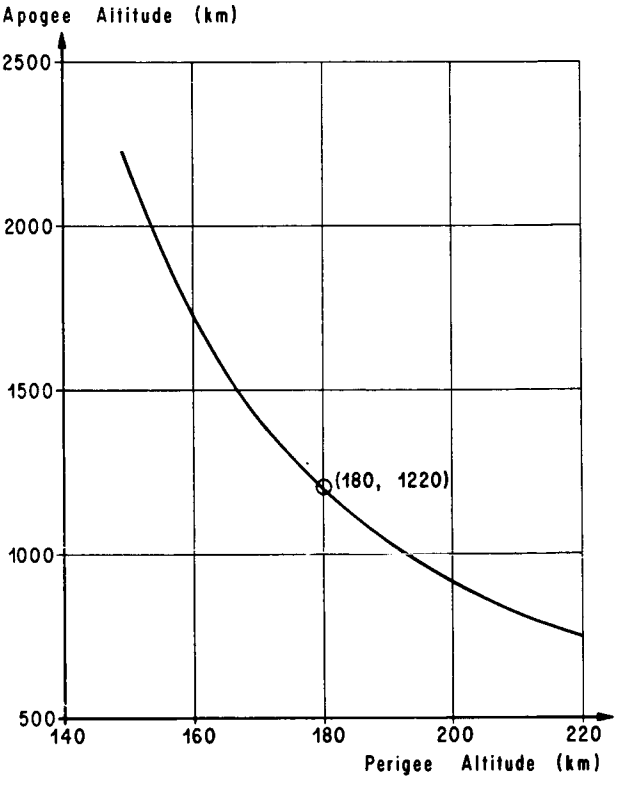

FIGURE 2. 180 DAY, -2σ LIFETIME, FOR .2 METER DIAMETER SPHERE

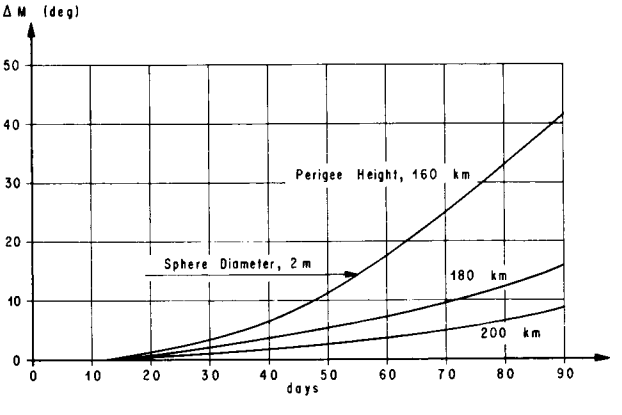

FIGURE 3. SEPARATION OF 2 METER DIAMETER SPHERE FROM .2 METER DIAMETER SPHERE

C. PADDLEWHEEL SATELLITE

From this experiment three independent types of measurements can be made using both the spin and orbit decay of a paddlewheel satellite combined with the orbit decay of two additional satellites in neighboring orbits (see Figure 4). The parameters to be determined are the ambient atmospheric density, the momentum accommodation coefficient, and the reflection coefficients.

One satellite ("Honeycomb") will be a diffusely reflecting sphere whose drag coefficient can be accurately calculated from the speed ratio. Therefore, the orbital decay of the diffusely reflecting sphere will determine the atmospheric density within one or two percent. A second satellite will be a paddlewheel ("Windmill") satellite whose drag coefficient will be directly calculable from its orbital decay because atmospheric density will be known from the diffusely reflecting sphere in a neighboring orbit. Knowing the absolute atmospheric density and the satellite velocity, we shall know the momentum imparted to the paddlewheel satellite by the incident air molecules. The rates of orbital decay and spin decay can then be used to calculate components of the momentum of the re-emitted molecules.

The drag and accommodation coefficients can then be calculated from Schamberg's [17] gas-solid surface interaction model or similar models.

In Schamberg's drag and accommodation coefficient model [17], the following assumptions are employed when applied to paddlewheel satellites:

(1) Free-molecular flow exists.

(2) The angle between the satellite velocity vector and spin vector is less than 33 degrees.

(3) No air molecules strike the satellite more than once.

(4) The only important torques are caused by air molecules striking the paddles.

(5) Air molecules have no random thermal motion due to the high satellite velocity.

Schamberg relates the angle of incidence, θ_i, to the angle of reflection, θ_r, by the equation

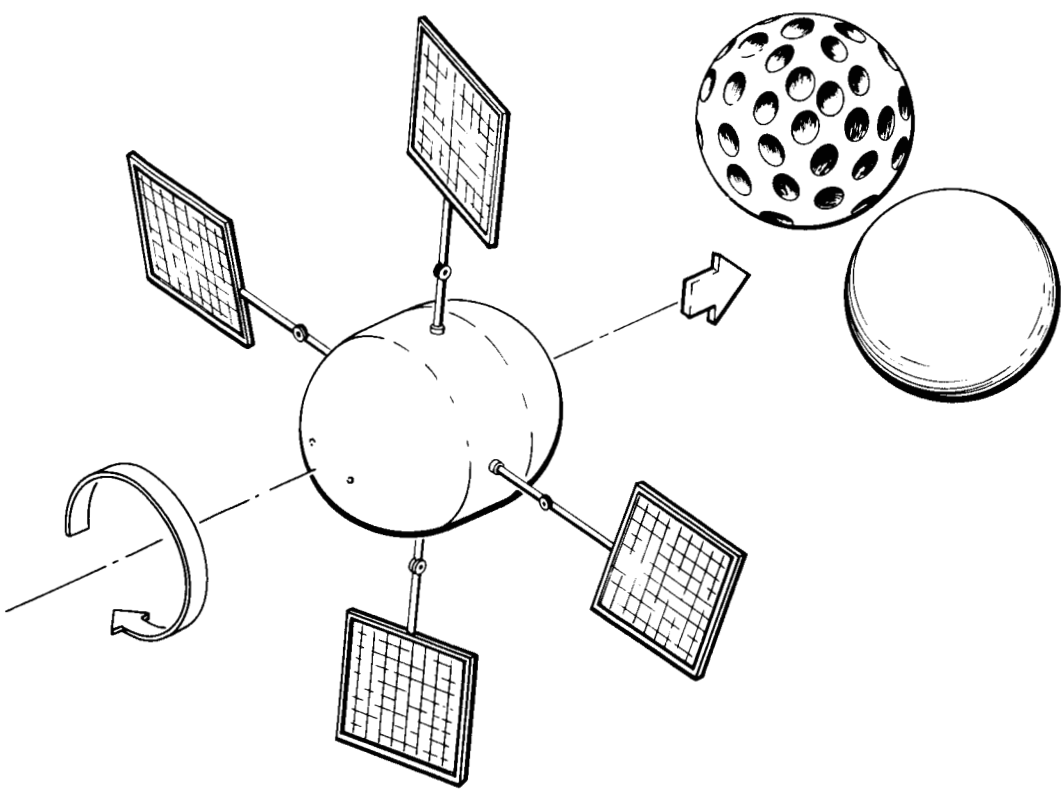

FIGURE 4. PADDLEWHEEL, SMOOTH AND DIFFUSE SPHERES

$$\cos \theta_r = (\cos \theta_i)^{\nu} , \qquad (22)$$

$\nu = 1$, specular reflection

$\nu = \infty$, diffuse re-emission.

Schamberg also determines the speed of re-emission, V_r, as related to the incident speed, V_i, as

$$\frac{V_r}{V_i} = \sqrt{\frac{T_r}{T_i}} = \sqrt{1 + \alpha\left(\frac{T_w}{T_i} - 1\right)} \qquad (23)$$

where α is the thermal accommodation coefficient and T_i, T_r, and T_w are the temperature of the incident molecules, re-emitted molecules, and surface walls, respectively.

By adding incident and re-emitted momentum fluxes, and dividing by half the incident flux,

$$C_D = 2\left[1 + \phi\,(\phi_o)\frac{V_r}{V_i} f(\nu, \text{shape})\right] , \qquad (24)$$

where (ϕ_o) is the ratio of the axial momentum carried away to the momentum that would be carried away if all the particles in the beam were aligned with the beam axis, Figure 5. Graphs and formulas for (ϕ_o) are contained in Schamberg's papers [17].

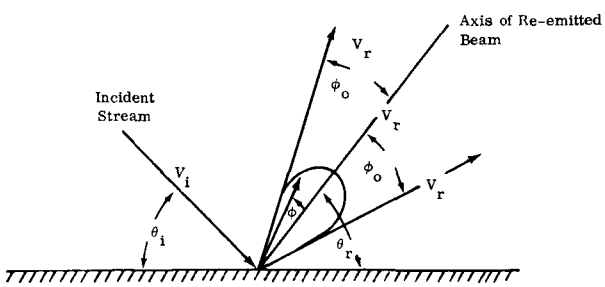

FIGURE 5. SCHAMBERG'S SURFACE-PARTICLE INTERACTION MODEL

Since only the paddles contribute to the spin drag, the value of $f(\nu, \text{shape})$ was shown to be

$$f(\nu, \text{shape}) = \cos \alpha \cos \theta \qquad (25)$$

as an average value per spin revolution of the satellite. The angle α is the angle between the normal to a paddle surface and the spin vector, and θ is the angle between the velocity vector and the spin axis at perigee. The value of $f(\nu, \text{shape})$ for the entire body, considering orbital and spin drag, was shown to be

$$f(\nu, \text{shape}) = 0.597 \cos \alpha \cos \theta + 0.403\left(\frac{2}{3}\right) \qquad (26)$$

where the value $(\frac{2}{3})$ corresponds to $f(\nu, \text{shape})$ for the spherical center portion of the satellite and the values 0.597 and 0.403 correspond to the proportional areas of the paddles and the spherical center portion, respectively.

The values proposed to be determined from this experiment are: absolute atmospheric density, satellite drag coefficient, accommodation coefficient, and the angular distribution of the momentum re-emitted from the surface of the satellite. The angular distribution can be assumed from Schamberg's model. The dependence of accommodation coefficient on satellite / substrate material and on angle of incidence has been assumed to be negligible.

Once the spin drag rates, orbital decay rates, paddle temperatures, and other orbital parameters have been determined, the torque, τ, about spin axis can be calculated from

$$\bar{\tau} = B\rho(\vec{R})\, V_i^2(\vec{R}) \ . \qquad (27)$$

where $\rho(\vec{R})$ is the density of the atmosphere at a point $\vec{R}$, V_i is the instantaneous satellite speed relative to the atmosphere, and B is given as

$$B = -4LSA\left(K_1 \frac{V_r}{V_1} + K_2\right) ,$$

where L is the perpendicular distance from a paddle center to the spin axis, A is the area of one side of a paddle, and S is given as

$$S = \left[1 - \frac{\cos^2 \alpha}{\cos^2 \theta}\right]^{\frac{1}{2}}$$

K_1 and K_2 depend on the gas-solid interaction model assumed. By equating the spin angular momentum change in one orbital revolution to the corresponding time integral of the average torque, $\bar{\tau}$, we obtain a relationship involving the observed spin rate change, B, and the atmospheric density at perigee. Expressing the density in terms of the change in the semi-major axis; a, or the orbit and the drag coefficient, C_D, B is given by

$$B = \frac{C_D P_o I_r A_m (1 + e)}{m(1 - e^2)^{1/2}} (\Delta\nu/\Delta a) \qquad (28)$$

where

P_o is the period of orbital motion

I_r is the satellite roll moment of inertia

A_m is the effective area of the satellite for orbital drag

m is the satellite's mass

e is the orbital eccentricity

$\Delta\nu$ is the observed spin rate change per revolution

Δa is the observed change in the semi-major axis per revolution.

Equating the above two expressions for B and employing Schamberg's equation for C_D to eliminate V_r, an expression is obtained relating C_d to the observed changes in spin rate and semimajor axis; namely,

$$C_d = \frac{2\left(1 - \frac{K_2 K_3}{K_1}\right)}{1 - \frac{2K_3 P_o I_r A_n (1 + e)}{K_1 m (1 - e^2)^{1/2}} \frac{\Delta\nu}{\Delta a}} \qquad (29)$$

where K_1, K_2, and K_3 are functions of the body geometry and the nature of the gas-solid surface interaction. Models developed by Schamberg or other investigators [18, 19] can be applied to determine which models best describe the actual interaction.

Since the energy accommodation coefficient, α, may be given as

$$\alpha = \frac{1 - \left(\frac{V_r}{V_i}\right)^2}{(T_i - T_w)/T_i} \simeq 1 - \left(\frac{V_r}{V_i}\right)^2 \qquad (30)$$

then, α becomes

$$\alpha = 1 - \left(\frac{C_d - 2}{2 K_3}\right)^2 . \qquad (31)$$

Values of α computed for several satellites at varying angles of incidence should yield the best value of α for satellite surfaces and indicate whether α varies with angle of incidence. If α varies with angle of incidence in a systematic manner, more general equations must be formulated to describe the gas-surface interactions. In the preceding drag calculations, the reference drag area was taken as the projected area normal to the incident velocity vector.

Absolute densitites can be calculated from the following relationship between the density at perigee ρ_P and the spin rate change, $\Delta\nu$, produced at that perigee:

$$\rho_P = \frac{-(1 - e^2)^{1/2} \Delta\nu}{1.08 \sqrt{2\pi k/a}\, a^2 f C_D \frac{A_m}{m} (1 + e)^2 (\Delta\bar{\nu}/\Delta\bar{a})},$$

where

k is the density scale height,

f is the atmospheric rotation factor,

$\Delta\bar{\nu}/\Delta\bar{a}$ is the ratio of the average spin rate change to the average change in the semi-major axis.

Once the drag, accommodation coefficients, and the atmospheric density have been determined, density comparisons can be made with model atmosphere. Analytical and experimental drag and accommodation coefficient models can also be used for comparison.

This tells us the accommodation coefficients of the satellite surface materials under the conditions prevailing in space. From this knowledge we can calculate the drag coefficient of any satellite made of these materials. A third sphere with a smooth surface would provide additional information about gas-surface interactions and energy accommodation

coefficients from a body when reflections are approaching specularity. The third sphere would be used primarily to relate the results of this experiment to the results of the multiple sphere experiment. Equations for this purpose are already available.

The area-to-mass ratios of the three satellites will be nearly the same, so that they will remain in neighboring orbits throughout their active lifetime. Should one satellite move farther away from the other than is desired, we can even move them back together by causing the paddles of "Windmill" to produce more or less orbital drag. Figure 6 presents the paddlewheel geometric and mass characteristics along with spin rates. This experiment employs an elliptical orbit configuration with perigee at 200 km and apogee at 2000 km. A complete description of this experiment can be found in Reference 16.

- *Dimensions*
  - Deployed, Tip to Tip — 1.45 m
  - Retracted — .50 m Cube
  - Central Structure — .40 m X .50 m (0.4 m Sphere With Elongated Midsection)
  - Paddles (each) — .25 m X .25 m X .012 m
- *Mass*
  - Central Structure — 18.22 kg
  - Paddles & Arms — 2.32
  - Total 20.54 kg
- *Moments of Inertia*
  - Spin Axis, I_{xx} — 1.30 kg m^2
  - $I_{yy} = I_{zz}$ — .78 kg m^2
  - I_{xx}/I_{yy} — 1.66
- *Initial Spin Rate* — *1.5 rev/sec*
- *Initial Spin Decay Rate (58° Angle of Attack)* — *2.79 X 10^{-2} rad/sec/orbit*
- *Estimated Mission Life* — *> 15 days*
- *Orientation* — *Measured Only*

FIGURE 6. PADDLEWHEEL CHARACTERISTICS

D. GAS-SURFACE INTERACTIONS

The physics of the interaction between a molecule and a solid surface has been a subject of interest to scientists in diverse disciplines for nearly a century. In recent years, interest has focused in particular on interactions with high relative velocities between the gas molecules and the surface, an interest motivated to a large extent by the need to solve engineering problems involved in high speed, high altitude flights, including earth satellite flights. For such studies, the theoretical models are necessarily quite crude because of the paucity of appropriate experimental information.

When experiments concerned interaction at low thermal velocities (below 1000°K), it was relatively easy to produce thermal molecules of precisely known and controlled properties. But when it became of interest to investigate interactions with neutral molecules or atoms at incident speeds of the order of 10^6 cm/sec (equivalent to about 10 e.v. for nitrogen molecules), the problem of producing in the laboratory such conditions became extremely difficult. In fact, no solution is in sight despite a decade of intensive efforts. The basic problem is with trying to produce neutral particles of such speeds; and all attempts to neutralize electrostatically accelerated ions and still obtain a fast beam (10^6 cm/sec) with adequate flux density (10^{16} 1/cm^{2}sec) have been unsuccessful.

With the availability of payload for scientific experiments on board large satellites, it becomes feasible to perform, in situ, gas-surface interaction experiments under actual flight conditions if proper test apparatus suitable for satellite-borne use can be developed.

1. Formulation of the Gas-Surface Interaction Problem. When a particle (molecule, atom or subparticles thereof) intercepts a solid surface at some relative velocity, the interaction with the force fields at the surface results in scattering of the incident particle, as well as possible dynamic changes in the surface and its constituent elements. The gas particle will leave the surface at some probable angle and with some probable momentum. It is usual to consider a stream of identical incident particles and express the interaction in terms of the angular distribution of exit particles and the angular distribution of momentum of these particles (thereby also the energy).

It has been found that at low incident velocity (of the order of 10^4 cm/sec, or 0.1 e.v.) the scattering is generally diffuse; that is, there is equal probability in the direction of scattering over the entire hemisphere on one side of the surface and the energy of the reflected molecules is that corresponding to the temperature of the solid surface. This is equivalent

to saying that the incident molecules attain complete thermodynamic equilibrium with the surface before being reflected. At higher incident velocities and at large incident angles (measured from the surface normal), there is some evidence that the reflection may tend to be specular and that thermodynamic equilibrium is far from being achieved between the incident molecule and the surface. At energies of the order of 100 e.v. and above sputtering begins.

In the low energy, diffuse reflection range, as well as in the high energy sputtering range, a great deal of experimental data exist for various gas-solid combinations. In the intermediate energy range (10 e.v.), which happens to be the range encountered by spacecraft at orbital velocities, there is no laboratory test data, primarily because of the inability to date to generate the appropriate molecular beam. Two basic techniques have been used in attempting to produce 1 to 10 e.v. molecules, and both involve inherent difficulties that do not appear to be amenable to solutions in the laboratory.

2. A Satellite-Borne Molecular Beam Experiment. In a proposed scheme a Molsink type of experimental chamber is mounted in an attitude-controlled satellite such that the axis of a collimator which admits molecules into the chamber is parallel to the flight direction. In the center of the chamber interior is a target plate of some specified material to be studied. The plate can be rotated to vary the incident angle of the impinging molecules. Densitometers are placed around the chamber to measure the reflected flux at various angles to the target plate. Two 20-kv electron beams (placed at right angles to each other) are used to measure local molecular density through electron-excited molecular fluorescence. A schematic of the components is shown in Figure 7.

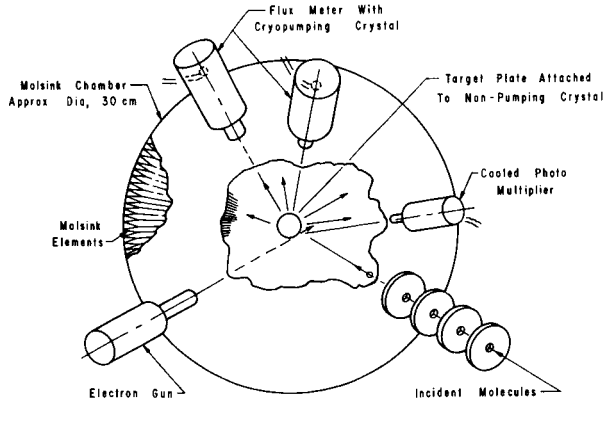

FIGURE 7. GAS-SURFACE INTERACTION EXPERIMENT USING DENSITOMETERS

The Molsink chamber is approximately spherical, with the interior lined with either wedge-shaped or honeycomb-shaped cryopump elements which have an array capture coefficient of at least 0.9 for molecules with single wall collision capture probability of 0.7. The diameter of the interior clear volume is about 20 cm, and the target plate is 1 cm^2 in area, as is the cross-sectional area of the collimator. The Molsink array is liquid helium (or liquid hydrogen) cooled and placed in a vacuum-tight super-insulated enclosure.

The experiment will consist of the following components, instruments and measurements:

(1) Molsink test chamber to provide contamination-free flux measurements.

(2) Flux meter to measure incident molecular flux, $\phi_0 = n_0 v_0$.

(3) Flux meters to measure reflected flux as function of angles $\phi(\theta, \varphi) = n(\theta, \varphi)\ v(\theta, \varphi)$.

(4) Molecular fluorescence densitometer to measure density $n(\theta, \varphi)$.

(5) From (3) and (4) determine momentum of reflected molecules as functions of angles, $mv(\theta, \varphi)$.

(6) Temperature-sensitive target to determine energy accommodation by calorimetry.

E. DENSITOMETER

The need for an accurate determination of the pertinent atmospheric property - mass density, i.e., mass per unit volume, at the orbital altitudes of concern has been shown in the preceding sections. The most direct way of measuring this quantity is to proceed by its definition, namely, to measure the mass of gas, regardless of composition, contained in a known ambient volume at orbital altitudes. Any technique attempting to make such a determination must be capable of (1) collecting the mass of gas, (2) sensing the collected mass, (3) determining the volume from which the mass was collected, and (4) determining spatial position.

Tracking provides the spatial position data, as well as spacecraft velocity; thus, an on-board instrument must consist of components capable of collecting, sensing, and volume determination.

The design approach is based upon the fact that a

gas collection element aligned parallel to the spacecraft flight direction will sweep out an ambient gas volume,

$$V_a = A_o u t, \tag{32}$$

where A_o is the projected inlet area of the collector, u is the spacecraft velocity, and t is the time of collection.

The continuous mass measurement technique is direct in that a cryogenically cooled, mass-sensitive quartz crystal cryopumps the entering mass onto the resonating crystal which responds to changes in system mass by a shift in the resonant frequency. Thus, mass flux is measured directly without intermediate measurements or calculations. The frequency shift is approximately a linear function of the collected mass until the shift becomes approximately one percent of the crystal's resonant frequency. For a crystal in thickness shear resonance, the sensitivity, i.e., the frequency shift with mass change, can be expressed as a function of the resonant frequency over the applicable linear range:

$$\Delta f = C \Delta m f_r^2, \tag{33}$$

where

C = constant = 2.26×10^{-6}

f_r = basic resonant frequency, cps

Δm = collected mass, gm/cm^2

Δf = frequency shift, cps.

The crystal response becomes nonlinear when the frequency shift due to mass addition becomes approximately one percent of the resonant frequency. The allowable mass change for linear crystal response is thus

$$\Delta m_{max} = \frac{4.42 \times 10^3}{f_r}. \tag{34}$$

Evaluating the system at 180-km altitude from available atmospheric property data then gives a maximum continuous collection time for linear response:

$$t_{max} = \frac{10^{10}}{(A_o/A_c) f_r} \text{ sec}, \tag{35}$$

where

A_o = aperture area

A_c = crystal area.

The area ratio value (A_c/A_o) should be approximately 100 to minimize measurement error due to escaping molecules; thus, the normalized maximum continuous collecting time becomes

$$\frac{t_{max}}{t_o} = \frac{1.8 \times 10^8}{f_r}, \tag{36}$$

where again t_o is one orbit period - in this case 5600 seconds.

The maximum altitude at which continuous collection for density measurement with a quartz crystal can be used is related to the minimum measurable condensed mass change and the length of time between measurements. The frequency shift, equation (33), can be related more directly to collector parameters and the collection time by rewriting as follows:

$$\Delta f = C f_r^2 (\dot{m}/A_o) \frac{A_o}{A_c} \frac{t}{t_o} t_o$$

or

$$\Delta f = C f_r^2 (\rho_a u) \frac{A_o}{A_c} \frac{t}{t_o} t_o. \tag{37}$$

The ratio t/t_o can be no larger than 0.1 in order to measure diurnal density variations. The orbital period, t_o, is not greatly affected by orbit altitude nor is the vehicle velocity, u, which together with the ambient density, ρ_a, forms a product which is the entering mass flux per unit area, $\dot{m}/A_o$. It is apparent then that the minimum measurable value of ambient density, ρ_a, is simply a function of the accuracy with which the frequency shift, Δf, can be measured. The percentage of frequency shift for a given mass change is proportional to the basic crystal resonant frequency:

$$\frac{\Delta f}{f_r} = C \Delta m f_r. \tag{38}$$

The maximum altitude at which the proposed instrument can measure density thus becomes a question of the desired accuracy of the measurement. The telemetry system results in a 5 cps uncertainty for the beat frequency system; thus, a frequency shift of 50 cps yields 10 percent uncertainty in the density determination. Equation (37) thus indicates the

following minimum measurable densities as determined by the crystal resonant frequency and assuming the use of a beat frequency system:

f_r	ρ_a	h
1 mc	5×10^{-9} kg/m^3	134 km
5 mc	2×10^{-10} kg/m^3	220 km
10 mc	5×10^{-11} kg/m^3	283 km

with an overall system measurement uncertainty of approximately 6.1 percent including telemetry error.

All major components of this system have been conservatively analyzed for all assumed flight, and reliable density measurements can be expected with an overall error (including telemetry) of only one percent. A summary description of the system follows.

The densitometer consists of these major components:

(1) A cylindrical orifice collector with a capture coefficient of 98 percent.

(2) A cooled piezoelectric crystal which responds to mass addition from cryopumping with a frequency shift.

(3) A measuring system consisting of a variable frequency oscillator and a beat frequency-to-voltage converter.

(4) A refrigeration system consisting of two heat sinks, one of lead to cool the crystal to a temperature not higher than 23.5 °K, and the other of aluminum which makes up the collector body and keeps itself at a temperature no higher than 100°K.

Figure 8 shows these components. Aside from electric power and telemetry, the densitometer system can operate independently of the vehicle. Vacuum and temperature conditioning of the system would be achieved on the ground either in a fixed or a mobile laboratory with relatively simple equipment requirements. Once conditioned and inserted into the vehicle, the system can withstand a hold of at least 24 hours without attention or umbilical connection. A complete description of this experiment can be found in Reference 20.

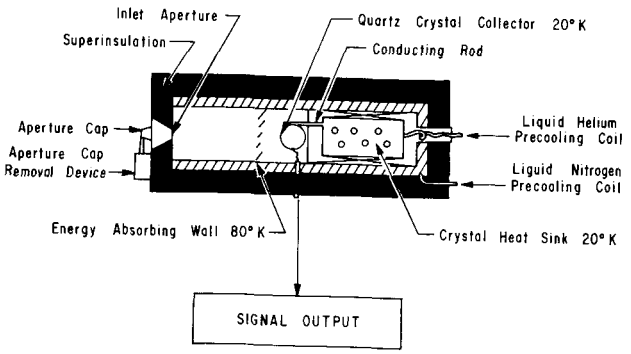

FIGURE 8. DENSITOMETER

III. OPERATIONAL CONSIDERATIONS

A. MISSION SEQUENCE

Before going into a brief explanation of the mission sequence depicted in Figure 9, let us consider the premises on which the mission is structured. First, the mission sequence is for a preliminary reference mission only; consequently, the operations which will be discussed can change as a function of the actual mission. Since no assignment to a carrier vehicle has yet been made, the experiment carrier (bus) configuration, trajectory, and propellant requirements cannot be completely defined. All experimental packages are ejected at perigee, and once the bus is stabilized, the only required maneuvers are in yaw. This simplifies the guidance and control package. For the preliminary reference mission, the S-IVB is assumed to be placed into a 448 km (240 n. mi.) circular, direct injection orbit, at an inclination of 28.9 degrees. The sequence shown in Figure 8 is a series of maneuvers and engine firings required to place the full complement of experiments into their respective orbits. Point 1 of the sequence is the orbital insertion of the S-IVB, and at point 2 bus separation is accomplished through the instrument unit. At next acquisition by a Satellite Tracking and Data Acquisition Network (STADAN) station, the bus systems are activated, the bus is stabilized in pitch and yaw, and the bus rolls (point 3) until the horizon sensor locks on. At a predetermined point in the third orbit the central sequence is updated for the first burn. First burn occurs (point 4), dropping the bus out of the parking orbit, to a 160 km perigee. At the first pass through the 160 km perigee (point

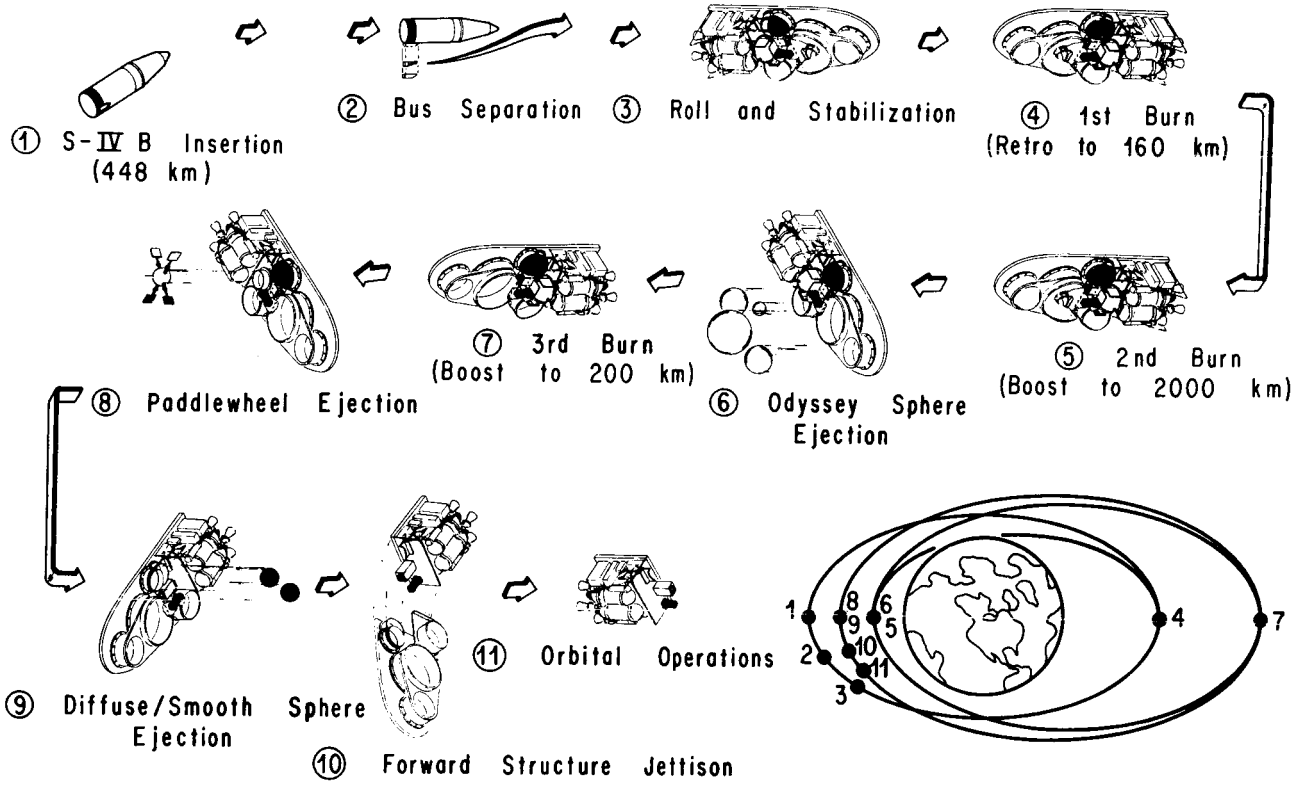

FIGURE 9. MISSION SEQUENCE

5), the second burn occurs which boosts the bus to a 2000 km apogee. At the second 160 km perigee (point 6) the passive spheres are released and ejected from the bus. The Smithsonian Astrophysical Observatory at this time assumes tracking responsibility for the spheres. Third burn occurs at the second 2000 km apogee (point 7) and boosts the bus to a 200 km perigee. At the first 200 km perigee (point 8), the paddlewheel is ejected with a ΔV of approximately 15 ft/sec. Preselected STADAN stations assume tracking responsibility for the paddlewheel. At the second 200 km perigee (point 9), the diffuse and smooth spheres are ejected. This effectively places the paddlewheel and the diffuse and smooth spheres in a 200 by 2000 km orbit. Following the diffuse sphere ejection the bus forward structure is jettisoned (point 10) in preparation for the on-board experiment. At this time (point 11), the recording and transmitting of experimental data and bus subsystems status data are initiated.

B. TRACKING AND DATA ACQUISITION

The ODYSSEY bus would be controlled through the STADAN which is operated by Goddard Space Flight Center. During the satellite pass over a STADAN station, azimuth and elevation data are recorded and punched on tape in teletype code, and then time-labeled and transmitted to Goddard for orbital calculations. Data received from the bus to ground station telemetry link are processed as required and transmitted to Goddard in a digital format. Inasmuch as real time information is required to determine burn time, attitude changes, etc., before commands can be generated by Goddard, the real time bus data rate will be compatible with the ground link telemetry system. Commands are generated at Goddard and sent over the ground link telemetry system to the ground stations where they are recorded on punched tape. At the next pass of the bus over the ground station, the prepared command sequence is transmitted up link to the bus. Command of the bus is required from insertion of the S-IVB to insertion of the bus into its final orbit (approximately 12 hours).

The Smithsonian Astrophysical Observatory Network (SAO) employs a system of Baker-Nunn

cameras to determine the declination and right ascension of the passive spheres. To fix the point in space, the satellite must be photographed against a background of stars. This requires that the satellite be in sunlight while the station is in earth shadow. SAO will continue to track the satellites until reentry, which is estimated to about 90 days for the passive spheres in a 160 km x 2000 km orbit.

During the insertion phase of the experiments, data handling in real time is required. The bus must be tracked, and its trajectory predicted. Approximately 3 1/2 to 4 orbits are provided in the mission plan for this function. During this time, STADAN will track the bus and transmit azimuth and elevation data to Goddard, where the trajectory will be predicted. Once the bus orbit has been determined, the command sequences must be completed by determining the points in time at which the sequences must be initiated and the ΔV's which are required to attain the proper elliptical orbits. Following the insertion phase of the bus, the data collected on the paddlewheel (STADAN) and the passive spheres (SAO) will be required for analysis by MSFC. Such data can be relayed through Goddard by the usual mailing of data tapes.

C. TELEMETRY

The ODYSSEY bus telemetry subsystem consists of the following items:

(1) Beacon

(2) Command receiver

(3) Command decoder

(4) Central computer and sequencer

(5) Central timer

(6) Digital encoder

(7) Transmitter

(8) Diplexer

(9) Recorder.

The beacon is a low-power transmitter which sends out a continuous tone. The frequency of this tone is designated by Goddard, but will be in the region of 136 megacycles per second. A beacon is required for satellite tracking by the ground stations. At a particular ground station, the acquisition radar scans the sky, searching for the satellite. The radar is tuned to pick up only the satellite whose beacon transmits at 136 MHz. As the satellite comes into range of a ground station, the acquisition radar, which has been searching the sky, will "see" the satellite. Once this happens, the radar antenna will point directly at the satellite and lock on. Once acquired, data can be transmitted or received from the bus.

The command receiver is a radio receiver tuned to a frequency designated by Goddard (approximately 148 MHz). The receiver is designed to pick up the signal transmitted by the ground station and change the signals to a series of pulses.

The command decoder is switching and logic network. Its function is to accept the pulses from the command receiver, close the switches as commanded in the signal, and perform the mission operations. Examples of these operations are "turn on the transmitter," "fire the engines," or "blow the aerodynamic shroud."

The central computer and sequencer function as a computer. It has built-in "programs" which are performed on ground command. It has the capability of storing commands such as ΔV and time so that the bus can perform some operation at a predetermined point even when the bus is not within radar visibility of ground station.

The central timer performs the functions of a clock, providing the central computer and sequencer with the time so that when some predetermined time for some function arrives, the sequence is started.

The digital encoder is a set of networks which change the bus system data into a series of pulses which can then be transmitted to the ground station. For example, an engine may have a thermocouple attached which indicates a certain temperature. The encoder will accept the signal whose magnitude represents the temperature and change it to a series of pulses. Since STADAN transmits and receives in pulses, all communication to and from the bus must be changed to pulse codes.

The telemetry transmitter is another transmitter on board the bus. Its function is to transmit the bus system status data which have been changed to a standard form (pulse coded) for STADAN to interpret. Since the beacon and transmitter have similar circuits, these two units are sometimes built into one unit. This is similar to an AM/FM radio where the one unit does two different jobs, but uses some of the same parts for both jobs. The transmitter does not operate until commanded by the ground station. When the transmitter is on, the beacon is off. The beacon is on at all other times.

The diplexer is a switch which allows one antenna to be used to both transmit and receive data. The command receiver is normally switched to the antenna so that it can hear commands. The switch closes the other way when the transmitter is transmitting.

The function of the recorder would be to store all data gathered while not over a ground station (in pulse format) and then transmit such data when ground station commands the recorder to dump the data.

D. EXPERIMENT CARRIER DESIGN

1. Configuration. In the initial examination, three areas on the S-IVB stage were considered for installation of the ODYSSEY experiment:

(1) In the vicinity of the ATM experiment.

(2) In the nose cone of the S-IVB.

(3) An external pod attached to the S-IVB aft skirt.

Further study showed that the space around the ATM was too congested to install the ODYSSEY experiments, and that the nose cone structure with the ODYSSEY experiments appeared to be of questionable structural integrity. Therefore, these two approaches were set aside, and a conceptual configuration for an externally mounted pod was developed as shown in Figure 10. Figure 11 shows some detail of the pod external mount configuration on the Saturn IB launch vehicle. The pod is compared in size to both the

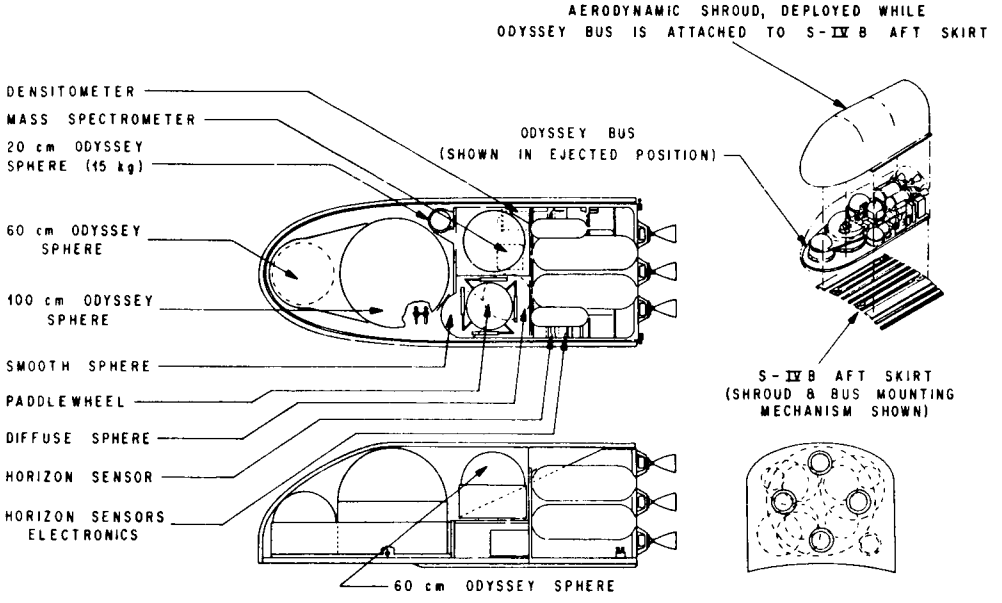

FIGURE 10. ODYSSEY BUS CONFIGURATION

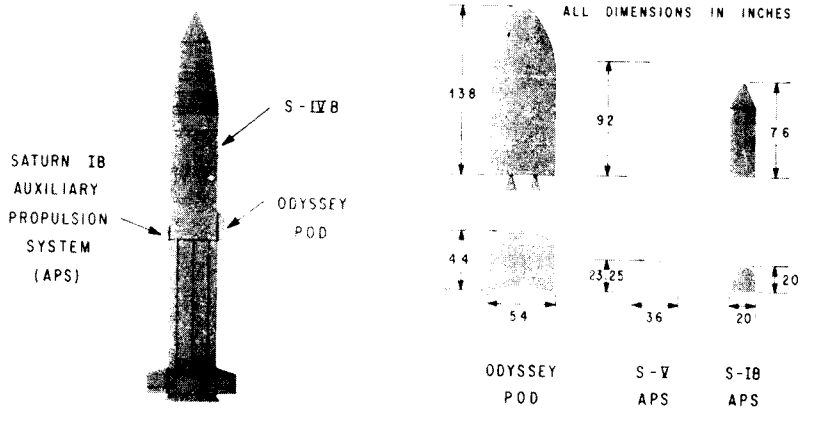

FIGURE 11. POD COMPARISON STUDY

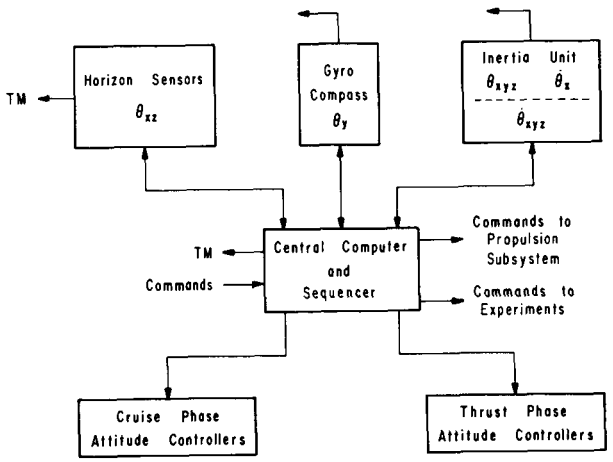

FIGURE 12. STABILIZATION AND CONTROL SUBSYSTEM

the power, weight, and volume requirements are not seriously affected and the accuracy of the control is superior to that possible using a timing system. Preliminary specifications are as follows:

Range 0 - 1500 ft/sec

Accuracy - ± 1 ft/sec or better

Output - Digital

Acceleration during operation - Maximum - 0.75 g
Nominal - 0.5 g

Life - maximum of 4 operations during a period of 12 hr

Power, weight, size - minimum.

The ODYSSEY bus is to be stabilized about the local vertical. To do this, horizon sensors are to be employed to sense the local vertical. Their signal will then be used to control the bus roll and pitch attitude. The sensors are to have sufficient dynamic range to be used during orbital changes. Preliminary specifications are as follows:

Two axes

Linear range ≈ 4°

Orbital parameters - perigee altitude 160-200 km
apogee altitude 1600-2000 km

Accuracy ≈ 0.5° or better

Life - 70-80 hr

Power, weight and size - minimum.

An internal reference unit will be required to perform three functions during the mission. First, the unit must be capable of sensing relatively high rate buildup during separation from the mother ship and controlling the reaction control system to reduce these rates to a level where the horizon sensors and gyro compass can stabilize the vehicle. The second function which the internal reference unit is to perform is to accept rate commands from the ground or the computer to yaw the bus for pointing the experiment ejection devices and to yaw the bus 180° after a retro fire. The third function is to replace the gyro compass as the yaw axis sensing element during main propulsion system burns and possibly during experiment ejection. Preliminary specifications are as follows:

Attitude reference

Life - maximum of 4 operational periods of maximum of 5 min each

Drift Rate - ≈ 2°/min or better

Rate Sensing

This mode is to be used to reduce high rates incurred during separation and similar maneuvers to less than 0.03°/sec

Life - maximum of 2 operational periods of less than 2 min each within 12 hr

Max Rate - 5°/sec

Linear Range - ± 0.5°/sec

Fixed Rate - to command thrusting attitude

This mode is to be used to command the vehicle to rotate to the desired heading by commanding a known rate for a given period of time. Anticipated command rate -0.25°/sec.

Life - maximum of 12 hr

Power, weight, size - minimum

Three-axis control rate, single-axis attitude reference.

A gyro compass is to be used to determine the vehicle heading with respect to the orbit plane. A gyro compass performs this task by detecting the misaligned orbit rate component. This indication is then used to stabilize the vehicle yaw axis.

The performance of a gyro compass is dependent upon vehicle motion, the noise content of the vertical reference, and, to a lesser degree, gyro drift. The first two error sources may be partly compensated for by filtering or by isolation of the gyro from the vehicle motions. Because of the relatively loose requirements of the ODYSSEY application, a filtering system may be sufficient.

Saturn V and IB auxiliary propulsion systems which are attached externally to the aft S-IVB skirt. Small scale wind tunnel tests were conducted in speed ranges corresponding to regions of maximum dynamic pressure to investigate possible pod effects on launch vehicle aerodynamics. Preliminary results indicate no adverse effects with the proper aerodynamic shroud configuration.

Mass, center of gravity, and moment of inertia of the preliminary ODYSSEY pod including experiments were determined and are summarized in Table III.

TABLE III. MASS, CENTER OF GRAVITY, AND MOMENTS OF INERTIA

Mass			
o Initial	4390 lbm		
o Terminal	815 lbm		
	Coordinates (in.)		
Center of Gravity	X	Y	Z
o Initial	82	+4	15
o Terminal	49	0	11
	Axes (slug-ft^2)		
Moment of Inertia	Roll	Pitch	Yaw
o Initial	183	1078	1135
o Terminal	39	65	89

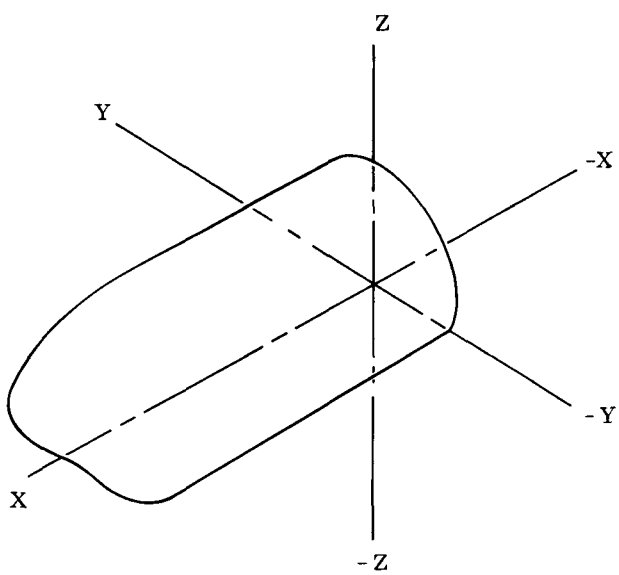

2. Propulsion. The hardware now being considered to provide energy for orbit transfer is the Thiokol C-1 engine. Four of these engines are used in the clustered configuration shown in Figure 10. The 100 lb thrust engine has a nozzle expansion ratio of 60:1 and employs N_2O_4/50-50 and N_2O_4 MMH propellants at a mixture ratio (oxidant to fuel weight ratio) of 1.6. Vacuum specific impulse is 301 seconds with a minimum impulse bit of 0.4 lb/sec. The engine combustion chamber is liquid-cooled, while the nozzle is radiatively cooled during burn.

The Saturn V/S-IVB auxiliary propulsion system provides capacities that closely match the ODYSSEY propulsion system requirements. Two sets of fuel and oxidizer tanks, along with pressurization tankage, are used in the preliminary configuration shown in Figure 9. Each set contains about 330 pounds of propellants for a total of 660 pounds, which exceeds ODYSSEY first-cut requirements of 558 pounds for transfer to the required orbit configuration.

3. Control and Stabilization. The ODYSSEY mission has the following control and stabilization requirements:

(1) Hold attitude ± 3° absolute with respect to the velocity vector during cruise phase.

(2) Hold attitude ± 0.5 absolute with respect to required thrust vector during orbital maneuvers. This limit sets errors of about 2 km in perigee and 40 km in apogee which is within requirements.

(3) Hold ΔV errors during thrust maneuvers to less than 0.3 m/sec which provides about 2-km errors in both apogee and perigee.

(4) Hold firing time errors to less than ± 1 min, which provides a 1 km perigee error and a 24 km apogee error.

A schematic of the control and stabilization subsystem for the ODYSSEY bus vehicle is shown in Figure 12. To insure that the required orbit changes are within tolerance, it is required that the velocity change imparted by the propulsion unit is held to some predetermined value. There are two ways of accomplishing this. The least complicated method is to time the duration of the propulsion unit burn. A more complex method requires a velocity meter, which is used to measure the change in velocity and terminate the engine burn at the required velocity. The ODYSSEY bus is to use the more complex system because of the uncertainty of the engine specific impulse due to a pulsed burn. Although the system is more complex,

The gyro compass must be capable of pointing the bus along the velocity vector and 180° to the velocity vector. Preliminary specifications are as follows:

Vehicle stability - will limit cycle ± 3° with a period of ≈ 250 sec

Linear range - ± 4°

Accuracy - establish orbital plane ± 1° or better

Lifetime - 70-80 hr

Power - minimum

Weight and size - minimum.

The possibility of contamination of the experiments by the reaction control thruster plume limits the selection of the propellant to a gas which will not be collected by the experiments. To insure that the gas will not be collected, it must have a boiling point below 20°K. Helium satisfies this requirement and has a reasonable I_{sp} (168 sec). Alternates to the helium system include a nitrogen and helium combination using nitrogen for yaw and pitch control firing aft and a helium roll control thruster set. The requirement for aft firing limits the moment arm without employing a foldout device, and the use of the dual gas imposes an additional weight penalty. The helium system has the disadvantage of requiring rather large tanks in proportion to the mass to be stored; however, this is in part offset by the increased moment arms allowed and higher specific impulse compared to nitrogen. By placing the yaw and pitch thrusters so that they fire radially or tangentially at the aft section of the bus the change in lever arms due to the aft movement of the bus center of gravity during the mission partly offsets the decreases in the yaw and pitch moments of inertia.

REFERENCES

1. Comparison of Air Densities Obtained from Orbital Decay and Instruments. Contained in Royal Society Discussion Meeting on Orbital Analysis. Royal Aircraft Establishment, Farnborough, England, October 17-18, 1966.

2. Observations of Resonance Between Satellites in a High-Drag Environment and High-Order Tesseral Terms of the Geopotential Expansion. Aerospace Report No. TR-669(6104-02)-1, July 1966.

3. Harris, I.; and Priester, W.: Institute for Space Studies, Goddard Space Flight Center, New York, 27, New York, August 25, 1964.

4. Schaaf, S. A.; and Chambre, P. L.: Flow of Rarefied Gases. High Speed Aerodynamics and Jet Propulsion, vol. 4, Part G, Section H. 8, Princeton Univ. Press, Princeton, New Jersey, 1958.

5. Maslach, G. J.; Willis, D. R.; Tang, S.; and Ko, D.: Recent Experimental and Theoretical Extensions of Nearly Free Molecular Flow. Fourth International Symposium on Rarefied Gas Dynamics, Toronto, Canada, 1964.

6. Heller, G.: Thermal Environment and Control of Space Vehicles. Handbook of Astronautical Engineering. H. H. Koelle, ed., McGraw Hill, New York, 1961.

7. Jacchia, L. C.: Static Diffusion Models of the Upper Atmosphere with Empirical Temperature Profiles. Smithsonian Contr. Astrophys., vol. 8, no. 8, 1965, pp. 215-257.

8. Sterne, T. E.: An Atmospheric Model, and Some Remarks on the Inference of Density from the Orbit of a Close Earth Satellite. Astron. Journ., vol. 63, no. 3, 1958, pp. 81-87.

9. Jacchia, L. G.: Variations in the Earth's Upper Atmosphere as Revealed by Satellite Drag. Rev. Mod. Phys., vol. 35, 1963, pp. 973-991.

10. Jacchia, L. G.; and Slowey, J.: Formulae and Tables for the Computation of Lifetimes of Artificial Satellites. Smithsonian Astrophys. Obs. Spec. Rep. No. 135, 1963, 23 pp.

11. Lundquist, C. A.: Procedures for a Near-Free-Molecule-Flow Aerodynamics Experiment. Presented at Amer. Chem. Soc. - Amer. Phys. Soc. Joint Section Meeting, March 17-18, Hartford, Connecticut. (Abstract in Bull. Amer. Phys. Soc., 1967, in press.)

12. Cook, G. E.: Satellite Drag Coefficients. Planet. Space Sci., vol. 13, 1965, pp. 929-946.

13. Sherman, F. S.; Willis, D. R.; and Maslach, G. J.: Nearly Free Molecular Flow, A Comparison of Theory and Experiment. Applied Mechanics, Proceedings of the Eleventh International Congress of Applied Mechanics, ed. by H. Görtler, Munich, 1964, pp. 871-877.

14. Jacobs, R. L.: Atmospheric Density Derived from the Drag of Eleven Low-Altitude Satellites. Journ. Geophys. Res., vol. 72, 1967, pp. 1571-1581.

15. Lam, Louisa S.; Mendes, Geraldine M.; and Lundquist, Charles A.: Design of a Satellite Experiment for Atmospheric Density and Near-Free-Molecular-Flow Aerodynamics. Smithsonian Institution Astrophysical Observatory, Cambridge, Mass., SAO special report no. 241, June 5, 1967.

16. Moe, Kenneth: The Calculations of Drag Coefficients from the Spin and Orbital Decays of Explorer VI. Presented at Fifth Symposium on Rarefied Gas Dynamics, Oxford, England, 1966.

17. Schamberg, R.: Analytic Representation of Surface Interaction for Free Molecule Flow with Application to Drag of Various Bodies. Project Rand, Aerodynamics of the Upper Atmosphere, R-339, 1959.

18. Alcalay, J.; and Knuth, E.: To be published in Proc. 5th International Conf. Rar. Gas. Dynamics, Oxford, England, 1966.

19. Maxwell, J. C.: Scientific Papers, vol. 21, 1951, p. 708.

20. Wallace, D. A.; Rogers, K. W.; Wainwright, J. B.; and Chuan, R. L.: An Orbiting Density Measuring Instrument. NASA TM X-53468, May 26, 1966.

V. SELENOGRAPHY

A POSSIBLE GEOLOGICAL-GEOPHYSICAL MISSION IN THE ALPHONSUS AREA OF THE MOON USING FLYING AND SURFACE VEHICLES

By

J. T. Stanley* , W. C. Lucas* and O. H. Vaughan, Jr.ψ

I. INTRODUCTION

This paper discusses a possible concept developed by the authors based on considerable study by various contractors, NASA Headquarters, MSFC and U. S. Geological Survey over the past few years.

The conceptual lunar mission considered here is a 14-day effort by two astronauts to investigate an area of interest about a landing site in the Alphonsus area of the moon. While Alphonsus has no official status as a landing site, it is an excellent area for mission analysis because of its diversity of geologic features and, with Ranger IX photographs, the relative abundance of details to support such analyses at this point in time. As shown in Figure 1, Alphonsus lies within the central highlands area and is one of a group of four large craters. It has a diameter of slightly more than 100 km (see Fig. 2), and rugged annular walls that rise more than 3000 meters above the relatively flat crater floor.

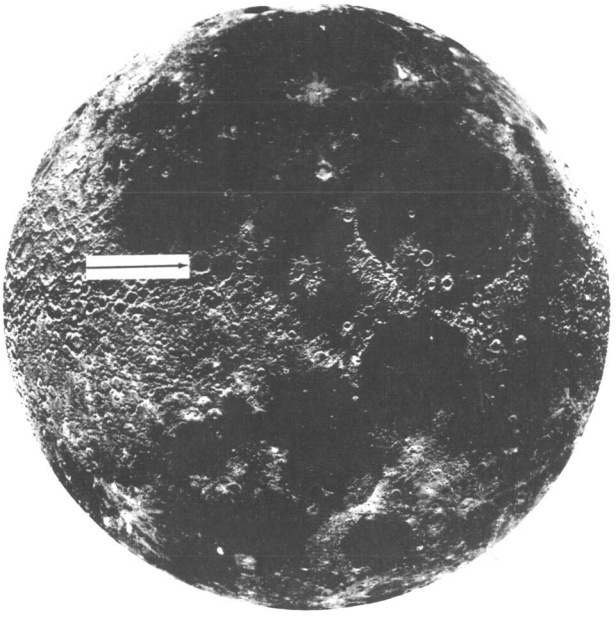

FIGURE 1. LUNAR INDEX MAP (Photo Courtesy Lick Observatory)

The general features that make Alphonsus interesting are the central peak, the large rilles, the dark halo crater on Rima Alphonsus I, the crater wall, and the variety of craters and materials on the floor.

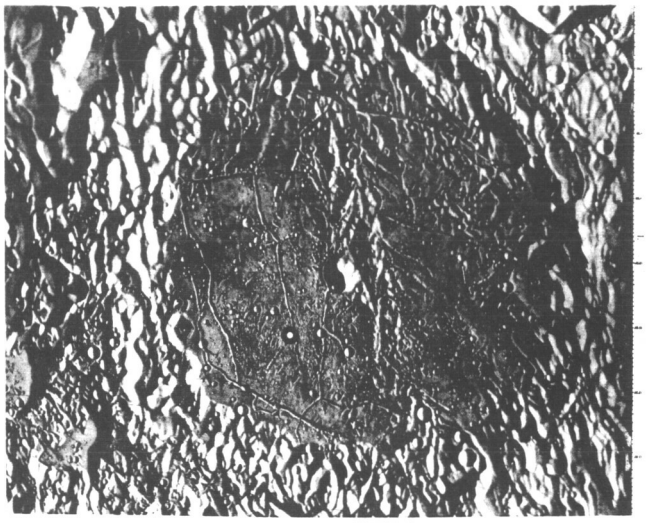

FIGURE 2. ALPHONSUS (From RLC 14)

II. OBJECTIVES

The general objectives of the mission are to determine the geological and geophysical nature of the area and to emplace four scientific stations, one at the landing site, and one at each of three widely separated points.

The geologic aspect of the mission will be concerned with determining contacts between major stratigraphic units, sampling both commonly occurring materials and erratic fragments, and describing

* Northrop Space Laboratories, Huntsville, Alabama.

ψ NASA, MSFC, Huntsville, Alabama

structures and geomorphic features. As well as investigating those areas of major importance such as the central peak and the area along Rima Alphonsus I, as many different and spatially distributed areas should be investigated as possible within vehicle limits. In addition to the surface surveys, a 30-meter hole will be drilled in strata not readily accessible on the surface.

The objectives of a geophysical nature are to obtain representative magnetic and gravity coverage throughout the area, and to obtain seismic coverage in selected locations.

Such objectives are not expected to be fully achieved within the time and mobility constraints imposed by lunar missions. However, it is reasonable to expect that judicious selection of investigation sites will yield critical data and permit extrapolation into other areas.

III. SUPPORTING EQUIPMENT

The mission centers around the Lunar Module (Fig. 3), which is used as a lunar shelter and base of operation supported by a roving vehicle, a flying vehicle, and scientific equipment.

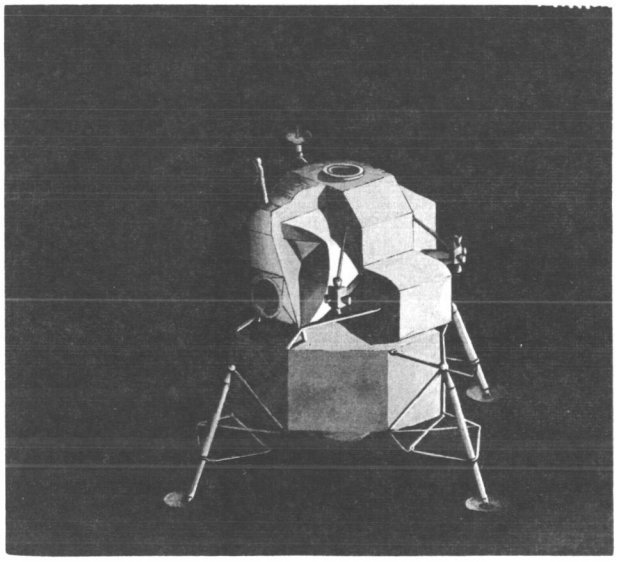

FIGURE 3. A CONCEPT OF THE LUNAR MODULE

The roving vehicle (Fig. 4) can be driven much like a jeep to carry an astronaut and his equipment on traverses of the area within an 8 km radius about the lunar shelter. A remote control capability is also provided in this analysis so that the vehicle can be remotely driven to more distant locations.

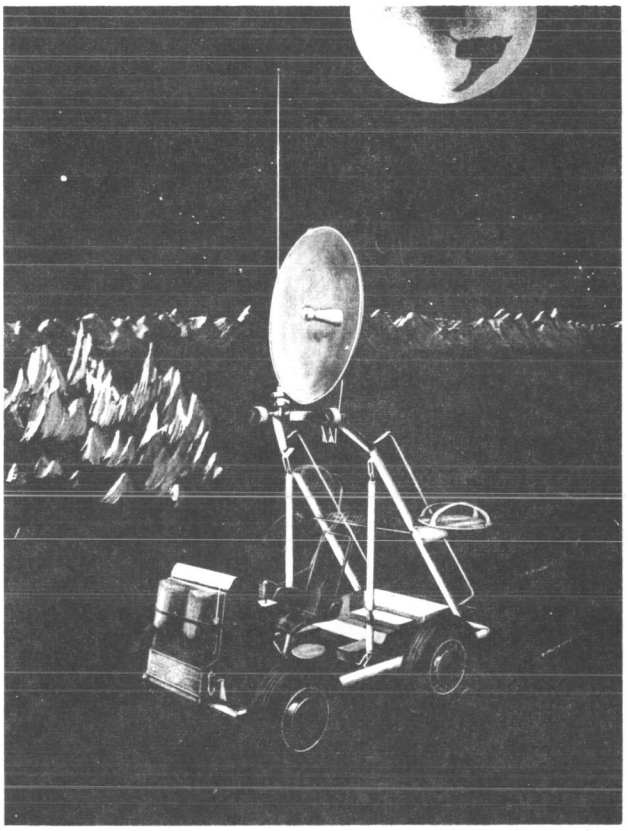

FIGURE 4. A CONCEPT OF THE LUNAR ROVING VEHICLE

The flying vehicle (Fig. 5) can be flown to areas within a 20 km radius about the lunar shelter. Although the vehicle furnishes a rapid method of reconnoitering large areas of the lunar surface, it has a limited cargo capability.

Scientific equipment consists of laboratory equipment, a 30-meter drill, a hand-held drill, a lunar surveying staff, geophysical instruments, and four scientific stations.

Table I summarizes the mission support equipment and their weights.

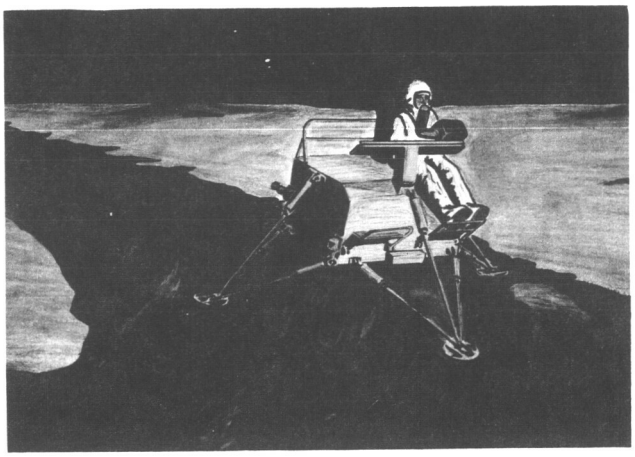

FIGURE 5. A CONCEPT OF THE LUNAR FLYING VEHICLE

TABLE I. MISSION PAYLOAD

EQUIPMENT	Kg	LBM
Flying Vehicle (Fully Fueled)	492.6	1086
Roving Vehicle	495.7	1093
Scientific Equipment		
Basic	149.7	330
Central Scientific Station	136.1	300
Satellite Scientific Stations	197.3	435
Basic Total	1471.4	3244
Additional Fuel for Flying Vehicle	446.3	984
Total	1917.7	4228

IV. GUIDELINES AND CONSTRAINTS

To effectively plan a geologic mission, it is necessary to establish guidelines and constraints based on the capabilities of the astronaut and the support equipment. The guidelines and constraints for this mission are as follows:

1. Limit the astronaut to 6 hours on the lunar surface during any one period.

2. Alternate astronaut assignments on the lunar surface and use only one astronaut on the surface at any time.

3. Stay within 8 km radius of the lunar shelter with the manned roving vehicle.

4. A roving vehicle remote control capability to permit unmanned operation to 20 km radius about the lunar shelter.

5. Stay within 20 km radius of the lunar shelter with the flying vehicle.

6. Stay within 3 km radius of the flying vehicle with the manned roving vehicle at remote sites.

7. Carry all scientific packages and extra life support system on the roving vehicle.

V. LANDING SITE CRITERIA

Considering the general objectives, the following criteria were used in selecting a landing site within Alphonsus.

1. Central location among the prominent relief features to permit some landing uncertainty.

2. Relatively smooth floor material with minimum slopes.

3. Accessibility to major features with mobility aids provided.

4. Permit a 30-meter core hole at the landing site, which would contribute to the overall geologic interpretation.

5. Make maximum use of geological data available at this point in time.

Thus, a landing site was selected as shown in Figure 2.

VI. MISSION PROFILE

Considering now the general mission objectives, the support equipment available, and constraints imposed by the lunar environment, the mission is planned with three main types of operations:

1. Investigations and scientific station emplacement involving use of both the roving and the flying vehicle.

2. Investigations involving use of the roving vehicle manned by an astronaut.

3. Drilling and laboratory activities at the lunar shelter.

The mission is developed around 12 surface excursions for geological-geophysical investigations and for the emplacement of scientific stations.

As shown in Figure 6, four of the surface excursions are devoted to use of both vehicles within a 20 km radius about the lunar shelter. The first excursion is to the dark halo crater marked by the large T on Rima Alphonsus I. The roving vehicle is driven remotely to the site, carrying scientific equipment and a life support system. A continuous magnetic survey is made, and periodic stops for gravity measurements are made along the way. An astronaut flies to the site in the flying vehicle. His time from shelter to site is about 12 minutes. The astronaut mans the roving vehicle and travels to points of interest within a 3 km radius about the flying vehicle, as shown in Figure 7. This traverse includes a look at the dark halo material surrounding the crater on Rima Alphonsus I, Rima Alphonsus I itself, a possible fumarole, a possible impact crater, and Alphonsus Crater wall material.

Investigations would include continuous magnetic measurements, periodic gravity measurements, and stops for detailed geological examinations. For this

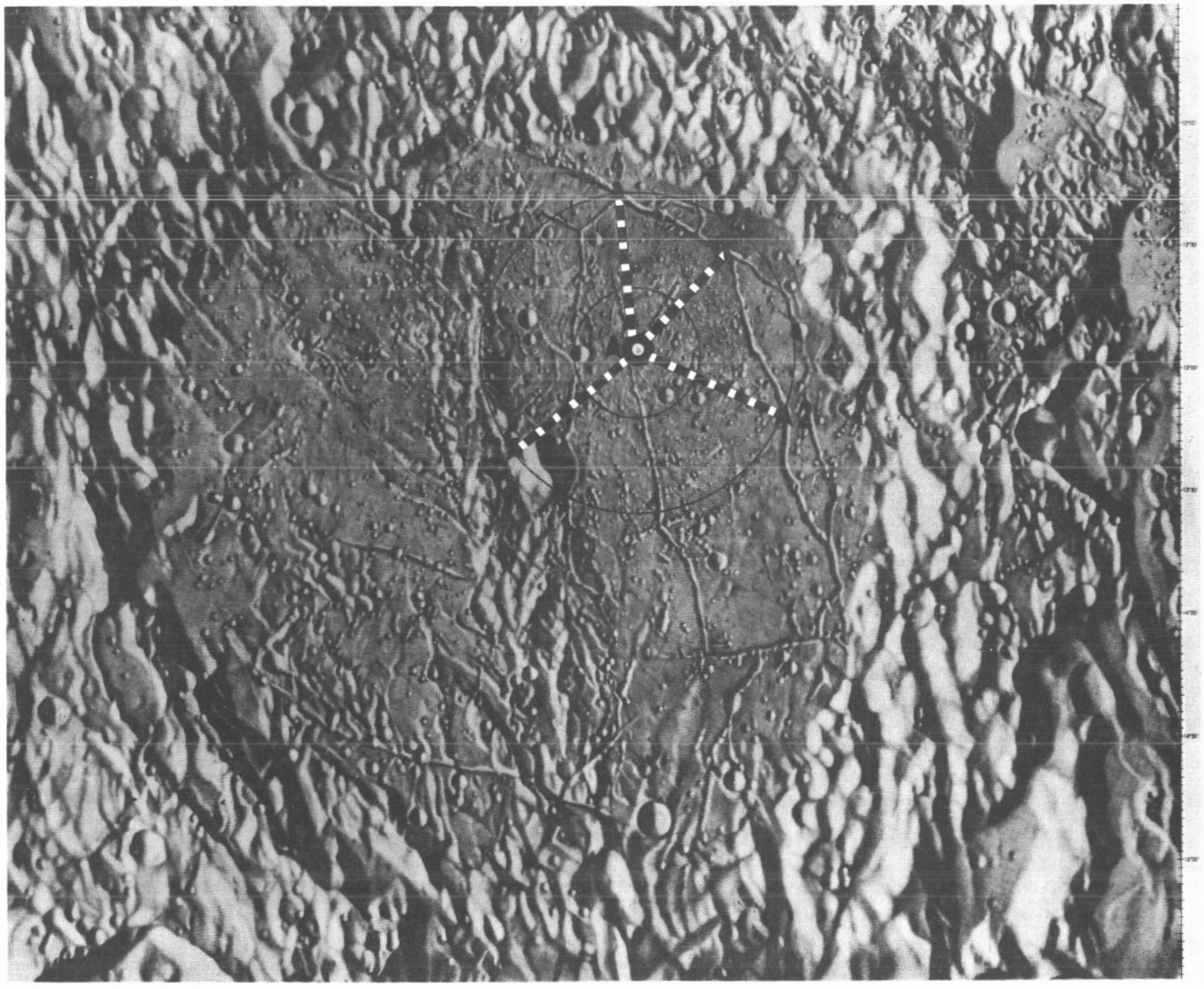

FIGURE 6. MAP OF ALPHONSUS SHOWING THE LANDING SITE, SCIENTIFIC STATIONS, AND FLYING VEHICLE FLIGHT PATHS (From RLC 13)

purpose the astronaut would be supported by a lunar surveying staff (Fig. 8) which would facilitate the usual strike and dip measurements, take stereoscopic photographs, transmit a television picture of his observations back to earth in real time, and in conjunction with other equipment, note the position and elevation of his observed points relative to the roving vehicle. Upon completion of the traverse, the

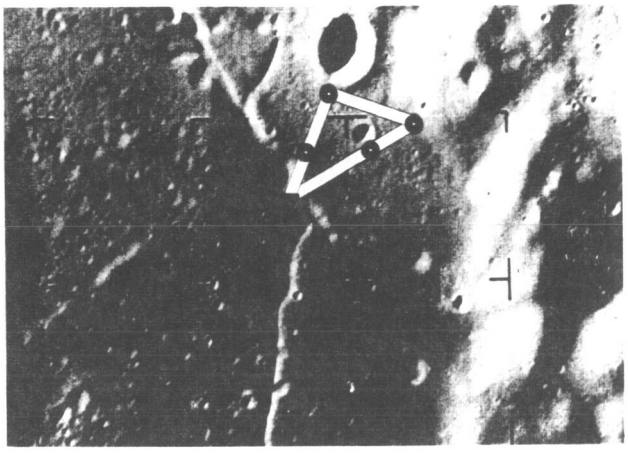

FIGURE 7. SHORT GEOLOGICAL-GEOPHYSICAL TRAVERSE AT RIMA ALPHONSUS I
(Ranger 9 Photograph)

astronaut would fly back to the lunar shelter; the roving vehicle would be returned by remote control.

The next three excursions (Fig. 6) are primarily for the emplacement of scientific stations, but include another look at Rima Alphonsus I and a look at the central peak. The six-hour period allotted permits setting up the scientific stations (Fig. 9), drilling a 3-meter hole for emplacing a thermal probe (Fig. 10), and short traverse to points of geologic interest.

The scientific stations are self-contained units which will operate automatically over a long period of time. It is anticipated that they will make seismic and tidal measurements and provide data related to the solar plasma and the moon's atmosphere.

Six traverses are planned for investigations closer to the lunar shelter, as shown in Figure 11. These involve use of the roving vehicle as mentioned earlier, including continuous magnetic measurements, and periodic stops for gravity measurements and geologic investigations. Traverse number 6 is considered typical of this type. The main points of interest along

FIGURE 8. A CONCEPT OF THE LUNAR SURVEYING STAFF

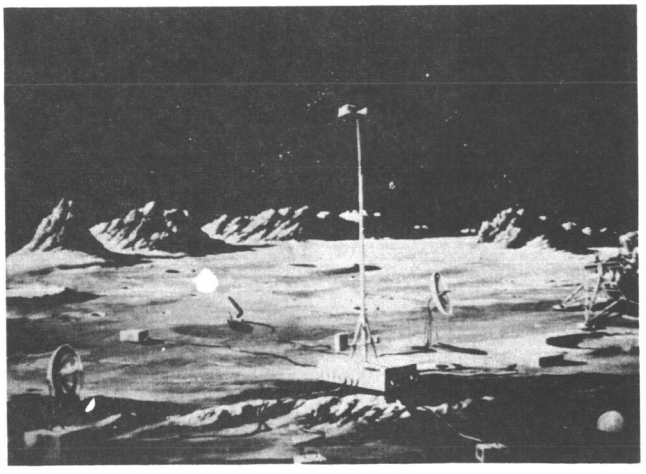

FIGURE 9. A CONCEPT OF THE SCIENTIFIC STATION

FIGURE 10. A CONCEPT OF THE THREE METER DRILL

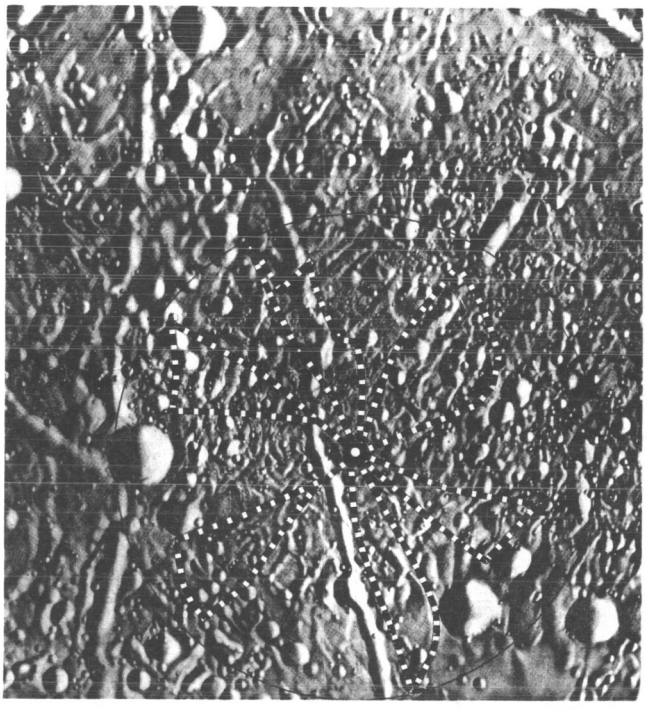

FIGURE 11. GEOLOGICAL-GEOPHYSICAL TRAVERSES USING A MANNED ROVING VEHICLE (From RLC 15)

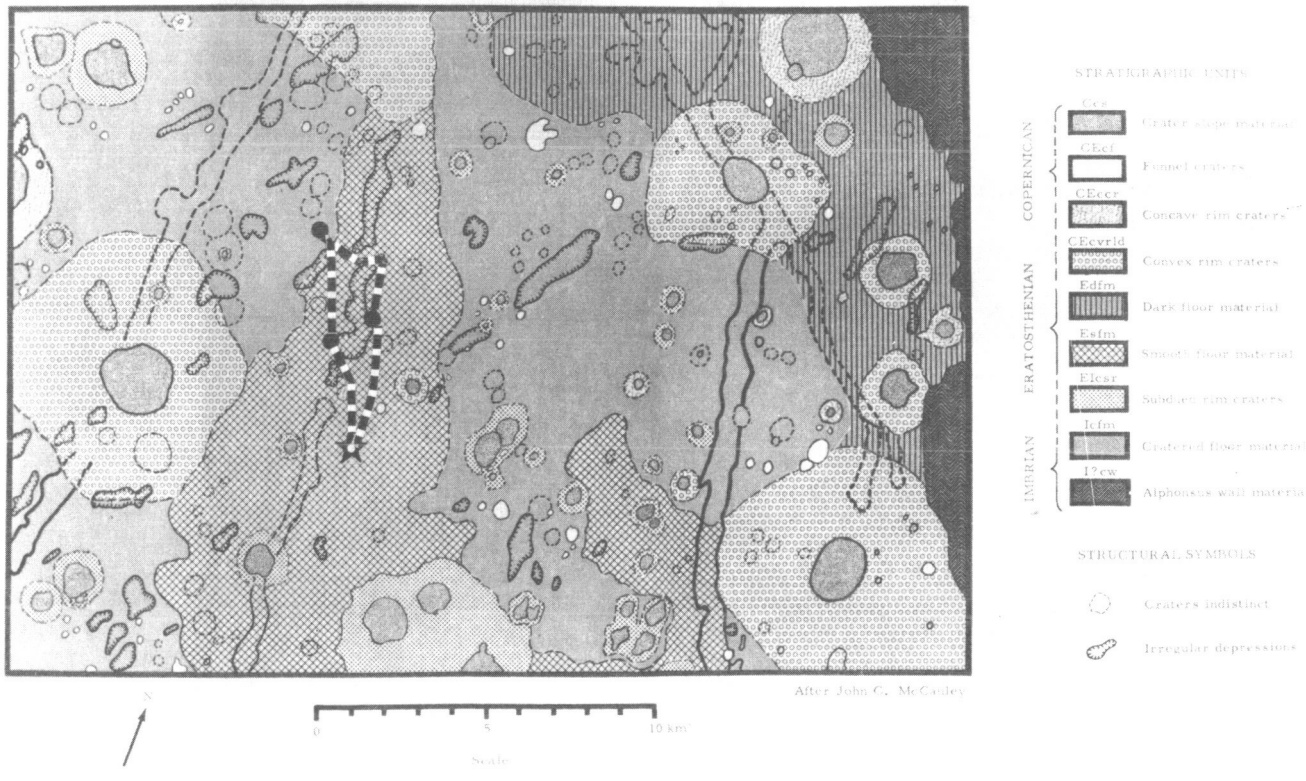

FIGURE 12. GEOLOGIC MAP OF PART OF ALPHONSUS

the way are shown in Figure 12. These include the impact point of Ranger IX, a contact between different types of material, and the large rille.

Two additional traverses are planned for seismic lines. These would be laid out with the roving vehicle within the 8 km radius. However, no attempt is made here to show how these traverses could best be laid out.

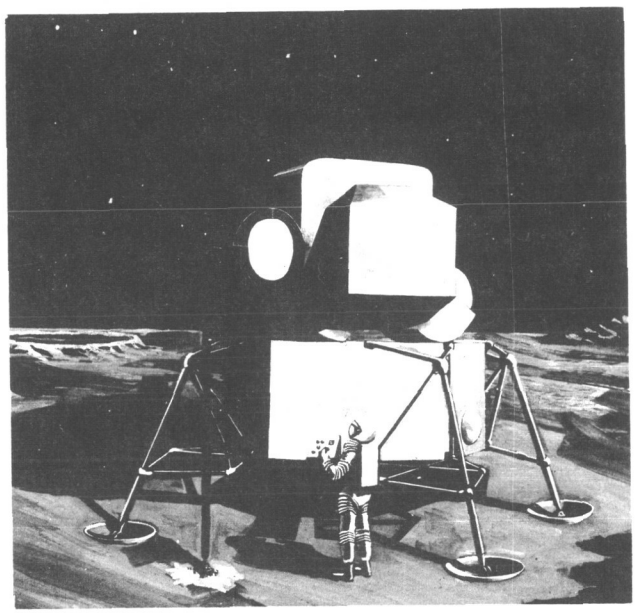

FIGURE 13. A CONCEPT OF THE THIRTY METER DRILL

Meanwhile, at the lunar shelter (Fig. 13), a 30-meter core hole has been drilled, preliminary petrographic analyses made of all samples, and samples prepared for the return trip to earth.

From the viewpoint of the whole mission, the time is budgeted as shown in Table II.

TABLE II. MISSION TIME BUDGET

Activity	Hours	Percent
Checkout and Equipment Handling	31.6	4.7
Travel Time in the Roving Vehicle	35.6	5.3
Travel Time in the Flying Vehicle	1.6	0.2
Scientific Surface Activity	68.8	10.2
Scientific Laboratory Activity	139.8	20.8
Communications & Planning	48.0	7.1
Airlock Monitoring	74.6	11.2
Rest, Meals and Personal Care	272.0	40.5
Total	672.0	100.0

From the foregoing brief description, it can be seen that achieving the greatest scientific return with the time and equipment available in an alien environment poses many engineering problems and offers the opportunity for numerous tradeoffs.

VI. SOLAR PHYSICS

CONSTRUCTION OF PROBABILITY ENVELOPES OF FLUX-ENERGY SPECTRUM FOR SOLAR PROTON EVENTS

By

T. S. Dollman and Anne T. Bechtelheimer*

ABSTRACT

Extreme model environmental flux values for solar flare protons are obtained for missions lasting 14 days, 60 days and 200 days. These models are obtained by an autocorrelation of flux data obtained during solar cycle 19. As a result, the data are applicable for missions outside the protection of the earth's magnetic field during the current maximum phase of solar cycle 20 (1967-1972). The various methods used and the final results and their significance are discussed.

I. INTRODUCTION

A method has been developed for calculating the probability of encountering various levels of integrated flux of solar radiation particles. The present analysis deals specifically with proton flux since solar cosmic rays are almost entirely composed of protons, the flux of which is closely associated with solar flare activity.

For extended space travel, there are three elements of space environment radiation which must be considered for crew protection: galactic cosmic rays, solar cosmic rays, and magnetically trapped radiation. Because the dose from solar cosmic rays is a major biological radiation hazard, it is necessary that solar proton events be given special consideration in spacecraft design.

There have been several synthetic models of proton events used in shielding estimates since there is a variance in the energy spectra and intensity of the events. The two models which are widely used in mission studies are the composite solar event model [1] and the D. K. Bailey model [2], the latter of which postulates that the intensity and spectrum are time-dependent. The composite solar event model represents the total of the flux of nearly all of the solar events from 1956 and 1961 and contains a time-integrated flux of about 9×10^9 protons/cm^2 above an energy of 30 Mev. This model was constructed to represent a large event and is twice the size of Bailey's model which, in turn, has an integrated intensity higher than any previous event. Thus, both models are extremely conservative.

* Aerospace Engineers, Space Environment Branch, Aerospace Environment Division, Aero-Astrodynamics Laboratory, MSFC, Huntsville, Alabama.

II. PRESENT TECHNIQUE OF CALCULATING FLUX-ENERGY SPECTRA AND DERIVATION OF PROBABILITY ENVELOPES

Only those integrated fluxes of particles with energies above 30 Mev and above 100 Mev have previously been studied. The main reasons for limiting the studies to these ranges are that (1) even the most lightly shielded vehicles afford protection against particles in the 10 Mev to 30 Mev range and (2) the extrapolation very far beyond 100 Mev might become relatively inaccurate. However, in this paper, the data observed and calculated in the 10 to 30 Mev range, as well as in the 100 to 140 Mev range, will be used so that the energy ranges extend from 10 to 140 Mev. This was done to more accurately estimate the flux-energy spectra of the solar flare percentile models.

In this analysis it is assumed that the distribution of the particles is isotropic, although this generalization might prove faulty during the initial phases of the solar storms. Previous analyses of these data in several authoritative papers have resulted in the establishment of a distribution of characteristic rigidities of these fluxes. However, the present analysis was prepared to provide more detailed information on the indicated probabilities of occurrence of an integrated flux of particles equal to or greater than a given particle flux whose energies equal or exceed a given energy level. This is an approach which does not deal in characteristic rigidities.

Our present method of calculation of flux probabilities is an extension of previous work by Webber [3] at the University of Minnesota. By manipulation of currently available data to their full extent, we obtained flux values at 10, 30, 50, 70, 100, and 140 Mev. With these energy level flux values, we obtained data points for "environmental" models which should be characteristic of the total flare radiation which will occur in the maximum phase of cycle 20.

There are several basic points to our analysis. First, we have assumed that the distribution of solar flares in cycle 20 will be the same as in solar cycle 19. This is probably not a bad assumption because, even though the next cycle may have a completely different overall distribution of its flares, the relative distribution (i.e., flare series) will probably be similar. Second, since the probabilities calculated are not a function of time, the phase of the solar cycle is not considered. Third, our values use only the flare data from January 1, 1956, to December 31, 1961. As a result, we exclude all data for solar cycle minimum, and our values are not representative of the entire solar cycle. We feel that an entirely new model should be used for the solar flare environment during a solar cycle minimum. The merit of using solar flare data from the maximum phase of solar activity is self-evident.

In the first method, the probability of encountering a flare whose flux values were equal to or greater than a specific flare size was determined for each day of a two-thousand-day period. These values were then extended to missions of greater than one day by the binomial expansion technique. These calculations were then taken to represent the probabilities of one encountering one or more flares at the flux intensities under consideration during the time period considered. These values of flux with associated probability were then subjected to a least squares curve fit. It was found that the percent error between the observed and computed flux values was far too large. The flux values were then converted into logarithmic form, from which new least squares curve fits gave relatively small percentage errors. Unfortunately, when the logs were converted into natural numbers, the error was still relatively large, even though improved.

In the next method, total flux for missions with the the same lengths was calculated. From this, the probability that for a given mission length a certain amount of flux would be exceeded was calculated. For a one-day mission, the probability is the number of days a given flux was exceeded divided by the total number of days of observation, 2192. Missions of more than one day were started each day of the period and total flux encountered during the mission length were calculated.

This process was repeated through 2192 days of the data. For each mission length, the probability of occurrence of a specific flux is determined by dividing the total number of missions in which this flux was exceeded by 2192, which is the total number of missions examined. This process was repeated for each energy level under consideration, i.e., 10, 30, 50, 70, 100, and 140 Mev.

The final method was similar to the previous one, but the flux values were sorted to find the total values for each different mission length beginning at day 1 and continuing. There were 2192 missions. The program printed out the total flux that occurred for each mission length and each energy level, dropping all zero sums. The program was then rewritten to print out the total flux encountered and the number of times each occurred. The values of the total flux were arranged in descending order with the number of times each occurred. In the probability and adding process, the probability was found for a certain flux being greater than a given value. From these values of flux versus the number of times of occurrence, the probable flare size was derived. These values were plotted, and assuming log normal distribution, we attempted to determine the statistical distribution. It became immediately apparent that the distribution was not log normal, but skewed toward large flux values. A study is now underway to determine the exact form of this skewed distribution. In the meantime, however, these data will provide a very good estimate of extreme model solar flare flux values. The models presented here hold for the maximum solar activity period, or in the current solar cycle, they hold from 1967-1972.

Between January 1, 1956, and December 31, 1961, there was a total of 29 recorded solar proton events in the 2192-day period with a probability of 0.01323 proton events per day. If a random distribution is assumed, the value $0.01323 = p_1$ may be used to determine the probability of occurrence of one or more flares in a time period lasting n days, p_n. Thus,

$$p_n = 1 - (1 - 0.01323)^n.$$

This analysis considered extraterrestrial missions lasting 14 days, 60 days, and 200 days, to determine the probability model envelopes for the total flux to be encountered during each of these periods. Table I presents these probability values for each of the three mission lengths considered.

TABLE I. PROBABILITY VALUES

p_n	Percent Probability
p_{14}	17
p_{60}	55
p_{200}	93

The distribution of total flux to be encountered per mission length was found by examining the proton flux sums discussed earlier. By autocorrelating these data, the flux distribution was derived with their associated probability limits. Thus, in Figure 1, the 99 percentile model, the 95 percentile model, and the 90 percentile model solar flare spectra are presented for a 14-day mission. The precise meaning of these envelopes are that, if solar proton events are encountered during any 14-day mission, there is a 99 percent, 95 percent, and 90 percent probability that these flux-energy envelopes will not be exceeded.

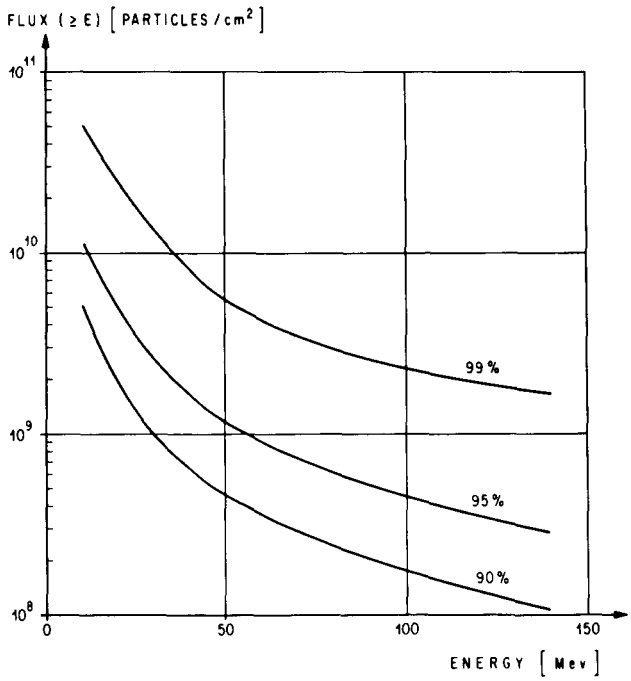

FIGURE 1. ENVIRONMENTAL MODELS FOR THE 99 PERCENT, 95 PERCENT, AND 90 PERCENT PROBABILITY FLUX-ENERGY SPECTRA TO BE ENCOUNTERED ON A 14 DAY EXTRATERRESTRIAL MISSION. THE FACTOR $p_{14} = 0.17$

Figure 2 was derived in the same way for a 60-day mission, and Figure 3 shows the same derivation for a 200-day mission. A comparison of these graphs shows that the spectra are not exceedingly hard for any of the mission profiles. If one closely examines and compares the flux energy spectra diagrams for each mission length, several interesting points become apparent. As mission length increases, the flux energy spectra profiles tend to become softer. That is to say that, whereas at low energy levels the flux values tend to have large separations from one mission to the next, they tend to merge at higher energy levels. This at first appears to be an error in the calculations, but if we re-examine the original solar flare flux energy spectra, we find that most flares have relatively soft spectra. The February 1956 flare spectrum has the most effect on higher energy levels so that the spectra for all mission lengths will reflect this event very strongly. At the lower energy levels, many flares appear which exhibit very large flux values at the 10 Mev level, but at the larger energies, their flux contributions are virtually negligible.

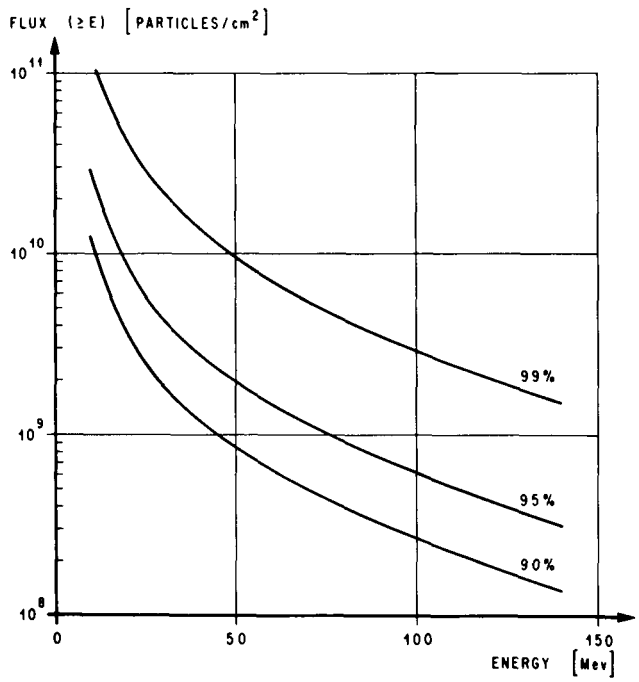

FIGURE 2. ENVIRONMENTAL MODELS FOR THE 99 PERCENT, 95 PERCENT, AND 90 PERCENT PROBABILITY FLUX-ENERGY SPECTRA TO BE ENCOUNTERED ON A 60 DAY EXTRATERRESTRIAL MISSION. THE FACTOR $p_{60} = 0.55$

The percentile graphs do exhibit a family of flux energy spectra curves. This tends to indicate that the approximate curves, fit to the probability graphs, were not too much in error. This method is being refined so that later data should reflect more reasonable models.

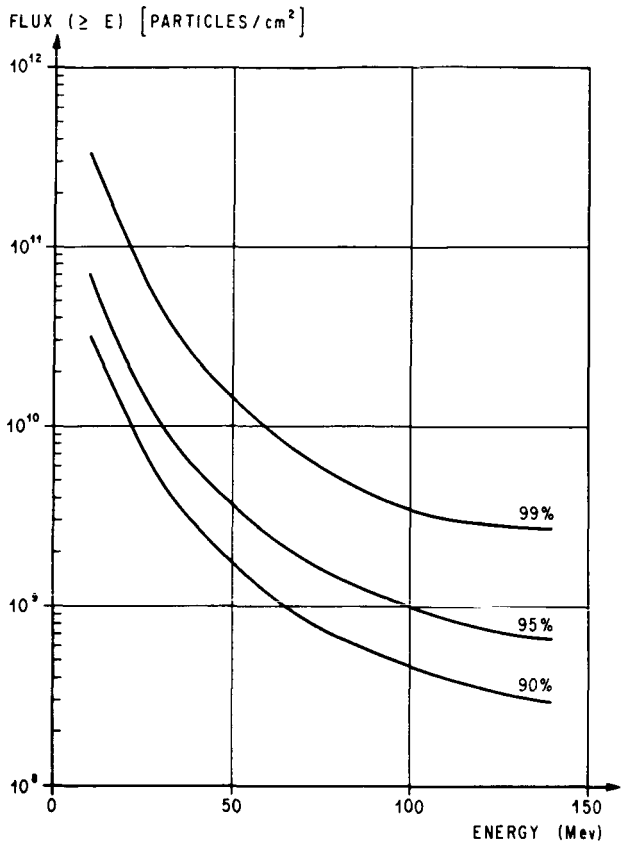

FIGURE 3. ENVIRONMENTAL MODELS FOR THE 99 PERCENT, 95 PERCENT, AND 90 PERCENT PROBABILITY FLUX-ENERGY SPECTRA TO BE ENCOUNTERED ON A 200 DAY EXTRATERRESTRIAL MISSION. THE FACTOR $p_{200} = 0.93$

If one wishes to obtain information on the flux of particles at energies greater than 140 Mev, this should not be done by extending linearly these plotted curves. One should rather obtain the flattened spectrum for the February 23, 1956, event and apply this fit to the data at 140 Mev.

REFERENCES

1. Modisette, J. L.; Vinson, Terence M.; and Hardy, Alva C.: Model Solar Proton Environments for Manned Spacecraft Design. NASA TN D-2746, Manned Spacecraft Center, Houston, Texas, April 1965.

2. Bailey, D. K.: Time Variations of the Energy Spectrum of Solar Cosmic Rays in Relation to the Radiation Hazards in Space. Journal of Geophysical Research 67, 391-396, 1962.

3. Webber, William R.: An Evaluation of the Radiation Hazard Due to Solar Particle Events. The Boeing Co., Document No. D2-90469, Seattle, Washington, November 12, 1963.

BIBLIOGRAPHY

1. Roberts, W. T.: Probabilities of Solar Flare Occurrence. NASA TM X-53463, MSFC, Huntsville, Ala., May 18, 1966.

2. Savin, R. C.; Deerwester, J. M.; and Massey, A. C.: Sensitivity of Manned Planetary Spacecraft Design to Radiation Uncertainties. Journal Spacecraft, vol. 4, no. 2, NASA Mission Analysis Division, Moffett Field, Calif., February 1967.

VII. THERMODYNAMICS

THE DETERMINATION OF THERMODYNAMIC PROPERTIES WITH OPTICAL CROSS-CORRELATION METHODS*

By

F. R. Krause** , W. O. Davies$^{\psi}$ and M.W.P. Cann$^{\psi\psi}$

ABSTRACT

A remote-sensing cross-beam cross-correlation method that will provide spatially resolved average thermodynamic properties is described. Two detection systems with crossed fields of view are used to monitor radiation emitted from or transmitted through a gas system. The measured cross-correlation coefficient, which depends on the average and fluctuating components of the observed signals, is interpreted in terms of atmospheric properties at the intersection of the fields of view. The average thermodynamic properties are obtained by (1) expanding the absorption coefficient in a Taylor series and evaluating the fluctuating components as derivatives of the average absorption coefficient, (2) evaluating the measured cross-correlation coefficient in terms of these derivatives, and (3) using absorption band models to relate the absorption coefficient derivatives to thermodynamic properties. The cross-correlation coefficient is given in terms of average thermodynamic properties and in terms of certain integral factors which may be used to study turbulent heat and mass transport independently of each other.

I. INTRODUCTION

In most remote-sensing methods, the attenuation or enhancement of a beam of electromagnetic radiation is measured along the entire path from the source to the detector. To interpret the results of such an observation, some assumption is generally required concerning the system being measured. This assumption is usually in the form of a model of the phenomenon being observed; for example, in atmospheric studies, one might use the adiabatic or isothermal model atmosphere. The important point is that, with single path observations, it is not generally possible to obtain spatially resolved measurements of the thermodynamic or flow properties without invoking such models.

Spectroscopic observations with a single beam can be used to provide average thermodynamic properties of a medium that is inaccessible to physical probes, and the spatial and temporal profiles of these properties can be inferred by applying a mathematical transformation with respect to one or more independent variables, which are generally space, time, and wavelength. A common technique, of which the Abel integral inversion method is an example [1-4], is to use the two spatial coordinates normal to the single beam. Emission and absorption are measured along one beam for a series of displacements normal to that beam, and the transformation of the optical properties yields a temperature profile. This method is useful for axially symmetric phenomena, but is of limited usefulness for nonsymmetric phenomena, such as the atmosphere and clustered rocket jets. The wavelength dependence of absorption and emission is the basis of the transformation in the zonal approximation method [5,6]. The single path is divided into a number of zones, each zone being characterized by an average temperature and pressure. Measurements are made at a number of wavelengths equal to the number of zones, and a transformation in wavelength yields a temperature profile.

---

* Corrected version of AIAA paper 67-149 presented at the 5th Aerospace Sciences meeting N.Y., January 25, 1967.

** Scientific Assistant, NASA, Marshall Space Flight Center, Huntsville, Alabama.

ψ Manager, IIT Research Institute, Chicago, Illinois.

$\psi\psi$ Research Physicist, IIT Research Institute, Chicago, Illinois.

In some recent investigations, the time aspect has been used to provide spatially resolved properties [7-10] using a remote-sensing technique called the cross-beam method. This cross-beam cross-correlation technique can be described briefly as follows: Two detection systems are used to monitor electromagnetic radiation that has passed through or originates in the gas system being studied. The fields of view of the two systems are arranged to cross in the region being investigated, and the radiation received at each detector is monitored to provide the fluctuations in intensity of the two beams. The statistical correlation of the fluctuating signals is examined, and the results are interpreted in terms of the gas properties at the intersection of the two beams.

In previous investigations, both beams operated at the same wavelength, and turbulence parameters were determined from the dependence of the cross-correlation coefficient on the beam separation in time and space. In this paper, the method is extended to cover the dependence of the beam correlation function on the optical wavelength of one beam. It will be shown that this theory of "cross-beam" spectroscopy permits an interpretation of the cross-beam observations in terms of spatially resolved average thermodynamic properties, without invoking assumptions concerning symmetry of the structure of the medium being investigated. Furthermore, the method allows us to disentangle the turbulent transport of mass and heat by operating the space-time correlation functions of partial pressure fluctuations and temperature fluctuations. Potential applications are considered by examining the expressions for the cross-correlation coefficient that would result from observations made for various combinations of strong and weak spectral lines. The combination of two weak or two strong line regions yields expressions for the temperature, which do not depend on the partial or static pressure , and a combination of weak and strong lines provide partial and static pressure profiles in addition to temperature.

II. REVIEW OF THE CROSS-BEAM METHOD

In a cross-beam arrangement, the local flow region of interest may be chosen by triangulation between two collimated beams. It extends between the two points $\vec{x}$ and $\vec{x} + \vec{\xi}$ of minimum beam separation. A typical test arrangement for jet noise studies is shown in Figure 1. The beam diameters (viewing angle) and orientation (azimuth and elevation) are set by a remote telescope. The collected radiative power is then filtered by a monochromator which is set at the wave length λ and the resolution $\Delta\lambda$. The remaining signal I_d is then monitored by a photodetector with a fast response such that the time history is not lost.

The remote-sensing device will see any local emission or extinction process inside the beam. We choose to express the contributions to the radiative power ΔI, which originate in a beam element Δx, by a generalized spectral extinction coefficient

$$K(\vec{x}, t, \lambda) = \frac{1}{I} \frac{\Delta I}{\Delta x} . \qquad (1)$$

The word "generalized" indicates that emission processes are included. As long as either emission or extinction is locally dominant, the equations of radiative transfer show that the total signal I may be expressed in terms of a line integral over the extinction coefficient.

$$I_d(t, \lambda) = I_{source} \exp\left(- \int_{source}^{detector} K(\vec{x}, t, \lambda)\, dx \right) . \qquad (2)$$

The detected signal thus accounts for any emission or extinction process along the entire line of sight. However, in most remote-sensing tests, we need local information $K(\vec{x}, t)$ at a point. In a cross-beam arrangement, the desired local information is retrieved from the integrated signal by considering the fluctuation of the integrated signal:

$$i = I_d - \bar{I}_d . \qquad (3)$$

The fluctuations are calculated by subtracting a mean value $\bar{I}$, which may be established by averaging over time and/or over repeated experiments. In case of ideal detectors, this fluctuation is related to the fluctuations of the extinction coefficient

$$K' = K - \bar{K} \qquad (4)$$

through the line integral of equation (2). As long as the integrated fluctuation can be treated as a small disturbance, the desired fluctuation may be expressed by [7]

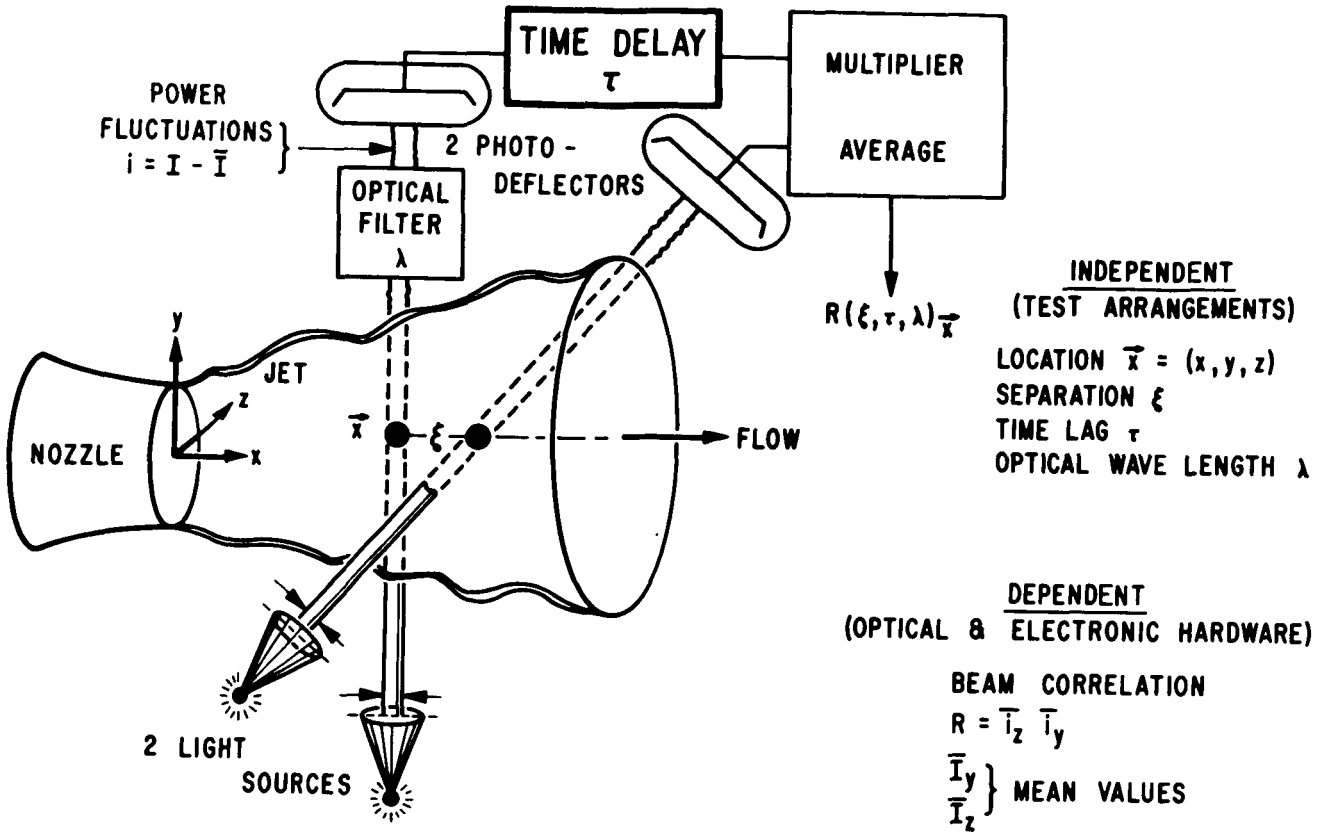

FIGURE 1. VARIABLES IN CROSS BEAM EXPERIMENTS

$$i = I_d - \bar{I}_d = \frac{\bar{I}_d}{\bar{I}_s} i_{source} - \bar{I}_d \int_{source}^{detector} K'(\vec{x}, t, \lambda)\, dx. \qquad (5)$$

The first term gives the contribution of the light source noise, and the second accounts for the fluctuations of the medium. Detector noise must be added for nonideal detection devices.

The small-perturbation assumption is not very restrictive. The mean absorption

$$\int \bar{K}\, dx$$

as well as the local values of the fluctuation K', could be large. Only the fluctuation integral over several statistically independent parts must be small enough to permit linearization.

The way in which correlation methods may be used to retrieve the local information at the region of minimum beam separation becomes clear by introducing the concept of a "correlation volume." This volume is defined in turbulence theory by an imaginary experiment with two observers as illustrated in Figure 2. Let us consider a special arrangement where the beams are aligned parallel to the y and z axes and cross in the space-fixed position $\vec{x}$. The first imaginary observer is attached to this position; the second observer monitors the K' fluctuations at the the variable position $\vec{x} + \vec{\xi}$. The imaginary experiment now calls for multiplying and averaging the observed fluctuations. This gives a "two-point product mean value"

$$R_k(\vec{\xi}, \tau, \lambda) = \overline{K'(\vec{x}, t, \lambda) K'(\vec{x} + \vec{\xi}, t + \tau, \lambda)} \qquad (6)$$

which is the basis of all analytical descriptions of random fields. The random nature of a fluctuation

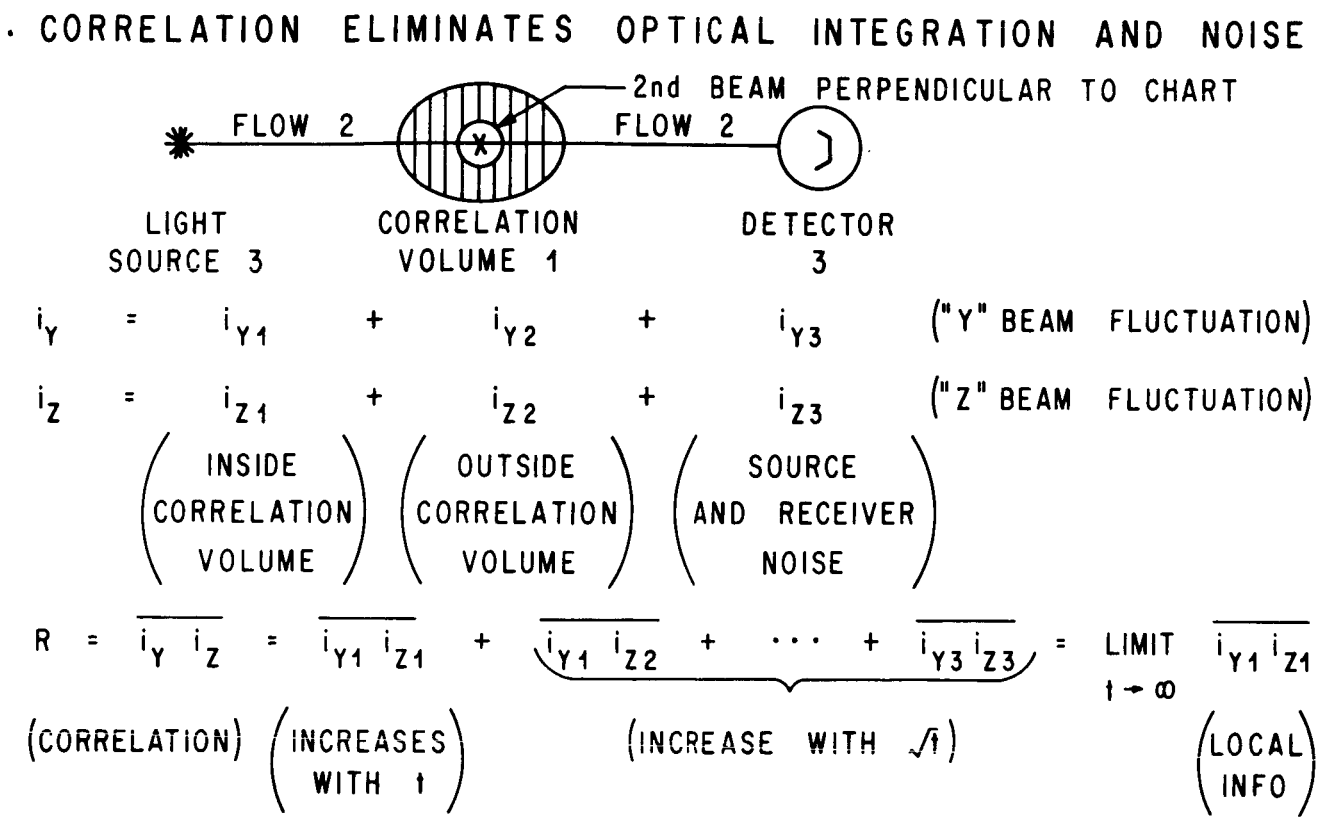

FIGURE 2. RETRIEVAL OF LOCAL INFORMATION

field such as $K'(\vec{x}, t, \lambda)$ is recognized by the fact that the two-point product mean value drops to zero over finite distances $|\vec{\xi}|$. This leads to the definition of the correlation volume. It is that volume surrounding a certain point $\vec{x}$ within which the two-point product mean value R_K remains finite. The average radius of this volume in the x-direction is used to define the integral length scale

$$L_x = \frac{1}{2} \int_{-\infty}^{+\infty} \frac{\overline{K'(x+\xi, y, z, t) K'(x, t)}}{\overline{K^2(\vec{x}, t)}}\, d\xi . \qquad (7)$$

Similar expressions hold for the extensions $2L_y$ and $2L_z$ of the correlation volume in the y and z directions. In wind tunnels, typical L values are between 1 mm and 10 cm. In the atmosphere, they vary between 10 m and 1 km.

A cross-beam experiment resembles the above imaginary experiments in that it performs exactly the same calculations. Only the local fluctuations of K are replaced with the fluctuations i of the detected signal I. This leads to the "two-beam product mean value"

$$R(\xi, \tau, \lambda)_{\vec{x}} = \overline{i_y(t, \lambda)\, i_z(t+\tau, \lambda)} . \qquad (8)$$

The method of isolating the information related to the correlation volume can now be understood by considering the signal contributions from (1) fluctuations that occur in the correlation volume, (2) fluctuations caused by events from all other regions along the beam, and (3) fluctuations generated by the source and the instrument. Thus, the measured correlation is the sum of nine time-averaged cross-products. Eight of these instantaneous products assume positive and negative values with time. Their sum will approach zero with the inverse square root of integration time or number of experiments. The remaining product contains the fluctuations that occur inside the correlation volume and that are common

to both lines of sight. The instantaneous product of these fluctuations is always positive, and its average value will approach a constant value with increasing integration time or number of experiments. Thus, for sufficiently long integration times, the product of fluctuations in the correlation volume will dominate the cross-correlation coefficient. The two-beam product mean value can thus be expressed as the product of two line integrals which are to be extended over the correlation volume. Introducing a beam-fixed coordinate system (Fig. 3), we may express the relation as

$$R = \overline{\int K'(x; y, z-\zeta, t)\, d\zeta \int K'(x+\xi, y+\eta, z, t+\tau) d\eta}$$

$$= \overline{\int\int K'(x, y, z-\zeta, t)\, K'(x+\xi, y+\eta, z, t+\tau)\, d\eta d\zeta}.$$

correlation volume (9)

The physical interpretation of equation (9) is difficult, since the integrand represents two points which move independently along each beam. However, if the fluctuations are statistically homogeneous along one beam,

$$\overline{K'(x, y, z-\zeta, t, \lambda_1)\, K'(x+\xi, y+\eta, z, t+\tau, \lambda_2)}$$

$$= \overline{K'(x, y, z, t, \lambda_1)\, K'(x+\xi, y+\eta, z+\zeta, t+\tau, \lambda_2)} = R_k, \quad (10)$$

then the integrand may be replaced with the two-point product mean value

$$R(\xi, \tau, \lambda)_{\vec{x}} = \bar{I}_y \bar{I}_z \int\int_{\text{correlation "disc"}} R_k(\vec{\xi}, \tau, \lambda)_{\vec{x}}\, d\eta d\zeta. \quad (11)$$

The integration accounts only for the position of the second imaginary point probe inside a plane which is parallel to both beams and which contains the second point of minimum beam separation $(x+\xi, y, z)$. Thus, the two-beam product mean value can be considered equivalent to an integral over the beam front (Fig. 3). Since no integration occurs normal to the beams, two-point product mean values can be resolved inside the correlation volume by repeating the experiment for a series of beam separations.

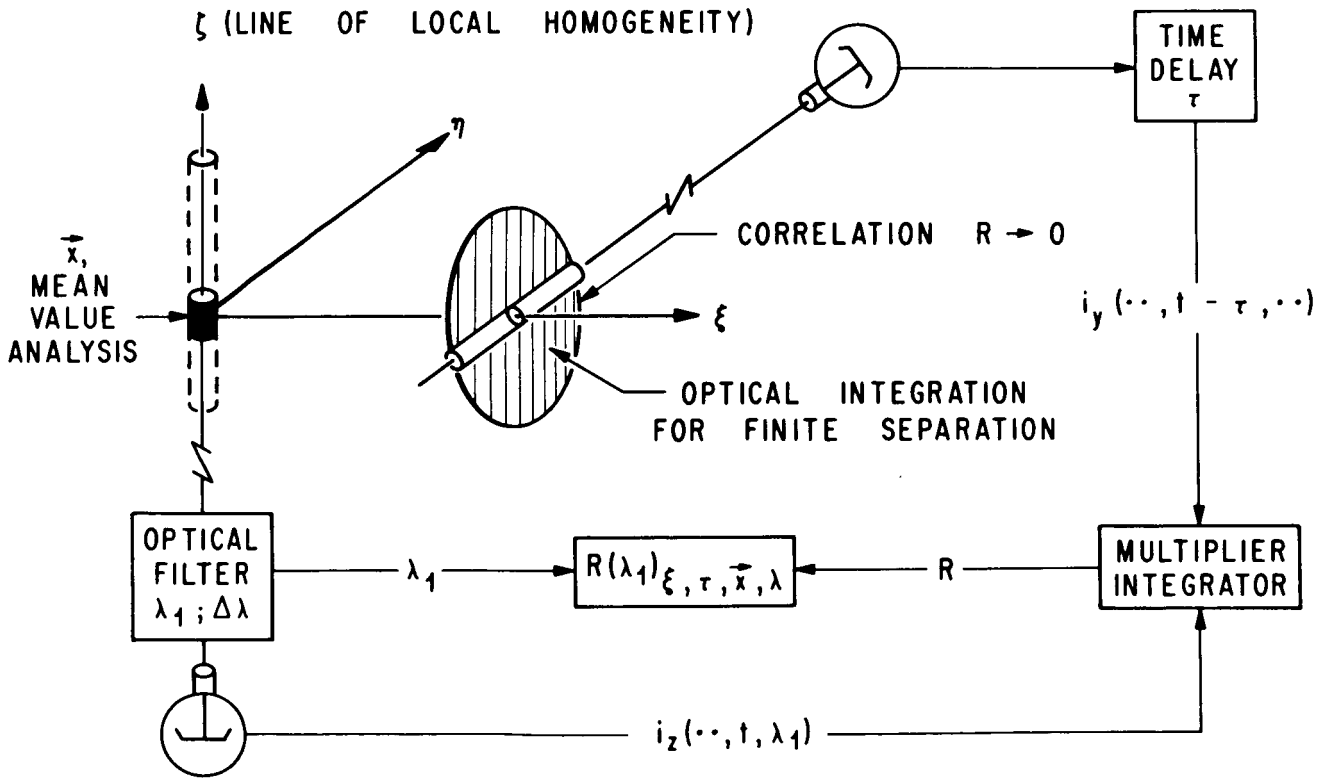

FIGURE 3. CROSSED BEAM SPECTROSCOPY

The validity of the cross-beam concept has been established in two experiments. M. J. Fisher tried to verify the accuracy to which two-beam product mean values approximate two-point product mean values by comparing hot-wire correlations [11, 12] with cross-beam results. Visible radiation beams were crossed in the free shear layer of a subsonic jet exhausting into the atmosphere, and the light extinction was produced by scattering from water droplets introduced into the flow. The velocities, eddy lifetimes, and moving-axis autocorrelation curves obtained with the optical measurements were in agreement with hot-wire measurements, within experimental error.

The second cross-beam measurement has been made on an atmospheric scale to determine the altitude of maximum airglow emission intensity [10]. Two photometers placed about 250 km apart, both viewing atomic oxygen emission at 5577 Å, scanned the atmosphere in such a manner that the intersection of their fields of view moved in a horizontal line at a constant speed. The altitude of maximum correlation [97 km] was assumed to be the height at which the maximum intensity of the 5577Å oxygen line originates; this is in agreement with results obtained from rocket flights and triangulation by time variation.

III. SINGLE-BEAM SPECTROSCOPY IN STAGNANT GASES

The method considered here is based on the same principles generally used in optical remote-sensing methods, in that the thermodynamic properties are derived from the dependence of the extinction coefficient on these properties. In this respect, remote sensing with cross-beam methods is similar to the use of single-beam remote-sensing systems; it is therefore desirable to discuss the relationship of the observables to the gas properties. For thermal equilibrium, the macroscopic thermodynamic properties can be expressed in terms of emissivity, fractional absorption or transmission as shown in Figure 4.

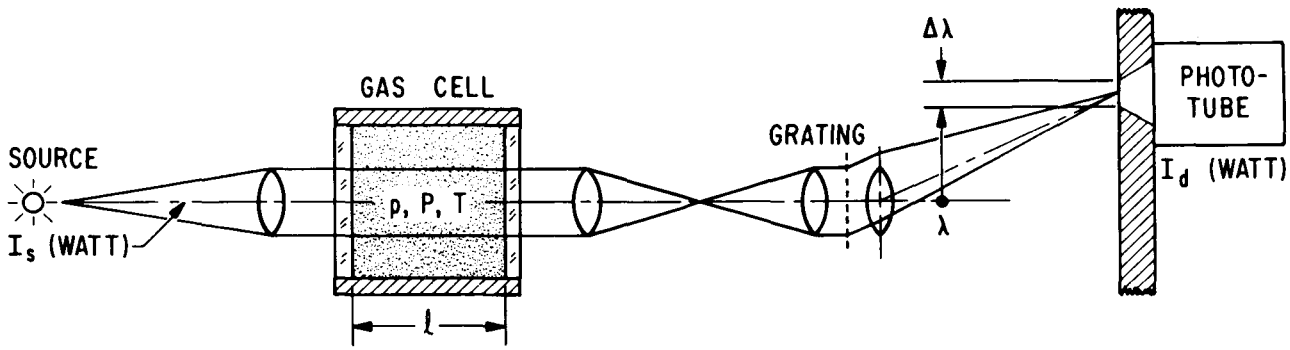

INDEPENDENT VARIABLES

$\omega = \frac{1}{\lambda}$ OPTICAL WAVE NUMBER

$I_s =$ RADIATIVE POWER EMITTED BY LIGHT SOURCE

$\ell =$ GEOMETRICAL PATH LENGTH

DEPENDENT VARIABLES

$I_d = \bar{I} + i$ DETECTED RADIATIVE POWER

$k = \frac{2.303}{\ell} \log_{10} \frac{I_d}{I_s}$ ABSORPTION COEFFICIENT

FIGURE 4. SINGLE BEAM SPECTROSCOPY

The fractional absorption of radiation,

$$a = \frac{\bar{I}_{source} - \bar{I}_{detector}}{\bar{I}_{source}}, \quad (12)$$

which is transmitted through a stagnant gas, can be represented functionally by

$$a = a(p, P, T, \ell, \lambda, \Delta\lambda), \quad (13)$$

where p is the partial pressure of the absorber, P is the total gas pressure, ℓ is the geometrical path length, T is the temperature, λ is the wavelength and $\Delta\lambda$ is the optical band pass. To replace this functional relation with an equation that would permit the determination of the thermodynamic properties, the dependence of absorption on the spectroscopic properties of the molecule and the thermodynamic properties of the gas must be known. These optical properties include (a) a measure of the absorption strength, which may be expressed as an integrated absorption, oscillator strength, transition probability, or radiative lifetime; (b) the line width which may result from collision, Doppler, or natural broadening; and (c) the line spacing, e.g., the distance between rotational lines in a molecular vibrational transition. In this discussion, these quantities are expressed as line strength (S), width (b), and spacing (d), respectively.

The determination of the thermodynamic properties requires (1) a measurement of radiative power that can be interpreted in terms of the optical properties, (2) a laboratory calibration that provides spectroscopic properties for the molecular band system, and (3) a model that relates the optical properties to the thermodynamic properties. The latter is available in the form of absorption band model theories. The optical properties of a gas are functions of the static gas pressure, temperature, absorber partial pressure, and path length; these functions depend on the distribution of position and intensity of spectral lines within the band [13-18]. A number of models have been developed that provide an approximate description of the absorption and emission characteristics of a band; these models include (1) the Elsasser model, which is composed of uniformly spaced lines of equal intensity [16], (2) the statistical model [17], which consists of an arbitrary intensity distribution and a random position distribution of spectral lines, (3) the random Elsasser model [13], which contains randomly distributed groups of lines in which each group is represented by an Elsasser model, and (4) the quasi-random model [18], which consists of a group of bands represented by the statistical model.

The general expression for fractional absorption in the statistical model is

$$a = 1 - \exp\left[-\bar{W}_s/d\right], \quad (14)$$

where

$$\bar{W}_s = \int_0^\infty W_s(S,\beta)\, P(S)\, dS, \quad (15)$$

$$\frac{W_s}{d} = \beta\chi e^{-\chi}\left[I_0(\chi) + I_1(\chi)\right], \quad (16)$$

$$\beta = \frac{2\pi b}{d}, \quad (17)$$

and

$$\chi = \frac{Su}{2\pi b}; \quad = \frac{Sp\ell}{2\pi b}. \quad (18)$$

S, b, and d are, respectively, the rotational line intensity, half-width, and spacing, u is the absorber path length, W_s is the equivalent width of a single line, I_0 and I_1 are Bessel functions of the imaginary argument, and P(S)dS is the probability that a spectral line of intensity S is in the interval dS.

The desired relation between the extinction coefficient and the thermodynamic state variables is found by comparing equations (14) and (16) with the optical integration (equation 2). The absorption coefficient for the statistical band model is

$$\bar{K}_{SM} = \frac{Sp}{d} e^{-Sp\ell/2\pi b}\left[I_0\left(\frac{Sp\ell}{2\pi b}\right) + I_1\left(\frac{Sp\ell}{2\pi b}\right)\right]. \quad (19)$$

In this expression, the rotational line intensity may be related to experimentally accessible quantities by comparing the absorbing gas molecule with a rigid rotator [19]. This approximation leads to

$$S \simeq \left(\frac{8\pi^3}{3k}\omega\, q_{r'r}\right)\frac{\Delta\omega}{T} e^{-\frac{hc(\Delta\omega)^2}{4kBT}} \quad (20a)$$

For a particular vibrational transition the Frank Condon factor $q_{r',r''}$ is a constant and the wave number ω of the band center is nearly constant. The

rotational line intensity may thus be abbreviated by

$$S \simeq C \frac{\Delta\omega}{T} e^{-\frac{hc}{4kBT}(\Delta\omega)^2} \qquad (20b)$$

where h, k, and c are Planck's constant, Boltzmann's constant, and the velocity of light, respectively, B is the rotational constant for the absorbing species, $\Delta\omega$ is the distance (in cm^{-1}) from the band center, as shown in Figure 5, C is a constant for a given molecular band. The distance from the band center ($\Delta\omega$) is used in wave numbers (cm^{-1}) here because of the convenience in using this notation in spectroscopic problems. The wave number for a particular measurement is the reciprocal of the wavelength, and the cross-correlation coefficient will still be considered a function of wavelength, although the wavelength dependence is described in terms of $\Delta\omega$ in cm^{-1}. For a pressure-broadened line, the line half-width can be expressed as

$$b = b_0 \frac{P}{P_0} \sqrt{\frac{T_0}{T}}, \qquad (21)$$

where b_0 is the half width at standard conditions (P_0, T_0).

In special cases the optical properties may be described by the weak line approximation, for which these properties depend linearly on absorber concentration and are independent of pressure, or the strong line approximation is valid when there is virtually complete absorption near the centers of the strongest lines in the band. The strong line approximation to the statistical model is

$$\bar{K}_{SL} = 2\sqrt{Sbp/d^2\ell}. \qquad (22)$$

When the absorption is small at all frequencies in the band, the absorption given by the weak line approximation for all the band models is

$$\bar{K}_{WL} = \frac{Sp}{d}. \qquad (23)$$

The criteria for the applicability of the weak and strong line approximations to various band models,

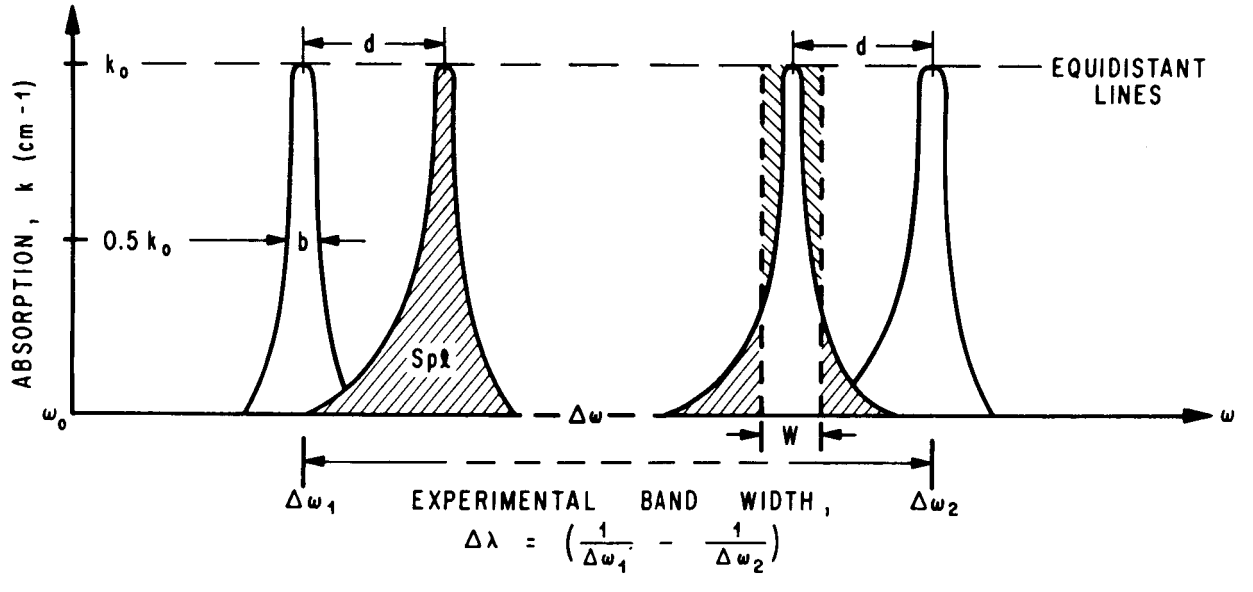

ω_0 = BAND CENTER - EQUIVALENT TO TRANSITION BETWEEN LOWEST ROTATIONAL LEVELS OF RESPECTIVE VIBRATION STATES

LINE SPACING, d = 2B FOR RIGID ROTATION

DISTANCE FROM BAND CENTER, $\Delta\omega = \omega - \omega_0 = 2BJ$

WHERE J = ROTATIONAL QUANTUM NUMBER

AND $B = \frac{h}{8\pi^2 c \times (\text{ROTATION MOMENT OF INERTIA})}$ = ROTATIONAL CONSTANT

FIGURE 5. BAND REPRESENTATION BY STATISTICAL MODEL AND RIGID ROTATION APPROXIMATION

which have been given by Plass [13, 14], are summarized for the statistical model in Table I. The applicability is given in the following terms: The approximation is accurate to within q percent if the parameters $\chi = Su/2\pi b$ and $\beta = 2\pi b/d$ lie within a given range.

TABLE I. APPLICABILITY OF APPROXIMATIONS TO THE STATISTICAL BAND MODEL [13]

(For lines of equal intensity with Lorentz profile.)

Approximation

Weak Line: $\beta < 1$;	$\chi < 0.02\ q$
$\beta > 1$;	$\chi < 0.02\ q\ \beta^{-1}$
Strong Line: $\beta < (7.1)\ 10^{-3}\ q^{3/2}$	$12.5\ q^{-1} < \chi < (6.28)\ 10^{-4} q^2 \beta^{-2}$

In general, the strong line approximation is valid at low pressures, where the rotational lines are narrow and the strength of the line is not used efficiently. The weak line approximation is appropriate when the total absorption is small at the centers of the strongest lines, or when the spectral distribution of absorbing strength is such that the absorption varies smoothly with wavelength. Experimentally, this may result from operating at high pressures where the rotational lines are broadened, or at high temperatures so that the transitions from those excited states are at different wavelengths from those for lower energy levels. The terms "high" and "low" pressure are, of course, relative; experimentally, it is found that at room temperature the weak line approximation is useful for polyatomic molecules (e.g., CO_2) at about 2 atm and for diatomic molecules (e.g., NO, CO) at about 10 atm.

For the purposes of this paper, we have chosen to restrict the discussion of spectroscopic methods to the use of the above statistical model, in particular, equations (19) through (23). The use of this model requires several additional assumptions which tend to simplify the analysis, but do not impose a limitation on the utility of the method. These assumptions are as follows: (1) The effects of scattering are neglected in the spectral region in which the observations are made, and (2) the absorption in this region is caused by a single absorbing species. Thus, the extinction coefficient is equivalent to the absorption coefficient, and the latter term will be used from this point forward. The scattering cross section generally varies slowly with wavelength; therefore, including these effects would introduce a nearly continuous background. Since absorption coefficients are additive, the existence of two or more overlapping absorption bands would present a complication in the interpretation and analysis of data, but would not significantly alter the following derivations.

IV. CROSS-BEAM SPECTROSCOPY IN RANDOM FIELDS

The combination of statistical and spectroscopic data analysis makes it conceivable to study the space-time variations of thermodynamic state variables in inaccessible, inhomogeneous and/or random fields. We consider a series of cross-beam experiments which differ only in the optical wavelength, λ, used on the first beam. These experiments contain spectroscopic information from the correlation disc around the line of minimum beam separation, Figure 3. The result of these experiments may be used to construct a "spectrum." As long as the random field of thermodynamic state variables is homogeneous along the optically filtered beam, this "spectrum" may be expressed by

$$R(\lambda_1)_{\vec{x},\,\xi,\,\tau,\,\lambda_2} = \overline{i^{(1)}(t,\lambda_1)\ i^{(2)}(t+\tau,\lambda_2)} = \tag{24}$$

$$\bar{I}_1\bar{I}_2 \int\int_{\text{correlation disc}} \overline{K'(x,t,\lambda_1)\ K'(\vec{x}+\vec{\xi};\ t+\tau,\lambda_2)}\ d\eta d\zeta .$$

The interpretation of this function in terms of thermodynamic state variables requires relating $R(\lambda_1)$ to these variables. The main difference between conventional spectroscopy and cross-beam spectroscopy, is now that we deal with local optical fluctuations,

$$K' = K(\rho;\ P;\ T) - K(\bar{\rho};\ \bar{P};\ \bar{T}), \tag{25}$$

which are caused by the fluctuations of the thermodynamic state variables:

$$\begin{aligned} \rho'(\vec{x},t) &= \rho(\vec{x},t) - \bar{\rho}(\vec{x}) \\ P'(\vec{x},t) &= P(\vec{x},t) - \bar{P}(\vec{x}) \\ T'(\vec{x},t) &= T(\vec{x},t) - \bar{T}(\vec{x}) . \end{aligned} \tag{26}$$

Cross-beam spectroscopy has, thus, to be based on the relation between optical and thermodynamical fluctuations. This relation is provided by a Taylor series approximation of the general relation (25) around the average values

$$K'(p, T, P, \lambda) = K'(\vec{x}, t, \lambda) = \left[p' \frac{\partial}{\partial p} + T' \frac{\partial}{\partial T} + P' \frac{\partial}{\partial P} \right] \bar{K}(\bar{p}; \bar{T}; \bar{P}; \lambda) + \frac{1}{2} \left[p' \frac{\partial}{\partial p} + T' \frac{\partial}{\partial T} + P' \frac{\partial}{\partial P} \right]^2 K(\bar{p} + \vartheta p'; \bar{T} + \vartheta T'; \bar{P} + \vartheta P'; \lambda) \qquad (27)$$

with $0 < \vartheta < 1$.

Substituting the Taylor series for $K'(\vec{x}, t)$ into equation (24), we may rewrite the spectral curve as:

$$\frac{R(\lambda_1)_{\vec{x}, \xi, \tau, \lambda_2}}{\bar{I}_1 \bar{I}_2} = \frac{\partial \bar{K}}{\partial p} \iint \overline{p'(\vec{x}, t) K'(\vec{x}+\vec{\xi}, t+\tau, \lambda_2)} \, d\eta d\zeta$$

$$+ \frac{\partial K}{\partial T} \iint \overline{T'(\vec{x}, t) \, K'(\vec{x}+\vec{\xi}, t+\tau, \lambda_2)} \, d\eta d\zeta$$

$$+ \frac{\partial \bar{K}}{\partial P} \iint \overline{P'(\vec{x}, t) K'(\vec{x}+\vec{\xi}, t+\tau, \lambda_2)} \, d\eta d\zeta$$

$$+ \frac{1}{2} \iint \left\{ \frac{\partial^2 \bar{K}}{\partial p^2} \overline{p'^2 K'} + \frac{\partial^2 \bar{K}}{\partial P^2} \overline{P'^2 K'} + \frac{\partial^2 \bar{K}}{\partial T^2} \overline{T'^2 K'} \right\} d\eta d\zeta$$

$$+ \iint \left\{ \frac{\partial^2 \bar{K}}{\partial P_i \partial P} \overline{P'_i P' K'} + \frac{\partial^2 \bar{K}}{\partial P_i \partial T} \overline{P'_i T' K'} + \frac{\partial^2 \bar{K}}{\partial T \partial P} \overline{T' P' K'} \right\} d\eta d\zeta. \qquad (28)$$

In this equation, the second order terms of the Taylor series are weighted with triple products. As long as the fluctuations of the thermodynamic state variables are small perturbations, these terms may be neglected. If these fluctuations are large, the second order terms may still be neglected, as long as two of the fluctuations in the triple product are not, or only weakly, correlated. If the fluctuations are both large and correlated, the second order terms may still be suppressed, in special cases where the optical absorption band can be chosen so that the mixed second derivatives of the mean extinction coefficient are small. The pure second derivatives in the fourth row of equation (28) should contribute very little since the associated triple product contains only one oscillating part. For example, these triple products would vanish even if the thermodynamic state variables p', P', or T' and the optical fluctuations K' are perfectly correlated by the same harmonic wave.

In view of the above considerations, we assume that second order terms of the Taylor series make no contribution in most cases of practical interest. The last relation may then be approximated by

$$\frac{R(\lambda_1)_{\vec{x}, \xi, \tau, \lambda_2}}{\bar{I}_1 \bar{I}_2} = \left[Q_p \frac{\partial}{\partial p} + Q_P \frac{\partial}{\partial P} + Q_T \frac{\partial}{\partial T} \right] \bar{K}(\bar{p}, \bar{P}, \bar{T}, \lambda_1). \qquad (29)$$

In this expression, the coefficients

$$Q_p = \iint \overline{p'(\vec{x}, t) \, K'(\vec{x}+\vec{\xi}, t+\tau, \lambda_2)} \, d\eta d\zeta$$

$$Q_P = \iint \overline{P'(\vec{x}, t) \, K'(\vec{x}+\vec{\xi}, t+\tau, \lambda_2)} \, d\eta d\zeta \qquad (30)$$

$$Q_T = \iint \overline{T'(\vec{x}, t) \, K'(\vec{x}+\vec{\xi}, t+\tau, \lambda_2)} \, d\eta d\zeta$$

are independent of λ_1, and may be treated as constants. The spectrum curve $R(\lambda_1)$ may thus be approximated as a linear superposition of the three mean value derivatives $\partial\bar{K}/\partial p$, $\partial\bar{K}/\partial P$ and $\partial\bar{K}/\partial T$, which may be functions of λ_1.

Equations (29) and (30) provide the basis for extending spectroscopic methods from stagnant gases to nonuniform gases with time variations. All radiation sources outside the correlation disc are suppressed by the correlation analysis. Furthermore, the optical integration inside the correlation disc considers only variable positions of the second observer. The position of the first observer, which was used in the Taylor series (equation 27) is not subject to integration as long as the K' is statistically homogeneous along the first beam, as expressed by equation (10). Thus, relations between the mean extinction coefficient $\bar{K}$ and the mean state variables $\bar{p}$, $\bar{P}$, and $\bar{T}$, which are derived for or measured in uniform gases, can be applied if we substitute the local thermodynamic mean values. In this paper,

such "equations-of-state" are provided by the statistical band model. Substituting equations (19) through (23) into equation (29), we get the following relation between cross-beam spectra and local thermodynamic state variables.

$$\frac{R(\lambda_1)\vec{x}\ldots\lambda_2}{\bar{I}_1\bar{I}_2} = \frac{\bar{K}_{SM}}{\bar{p}}\left[1 - \frac{S\bar{b}_\ell}{4\pi b}\,\frac{I_0(\chi) - I_2(\chi)}{I_0(\chi) + I_1(\chi)}\right] Q_p$$

$$+ \frac{\bar{K}_{SM}}{\bar{p}}\left[\frac{S\bar{p}\ell}{4\pi b}\,\frac{I_0(\chi) - I_2(\chi)}{I_0(\chi) + I_1(\chi)}\right] Q_p + \frac{K_{SM}}{\bar{T}}\left[\frac{hc(\Delta\omega)^2}{4kBT} - 1\right.$$

$$\left. - \left(\frac{hc(\Delta\omega)^2}{4kBT} - \frac{1}{2}\right)\frac{S\bar{p}\ell}{2\pi b}\,\frac{I_0(\chi) - I_2(\chi)}{I_0(\chi) + I_1(\chi)}\right] Q_T. \qquad (31)$$

The length ℓ was originally introduced as the geometrical path length occupied by the contributing radiation sources. This path length is now given by the beam diameter at the point $\vec{x}$ of minimum beam separation.

The weak line and strong line approximations to equation (29) become

$$R(\lambda_1)\vec{x}\ldots\lambda_2 = \frac{\bar{K}_{WL}}{\bar{p}}\,Q_{\bar{p}}$$

$$+ \frac{K_{WL}}{\bar{T}}\left(\frac{hc(\Delta\omega)^2}{4kBT} - 1\right) Q_T(\vec{x}, \xi, \tau, \lambda_2) \qquad (32)$$

and

$$K(\lambda_1)\vec{x}\ldots\lambda_2 = \frac{\bar{K}_{SL}}{2\bar{p}}\,Q_p + \frac{\bar{K}_{SL}}{2\bar{p}}\,Q_p(\vec{x}, \xi, \tau, \lambda_2)$$

$$+ \frac{\bar{K}_{SL}}{2\bar{T}}\left(\frac{hc(\Delta\omega)^2}{4kBT} - \frac{3}{2}\right) Q_T(\vec{x}, \xi, \tau, \lambda_2). \qquad (33)$$

Either equation (31), (32), or (33) offers the possibility of determining both the thermodynamic mean values $\bar{p}$, $\bar{P}$ and $\bar{T}$, as well as the space-time correlation functions $Q_{\bar{p}}$, Q_p, and Q_T of the associated fluctuations by repeating the cross-beam measurement $R(\lambda_1)$ for several lines of the same molecule and by solving the resulting system of equations. Cross-beam spectroscopy could thus, at least in principle, be used to remotely sense the mean value profiles of partial pressures, static pressures, and temperatures. Furthermore, the integrals $Q_{\bar{p}}$, Q_p, and Q_T make it possible to disentangle partial pressure fluctuations, static pressure fluctuations, and temperature fluctuations. They may thus be used to find (1) which thermodynamic state variable is primarily responsible for the optical fluctuations K, and (2) how the space-time correlations of these fluctuations differ. Thus, heat and mass transfer studies become conceivable, as well as investigations of two-phase flows.

V. SPECIAL CASES OF WEAK AND STRONG LINE COMBINATIONS

The feasibility of obtaining mean value information from cross-beam fluctuation measurements is considered for special cases where the "equations of state" correspond to the weak or strong line approximations as given by equations (32) and (33). These special cases are valid for molecular vibrational bands consisting of a number of pressure broadened rotational lines. The vibrational transitions may occur between different electronic energy levels or within one electronic level.

Pressure broadened lines are considered in this initial paper because the majority of laboratory and atmospheric applications being pursued involve experimental conditions for which Doppler broadening is relatively less important. At temperatures of the order of 300°K, the collision half-width exceeds the Doppler half-width for pressures down to about 10^{-2} atm, and at these low pressures, the optical properties still depend on the pressure broadening. This is because the variations of absorption or emission depend primarily on the wings of the rotational lines; the Doppler profile falls off exponentially with distance from the band center, which the pressure-broadened lines vary as the square of this distance. Thus, even for equal contributions to the line width, the optical properties will depend on the collision term. While the initial development of this theory is restricted to the models considered most applicable to experiments of immediate interest, there is, in principle, no inherent difficulty in extending the method of atomic lines, Doppler-broadened lines, or combined collision and Doppler-broadened lines.

A. TWO WEAK LINES

1. Pressure Fluctuations. Let us consider the observation of two spectral regions where the absorption can be represented by the weak line approximation and where the temperature fluctuations are negligible. In the weak line approximation, variations of the static gas pressure that are not accompanied by fluctuations of absorber pressure concentration will not contribute to the cross-correlation coefficient. The ratio of the cross-correlation coefficients measured at two different wavelengths yields an average gas temperature of

$$\bar{T} = \frac{\frac{(\Delta\omega)_1^2}{B_1} - \frac{(\Delta\omega)_2^2}{B_2}}{\frac{hc}{4k}\, \ell n \frac{R_1 C_2 (\Delta\omega)_2 d_1}{R_2 C_1 (\Delta\omega)_1 d_2}} , \qquad (34)$$

where $\Delta\omega_{1,2}$ are the distances (in cm^{-1}) from the band center to the wave numbers, ω_1, ω_2; $B_{1,2}$ are the rotational constants for the molecular bands used; and the other symbols are as defined above. (The dependence of the cross-correlation coefficient on position and wavelength is omitted in this and the following equations; the terms $R_{1,2}$ refer to the quantity measured at the two wavelengths.) If the observations are made at two weak line spectral regions of the same molecular band, this expression is reduced to

$$\bar{T} = \frac{hc}{4kB} \frac{(\Delta\omega)_1^2 - (\Delta\omega)_2^2}{\ell n \left(\frac{R_1 (\Delta\omega)_2}{R_2 (\Delta\omega)_1} \right)} \qquad (35)$$

Thus, in principle, an average temperature can be obtained from observations of intensity fluctuations produced by variations in the absorber concentration.

2. Temperature Fluctuations. For two weak line regions in which the temperature fluctuation term is predominant, the same procedure yields the expression

$$\bar{T}\, \ell n \frac{R_1 C_2 (\Delta\omega)^2 d_2}{R_2 C_1 (\Delta\omega)_1 d_2} - \bar{T}\, \ell n \frac{\frac{hc\,(\Delta\omega)_1^2}{4kB_1\bar{T}} - 1}{\frac{hc\,(\Delta\omega)_2^2}{4kB_2\bar{T}} - 1}$$

$$= \frac{hc}{4k} \left(\frac{(\Delta\omega)_2^2}{B_2} - \frac{(\Delta\omega)_1^2}{B_1} \right) , \qquad (36)$$

which can be solved iteratively to yield the temperature. If the observations are made on the same molecular band at a region far from the band center, this expression reduces to

$$\bar{T} = \frac{hc}{4kB} \frac{(\Delta\omega)_2^2 - (\Delta\omega)_1^2}{\ell n \frac{R_1 (\Delta\omega)_2^3}{R_2 (\Delta\omega)_1^3}} , \qquad (37)$$

which resembles the expression derived for the partial pressure fluctuations except for the denominator.

3. Combined Temperature and Partial Pressure Fluctuations. If simultaneous fluctuations of both the temperature and the absorber pressure exist, the ratio of cross-correlation coefficients does not yield an explicit expression for the temperature. The cross-correlation coefficient at a single wavelength contains four unknowns, two of which are the unknown integrals, Q(p) and Q(T), and two the thermodynamic properties, p and T. Thus, in principle it would be possible to eliminate the two unknown integrals and determine the temperature and absorber partial pressure from observations at four wavelengths.

It is of interest to consider the relative importance of the terms that arise from the temperature and partial pressure fluctuations. The ratio of the temperature fluctuation term to the pressure fluctuation term in equation (32) is approximately

$$\frac{\Delta R(\lambda_1)|_{T'}}{\Delta R(\lambda_1)|_{P'}} = \left(\frac{hc\,(\Delta\omega)^2}{4kBT} - 1 \right) \frac{Q_{T/\bar{T}}}{Q_{p/\bar{p}}} . \qquad (38)$$

Thus, the relative importance of the temperature and pressure fluctuations depends on the ratio of those fluctuating quantities, the distance from the band center at which the measurements are made, the temperature, and the molecular rotational constant.

This ratio can be evaluated only for a particular molecule in a given thermodynamic ensemble. The value of hc/4kB is about one for polyatomic molecules and about 0.2 for diatomic molecules; for atmospheric measurements, the temperature is of the order of 250 °K. Thus, for problems involving absorption by polyatomic molecules in the atmosphere, this ratio is approximately

$$(250)^{-1}\ [(\Delta\omega)^2 - 250]\ \frac{Q_{T/\bar{T}}}{Q_{p/\bar{p}}}$$

If the pressure and temperature fluctuations are equal (i.e., $Q_{p/p} = Q_{T/T}$), the temperature fluctuation term is dominant for $\Delta\omega^2 - 250 \gg 250\ cm^{-1}$, or for approximately $\Delta\omega \gg 22\ cm^{-1}$. For $\Delta\omega \simeq 16\ cm^{-1}$, the contribution of the temperature fluctuation to the cross-correlation coefficient is zero, and for $\Delta\omega \lesssim 16\ cm^{-1}$ the ratio is negative. The same general discussion holds for diatomic molecules, but the numerical values are different. In this case, the ratio of temperature and pressure terms in the cross-correlation coefficient is

$$(1250)^{-1}\left[(\Delta\omega)^2 - 1250\right]\frac{Q_{T/\bar{T}}}{Q_{p/\bar{p}}}\ .$$

The temperature fluctuation term would be dominant for $\Delta\omega \gg 50\ cm^{-1}$, while the pressure term would be dominant for $\Delta\omega \simeq 50\ cm^{-1}$. For $\Delta\omega < 35\ cm^{-1}$, the temperature term would be negative, and would therefore cancel the pressure term to some extent.

Including spectroscopic analysis in cross-beam experiments offers the important possibility of determining experimentally whether fluctuations are generated predominantly by pressure or temperature variations. When the measurement is made at a distance of $\Delta\omega \simeq (4kBT/hc^2)^{1/2}\ (cm^{-1})$ from the band center, the cross-correlation coefficient for the temperature fluctuations is zero regardless of the magnitude of the temperature fluctuation. Thus, in an ideal case, there is a wavelength in each branch of a vibrational band at which any observed correlation is due to variations of the absorber partial pressure.

This result is illustrated with a specific example in Figure 6 in which the cross-correlation coefficient is given for the 2.7μ CO_2 bands for several values of

$$\frac{Q_{T/\bar{T}}}{Q_{p/\bar{p}}}\ .$$

The experimental conditions considered here are $p = 10^{-1}$ atm, P = 1 atm, T = 300°K, and $\ell = 10$ cm. For these conditions, $\beta = 2\pi b/d$ is approximately 0.8 and $\chi = S\mu/2\pi b$ is approximately 0.16. Based

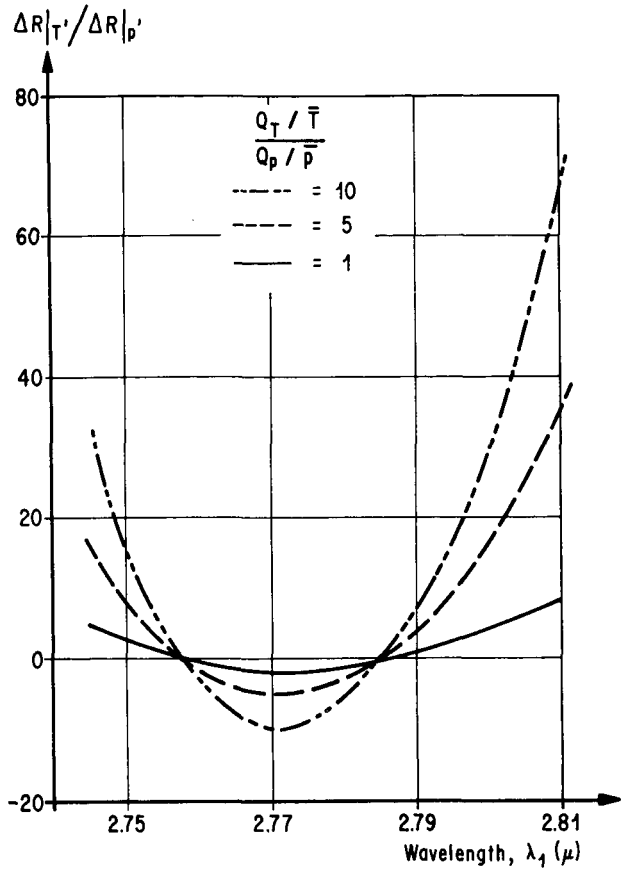

FIGURE 6. RATIO OF TEMPERATURE AND PRESSURE CONTRIBUTIONS TO CROSS CORRELATION COEFFICIENTS FOR 2.7μ CO_2 BANDS
($p = 10^{-1}$ atm, P = 1 atm, T = 300°K, $\ell = 10$ cm)

on the criteria given in Table I, the weak line approximation should be accurate to better than 10 percent. If the cross-correlation coefficient contains contributions from both temperature and pressure fluctuations, a comparison of the measured correlation coefficient with a series of curves such as shown here would permit a graphical determination of the relative contributions of the pressure and temperature fluctuations.

B. TWO STRONG LINES

1. Pressure Fluctuations. Absorption or emission observations made on two strong line spectral regions can be analyzed in the same manner. If the fluctuations are produced by variations of the absorber partial pressure, while the total pressure and temperature remain constant,

$$T = \frac{(hc/8k)\left[\frac{(\Delta\omega)_2^2}{B_2} - \frac{(\Delta\omega)_1^2}{B_1}\right]}{\ell n \frac{R_1}{R_2}\left(\frac{C_2(\Delta\omega)_2 d_1^2 b_{02}}{C_1(\Delta\omega)_1 d_2^2 b_{01}}\right)^{1/2}} . \quad (39)$$

If the observations are made on the same molecular band, this expression reduces to

$$T = \frac{(hc/8kB)\left[(\Delta\omega)_2^2 - (\Delta\omega)_1^2\right]}{\ell n \frac{R_1}{R_2}\left(\frac{(\Delta\omega)_2}{(\Delta\omega)_1}\right)^{1/2}} \quad (40)$$

For independent fluctuations of the static pressure (i.e., no partial pressure fluctuations), the result is identical. If the partial pressure is a constant fraction of the total pressure, the cross-correlation coefficient may be evaluated in terms of either the absorber partial pressure or the static pressure, yielding a cross-correlation coefficient of

$$R(\lambda_1)\underset{x}{\rightarrow}\ldots\lambda_2 = \frac{\bar{K}_{SL}}{\bar{p}} Q_p = \frac{\bar{K}_{SL}}{\bar{P}} Q_P . \quad (41)$$

In this case, the ratio of cross-correlation coefficients measured at two different wavelengths yields the same expression for temperature as for the independent fluctuations of partial or static pressure.

2. Temperature Fluctuations. For observations of two strong line spectral regions in which the temperature fluctuations are dominant, the ratio of the cross-correlation coefficients yields the expression

$$\bar{T}\,\ell n \frac{R_1}{R_2}\left(\frac{C_2(\Delta\omega)_2 d_1^2 b_{02}}{C_1(\Delta\omega)_1 d_2^2 b_{01}}\right) - \bar{T}\,\ell n \left[\frac{\frac{hc(\Delta\omega)_1^2}{4kB_1T} - \frac{3}{2}}{\frac{hc(\Delta\omega)_2^2}{4kB_2T} - \frac{3}{2}}\right]$$

$$= (hc/8k)\left[\frac{(\Delta\omega)_2^2}{B_2} - \frac{(\Delta\omega)_1^2}{B_1}\right] . \quad (42)$$

If the observations are made on the same molecular band far from the band center, this reduces to

$$T = \frac{(hc/8kB)\left((\Delta\omega)_2^2 - (\Delta\omega)_1^2\right)}{\ell n \frac{R_1}{R_2}\left(\frac{(\Delta\omega)_2}{(\Delta\omega)_1}\right)^{5/2}} \quad (43)$$

The criteria for being "far from the band center" are approximately $\Delta\omega \gg 20$ cm^{-1} for polyatomic molecules and $\Delta\omega \gg 45$ cm^{-1} for diatomic molecules.

3. Combined Pressure and Temperature Fluctuations. To analyze the case for which there exist simultaneous pressure and temperature fluctuations, it is assumed that the mole fraction of the absorber is constant. This will permit the use of only one of the terms involving the pressure, but is not very restrictive since the extension to include a variable mole fraction is straightforward. The ratio of the temperature and pressure fluctuation terms is approximately

$$\left(\frac{hc(\Delta\omega)^2}{4kBT} - \frac{3}{2}\right)\frac{Q_{T/\bar{T}}}{Q_{p/\bar{p}}} ,$$

and a similar relation holds if the partial pressure is replaced with total pressure. This expression differs from the weak line case (equation 38) only with respect to the ratio 3/2 in parentheses, which accounts for the temperature dependence of the strong line half-width. Once again, a special choice of $\Delta\omega$ would be used to determine experimentally whether the optical fluctuations are generated predominantly by pressure or temperature variations.

For absorption by polyatomic molecules in the atmosphere, the ratio is approximately

$$(250)^{-1}(\Delta\omega^2 - 325)\frac{Q_{T/\bar{T}}}{Q_{p/\bar{p}}} .$$

If the temperature and pressure fluctuations are equal (i.e., $Q_{T/\bar{T}} = Q_{p/\bar{p}}$) the cross-correlation coefficient would be dominated by the temperature fluctuation term for $\Delta\omega \gg 25$ cm^{-1}; at $\Delta\omega \simeq 18$ cm^{-1}, the temperature fluctuation term would be zero regardless of magnitude of the temperature fluctuation ($Q_{T/\bar{T}}$), and for $\Delta \lesssim 18$ cm^{-1}, the temperature contribution to the cross-correlation coefficient is negative. For diatomic molecules, the same general conclusions hold except that the factor of 18 cm^{-1} is replaced by approximately 55 cm^{-1}.

For comparison with the weak line situation, the pressure and temperature contributions to the cross-correlation coefficient are illustrated in Figure 7 for absorption by the CO fundamental vibration band at 4.7μ. The experimental conditions considered here are $p = 10^{-1}$ atm, $P = 10^{-1}$ atm, $T = 300°K$, and $\ell = 10$ cm. For these conditions, $\beta = 2\pi b/d$ is approximately 1.5×10^{-2}, and $\chi = Su/2\pi b$ is approximately 16. Based on the values

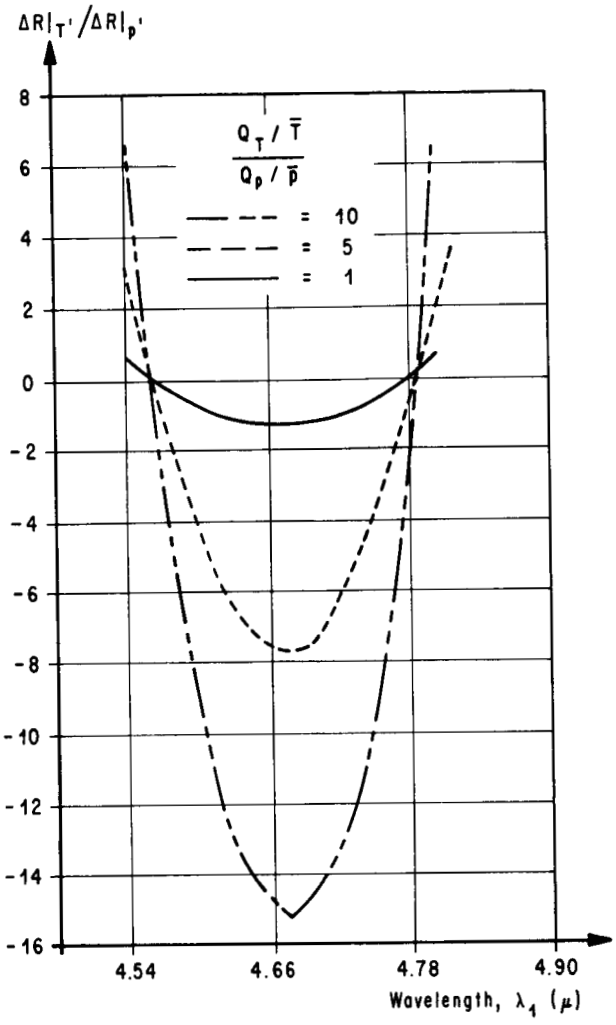

FIGURE 7. RATIO OF TEMPERATURE AND PRESSURE CONTRIBUTIONS TO CROSS CORRELATION COEFFICIENTS FOR 4.67 μ CO BAND
($p = 10^{-1}$ atm, $P = 10^{-1}$ atm, $T = 300°K$, $\ell = 10$ cm)

in Table I, the strong line approximation is valid to better than ten percent. The results are similar to those obtained for the weak line case.

C. COMBINATION OF STRONG AND WEAK LINE REGIONS

1. Pressure Fluctuations. The ratio of the partial pressure fluctuation terms in the cross-correlation coefficient for one strong and one weak line region yields the expression

$$(\bar{p}/\bar{P})^{1/2} = \frac{R_1/R_2}{\sqrt{C_1(\Delta\omega)_1 P_0}} \left(\frac{C_2(\Delta\omega)_2\, b_0 d_1^2}{C_1(\Delta\omega)_1\, \ell\, d_2^2}\right)^{1/2} \cdot T^{1/2} \times (T_0/T)^{1/4}\, e^{-\frac{hc}{8kT}\left[\frac{(\Delta\omega)_2^2}{B_2} - 2\frac{(\Delta\omega)_1^2}{B_1}\right]}, \quad (44)$$

where the subscripts (1) and (2) refer to the weak line and strong line measurements, respectively. A similar expression is obtained for static pressure fluctuations except that p and P are interchanged. In either case, the expression contains all three thermodynamic properties, as well as path length. If the strong and weak line regions are for the same molecular band, this expression reduces to

$$(\bar{p}/\bar{P})^{1/2} \frac{R_1/R_2}{\sqrt{C_1(\Delta\omega)_1 P_0}} (T_0 \cdot T)^{1/4} \times \left(\frac{b_0 \Delta\omega_2}{\ell \Delta\omega_1}\right)^{1/2} e^{-\frac{hc}{8kTB}\left((\Delta\omega)_2^2 - 2(\Delta\omega)_1^2\right)}. \quad (45)$$

2. Temperature Fluctuations. For temperature fluctuations alone, the ratio of cross-correlation measurements for strong and weak line regions yields the expression

$$(\bar{p}/\bar{P})^{1/2} = \frac{R_1\left(\frac{hc(\Delta\omega)_2^2}{4kB_2\bar{T}} - \frac{3}{2}\right)}{R_2\left(\frac{hc(\Delta\omega_1)^2}{4kB_1\bar{T}} - 1\right)} \times \frac{(\bar{T}_0/\bar{T})^{1/4}\, T^{1/2}}{\sqrt{C_1(\Delta\omega)_1 P_0}} \times \left(\frac{C_2(\Delta\omega)\, b_0}{C_1(\Delta\omega)_1 \ell}\right)^{1/2} \exp\left[-\frac{hc}{8k\bar{T}}\left(\frac{(\Delta\omega)_2^2}{B_2} - 2\frac{(\Delta\omega)_1^2}{B_1}\right)\right] \quad (46)$$

which reduces to

$$(\bar{p}/\bar{P})^{1/2} = \frac{R_1}{R_2}\left(\frac{(\Delta\omega)_2}{(\Delta\omega)_1}\right)^{5/2} (T_0 \cdot T)^{1/4} \times \frac{(b_0/\ell)^{1/2}}{\sqrt{C_1(\Delta\omega)_1 P_0}} \exp\left[-\frac{hc\,(\Delta\omega)_2^2 - 2(\Delta\omega_1)^2}{8kB\bar{T}}\right] \quad (47)$$

for measurements within the same band. The use of these equations in a particular problem would be essentially the same as discussed for the pressure fluctuations.

3. Combined Temperature and Pressure Fluctuations. The analysis of systems with both temperature and pressure fluctuations for simultaneous observations of strong and weak line spectral regions is essentially the same as described above for two strong or two weak line regions. With observations at a sufficient number of wavelengths, it might be possible to eliminate the unknown integrals and evaluate the thermodynamic properties; however, this system of equations has not yet been evaluated. The only addition that might be offered is expressions that are applicable when the strong line is controlled by temperature fluctuations and the weak line by pressure fluctuations, or vice versa. Since these equations are also functions of (p, P, T, ℓ), they are not listed here.

Thus, it is seen that cross-correlation coefficient for observations of strong and weak line spectral regions carries information concerning the mixing ratio, partial pressure, static gas pressure, and the temperature, but this information is combined in one equation. There are several possible ways to use the combined observations of strong and weak line regions, each of which requires some knowledge concerning one or more thermodynamic properties. If the temperature is known (for example, from two weak line measurements) and the value of ℓ is set by the geometry of the experiment, it would be possible to determine the mole fraction of the absorber from equation (44). There are a large number of other potential applications, each of which must be considered quantitatively to establish the usefulness of this method.

VI. CONCLUSIONS

A remote-sensing system consisting of two active or passive beams could be used to provide spatially resolved average thermodynamic properties in planetary atmospheres or gas flows. The method requires a determination of the cross-correlation coefficient from the fluctuating components of the signal received at each detector. Turbulence parameters can be determined from the variation of the cross-correlation coefficient beam separation in space and time. The contribution to the cross-beam theory contained in this paper is a description of the additional information about the gas system that can be obtained from a spectroscopic analysis of the cross-correlation coefficient.

A number of assumptions have been made in this development, and the applicability of this theory of a particular experiment will be governed by the extent to which these limitations are met in practice. First, this is a "first order" theory, in that the second and higher order terms are neglected in the series expansion for the absorption coefficient. This is justified even for large higher order terms if the triple product between different thermodynamic and optical fluctuations are uncorrelated. Second, the equations are developed for vibrational transitions composed of pressure-broadened rotational lines. Since the temperature is related to the population distribution in rotational energy levels, this temperature is meaningful only for thermal equilibrium or as the rotational temperature. Third, the expressions relating the thermodynamic properties to the measured cross-correlation coefficient are developed only for the strong and weak line approximations to the statistical band model. None of these approximations represent any inherent limitation to the use of spectroscopic analysis in cross-beam studies. The extension of this method to either Doppler-broadened or combined Doppler and collision-broadened lines, atomic lines and other absorption band models would be a straightforward application of the same principles.

Within these limitations, it appears that spectroscopic applications of the cross-beam method would provide information that cannot be obtained with single-beam remote-sensing systems. The most important features of the method are as follows: (1) By using combinations of measurements for wavelengths at which the absorption is adequately described by the strong and weak line approximations, it would be possible to obtain spatially resolved measurements of the temperature, and the ratio of absorber pressure to total pressure. (2) A spectral analysis of the cross-correlation coefficient offers the possibility of distinguishing between the contributions of pressure and temperature fluctuations to the cross-correlation coefficient. (3) It would be possible to select wavelengths at which the pressure or temperature fluctuations were predominant, thus permitting the use of a rather simple expression for the temperature. It is interesting to note that there are one or more wavelengths at which the contribution of temperature fluctuations to the cross-correlation coefficient would be zero regardless of the magnitude of the temperature fluctuations.

The analysis of measurements made at two or more wavelengths in either weak or strong line spectral regions would provide an average temperature over a typical beam diameter. A series of measurements made throughout the medium would provide a temperature profile. This expression for the temperature is independent of the absorber pressure and static pressure regardless of whether the fluctuating signal is produced by pressure or temperature fluctuations. The ratio of cross-correlation coefficients for observations of a combination of strong and weak line spectral regions will provide a single equation relating the three thermodynamic properties (ρ, P, and T); some additional information is required to provide a measure of one of these parameters.

REFERENCES

1. Nestor, O. H.; and Olsen, H. N.: SIAM, Rev., vol. 2, no. 200, 1960.

2. Freeman, M. P.; and Katz, S.: J. Opt. Soc. Am.,vol. 50, no. 826, 1960.

3. Bockasten, K.: J. Opt. Soc. Am.,vol. 52, no. 885, 1961.

4. Barr, W. L.: J. Opt. Soc. Am.,vol. 52, 885, 1962.

5. Tourin, R. H.; and Krakow, B.: Applied Optics, vol. 4, no. 237, 1965.

6. Krakow, B.: AIAA Journal, vol. 3, no. 1359, 1965.

7. Fisher, M. J.; and Krause, F. R.: NASA TM X-53295, p. 66, April 1965.

8. Krause, F. R.; and Fisher, M. J.: NASA TM X-53462, p. 36, April 1966.

9. Fisher, M. J.; and Krause, F. R.: To be published, J. Fluid Mechanics.

10. Wolf, M.: J. Geophys. Res.,vol. 71, no. 2743, 1966.

11. Fisher, M.J.; and Davies, P.O.A.L.: J. Fluid Mech., vol. 18, no. 97, 1964.

12. Davies, P.O.A.L.: J. Fluid Mech., vol. 15, no. 337, 1962.

13. Plass, G.N.: J. Opt. Soc. Am.,vol. 48, no. 690, 1958.

14. Plass, G. N.: J. Opt. Soc. Am., vol. 50, no. 868, 1960.

15. Plass, G. N.: J. Opt. Soc. Am., vol. 49, no. 821, 1959.

16. Elsasser, M. W.: Phys. Rev.,vol. 54, no. 126, 1938.

17. Goody, R. M.; and Roy, J.: Meteorol. Soc., vol. 78, no. 165, 1952.

18. Wyatt, P.J.; Stull, V. R.; and Plass, G.N.: J. Opt. Soc. Am., vol 52, no. 1209, 1962.

19. Penner, S.S.: Quantitative Molecular Spectroscopy and Gas Emissivities. Addison-Wesley Pub. Co., Inc., Reading, Mass., 1959.

BIBLIOGRAPHY

1. O'Brien, B. J.; Allum, F. R.; and Goldwire H. C.: J. Geophys. Res., vol. 70, no. 161, 1965.

VIII. PUBLICATIONS AND PRESENTATIONS

A. PUBLICATIONS

TECHNICAL NOTE D-3578

October 1966

ANALYSIS OF THE LINEARIZED SUPERSONIC FLOW ABOUT POINTED BODIES OF REVOLUTION BY THE METHOD OF CHARACTERISTICS

By Alan D. Sherer

George C. Marshall Space Flight Center
Huntsville, Alabama

ABSTRACT

The method of characteristics applicable to the linear potential equation governing the supersonic flow over bodies of revolution at zero and small angles of attack is presented. For axisymmetric flow the equations used are those derived by Sauer and Heinz, whereas for flow due to angle of attack the equations are those derived by Oswatitsch and Erdmann. This analysis investigates the limits of applicability of these methods. The flow field computation was programmed in Fortran IV to be used for computing the axisymmetric and angle of attack flow fields about convex and concave parabolic ogives and cone-cylinder bodies of various body fineness ratios at low supersonic Mach numbers. The results of these computations were compared with J. L. Sims' exact method of characteristics, the linear theory of Reference 1, and, whenever available, with experimental data. It was found that these methods are applicable to flow fields where the hypersonic similarity parameter, $M_\infty \epsilon$, is less than about 0.6.

TECHNICAL MEMORANDUM X-53372

December 21, 1966

ESTIMATION IN THE NEGATIVE BINOMIAL DISTRIBUTION (U)

By A. Clifford Cohen, Jr.*

* Professor of Mathematics, University of Georgia, Athens, Georgia. The research reported was performed under NASA Contract NAS8-11175 with the Aerospace Environment Office, Aero-Astrodynamics Laboratory, Marshall Space Flight Center, Huntsville, Alabama.

George C. Marshall Space Flight Center
Huntsville, Alabama

ABSTRACT

Practical simplified procedures are developed in this paper for calculating estimates of parameters of the negative binomial distribution with probability function

$$f(x) = \frac{\Gamma(x+k)}{x!\,\Gamma(k)} p^k (1-p)^x; \quad x = 0, 1, 2\ldots$$

where $0 < p < 1$ and $k > 0$. Moment estimators, maximum likelihood estimators, and estimators based on moments and frequencies in selected classes are given both for the complete and for the truncated (with missing zero class) distribution. To facilitate calculation of the various estimators given, a table of the function $-p \ln p/(1-p)$ with entries to six decimals at intervals of 0.001 for the argument p, is included. Illustrative examples are also included.

TECHNICAL MEMORANDUM X-53397

February 21, 1966

THE ALLEVIATION OF AERODYNAMIC LOADS ON RIGID SPACE VEHICLES (U)

By Mario H. Rheinfurth

George C. Marshall Space Flight Center
Huntsville, Alabama

ABSTRACT

A necessary condition for the successful flight of a space vehicle through atmospheric disturbances is to maintain stability at all flight times. It is, however, equally important to keep the responses within the design limits of control deflections and structural loads of the vehicle. The study demonstrates how the control systems engineer can assist in this task by a judicious choice of the control system parameters. To this effect, several typical control modes are analyzed for some basic wind profiles. The extent to which a reduction of aerodynamic loads and control excursions can be expected is discussed for various wind, wind shear, and gust conditions. By restricting the analysis to planar and

linearized motion of the vehicle, it is possible to derive a set of preliminary design rules, which allows one to predict the relative merits of the discussed control principles when system parameters or wind structure is changed. In addition, the study provides nomograms for the quick determination of gain settings for accelerometer-controlled vehicles if the gain values are given for angle-of-attack control and vice versa.

TECHNICAL MEMORANDUM X-53495

July 28, 1966

EXPLICIT RUNGE-KUTTA INTEGRATION (U)

By Lyle R. Dickey

George C. Marshall Space Flight Center
Huntsville, Alabama

ABSTRACT

A fourth order Runge-Kutta method is applied to a system of linear differential equations. The solution over one time step is obtained explicitly as a function of initial conditions and the forcing function evaluated at the initial time, the final time, and the midpoint. Successive applications of this result can be employed to obtain an explicit solution for a number of time points which can later be used to rapidly determine solutions for a large number of different sets of initial conditions and forcing functions.

TECHNICAL MEMORANDUM X-53497

May 1, 1967

THE ENVIRONMENT OF VENUS: A DISCUSSION OF ITS ATMOSPHERE AND SURFACE (U)

By Robert B. Owen, C. L. Hasseltine, William T. Roberts, George S. West, and Jeanette A. Scissum

George C. Marshall Space Flight Center
Huntsville, Alabama

ABSTRACT

Presented is a self-consistent model atmosphere for the planet Venus, with emphasis on parameters of general use in developing vehicle design criteria. Kern and Schilling's program for generation of atmospheric parameter values is coupled with the most recent estimates of surface conditions in order to derive the atmospheric environment at different altitudes. A range of initial values is used to produce a parametric band most representative of actual conditions. Because of the extreme pressures and temperatures involved, it is felt that design for such an environment presents an engineering problem of the first magnitude.

(This document supersedes NASA TM X-53327, "Derivation of Parameteric Values for a Greenhouse Model of the Cytherean Atmosphere," dated September 7, 1965.)

TECHNICAL MEMORANDUM X-53498

August 5, 1966

MISSION ANALYSES AND TRAJECTORIES FOR THREE ZERO-DEGREE INCLINATION EARTH SYNCHRONOUS ORBIT MISSIONS USING THE SATURN V VEHICLE WITH THREE BURNS OF THE S-IVB STAGE (U)

By Bobby Ellison, Bobby G. Noblitt, and Archie C. Young

George C. Marshall Space Flight Center
Huntsville, Alabama

ABSTRACT

Three detailed zero-degree inclination earth synchronous orbit trajectories are presented for position sites of 103.4°, 208.9° and 231.4° east longitude from Greenwich. The trajectories presented use the Saturn V launch vehicle with three burns of the S-IVB stage. Propellant used to establish the 185.2 km altitude parking orbit (first burn of S-IVB) is limited to 40,000 lbs to allow sufficient remaining S-IVB propellant for perigee burn, boil-off, performance reserves, and apogee burn for establishing the synchronous orbit.

A typical synchronous orbit trajectory is presented. Also given are analyses of the major steps

required in positioning a spacecraft in a synchronous orbit, details of the Hohmann transfer ellipse, and a parametric analysis of deorbit and earth entry requirements and conditions.

TECHNICAL MEMORANDUM X-53500

August 8, 1966

AERO-ASTRODYNAMICS CONSIDERATIONS FOR THE APOLLO TELESCOPE MOUNT (U)

By Robert E. Lavender

George C. Marshall Space Flight Center
Huntsville, Alabama

ABSTRACT

This report presents the results of preliminary analyses which have been conducted by the Aero-Astrodynamics Laboratory relative to the Apollo Telescope Mount (ATM). The ATM is an experimental package consisting of a group of sensors in the visual, ultraviolet (UV), extreme ultraviolet (XUV), and X-ray spectral regions, and the necessary experimental support equipment to obtain scientific data by solar observations from earth orbit. The ATM package is considered to be hard-mounted to the Lunar Module (LM). Mission analysis, orbital aerodynamics, aerodynamic torque, orbital lifetime, dynamics and control are discussed. Preliminary mission timelines are included.

TECHNICAL MEMORANDUM X-53506

August 29, 1966

ON DYNAMIC RESPONSE OF A RECTANGULAR PLATE TO A SERIES OF MOVING LOADS (U)

By Frank C. Liu

George C. Marshall Space Flight Center
Huntsville, Alabama

ABSTRACT

This report examines the effect of a series of evenly spaced moving loads on an elastic rectangular plate that is clamped at all edges. Two types of loads are treated: (1) a uniformly distributed pressure over a fractional length of the plate and (2) an impulsive load. All loads across a plate are considered uniform.

The solution of the partial differential equation of vibration of a plate is assumed in the form of a double series with the generalized coordinates solved by using the Laplace transform method. Viscous damping is included.

Based on a two-term approximation, the steady-state dynamic response of the plate is obtained in analytical form from which the upper bounds of the maximum deflection and maximum bending stress are formulated. Numerical examples are given to illustrate the effect of the thickness of the plate, the aspect ratio, and the velocity of loads on the dynamic response. Three types of resonance conditions are derived.

TECHNICAL MEMORANDUM X-53511

October 6, 1966

MULTIPLE PLANET FLYBY MISSIONS TO VENUS AND MARS IN 1975 TO 1980 TIME PERIOD

By Archie C. Young

George C. Marshall Space Flight Center
Huntsville, Alabama

ABSTRACT

A detailed analysis of multiplanet flyby missions to Venus and Mars during 1975 to 1980 time period is presented. Results for multiplanet flyby mission opportunities in 1975, 1977, and 1978 are given. Data are presented for earth departure, planet encounter, and earth return phases of the mission.

A comparison of the desirable and undesirable features of a singleplanet (Mars) flyby mission and a multiplanet flyby mission is made. A timeline for all of the flyby missions studied is given in terms of earth departure date, planet encounter date, and earth return date.

TECHNICAL MEMORANDUM X-53512

September 7, 1966

EFFECTS OF RECENT NASA-ARC* HYPERVELOCITY IMPACT RESULTS ON METEROID FLUX AND PUNCTURE MODELS

By Charles C. Dalton

George C. Marshall Space Flight Center
Huntsville, Alabama

ABSTRACT

Recent NASA-ARC laboratory hypervelocity impact results are used to derive a formula for the just-puncturable thickness of a metallic target sheet. The derived formula is used for an interpretative comparison of photographic meteor data and the puncture data from the three Pegasus and two Explorer meteoroid measurement satellites. The logarithm of the mass-cumulative influx of meteoroids per square meter per second is found to be a nonlinear function of the logarithm of the least-particle mass in grams. A cubic polynomial for this function, with -14.52, -1.406, -0.0490, and -0.00074 for the values of the coefficients of respective ascending powers, fits the data and seems most appropriate for extrapolation over the mass range for cometary particles. The influx of asteroidal particles is estimated separately.

TECHNICAL MEMORANDUM X-53517

September 16, 1966

STATIC AERODYNAMIC CHARACTERISTIC OF THE APOLLO-SATURN V VEHICLE (U)

By Vehicle Aerodynamics Section
Aerodynamic Design Branch

George C. Marshall Space Flight Center
Huntsville, Alabama

ABSTRACT

This report presents the static aerodynamic characteristics of the Apollo-Saturn V total launch vehicle. The data are based primarily on wind tunnel tests of scale models. Normal and axial force characteristics and local force distributions necessary for performance, control, and basic structural analyses of the vehicle are presented. All results are presented for various Mach numbers between 0 and 3.0, with certain portions of the data extended to a Mach number of 8.0. These data are recommended for use in final analyses of the Saturn V vehicle.

TECHNICAL MEMORANDUM X-53521

February 1, 1967

SPACE ENVIRONMENT CRITERIA GUIDELINES FOR USE IN SPACE VEHICLE DEVELOPMENT (1967 REVISION) (U)

Edited by Robert E. Smith and Otha H. Vaughan, Jr.

George C. Marshall Space Flight Center
Huntsville, Alabama

ABSTRACT

This document provides a cross section of space environmental data applicable for use as design criteria guidelines in Marshall Space Flight Center Vehicle development programs and advanced studies related to future NASA programs.

Extensive use has been made of data from scientific literature and MSFC reports, as well as the data exchange between other NASA Centers and contractors. Particularly, data prepared by the Manned Spacecraft Center have been incorporated wherever possible to insure compatibility of development between Marshall Space Flight Center and Manned Spacecraft Center, especially in those areas where there are insufficient data to make definite conclusions. For more information relating to a specific environmental parameter the reader should contact the editors.

(This document supersedes NASA TM X-53273, dated May 27, 1965, which is now obsolete.)

TECHNICAL MEMORANDUM X-53528

October 21, 1966

* Ames Research Center

PERCENTAGE LEVELS OF WIND SPEED DIFFERENCES COMPUTED BY USING RAWINSONDE WIND PROFILE DATA FROM SANTA MONICA, CALIFORNIA

By Dennis W. Camp and Patricia A. Fox

George C. Marshall Space Flight Center
Huntsville, Alabama

ABSTRACT

Presented are percentage levels of wind speed differences computed from AN/GMD-1 wind profile data obtained at Long Beach and Santa Monica, California. Compiled in 13,152 profiles are nine years of rawinsonde wind profile data: January 1, 1956, through December 31, 1964. The results presented in this report are based on each kilometer of wind velocity data for the 1.0 through 25.0 km altitude interval. These results may be used as an aid in predicting statistical limits of upper level winds and to provide an understanding of the statistical probabilities of wind speed change as a function of time. Information such as this is also important for space vehicle launch and related operations.

TECHNICAL MEMORANDUM X-53534

November 4, 1966

SATURN SA-203 POSTFLIGHT TRAJECTORY (U)

By Jonathan B. Haussler

George C. Marshall Space Flight Center
Huntsville, Alabama

ABSTRACT

This report presents the postflight trajectory for the Saturn SA-203 test flight. The primary mission of SA-203, the second of the Saturn IB series, was to study the behavior of liquid hydrogen in an orbital environment. Trajectory-dependent parameters are given in earth-fixed, space-fixed ephemeris and geographic coordinate systems. A complete time history of the powered flight trajectory is presented at 1.0 sec intervals from guidance reference release to S-IB/S-IVB separation and at 5.0 sec intervals from S-IB/S-IVB separation to insertion. Tables of insertion conditions and various orbital parameters are included in a discussion of the orbital portion of flight.

TECHNICAL MEMORANDUM X-53538

November 14, 1966

ON CROSSED-BEAM MONITORING OF ATMOSPHERIC WINDS AND TURBULENCE WITH TWO ORBITING TELESCOPES (U)

By F. R. Krause, S. S. Hu, and A. J. Montgomery

George C. Marshall Space Flight Center
Huntsville, Alabama

ABSTRACT

This report documents the phase A feasibility study on the MSFC inflight experiment No. 23, entitled "Crossed-Beam Arrangements for Remote Sensing Missions." The crossed-beam test arrangement employs triangulation of two collimated beams of radiation for the remote sensing of the space and time variations of thermodynamic state variables such as tracer concentrations. The generation, convection and decay of trace constituents (aerosols, ozone, and water vapor) will modulate the mean radiation background such as scattered sunlight or thermal emission. The associated fluctuations of radiative power are then correlated to retrieve local information at the beam intersection from the integrated optical signals. The potential of crossed-beam test arrangement is illustrated by discussing analytically the measurement of horizontal wind profiles. It is conceivable to conduct crossed-beam missions with two astronomical telescopes (ATM) which are mounted on a single spacecraft in such a way that they point towards the earth.

TECHNICAL MEMORANDUM X-53542

December 1, 1966

ORBITAL INVESTIGATION OF PROPELLANT DYNAMICS IN A LARGE ROCKET BOOSTER (U)

By H. J. Buchanan and F. M. Bugg

George C. Marshall Space Flight Center
Huntsville, Alabama

ABSTRACT

Experimental data on the dynamics of liquid hydrogen in the 6.6 m (260 in.) diameter tank of an S-IVB stage during boost, at S-IVB stage cutoff, and in orbit are presented. For the boost phase of flight, the amplitude of the sloshing liquid decreased from approximately 0.25 m (10 in.) at the beginning of S-IVB stage boost to a minimum of about 0.038 m (1.5 in.) as the liquid level moved past the baffle. The frequency during the S-IVB stage engine burn increased from approximately 0.44 cycles per second to 0.70 cycles per second and showed good agreement with predicted values.

During orbital coast, periods of the liquid hydrogen oscillation were measured through a range of accelerations from $8.0 \times 10^{-5}\ g_o$ to $4.4 \times 10^{-4}\ g_o$. Period data taken while the acceleration was varying with time did not agree with either the predicted natural or coupled periods. Nearly steady-state conditions existed for the $8.0 \times 10^{-5}\ g_o$ acceleration and the 300 sec to 330 sec slosh periods measured at this acceleration were close to the predicted value of 315 sec. The good agreement between experiment and "high-g" theory (i.e., theory neglecting surface tension and contact angle effects) at this very low acceleration tends to verify the validity of Bond number as a criterion for defining "high-g" conditions with regard to liquid sloshing.

TECHNICAL MEMORANDUM X53545

December 5, 1966

PROPOSED MANNED DYNAMIC TESTING OF SPACE STRUCTURES

By Larry Kiefling

George C. Marshall Space Flight Center
Huntsville, Alabama

ABSTRACT

Dynamics problems likely to be encountered in orbital structures and some possible investigations to study these problems are outlined. The items proposed are dynamic measurements at each step in space station development, inclusion of failure analysis capability with space rescue mission, and an orbiting structures laboratory. Role of manned participation is emphasized.

A more detailed outline of one possible vibration test experiment is included as an appendix. The prime objective of this experiment to evaluate test equipment and procedures in orbit.

TECHNICAL MEMORANDUM X-53561

December 27, 1966

AN ORBITAL FACILITY FOR LOW GRAVITY FLUID MECHANICS EXPERIMENTS (U)

By H. E. Worley, F. M. Bugg, and H. J. Buchanan

George C. Marshall Space Flight Center
Huntsville, Alabama

ABSTRACT

A rotating, cable-connected space laboratory for conducting extensive low gravity fluid mechanics experiments is described. The advantages of the various types of existing experimental facilities are discussed in terms of the proposed facility. Existing low-g sloshing data are reviewed. The additional information needed is outlined, and a series of experiments for obtaining this information is proposed.

TECHNICAL MEMORANDUM X-53559

December 22, 1966

EFFECT OF REYNOLDS NUMBER ON SLOSH DAMPING BY FLAT RING BAFFLES (U)

By Larry Lott

ABSTRACT

This paper examines the existing slosh data for flat ring baffles revised for the purpose of defining

the effect of Reynolds number on damping. For this purpose, baffle drag coefficient is presented in terms of Reynolds number. These results show that drag coefficient increases sharply as Reynolds number approaches zero. This implies that, for very low Reynolds numbers such as those encountered under low g, slosh damping due to ring baffles will be significantly increased.

TECHNICAL MEMORANDUM X-53565

January 13, 1967

THE INFLUENTIAL ASPECTS OF ATMOSPHERIC DISTURBANCES ON SPACE VEHICLE DESIGN USING STATISTICAL APPROACHES FOR ANALYSIS (U)

By Robert S. Ryan and Alberta W. King

George C. Marshall Space Flight Center
Huntsville, Alabama

ABSTRACT

The influential aspects of various wind profile disturbances on the dynamic response of the vehicle are considered. Particular emphasis is given to separating the influence of wind shears, turbulence and quasi-steady wind speed on the dynamic response during the boost phase of flight. Four hundred and seven individual detailed (Jimsphere) wind profiles are the primary wind inputs, although the MSFC synthetic profile is also discussed. The time response to each profile is run and a statistical analysis made. Severe profiles are ranked in terms of the bending moment at two vehicle stations for the Saturn V vehicle. The influence of results on vehicle design and flight operational procedures is determined.

TECHNICAL MEMORANDUM X-53571

January 31, 1967

FEASIBILITY STUDIES OF A SHORT DURATION HIGH REYNOLDS NUMBER TUBE WIND TUNNEL (U)

By John W. Davis and Hal S. Gwin

ABSTRACT

A relatively inexpensive short duration test facility is described in which extremely high Reynolds number flows are practical in the subsonic, transonic, and supersonic speed ranges. Basically, the method described is a type of blowdown wind tunnel in which the air storage vessels have been replaced by a long tube filled with high pressure gas. Upon bursting of a diaphragm, a short duration steady flow is achieved behind the centered rarefaction fan which propagates into the supply tube. Useful testing may be accomplished during this period by expanding the gas to the desired test condition by conventional means.

Experimental results are presented indicating primarily the transient starting characteristics of a small scale pilot model facility tested. Experimentally determined test data showed close agreement with those predicted by unsteady expansion theory.

TECHNICAL MEMORANDUM X-53572

January 31, 1967

A COMPARISON OF FOUR CONTROL SYSTEMS PROPOSED FOR SATURN V LAUNCH VEHICLES (U)

By Phil Sumrall

George C. Marshall Space Flight Center
Huntsville, Alabama

ABSTRACT

Presented are the results of a study comparing four proposed control systems for the first stage flight of Saturn V launch vehicles. The primary basis of comparison is the effect on structural loads, using the bending moments at three stations as load indicators. Two of the systems sense only the vehicle attitude and attitude rate, while the other two systems also sense the lateral acceleration.

A yaw plane wind response analysis, including rigid body translation, rigid body rotation, four bending modes, five slosh modes, and a nonideal control system, was performed. The winds used in the study

were the Marshall synthetic profile and three selected Jimsphere-measured real wind profiles. Load relief obtained from the addition of accelerometer feedback in the control loop amounted to about 10 percent at maximum bending moment station. In view of predicted structural capabilities of the vehicle, this reduction in loads was not considered sufficient to offset the added complexity and the slight reduction in rigid body stability.

TECHNICAL MEMORANDUM X-53579

February 20, 1967

REVIEW OF THERMAL RADIATION FROM LIQUID AND SOLID PROPELLANT ROCKET EXHAUSTS (U)

By William C. Rochelle

George C. Marshall Space Flight Center
Huntsville, Alabama

ABSTRACT

A comprehensive review of the general theory of thermal radiation from liquid and solid propellant rocket exhausts is presented. More than 600 references are discussed and almost 500 equations describe the details of gaseous radiation, radiation from carbon particles, and radiation from aluminum oxide (Al_2O_3) particles. The equation of radiation transfer is derived in detail, and solutions include the effects of scattering (Mie and Rayleigh), as well as emission and absorption. The analyses of spectral line broadening and band models are presented for gaseous radiation, and formation and sizes of carbon and Al_2O_3 particles are discussed for particle radiation. Numerous methods of predicting gas and particle emissivities and radiative heating are critically analyzed, and the most accurate methods currently available are discussed in detail. Although the application of the general theory is directed toward radiation from the exhausts of the Saturn H-1, F-1, J-2 and RL-10 liquid propellant engines (for base heating) and of the solid propellant ullage and retro motors (for stage-separation heating), the basic theory applies to radiation from the exhaust of any liquid propellant engine or solid propellant motor.

TECHNICAL MEMORANDUM X-53580

February 23, 1967

ANALOG SIMULATION OF S-II STAGE PROPELLANT UTILIZATION SYSTEM

By James W. McCarter

George C. Marshall Space Flight Center
Huntsville, Alabama

ABSTRACT

The analog computer simulation of the Saturn V, S-II stage propellant utilization system and the programming procedure are presented. The amount of coupling between propellant sloshing and engine thrust through the PU system was determined. The frequency response of the system is plotted, using input frequencies covering the expected range of slosh frequencies. Also included are plots of engine thrust variation due to sloshing versus slosh frequency.

TECHNICAL MEMORANDUM X-53583

March 1, 1967

PRELIMINARY ANALYSIS OF A CABLE RETRIEVAL TECHNIQUE FOR THE TETHERED ATM WORKSHOP (U)

By H. Eugene Worley, W. L. Brady, and George F. McDonough

George C. Marshall Space Flight Center
Huntsville, Alabama

ABSTRACT

This paper presents a feasibility study of a cable retrieval technique for the tethered ATM workshop. The two-dimensional differential equations of motion are derived, and a time optimal control law is obtained using four cables to align the docking structures. Also, the capabilities of manned operation are investigated. The results of this study indicate that the cable technique is feasible and that a man can adequately control the retrieval.

TECHNICAL MEMORANDUM X-53587

March 9, 1967

STATIC AERODYNAMIC CHARACTERISTICS OF THE ABORTED APOLLO-SATURN V VEHICLE

By Robert M. Glasgow*

George C. Marshall Space Flight Center
Huntsville, Alabama

ABSTRACT

Presented are the static aerodynamic characteristics of the aborted Apollo-Saturn V vehicle. The data are based primarily on wind tunnel tests of scale models. Total normal and axial force characteristics with local normal, local axial, and local pressure force distributions necessary for performance, control, and basic structural analyses of the vehicle are presented. All results are presented for various Mach numbers between 0 and 3.0 and vehicle angle-of-attach variations between 0 and 16 degrees.

TECHNICAL MEMORANDUM X-53588

March 10, 1967

PRELIMINARY SATURN V/VOYAGER TRAJECTORY FROM EARTH TO MARS (U)

By J. Reynolds Duncan, Jr.

George C. Marshall Space Flight Center
Huntsville, Alabama

ABSTRACT

A preliminary Saturn V/Voyager trajectory to Mars is presented which conforms to the major guidelines as set forth in Voyager Project Estimate - 14 (VPE-14). It includes a typical boost to orbit and a sample interplanetary flight history for a 1973 mission. The intent of this trajectory is to complement the voluminous conic information already available. Some comments are made on the constraints considered, and the significant characteristics of the trajectory are pointed out.

---

* Mr. Glasgow is associated with Northrop Space Laboratories, Huntsville, Alabama.

TECHNICAL MEMORANDUM X-53593

March 30, 1967

SURVEY OF SOLAR CYCLE PREDICTION MODELS

By Jeanette A. Scissum

George C. Marshall Space Flight Center
Huntsville, Alabama

ABSTRACT

As scientists make greater strides toward unfolding the secrets of the activities of the sun, we become more aware of its influence on the activities of the earth. In recent years, a more definite correlation has been found between the number of spots on the sun and the density of the upper atmosphere. Since the lifetimes of satellites in orbit depend upon this density, future plans for space research on these satellites depend upon an adequate forecasting of the sunspot cycle. Some prediction techniques now in existence are presented in this report.

Although much literature is available on the solar cycle, the literature on solar cycle prediction is limited. Since many of the techniques are essentially duplicates, an effort is made to present the basic types in terms of procedures and results.

As an evaluation of the techniques becomes necessary, the need for greater prediction reliability becomes obvious. The ultimate means to this end is the formulation of an adequate theory on the reason and formation of sunspots. As we try to achieve this, an immediate objective is the synthesis of current ideas and theories on solar activity into a comprehensive theory having a statistically acceptable degree of reliability when applied to prediction.

TECHNICAL MEMORANDUM X-53599

April 21, 1967

RANGE SAFETY AERODYNAMIC CHARACTERISTICS OF THE APOLLO/SATURN V VEHICLES (U)

By Billy W. Nunley

George C. Marshall Space Flight Center

Huntsville, Alabama

ABSTRACT

The high angle of attack aerodynamic characteristics of the Apollo/Saturn V vehicles for range safety and emergency detection system studies are presented. Should a malfunction occur during vehicle boost, the emergency detection system senses the malfunction and initiates either spacecraft jettison or vehicle destruct or both. Launch range safety requires a definition of the impact area for the various debris resulting from vehicle destruct. For these analyses, aerodynamic characteristics are defined for the first, second, and third stage flight configurations. Normal force coefficient, axial force coefficient, and center of pressure are defined for power-on and power-off conditions at various Mach numbers (0 - 8.0) as a function of angle of attack (0° - 180°). These data are also defined for the S-IC stage alone for the power-off case. Drag coefficients for various stages, interstages, components, and combinations of stages and components are presented as a function of Mach number at angles of attack of 0°, 90°, 180°, and tumbling. For emergency detection system studies, local normal force coefficient distributions at high angles of attack ($20° \leq \alpha \leq 40°$) are defined for Mach numbers 0.2 to 7.0.

TECHNICAL MEMORANDUM X-53601

April 26, 1967

A PRELIMINARY ANALYSIS OF ORBIT INSERTION GUIDANCE FOR THE VOYAGER MISSION (U)

By Cort R. Flint

George C. Marshall Space Flight Center
Huntsville, Alabama

ABSTRACT

The terminal orbit insertion guidance maneuver for the Voyager mission was investigated. The study consists of two parts, the first a comparison of four types of possible guidance laws in terms of propellant efficiency with an optimum thrust program, the second an analysis of the accuracy characteristics of two of these schemes. This analysis was done by introducing navigation and implementation errors into these two guidance laws and observing the resulting error in the parameters of the terminal orbit. The gravity-turn law and constant direction in inertial space law, which compared favorably with the optimum thrust program, were chosen from part one to be used in part two. Both laws responded adequately to the induced errors without critical results. It was concluded that the preferred law would probably be the constant inertial law because it is the easier to mechanize.

TECHNICAL MEMORANDUM X-53608

May 15, 1967

LOW GRAVITY SIMULATION BY HIGH ALTITUDE DROP TESTING (U)

By Frank Bugg

George C. Marshall Space Flight Center
Huntsville, Alabama

ABSTRACT

A high altitude drop test technique for simulation of low gravity environments has been investigated. It was found that continuous low gravity test times of 24 to 26 seconds could be achieved with a maximum drag shield velocity of 820 ft/sec. Thrust applied to the drag shield opposing the drag force was required to limit the travel of the experiment package relative to a drop, application of a thrust increasing at a constant rate, and delayed application of a constant thrust were studied. The latter two thrust methods gave the better results (i.e., longer test times with shorter drag shield required). In some cases, 22 to 24 seconds of low gravity test time were indicated with a drag shield which allowed 15 feet of longitudinal travel of the experiment package relative to the shield.

The effects of changes in longitudinal aerodynamic stability and wind profile on the drag shield and experiment package dynamics were also studied. A wide range of values for the stability parameter was found to be acceptable. The lateral motion of the experiment package relative to the drag shield was less than one-half foot for the most severe conditions of wind and aerodynamic stability investigated.

TECHNICAL MEMORANDUM X-53609

May 18, 1967

SPECTRAL DECOMPOSITION OF THE CROSS-CORRELATION FUNCTION (U)

By Robert E. Cummings, Quintin D. Peasley, Jack W. Bradford, and William E. Hinds

George C. Marshall Space Flight Center
Huntsville, Alabama

ABSTRACT

The development and evaluation of numerical and logical procedures for computing co-Spectral and quad-Spectral Density estimates from given cross-correlation data points, together with the first and second differences at these points, are documented. The relative merits of linear versus logarithmic spacing of the time lags for the chosen cross-correlation points are tested and demonstrated. These results fail to show a sufficient advantage in using logarithmic spacing to overcome the inherent operational and numerical error problems; thus, linear spacing of time lags is recommended for use with these numerical procedures.

TECHNICAL MEMORANDUM X-53613

May 24, 1967

SUMMARY OF HEAT FLUX AND PRESSURE INSTRUMENTATION USED IN RECENT SATURN ROCKET EXHAUST TESTS (U)

By William C. Rochelle

George C. Marshall Space Flight Center
Huntsville, Alabama

ABSTRACT

Various types of instrumentation used in obtaining heat flux and pressure measurements in the exhausts of a number of Saturn rockets fired in the last two years are discussed. Analysis of experimental data obtained by various measuring techniques is an important factor in correlating predictions of pressure and heating from exhausts of liquid propellant main stage engines and solid propellant ullage and retromotors used for stage separation purposes. The testing techniques at various facilities including type and location of instrumentation used and principal results obtained from the instrumentation are described.

TECHNICAL MEMORANDUM X-53616

June 8, 1967

NATURAL ENVIRONMENT DESIGN CRITERIA FOR MSFC VOYAGER SPACECRAFT FOR MARS 1973 MISSION (U)

Edited By Don K. Weidner and C. L. Hasseltine

George C. Marshall Space Flight Center
Huntsville, Alabama

ABSTRACT

This document contains the natural environment information that is essential to the design of the Voyager spacecraft for the 1973 Mars mission.

Since much of this information is in a state of flux because of the rapid advancement of the state-of-the-art, a continuing effort will be made to update and refine these specifications as later data become available. For more information relating to a specific environmental parameter, the reader should contact the Space Environment Branch.

TECHNICAL MEMORANDUM X-53617

June 8, 1967

By W. H. Heybey

George C. Marshall Space Flight Center
Huntsville, Alabama

ABSTRACT

Light falling on an engineering surface will be reflected partly in a preferred direction (specularly), partly in a diffuse manner. The scattering of the

light energy is assumed to follow Lambert's cosine rule. The force differential acting on an elemental surface is set up for such cases of mixed reflection. A smoothness coefficient ($\leqq 1$) accounts for that portion of the reflected energy that is rediated specularly. A loss coefficient, also $\leqq 1$, gives the fraction of the incident energy that enters into the reflected light.

Applications are made to the sphere and its motion under the impact of light, and to the circular cone with fully illuminated curved surface, some results being added when a shadow region exists on it.

TECHNICAL MEMORANDUM X-53622

June 19, 1967

A GENERAL PROGRAM FOR THE CALCULATION OF RADIATION FROM AN INHOMOGENEOUS, NONISOBARIC, NONISOTHERMAL ROCKET EXHAUST PLUME (U)

By Robert M. Huffaker and Marcus J. Dash

George C. Marshall Space Flight Center
Huntsville, Alabama

ABSTRACT

This report describes a computer program for evaluating radiation from an axisymmetric gas body with water vapor, carbon dioxide, carbon monoxide, and solid carbon particles as radiating constituents, and hydrogen as a non-radiating constituent. The program uses band-averaged absorption coefficients with the Curtis-Godson method of approximating inhomogeneous gas properties. This program provides a convenient method of evaluating a great many problems of radiation from rocket exhaust plumes, but available theory is somewhat limited by simplifications in the geometry and input of the program. A more advanced program is being formulated to remove these restrictions.

TECHNICAL MEMORANDUM X-53624

June 20, 1967

PEAK SURFACE WIND EXPOSURE PERIOD STATISTICS FOR CAPE KENNEDY, FLORIDA (U)

By Lee W. Falls

George C. Marshall Space Flight Center
Huntsville, Alabama

ABSTRACT

The many estimates of peak wind speed probabilities derived from empirical statistics have not been completely satisfactory. The purpose of this paper is to present theoretical probabilities of encountering peak surface winds at Cape Kennedy, Florida, for aerospace vehicle operations and mission analysis. The theory of extreme values developed by E. J. Gumbel was found to be an adequate statistical model for the analysis of extreme surface winds. Comprehensive peak surface wind statistics derived from this model are on file within the Aero-Astrodynamics Laboratory, Aerospace Environment Division.

TECHNICAL MEMORANDUM X-53630

June 30, 1967

INHOMOGENEOUS RADIANT HEAT TRANSFER FROM SATURN ROCKET EXHAUST PLUMES (U)

By Robert M. Huffaker

George C. Marshall Space Flight Center
Huntsville, Alabama

ABSTRACT

A radiant heat transfer computer program has been developed to calculate radiation from inhomogeneous gases prevalent in rocket exhaust plumes from clustered engines. The infrared spectral absorption characteristics of the radiating species considered in this computer program - water vapor, carbon dioxide, carbon monoxide and carbon particles - have been determined. Band model parameters have been used to represent the infrared spectral absorption coefficients over 25 cm^{-1} increments. A modified Curtis-Godson approximation, used in the inhomogeneous heat transfer calculation, has been shown to give satisfactory results over the temperature and pressure range of interest in Saturn exhaust plumes. Results are shown for the Saturn-type engines for specific

flow field assumptions. Some comparison with experimental spectroscopic data will also be presented. The effects of wavelength increment, field of view, and distance increment along the line of sight on the heat transfer, as well as the computer techniques for minimum computer time in calculating radiation from a three-dimensional flow field, are discussed.

TECHNICAL MEMORANDUM X-53631

June 30, 1967

APPLICATION OF HIGHER-ORDER RUNGE-KUTTA INTEGRATION TECHNIQUE DEVELOPED BY ERWIN FEHLBERG TO LOW-THRUST TRAJECTORIES (U)

By John Thomas Wheeler

George C. Marshall Space Flight Center
Huntsville, Alabama

ABSTRACT

The differential equations of motion including the perturbative terms for a point mass under low thrust in an inverse-square central force field are formulated in terms of the Lagrangian function using the variational method (the Euler-Lagrange equations). First-order Hamiltonian equations of motion are obtained. Derived in the form by use of power series expansions, the recurrence formulas are developed to provide the coefficients for two thrust-direction control programs. Fehlberg's higher-order Runge-Kutta formulas with step-size control is used as an integration method of calculating low-thrust trajectories. Shanks' integration method is computed to provide an accuracy comparison with Fehlberg's technique.

B. PRESENTATIONS

SATURN FLIGHT CONTROL SYSTEMS

By J. A. Lovingood and E. D. Geissler

ABSTRACT

The flight control systems of the Saturn launch vehicles are described and discussed. In order to provide insight into the basis for the Saturn control configurations, the functional control design process is described in its various stages, including a discussion of control objectives, determination of vehicle and wind models, selection of sensors and control law, consideration of structural loading and elasticity effects, and final system evaluation through simulation. The resulting designs are shown to be simple and effective in meeting the many requirements and objectives.

Published in Astronautics and Aeronautics, vol. 4, no. 5, May 1966.

THE LUNAR SURFACE: INTERPRETATIONS OF DATA FROM RANGER VII, VIII, IX, AND THE SURVEYOR I MISSION

By O. H. Vaughan

ABSTRACT

Lunar Surface as seen by earth based telescopes is reviewed. Major theories for the formation of lunar features are discussed, data from Ranger VII, VIII, and IX are summarized. An interpretation for the formation of the central peak in the crater Alphonsus is presented. Data from Surveyor I are summarized and a hypothetical surface model is presented.

Speech delivered to the ASEE-NASA Summer Fellowship Conference, Marshall Space Flight Center, Huntsville, Alabama, July 5, 1966.

THE AUTOMATION OF OPTIMIZATION PROBLEMS

By Hugo L. Ingram

ABSTRACT

The mathematical simulation of optimal powered flight trajectories for space vehicles can be accomplished in a variety of manners. This paper is intended to show how the development of the differential associated with an optimal simulation can be determined and programmed using the IBM-FORMAC language. The IBM-FORMAC programming language is able to accept functional expressions in a Fortran format and perform addition, subtraction, multiplication, division, and partial differentiation operations on these functional expressions. The results of the operations are produced in a Fortran format which can then be executed with desired numbers for the variables in the Fortran expressions.

Presented at the American Astronautical Society Space Flight Mechanics Specialist Conference, Denver, Colorado, July 6-8, 1966.

OPTIMIZATION PROBLEMS CAUSED BY INTERACTION OF GUIDANCE AND PROPELLANT SYSTEMS

By Doris C. Chandler, Helmut J. Horn and Robert S. Ryan

ABSTRACT

Optimization of the power flight of a liquid propellant space vehicle requires a guidance system which determines the instantaneous optimum thrust attitude, a control system which executes this steering command, and a propellant utilization (P.U.) system which assures simultaneous depletion of both propellants (e.g., liquid hydrogen and liquid oxygen).

As these systems interact, stability problems can occur, even while each system by itself may work perfectly. This paper treats the solution of such a problem encountered in the Saturn vehicles.

Presented at the Space Flight Mechanics Specialist Conference, University of Denver, Denver, Colorado, July 6-8, 1966.

ADVANCED CONTROL SYSTEMS FOR LAUNCH VEHICLES

By E. D. Geissler, James C. Blair, and Judson A. Lovingood

ABSTRACT

This article discusses the problem areas foreseeable in launch-vehicle control, presents certain systems proposed as solutions, and indicates where some of the wealth of modern control theory that has been developed over the past few years may be applied.

Published in Astronautics and Aeronautics, vol. 4, no. 8, August 1966.

INTRODUCTION TO THE MOON

By John Bensko and Otha H. Vaughan, Jr.

ABSTRACT

This article presents reasons for going to the moon and answers such questions as: What do we know about the moon? Where will we land and explore the moon? A discussion of orbiter spacecraft and photography is presented. Other topics in this article include: a discussion of the moon's environment; development of a lunar drill; and lunar basing and surface exploration.

Speech for "Alabama in Space" Program sponsored by Marshall Space Flight Center, NASA and WHNT as a public service, August 9, 1966.

THEORY OF A REFINED EARTH FIGURE MODEL

By Helmut G. L. Krause

ABSTRACT

Starting from the expansion in spherical harmonics of the geopotential, $U(r, \phi, \lambda)$, of a rotating oblated, inhomogeneous three-axial earth model, the three components of the gravity acceleration vector, $\bar{g}$ = grad U, were obtained. Inserting the generalized equation for the surface of the geoid, $R = R(\phi, \lambda)$ - also as expansion in spherical harmonics and transformed into a power series of the sine of the geocentric latitude ϕ - into the equation for the constant surface potential (equipotential surface), U_0, quantitative mathematical relationships have been obtained between the oblateness coefficients of the zonal and tesseral harmonics and the geometrical and gravitational parameters of the earth, especially between the oblateness coefficients of the odd harmonics and the difference of the polar radii (respectively, ellipticities and polar gravity accelerations) in the northern and southern hemispheres. A more accurate form of Clairaut's theorem of the earth's figure is given. This new refined theory of the earth replaces the first, second, and third order theories of the earth's figure developed by Clairaut, G. H. Darwin, Callandreau, Helmert, deSitter, Herrick, Cook and others.

Paper Presented at Symposium on Celestial Mechanics Oberwolfach, West Germany, September 12-16, 1966. Paper will be published as a NASA-Technical Report (TR).

A NEW TECHNIQUE FOR SIMULATING ROCKET ENGINE FLOW FOR STUDY OF BASE HEATING PROBLEMS

By Homer B. Wilson, Jr.

ABSTRACT

A short-duration technique has been developed which provides excellent simulation of thermodynamic properties and composition of the exhaust products of long-duration model and full-scale rocket engines using liquid or solid propellant. Flow durations through the scale model rocket nozzle (on the order of 10 milliseconds) are sufficient to achieve steady-state operation and establishment of proper flow fields, but short enough to alleviate many of the usual complex engineering problems associated with conventional continuous operating hot flow rocket models. The short-duration technique has been used to generate design data for all stages of the Saturn vehicle. The results show reasonable agreement with flight results. Extensive measurements have been made of the flow field for a four-engine base configuration. The results show the effect of Reynolds number on base film coefficient and recovery temperature and the effect of temperature discontinuity on base film coefficient.

Also, a short-duration wind tunnel capable of producing flow over a range of Mach numbers has been developed and is currently in operation with short-duration base heating tests. The short-duration wind tunnel and some typical results are briefly described.

Presented at the AIAA Testing Conference, Los Angeles, California, September 22, 1966.

REMOTE SENSING OF LOCAL FLOW INSTABILITIES AND TURBULENCE

By

F. R. Krause
George C. Marshall Space Flight Center
Huntsville, Alabama

M. J. Fisher
IIT Research Institue
Chicago, Illinois

ABSTRACT

A new test arrangement and a new statistical data analysis have been developed for remote sensing methods. Previous publications discuss how to obtain statistical, reliable, and local information where other remote sensors average over single optical paths. The new arrangement uses two narrow light beams for remote sensing. The second beam is adjusted to intersect the first at the local and distant area of interest. The optical integration along each beam is then partially eliminated by a cross correlation of the detected fluctuations.

The method estimates the space-time correlation between two fluctuations in separate locations. A comparison with hot-wire probes shows that the spatial and temporal variation of turbulence parameters, such as scales, convection speeds, eddy lifetimes, spectra, etc., can be resolved. The measurement of three- and four-dimensional wave number components is made possible by an automatic optical integration over plane gas dynamic wave fronts. The theoretical restrictions and practical limitations are reviewed.

Presented at the ASME Flow Measurement Symposium, Pittsburg, Pa., September 26-28, 1966.

THE USE OF WIND SHEARS IN THE DESIGN OF AEROSPACE VEHICLES

By Robert S. Ryan and James R. Scoggins

ABSTRACT

The relative influence of various wind profile properties and disturbances on launch vehicle flight dynamic response is studied. Particular emphasis is placed on the influence of wind shears and turbulence on dynamic response during the boost phase of the flight. Four hundred and seven individual detailed (Jimsphere) wind profiles are the primary wind inputs for this analysis. Time response of the vehicle to each profile is computed and a statistical evaluation of the results is made. Results are obtained for the Saturn V space vehicle and conclusions are drawn as to the relative influence of wind shears and turbulence vs the degree of refinement of the dynamic model of the space vehicle.

Presented at the 23d meeting of the Structures and Materials Panel, AGARD, ONERA, Paris, France, October 4-11, 1966.

ADVANCED FLIGHT CONTROL TECHNIQUES FOR LARGE LAUNCH VEHICLES

By Jerome R. Redus

ABSTRACT

The advance theory and synthesis techniques being developed for future launch vehicle flight control are discussed. Emphasis is placed on linear optimal control theory which eliminates much of the trial and error approach to conventional control system synthesis.

Presented at the Fourth Annual DOD/NASA/FAA Navigation, Guidance Control Symposium, Wright-Patterson AFB, Ohio, October 11-12, 1966.

A REVIEW OF SOME EXISTING LITERATURE CONCERNING DISCONTINUOUS STATE VARIABLES IN THE CALCULUS OF VARIATIONS

By Rowland E. Burns

ABSTRACT

The important problem of determining optimal trajectories for problems with discontinuous state variables has been treated by a few authors in rather esoteric papers. This paper summarizes the contents of two of these in a fairly detailed discussion. An attempt has been made to develop explicitly those relationships which are not contained in material dealing with the case of continuous state variables.

The essential feature of the discussion is a transformation from a set of state variables with points of discontinuity to a set of new variables which, though greater in number, are continuous. The necessary conditions of Euler, Weierstrass, and Clebsch, along with the transversality conditions, are discussed in the transformed problem; the results are rewritten in the original variables.

The bulk of material covered assumes that the magnitudes of the discontinuities are known a priori, but the case of unknown discontinuities is treated in the latter portion of the paper.

Presented at the Southeastern Section of the American Astronautical Society's Missiles and Aerospace Vehicle Sciences Symposium, Huntsville, Alabama, November 29, 1966.

RANDOM NUMBER SOLAR CYCLE PREDICTION TECHNIQUE

By

Harold C. Euler

George C. Marshall Space Flight Center
Huntsville, Alabama

ABSTRACT

The object of this paper is to present a solar cycle twenty prediction based upon random number techniques, Fourier curve fits, and power spectra.

The approach was to attempt to produce an accurate Fourier curve fit of each of the first nineteen sunspot cycles plotting corresponding coefficients versus time, with the objective of selecting a set of coefficients which approximate cycle twenty. Then, using the first 770 days of cycle twenty, we produced what appears to be a more accurate set of cycle twenty coefficients using a random walk method.

Results are based on an extensive statistical analysis including arithmetic means, standard deviations, variance, skewness coefficients, kurtosis coefficients, auto correlations, covariance, power spectral, and Fourier coefficients. Included are tables of Fourier sunspot coefficients using positive cycles followed by the same negative cycle. By considering the same cycle as both positive and negative, the sum of the Y sub I's from the initial to the terminal point is essentially zero, thus, eliminating the average value, A_0 with one less coefficient to keep track of. Various choices of end points were considered. Plots of a best curve fit of each of nineteen cycles are included with coefficients to n = 10.

Also included is supplementary and supporting data on spectral analysis of sunspot numbers such as a plot of the unsmoothed power spectral density for each of nineteen cycles.

The random walk method essentially used numerous combinations of trial guess coefficients and trial periods. The initial values were extrapolated from the Fourier curve fit of the first nineteen cycles. We first concentrated on the fundamental and permitted the coefficients to be random within an arbitrary path width which was decreased as the residual decreased. The harmonic number and period was also allowed to be random within a path width. The computer produced a printout only when an improvement in the residuals was found. After the fundamental we progressively used the 3, 5, 7, 9, 11, 13, 17, 19, 21, 65, 90, and 332 harmonic.

Presented at the American Astronautical Society meeting in Huntsville, Alabama, on December 5, 1966.

PROBABILITY OF SOLAR FLARE OCCURRENCES

By William T. Roberts

Aero-Astrodynamics Laboratory
George C. Marshall Space Flight Center
Huntsville, Alabama

ABSTRACT

Solar flares are observed on the solar surface as sudden increases in light intensity, especially in the hydrogen-alpha spectral line at 6563 Å. They are generally observed in the vicinity of sunspots and have a duration of a few minutes to a few hours. The phenomenon apparently occurs as a result of the catastrophic expulsion of high energy particles, which erupt from the photosphere into interplanetary space.

When and if these particles reach the earth, they may create atmospheric disturbances, such as aurora, or geomagnetic field disturbances, such as magnetic storms. To a spacecraft outside the protection of the earth's magnetic field, however, they may represent a lethal hurricane. Whereas these particles raining down upon the spacecraft may not veer its course nor cause it to incandesce as the typical t vision audience is asked to believe, the resulting radiation from these particles may cause irreparable damage to the spacecraft, its experiments, or its occupants.

Presented at the American Astronautical Society meeting in Huntsville, Alabama, on December 5, 1966.

THE ATMOSPHERE OF MARS: A DERIVATION OF ENGINEERING AND DESIGN PARAMETERS

By W. T. Roberts and G. S. West

Aero-Astrodynamics Laboratory
George C. Marshall Space Flight Center
Huntsville, Alabama

ABSTRACT

The successful Mariner IV mission to Mars yeilded a wealth of new information on surface conditions, atmospheric conditions, the planetary magnetic field and the planetary mass. From these data, three model atmospheres have been constructed for use in mission analyses, lander capsule and probe design, and orbiter and fly-by studies. Atmospheric parameters have been calculated from the surface to 10,000 kilometers. Three models of differing composition, surface pressure, and temperature provide an envelope of values of atmospheric parameters at each altitude.

The new data from Mariner IV together with some assumptions concerning the ionizing effects of the solar radiation were used as input data to MODAT, the computer program of Kern and Schilling.

The results of this study indicate, in the case of Model I (Upper Density Model), the atmospheric drag on aerospace vehicles is correspondingly less on Mars than on Earth below 700 kilometers and correspondingly greater on Mars than on Earth for altitudes greater than 700 kilometers. In the three models considered here, the absence of an extensive isothermal region results in large scale heights above 200 kilometers. In addition to the factors contributed by the 100 percent CO_2 atmosphere considered in Model II (Mean Density), the inclusion of argon in Model III (Lower Density) and nitrogen in Model I provides output data of interest in the consideration of aerodynamic heating factors in the Martian atmosphere.

Presented at the American Astronautical Society meeting in Huntsville, Alabama, on December 5, 1966.

ENVIRONMENT OF JUPITER

By Carroll L. Hasseltine

Aero-Astrodynamics Laboratory
George C. Marshall Space Flight Center
Huntsville, Alabama

ABSTRACT

The clouds surrounding Jupiter are discussed as to type, composition, and temperature. An upper atmospheric model for that portion above the clouds is developed following the upper atmospheric properties described by Gross and Rasool. Estimates are made of what one might find beneath the cloud cover and on the surface of Jupiter.

The planet Jupiter is the largest and most massive of the planets in the solar system. It has also the shortest rotation period, approximately 9 hours and

55 minutes; the highest value of gravitational acceleration, 26 meters per second; and the most moons, a total of 12.

Viewed through a telescope, Jupiter has a distinct elliptic appearance with alternate light and dark bands of clouds running parallel to the equator. These bands are probably created from the planet's high rotation speed. In addition, a marking known as the "Great Red Spot, " an area of some 1.84×10^9 square kilometers, is present in the south tropical zone.

Spectrograms of light reflected from Jupiter first identified the presence of ammonia and methane in its atmosphere. It was later realized that considerable amounts of hydrogen and helium also were present. It is now believed that the atmosphere above the cloud tops is dominantly hydrogen and helium and that the outer cloud layer of Jupiter is composed of very small crystals of ammonia.

Temperature measurements of Jupiter at different infrared wavelengths indicate an increase in temperature below this ammonia cloud layer. The cloud top temperature was determined by Menzel using radiometric measurements to be 130° K. Others have estimated this temperature to be as high as 158°K. Due to the probable increase in temperature below the cloud tops, it has been suggested that there may be liquid and vapor ammonia below the ammonia crystals.

Model atmospheres of Jupiter have been few due to the scarcity of data on which to base them, and these pertain only to elevations above the cloud top. Gross and Rasool have published a temperature-height distribution above the clouds based on radiative equilibrium. This, with an assumed molecular weight for the atmospheric composition and a pressure of three atmospheres at the cloud top, permits computation of a pressure and density height distribution. Trafton has also computed a pressure, temperature, height distribution above the cloud top height.

The height of the cloud tops above the surface of Jupiter is unknown as is the composition. The temperature, however, probably is greatest near the planet, and the surface pressure is on the order of 1000 earth atmospheres.

Presented at the American Astronautical Society Meeting in Huntsville, Alabama, on December 5, 1966.

PREDICTION OF THE LUNAR THERMAL ENVIRONMENT

By

Otha H. Vaughan, Jr.
George C. Marshall Space Flight Center

Frank B. Tatom and K. V. Ramakrishna
Northrop Space Laboratories

ABSTRACT

A research effort has been carried out to provide a means of predicting the lunar surface temperature. The analytical model, developed during the study, consists of two parts. The first part locates the subsolar point, and then calculates the shape factor of the Sun with respect to the point of interest on the lunar surface. The model treats the Moon as a non-gray (absorptance thermal conductivity) covering a homogeneous interior. The governing heat transfer equations, which are expressed in finite difference form, are based on a periodic heat transfer process involving thermal radiation and conduction.

Based on the analytical model a digital computer program capable of predicting the lunar surface temperature at any time in the past or future for any point on the Moon has been developed. As by-products, the radial temperature distribution beneath the lunar surface, the selenographic coordinates of the subsolar point, and the local zenith angle of the Sun are generated. The most noteworthy feature of the program is its self-sufficiency. The inputs required are basically the location of the point of interest (expressed in selenographic latitude and longitude), the time of interest (expressed in Greenwich Mean Time and calender date), and the thermophysical properties assumed to exist at the point under analysis. No reference to astronomical tables is necessary. Thus, the program can be used by individuals who are relatively unfamiliar with the actual problem of predicting the lunar surface temperature.

Generally good agreement has been observed in comparison between predicted values of temperatures by the program and observed values reported by various authors. Judicious selection of thermophysical properties has proved extremely important in obtaining good correlation.

This paper covers the first phase research effort, that of predicting the surface temperature. The second phase of this effort will be to predict the surface temperature of objects which are in direct contact or can see the surface.

Presented at American Astronautical Society Southeastern Symposium on Missiles and Aerospace Vehicle Sciences, December 5-7, 1966, Huntsville, Alabama.

THEORY OF A REFINED EARTH FIGURE MODEL WITH APPLICATIONS

By Helmut G. L. Krause

ABSTRACT

A new theory of the earth's figure is developed taking as reference for the surface of the earth no longer the surface of a three-axial ellipsoid but the surface of the geoid, assumed as the equipotential surface at sea level. Quantitative mathematical relationships have been obtained between the coefficients of the zonal and tesseral harmonics in the geopotential and the geometrical and gravitational parameters of the northern and southern hemispheres of the earth.

Starting from the newest values for the oblateness coefficients of the even and odd spherical harmonics up to the 14th degree, given by Y. Kozai in 1964, the new theory gives a mean meridional reciprocal flattening $1/f = 298.17$. The corresponding values for the northern and southern hemispheres are, respectively, $1/f_N = 298.43$ $1/f_S = 297.91$. The difference of the polar radii is $\Delta R_p = R_{p_N} - R_{p_S} = 37.8$ m, and the difference of the polar gravity accelerations is $\Delta g_p = g_{p_S} - g_{p_N} = 13.4$ mgal. The equator has an ellipticity of $f_e = 1.082 \times 10^{-5} = 1{:}92400$, corresponding to a difference between the largest and smallest equatorial radius $\Delta R_e = 69.0$ m and a maximum difference in the equatorial gravity accelerations $\Delta g_e = 31.8$ mgal.

Using the same earth constants, a numerical formula has been derived for the radius of the geoid (equipotential surface at sea level), expressed in meters, as function of the geocentric latitude ϕ and the geographic longitude λ. This formula contains 14 terms, depending on the zonal harmonics up to the 14th degree, and one term, which is the main term due to the tesseral harmonics. A formula for the equation of the surface of a three-axial ellipsoid has been derived and developed into a series. The numerical form for the radius of the ellipsoid, based on the same earth constants, gives the same values for the equatorial radius and the mean polar radius of the earth as the formula for the geoid. The radial difference between the geoid and the ellipsoid is 1.76 m for $\phi = +45°$ and 7.98 for $\phi = -45°$. A formula with 15 terms has also been derived for the normal gravity acceleration at sea level, expressed in mgals.

Paper Presented at the Southeastern Symposium in Missiles and Aerospace Vehicles Sciences of the American Astronautical Society, Huntsville, Alabama, December 5-7, 1966. Proceedings of the Symposium vol. 1, December 1966, pp. 7-1 to 7-14.

THE DETERMINATION OF AVERAGE THERMODYNAMIC PROPERTIES WITH OPTICAL CROSS-CORRELATION METHODS

By

F. R. Krause, Scientific Assistant
George C. Marshall Space Flight Center
Huntsville, Alabama

W. O. Davies, Manager
M. W. P. Cann, Research Physicist
Plasma Physics Section, IIT Research Institute
Chicago, Illinois

ABSTRACT

A remote sensing cross-beam cross-correlation method is described that will provide spatially resolved average thermodynamic properties. Two detection systems with crossed fields of view are used to monitor radiation emitted from or transmitted through a gas system. The measured cross-correlation coefficient, which depends on the average and fluctuating components of the observed signals, is interpreted in terms of atmospheric properties at the intersection of the fields of view. The average thermodynamic properties are obtained by (1) expanding

the absorption coefficient in a Taylor series and evaluating the fluctuating components as derivatives of the average absorption coefficient, (2) evaluating the measured cross-correlation coefficient in terms of these derivatives, and (3) using absorption band models to relate the absorption coefficient derivatives to thermodynamic properties. The cross-correlation coefficient is given in terms of average thermodynamic properties and an unknown integral, which can be eliminated with measurements at different wavelengths. An example in which fluctuations occur in an isolated absoprtion cell is used to demonstrate that such measurements are possible in principle, and some atmospheric applications are suggested.

Presented at the AIAA 5th Aerospace Sciences Meeting, New York, New York, January 23-25, 1967.

THE INFLUENTIAL ASPECTS OF ATMOSPHERIC DISTURBANCES ON SPACE VEHICLE DESIGN USING STATISTICAL APPROACHES FOR ANALYSIS

By

Robert S. Ryan and Alberta C. King
NASA Marshall Space Flight Center
Huntsville, Alabama

ABSTRACT

The interaction between vehicle dynamics, vehicle control, mean wind speeds, wind shears, and gust, is isolated by separating 407 individual detailed Jimsphere wind profiles into three ensembles of profiles, one containing only turbulence, one containing unfiltered winds, and one containing filtered winds. Using these three ensembles of individual wind profiles as forcing functions, the vehicle response is determined in a statistical manner using a high speed analog computer and the results compared with previous methods of representing wind inputs, such as MSFC synthetic profile and generalized harmonic analysis. Turbulence influence is significant where bending dynamics influence on the bending moment is large. Severe wind profiles are of two types: high wind speed with moderate shear and low wind speed with high turbulence. The second type of wind is severe only for vehicle stations where bending dynamics significantly influence the bending moment. The results show that detailed vehicle simulation and wind turbulence must be combined to have an adequate structural design. The MSFC design profile offers a possible means of obtaining accurate design values.

Presented at the 5th AIAA Aerospace Sciences Meeting, New York, New York, January 23-26, 1967.

A TECHNIQUE FOR ANALYZING CONTROL GAINS USING FREQUENCY RESPONSE METHODS

By

Robert S. Ryan
George C. Marshall Space Flight Center
Huntsville, Alabama

and

Harry Harcrow
Martin Company
Denver, Colorado

ABSTRACT

Minimum control gains are determined by writing the control equation dependent upon ratios rather than specific gains. These ratios of alpha meter or accelerometer gains to attitude gains are varied to achieve an optimum control system. Optimum gains are those that occur for a load minimum condition at some specified vehicle station. The vehicle is described as a linear, dynamic system consisting of 10 degrees of freedom. Rigid-body motion consists of lateral translation and rotation in either the pitch or yaw plane. Effects of elastic deformation are incorporated. Propellant oscillations are described by an equivalent spring-mass-damper system using only the first mode of each propellant tank. Vehicle responses are determined over all significant frequencies. Vehicle bending moment, assumed as the only effective structural load, is determined using a load separation technique. The effects of control system gains are determined by comparisons of exceedances, probabilities of such an occurrence, and the number of cycles of response expected. Root mean squares and variances are used in determining response levels. These results are directly applicable to both control synthesis and structural response since they indicate

frequency sensitivity to atmospheric turbulence. Nonstationary effects are synthetically introduced by completing studies at different flight bandwidth periods.

Published in the Journal of Spacecraft and Rockets, vol 4, no. 3, March 1967.

TURBULENCE MEASUREMENTS IN SUPERSONIC FREE SHEAR LAYERS

By

M. J. Fisher
IIT Research Institute
Chicago, Illinois

K. D. Johnston and D. W. Prosser
George C. Marshall Space Flight Center
Huntsville, Alabama

ABSTRACT

Measurements have been made of local turbulent properties of free shear layers generated by supersonic jets at Mach numbers of 2.5 and 3.4 respectively.

Since probe-type instruments cannot be conveniently employed in flows of this type, an optical method, the crossed beam correlation technique, was employed. This technique involves the use of two beams of radiation which traverse the entire flow in two mutually perpendicular directions. The radiation employed is arranged so that it is partially absorbed by a constituent of the flow. Thus turbulence induced fluctuations of either the thermodynamic properties or concentration of the chosen constituents are reflected as fluctuations of intensity of the resultant beams. Each beam alone, of course, reflects only an integral of the flow properties along its entire path. However, it has been demonstrated previously that statistical correlation of the two resultant beam intensities eliminates this integration yielding local turbulent information instead. Specifically, using this method, local estimates of the intensity, eddy scales in both the streamwise and radial directions, frequencies, convection speeds, and eddy lifetimes are obtained.

In the present work, two compressed air driven nozzles have been employed, both run "on design," to generate jet efflux Mach numbers of 2.5 and 3.4 respectively. The radiation employed was from the vacuum ultraviolet portion of the spectrum, circa 1858 Å. This radiation is absorbed by the oxygen content of the air so that fluctuations of light intensity reflect changes of flow density. Radial profiles of the statistical properties listed above are presented for the first eight diameters of the flow fields and a comparison with subsonic jet data is included.

It is shown that while many of the empirical relationships, previously obtained from subsonic data, still apply, the magnitude of the turbulent scales and frequencies are changed by a factor of approximately two due to the less rapid growth of the shear layer in the supersonic case.

Presented by Dr. Fisher at the Symposium on Structure of Turbulence, I.S.V.R., University of Southhampton, Southhampton, England, March 29-31, 1967.

QUALITATIVE SOLUTION BEHAVIOR ON A FINITE INTERVAL

By Robert W. Gunderson
George C. Marshall Space Flight Center
Huntsville, Alabama

ABSTRACT

Several theorems are presented which provide necessary and sufficient conditions for certain types of solution properties over a finite interval. Results on uniqueness and continuability of solutions are developed following Yoshizawa (Stability Theory by Liapunov's Second Method, Marazen Co., Tokyo, 1966) in which Okamura's function and the generalized derivative of Yoshizawa play particularly important roles. A boundedness property, $b(\alpha,\beta)$, is introduced which corresponds essentially to a solution property previously investigated by Weiss and Infante (Finite Time Stability Under Perturbing Forces and on Product Spaces, Proc. International Conf. on Differential Equations, Mayaguez, Puerto Rico, 1965, to be published by Academic Press) for which only sufficient conditions have previously been obtained. Since the proofs to these theorems are not constructive, however, the actual determination of suitable Liapunov functions remains a formidable problem. Thus, it is important to obtain sufficient conditions for various types of stability and boundedness properties, which increase the likelihood of detecting

suitable functions. Such theorems are provided by combining the concepts of ordinary differential inequalities with the generalized derivative of Yoshizawa. This approach is first used to obtain conditions for the boundedness property $b(\alpha, \beta)$ and leads to several theorems which substantially improve existing results. Next, the property $C(\alpha, \beta, T_1)$ is defined, which corresponds roughly to the "contractive stability" concept of Weiss and Infante, but which overcomes some shortcomings of the contractive stability definition. Several theorems are provided for this property which should prove particularly useful for the applications and which are shown to include, as special cases, the corresponding theorems of contractive stability. A thorough investigation of the definition of stability in the sense of Liapunov is then carried out, prior to defining an analogous property on a finite time interval. Certain solution properties are defined which correspond to the explicit solution behavior required by definitions found in several well known references. The relationship between these definitions is then clarified by establishing the equivalence of the explicit solution properties as successively stronger assumptions are placed on the right-hand sides. The property $S(\epsilon, \delta)$ is then defined and shown to preserve the essence of the stability concept on a finite interval. Finally, as a consequence of a theorem providing sufficient conditions for this property, an extension of a theorem of Halanay (Differential Equations, Academic Press, New York, 1966) is obtained, useful for studying the stability behavior of certain classes of relay control systems.

Ph. D. dissertation, April 1967, University of Alabama.

A PASSIVE OPTICAL TECHNIQUE FOR REMOTE SENSING OF HORIZONTAL WIND PROFILES AND ATMOSPHERIC TURBULENCE

By Fritz R. Krause
George C. Marshall Space Flight Center
Huntsville, Alabama

ABSTRACT

The theory of optical cross-correlation methods is extended to include space and time separations between the collimated fields of view of two astronomical telescopes, which are flown on the same space station. Introducing a time lag in the output signal of the first telescope may be compared to having an undelayed telescope trailing in the same orbit such that its line of sight intersects the line of sight of the second telescope at a chosen altitude. Extended natural radiation backgrounds such as scattered sunlight and thermal emission put radiative power into each telescope's field of view. This power is modulated by the generation, convection and decay of trace constituents such as aerosols and water vapor. The associated fluctuations of radiative power are then detected and correlated to retrieve the common information at the desired crossing height in a way which is known from random vibrating analysis and communication engineering. The potential of crossed-beam missions is illustrated by discussing analytically the simultaneous measurement of horizontal wind profiles and turbulence scales, which is required in numerical methods of weather prediction and water budget surveys to account for the transfer of energy between motions of a different scale.

Presented at the 48th Annual Meeting of the American Geophysical Union, National Academy of Sciences, Washington, D. C., April 17-20, 1967.

EPSILON-FIXED STABILITY AND VECTOR LIAPUNOV FUNCTIONS

By

John H. George and Robert W. Gunderson
George C. Marshall Space Flight Center
Huntsville, Alabama

ABSTRACT

The Liapunov stability definition is "weakened," and necessary and sufficient conditions are obtained for solutions to have this property. Since the necessity proof is not constructive, vector Liapunov functions are introduced to obtain sufficient conditions. These results have proven useful in the practical applications of the theory.

Presented at a seminar, "Guidance Theory and Trajectory Analysis," M. I. T., Cambridge, Mass., May 1967.

INTERPRETATION OF LIAPUNOV STABILITY REGIONS

By John H. George

ABSTRACT

This paper describes a procedure for interpreting results obtained by the direct method of Liapunov. The proposed procedure consists of imbedding a parallelepiped into an approximation to the region of asymptotic stability. The boundary of the approximate region of asymptotic stability is given by a suitable convex Liapunov function equal to a constant. The method consists of maximizing the volume of the parallelepiped with respect to the constraint that the parallelepiped is contained in the approximate region of asymptotic stability.

Published in the AIAA Journal, vol. 5, no. 5, May 1967 and presented at the 1966 JACC Meeting, Seattle, Washington.

THE INSTRUMENTATION OF A MULTICHANNEL ACOUSTIC MODEL

By Herbert T. Bush
George C. Marshall Space Flight Center
Huntsville, Alabama

ABSTRACT

A description is given of the instrumentation and frequency multiplex recording system used in a recent series of acoustic model wind tunnel tests. The retention of phase relationships among groups of acoustic stations was of primary importance.

Presented at the 27th semiannual meeting of the Supersonic Tunnel Association, May 1967.

AEROSPACE NOISE

By G. A. Wilhold

ABSTRACT

A review is made of the problems associated with the prediction of acoustic environments of current and future space vehicles and the resulting consequences of the limitations due to these problems. The noise produced by the hot rocket exhaust and the fluctuating pressure field on the vehicle surface in-flight is discussed. A critique is made of the theoretical, and experimental approaches for estimating these environments. Future work necessary to provide a solid foundation for advancement is delineated.

Published in Astronautics and Aeronautics, May 1967.

FEASIBILITY STUDIES OF A SHORT DURATION HIGH REYNOLDS NUMBER TUBE WIND TUNNEL

By John W. Davis and Hal S. Gwin

ABSTRACT

A relatively inexpensive short duration test facility is described in which extremely high Reynolds number flows are practical in the subsonic, transonic, and supersonic speed ranges. Basically, the method described is a type of blowdown wind tunnel in which the air storage vessels have been replaced by a long tube filled with high pressure gas. Upon bursting of a diaphragm, a short duration steady flow is achieved behind the centered rarefaction fan which propagates into the supply tube. Useful testing may be accomplished during this period by expanding the gas to the desired test condition by conventional means.

Experimental results are presented indicating primarily the transient starting characteristics of a small scale pilot model facility tested. Experimentally determined test data showed close agreement with those predicted by unsteady expansion theory.

Presented at the "27th Semi-Annual Meeting of the Supersonic Tunnel Association" at AEDC, Tullahoma, Tennessee, May 1967.

CONTROL SYSTEMS FOR REUSABLE LAUNCH VEHICLES

By J. C. Blair and J. R. Redus

ABSTRACT

Flight control requirements of reusable launch vehicles are reviewed and compared to those of aircraft, current launch vehicles, and spacecraft. Areas are identified in which more work on the flight control system will improve mission performance. Current work in three areas is briefly reviewed - the use of man in the control loop, the development of systems which can accommodate large changes in the flight conditions, and use of the flight control system to reduce wind-induced loading.

Published in the Proceedings of SAE 2nd Space Technology Conference, Palo Alto, California, May 9-12, 1967.

LUNAR EXPLORATION

By O. H. Vaughan

ABSTRACT

Major theories for the formation of lunar features are discussed. Terrain as seen by earth based telescopes, orbiter photography and surveyor spacecraft is presented and compared with terrestrial topography. Landing sites for the Apollo program and modes of transportation are discussed for use in lunar exploration. Testing of lunar vehicles on earth sites is also presented.

Speech delivered to Huntsville Kiwanis Club, Huntsville, Alabama, May 22, 1967.

THE SECULAR PERTURBATIONS OF THE ORBIT OF A SATELLITE DUE TO THE OBLATENESS OF THE CENTRAL BODY FOR THE 2m-th ZONAL HARMONICS AND DUE TO THE GRAVITATIONAL ATTRACTION OF A THIRD BODY

By Helmut G. L. Krause

ABSTRACT

The most general theory is developed for the secular perturbations of the orbit of a satellite due to the oblateness of the central body for the 2m-th zonal harmonics (where m can be any positive natural number) and due to the gravitational attraction of a third perturbing body under the most general assumption for the orbital shapes and inclinations of the perturbed and the perturbing bodies.

The constant part of the perturbations in the radius vector is also given as well as the different definitions for the mean motion and the semi-major axis, and finally, Kepler's third law in the perturbed motion.

The problem of why authors have found different second-order terms is also discussed. For any planet there exists a distance where the perturbations due to a third perturbing body (Sun) overcome the oblateness perturbations due to the planet.

Paper presented at the 1967 National Symposium: "Saturn V/Apollo and Beyond" of the American Astronautical Society, Huntsville, Alabama, June 11-14, 1967. Proceedings of the Symposium, vol. II, p. (FM-3)-1 to 32. AAS Preprint 67-343, June 1967.

ON PARAMETER STABILITY REGIONS FOR SEVERAL PARAMETERS USING FREQUENCY RESPONSE

By John H. George

ABSTRACT

The goals of this short paper are twofold. First, the parameter stability region, or the D-decomposition technique as it is called in the Russian literature, for obtaining regions of stability in terms of one complex or two real parameters is shown to be applicable when certain elements of the system are given by numerical frequency response data. Second, a technique is presented for interpreting the parameter regions of stability obtained by the D-decomposition method in a space of several parameters.

Published in IEEE Transactions on Automatic Control, June 1967.

ENGINEERING CONSIDERATIONS IN LIFETIME PREDICTIONS

By Robert J. Hill

Aero-Astrodynamics Laboratory
Marshall Space Flight Center
Huntsville, Alabama

ABSTRACT

The S-IVB workshop mission, which involves multiple rendezvous, will require very accurate orbital decay prediction in order to be assured that the object of rendezvous is still in orbit.

Orbital decay and lifetime theories, essentially after Sturm, are applied to the prediction of orbital decay in the presentation.

The orbital lifetime of a vehicle depends on two factors: one, the initial state variables or the initial total energy and two, the time history of its rate of energy loss.

If the initial state were known exactly and all of the variables pertaining to the rate of energy loss had no uncertainties associated with them, the orbital lifetime could be computed very accurately. The uncertainties in the initial state are due primarily to guidance uncertainties and mass uncertainties. Guidance errors are usually relatively small while the mass uncertainties can become significant. An example of this would be a large space vehicle, such as the S-IVB where venting of residual fuel is going on while the vehicle is orbiting.

The variables which are predominate in computing the rate of energy loss, are the atmospheric density, the coefficient of drag and the effective drag area or the attitude of the orbiting body.

Presented at the Symposium on "Environment Induced Orbital Dynamics," Marshall Space Flight Center, Huntsville, Alabama, June 6-7, 1967.

ON OBTAINING DECAY PARAMETERS FROM ORBIT DETERMINATION

By Robert H. Benson

Aero-Astrodynamics Laboratory
Marshall Space Flight Center
Huntsville, Alabama

ABSTRACT

A synopsis of some work which has been done on obtaining decay parameters from orbit determination are presented. Decay parameters are those parameters in the equations of motion which pertain to the aerodynamic perturbations on a satellite. A brief discussion of the orbit determination process, or at least that portion of the orbit determination process which is of prime importance, and a summary of the programs which have been used at MSFC in the Saturn flights to date are presented. Finally, some early results that have been obtained are presented along with idealized results which could be expected under controlled conditions.

Presented at the Symposium on "Environment Induced Orbital Dynamics," Marshall Space Flight Center, Huntsville, Alabama, June 6-7, 1967.

A CONSTRUCTION OF PROBABILITY ENVELOPES OF FLUX-ENERGY SPECTRA

By Tom S. Dollman
Aero-Astrodynamics Laboratory
George C. Marshall Space Flight Center
Huntsville, Alabama

ABSTRACT

During 2,000 days of the previous solar cycle, data were collected which yielded, upon analysis, the fluxes of solar particles with energy levels equal to or greater than 2 given energy levels (30 Mev and 100 Mev). The observed events which yielded these data consisted of a group of 29 sporadically occurring, separate solar storms during which a number of protons for limiting the studies to these ranges are that (1) even the most lightly shielded vehicles afford protection against particles in the 10 Mev to 30 Mev range and (2) the extrapolation very far beyond 100 Mev might tend to become relatively inaccurate. However, the data observed and calculated in the 10 to 30 Mev range, as well as in the 100 to 140 Mev range, will be used so that the energy ranges in this paper extend from 10 to 140 Mev. This was done to more accurately estimate the flux-energy spectra of the solar flare percentile models.

It is assumed that the distribution of the particles is isotropic, although this generalization might prove faulty during the initial phases of the solar storms. Previous analyses of these data in several authoritative papers have resulted in the establishment of a distribution of characteristic rigidities of these fluxes. However, the present analysis is being prepared to provide more detailed information on the indicated probabilities of occurrence of proton fluxes. The probabilities of occurrence of an integrated flux whose energies equal or exceed a given energy level are determined for various mission lengths. This is a relatively new approach, and does not deal in characteristic rigidities.

Presented at the American Astronautical Society meeting "Apollo and Beyond" in Huntsville, Alabama, June 11-14, 1967.

THE ENVIRONMENT OF MERCURY

By

Otha H. Vaughan, Jr. and Don K. Weidner
Aero-Astrodynamics Laboratory
George C. Marshall Space Flight Center
Huntsville, Alabama

ABSTRACT

This paper presents the results of a very extensive literature survey performed to establish engineering environmental criteria for the planet Mercury. Three model atmospheres, which have been developed based on the studies of Rasool, Gross, and McGovern, are discussed.

The atmospheric models developed during the course of the survey were based on a surface temperature of 520°K and a surface pressure of the following ranges:

	Pressure	Mean Molecular Weight
Maximum Density Model	1000 dyn/cm^2	44
Mean Density Model	5000 dyn/cm^2	42
Minimum Density Model	5000 dyn/cm^2	35.6

The atmospheric constituents assumed for our models were CO_2, N_e, A, and N_2.

The surface conditions expected on Mercury are discussed and are based on analysis of radar and other data. Since Mercury exhibits a radar reflectivity (0.060) similar to the moon, the surface roughness based on a scale of radar wavelengths appears to be comparable with the moon's surface roughness as deduced by radar studies.

Additional information on the magnetic field, rotation rate, albedo, temperature, and other environmental design criteria data is also discussed.

Presented at the American Astronautical Society meeting "Apollo and Beyond" in Huntsville, Alabama, June 11-14, 1967.

RC TRANSFER-FUNCTION SYNTHESIS AND DIGITAL COMPUTER APPLICATION

By

James W. Fontenot
Northrop Space Laboratories
Huntsville, Alabama

Don H. Townsend
Aero-Astrodynamics Laboratory
George C. Marshall Space Flight Center
Huntsville, Alabama

ABSTRACT

This paper presents a study of techniques for RC synthesis of minimum-phase transfer functions into passive networks. The selected techniques are simulated by a computer program. Network and design constraints required the realization to have a resistance termination, a d.c. path to ground from input to output terminals, and a frequency response which does not deviate from the desired filter characteristic. The problem was divided into two parts where one method synthesizes functions of order equal to or larger than two-over-two and the other method applies to functions of order less than two-over-two. The first method uses network partitioning which requires two cascaded networks. One network realizes the complex transmission zeros and the other yields the negative real transmission zeros and, in most cases,

all of the poles. The second method is based upon the solution of simultaneous algebraic equations which yields the circuit parameters. Each different order function yields a unique solution and the computer logic decisions increase rapidly for higher order functions. The uniqueness of the realization and practical applications dictated that five-over-five order functions be the upper limit for synthesis by a single computer program. Numerical examples are given for the purpose of clarifying these methods.

Presented at the American Astronautical Society Meeting, "Apollo and Beyond," Huntsville, Alabama, June 11-14, 1967.

STUDY OF THE LUNAR THERMAL ENVIRONMENT

By

Frank B. Tatom

and

K. V. Ramakrishna
Northrop Space Laboratories
Huntsville, Alabama

Otha H. Vaughan
Aero-Astrodynamics Laboratory
George C. Marshall Space Flight Center
Huntsville, Alabama

ABSTRACT

A research effort has been carried out to provide a means of predicting the surface temperature of objects near the Moon. This effort has been in two phases and the first phase has been presented in a previous paper. This paper discussed the second phase and its results.

The research efforts have resulted in a digital computer program. This program is capable of predicting the temperature at a specified point on the surface of an object located near the lunar surface. The concept of self-sufficiency is employed in this program. The only input items required are the location of the object, the time period of interest, the assumed lunar surface thermophysical properties, the shape, dimensions, and orientation of the object, the location of the point on the object, and the thermophysical properties of the object's surface. The program can handle objects of three shapes: a rectangular box, a circular cylinder, and a sphere.

Extensive use was made of coordinate transformations, vector analysis, and a modified version of Oppenheim's network analogy to develop the analytical model, which is the basis for the computer program. That portion of the lunar surface which is "seen" by the point on the surface of the object is divided into a number of incremental areas. The coordinates of the center of each such area increment are established in such a manner as to yield the most representative value for each shape factor corresponding to an area increment. These shape factors are calculated and then grouped according to the surface temperature of the area which each factor represents. To avoid excessive computation time, surface temperatures are calculated only for perimeter points of the region viewed. Based on the temperature at these points, the temperature at all points within the region can be established. Solution of the appropriate thermal network equations then yields the temperature of the surface of the object at the point of interest.

The surface temperature of Surveyor I has been predicted by means of the analytical technique with generally good agreement between prediction and measured data. The surface temperature of Surveyor III has also been predicted but measured data is not yet available for purposes of comparison.

The program and the unified analytical model upon which it is based, represent a flexible engineering tool which is capable of predicting with good accuracy the lunar thermal environment.

Presented at the American Astronautical Society Meeting "Apollo and Beyond", Huntsville, Alabama, June 11-14, 1967.

CROSSED-BEAM TEST ARRANGEMENTS FOR REMOTE SENSING OF ATMOSPHERIC PHENOMENA

By Fritz R. Krause

ABSTRACT

The crossed-beam is a new test arrangement for remote sensing of atmospheric phenomena. The method employs triangulation of two collimated light beams to study turbulence and thermodynamic properties in a preselected region. Atmospheric phenomena in each beam modulate the mean radiative power, which is put into the beam by extended natural sources such as scattered sunlight. The associated fluctuations which are received along both beams, are multiplied and averaged for several beam separations in space and time. This "two beam product mean value" is shown to approximate the space time correlation between the fluctuations of radiative power which occur at the two points of minimum beam separation. The method thus approximates two point product mean values, which are commonly used in the mathematical description of random fields to derive turbulence parameters such as scales, spectra, eddy lifetimes, convection speeds, etc.

The feasibility to remotely sense atmospheric phenomena is established by considering measured atmospheric modulations of radiative power, which were produced by light extinction and emission processes in a single collimated beam. The potential of crossed-beam test arrangement is illustrated by describing the operations, which would approximate altitude profiles of horizontal winds from a single sweep with orbiting detectors or a multiple sweep with ground detectors.

Presented at the Institute for Telecommunication Sciences and Aeronomy, Boulder, Colorado, September 26, 1966.